

# Synthesis and Characterisation of Iron- based Nanoparticles for Magnetic Hyperthermia

**Simone Famiani**

Supervisors

Professor Nguyễn Thi Kim Thanh (UCL)

Professor Shinya Maenosono (JAIST)

A thesis submitted for the degree of Doctor of Philosophy in the Faculty of  
Mathematical and Physical Sciences, Department of Physics & Astronomy at

**University College London**

August 2019

## **Declaration of Originality**

*“I, Simone Famiani, confirm that the work presented in this thesis is my own. Where information has been derived from other sources, I confirm that this has been indicated in the thesis. This thesis has not been submitted elsewhere for examination purposes.”*

March 2019.

**Simone Famiani**

## Acknowledgment

This PhD has been an incredible and challenging journey that I would have never been able to complete without the help of wonderful people I met along the way. Some of them have been amazing colleagues and others became also great friends. I would like, therefore, to use this section to warmly thank all of them for their support and recognise all the value they added to this journey.

Firstly, I want to thank my supervisors Professor Nguyễn Thị Kim Thanh and Professor Shinya Maenosono for giving me the opportunity to carry out my PhD under the University College London/Japan Advanced Institute of Science and Technology scheme.

I would like to thank all my lab colleagues at the UCL Healthcare Biomagnetics Laboratories that were present during my first year for the warm welcome and the time they devoted me, training me on the different characterisation techniques and laboratory equipment at the Royal Institution of Great Britain, including Dr. Roxanne Hachani and Dr. Kuan Boone Tan. Also, my thanks go to Dr. Paul Southern and Dr. Lara Bogart for their help on the topic of magnetism and magnetic hyperthermia and Mossbauer spectroscopy. My special thanks go to Dr. Stephen Nesbitt who has always been available to help me and answer any questions when I needed. In particular, I am really thankful to Dr. Aziliz Hervault, her competence and attitude towards life and science have really been insightful to me and I am grateful we had the chance to know each other and work together.

I would also like to thank the other team members of the research team at UCL Healthcare Biomagnetics Laboratories that started the same journey with me and with whom I shared many precious moments, including Georgios Kasparis, Francesco Rossi, Lilin Wang for always finding the time to help me anytime I needed it, Fang-Yu

Lin for the valuable discussions on magnetic hyperthermia and Andreas Sergides, for the invaluable moral support throughout the whole PhD.

Finally, I would also like to thank the new members of the research team at UCL Healthcare Biomagnetics Laboratories that were there during my last year as a PhD student, Dr. Stefanos Mourdikoudis, Diana Raie, Thithawat Trakoolwilaiwon and Matej Sebek. My distinctive thanks go to Alec La Grow for all the amazing discussions about nanochemistry, the invaluable help given during my last year of PhD, the professional advice and for providing great tips on artisanal beers and how to brew your own one. I would also thank the people from the Chemical Engineering group at UCL for their help and collaboration, including Dr. Maximilian Besenhard for all the help with magnetic hyperthermia measurements and Dr. Katerina Loizou for the useful science discussions and the help to navigate through my PhD. Special distinctions go to Dustin Bauer for the help with XPS and other techniques, and the wonderful late conversations during my year at JAIST.

I would like to thank all the people in my Japanese research team at the Japan Advanced Institute of Science and Technology, my supervisor Professor Shinya Maenosono, Dr. Derrick Mott, Dr. Pryiank Mohan, Dr. Maninder Singh, Dr. Mari Takahashi, Masahito Hatsukano, Wei Zhou, Kitaura and many others. They all helped me to settle in Japan, especially Kitaura, thank you so much for all the length you went to help me out. More particularly, I give my special thanks to Professor Shinya Maenosono who had an important impact on the development of this project and was always available and willing to help when I needed his expertise, also allowing me to attend several international conferences. I would also like to thank Professor Yoshifumi Oshima for dedicating his time and knowledge to help me out with the EELS characterisation of nanoparticles at JAIST.

I want to also thank the University College London and the Japan Advanced Institute of Science and Technology for my PhD scholarship and their financial support that

allowed me to attend national and international conferences during those three years, where I was given the opportunity to give talks, present posters, network with other scientists and students from all over the world.

Last but not least, I want to thank my family and friends and particularly my parents, who always supported and had my back during these years. Luca, Mattia, Chiara, Claudia thank you so much for undoubtedly believing in me. To Stefan, my partner and best friend. You have always been there for me, supporting me in all my choices during this past 4 years. I cannot thank you enough for all the support and confidence you gave me, always believing in me even in the toughest moments and there is no way I can properly express how grateful I am and will always be. Thank you.

Simone Famiani

## Abstract

Magnetic nanoparticles (MNP) have been recently gaining much attention thanks to their application as cancer-killing agents through heat delivery in magnetic hyperthermia treatment. Although MNP are considered very promising, there is still the need to investigate different magnetic materials and nanoparticles size to improve the performances of MNP in magnetic hyperthermia. Therefore, it is important to expand the knowledge on the chemistry of the formation of Fe-based MNP.

In this work, different Fe-based, MNPs were synthesised and their efficiency in magnetic hyperthermia was also evaluated. The NPs were fully characterised to confirm the final phase and composition and the characterisation techniques used are described in Chapter 2.

Chapter 3 describes the synthesis and characterisation of metallic Fe NPs. As this material is sensitive towards oxidation, to overcome this limitation, Fe NPs of different size were synthesised using a novel approach that allowed a greater size control, and the study of oxidative processes that depends on the size of the synthesised NPs. In this chapter an easy and optimal ligand transfer of the synthesised NPs in water was investigated and different strategies were employed, including polymer encapsulation, silica coating and ligand exchange with a dopamine-functionalised polymer. The latter resulted in the best performances and it was used for the transfer in water of Fe NPs of different size. The  $\approx 20$  nm Fe NPs, can maintain a metallic core even after ligand exchange for 2 months, with high magnetic heating efficiency, whereas smaller Fe NPs ( $\approx 15$  nm) oxidised completely.

In Chapter 4, the synthesis of  $\text{Fe}_2\text{C}$  NPs was investigated. This alloy possesses the magnetic and metallic feature of metallic Fe with an increased stability towards oxidation thanks to the C atoms in the crystal structure. After optimising the

synthesis, the material was fully characterised to ensure the uniformity of the final phase. The NPs were then transferred in water using the strategy optimised in Chapter 3 and the enhanced chemical stability of the Fe<sub>2</sub>C NPs towards oxidation was shown by the fact that the Fe<sub>2</sub>C phase was fully retained even in  $\approx$  14 nm NPs. The NPs are also tested as magnetic hyperthermia agents.

In Chapter 5 Fe<sub>3</sub>O<sub>4</sub> NPs are studied. In this case, novel plate-like Fe<sub>3</sub>O<sub>4</sub> NPs were synthesised, as anisotropic shaped NPs are known to possess enhanced performances in magnetic hyperthermia. It was shown that the main agent affecting the final shape of NPs during the reaction was the chloride contained in the molecule hexadecyl ammonium chloride (HDA-Cl). The synthesis of plates-like NPs was optimised and different size of nanoplates were obtained by using different ligand with the best performing being sodium oleate. Plates NPs of different size were then tested for magnetic hyperthermia.

In Chapter 6 the results from the previous chapters were summarised and the magnetic hyperthermia performances of different NPs were discussed and compared, including also commercially available magnetic NPs for biomedical applications.

## Impact Statement

The research carried out in this work, led to the synthesis and optimisation of magnetic nanoparticles for magnetic hyperthermia, which has had a tremendous growth as promising technique to treat patients with tumours in areas that are hard to reach by surgical means. Magnetic hyperthermia is a non-invasive therapy and can be delivered locally using magnetic nanoparticles as probes to deliver heat on specific tumour cells. This makes magnetic hyperthermia able to potentially replace or decrease the use of chemotherapy, which is a non-local and very invasive therapy. In the present work the focus is on the development of the nanoparticles to be used in magnetic hyperthermia and the insights found here can have a broad impact in the in terms of advancement for the use of nanomaterials in biomedical applications and, more generally, in the nanochemistry field.

In the first experimental chapter the synthesis of metallic Fe NPs provided useful insights on the formation of metallic NPs using sequential addition of precursor in the reaction solution. Allowing a greater tunability of the final size of NPs, this approach could be translated into the synthetic approach of other NPs wherever a great degree of size control is required. Its simplicity, yet its effectiveness, makes it a versatile approach for the synthesis of NPs where the final properties are highly dependent on the size. Moreover, specifically for the case of Fe NPs, it has been proven their potential and employability in magnetic hyperthermia and this can further boost new research on the use of such material in those biomedical applications that requires highly magnetic NPs.

Fe<sub>2</sub>C is among the newest materials being considered for biomedical applications thanks to its unique properties which combine high chemical stability and high magnetic moment. Being the research on iron carbides NPs for biomedical applications still on the early stages, the work done here sheds a light on the

formation and phase composition of such material at the nanoscale. Such information is vital to fully understand the system and to progress on the optimisation of iron carbide NPs, whose colloidal synthesis has proven challenging in the past. The progress made here can be used as a starting step to achieve efficient tools for magnetic hyperthermia, but also for modern technology where iron carbide plays an important role in many catalytic reactions like the formation of syngas.

Furthermore, even though  $\text{Fe}_3\text{O}_4$  NPs are among the most studied for biomedical applications, the work done here introduces new ways to produce anisotropic magnetic nanoparticles which possess superior heating capabilities in magnetic hyperthermia. The work adds on the recent efforts of synthesising shaped magnetic nanoparticles exploiting the interaction of chloride species with the forming NPs. This ability of synthesising plate-like nanoparticles has also the potential to be used for the anisotropic growth of nanoparticles made of different materials.

Finally, special attention was paid on the development of a general procedure able to transfer any kind of iron-based nanoparticles from the reaction solvent to water using a dopamine modified polymer. The versatility of the transfer could be beneficial for many other nanoparticles-based applications where dispersibility in biological environment is required.

## Table of Contents

<b>Declaration of Originality</b> .....	<b>2</b>
<b>Acknowledgment</b> .....	<b>3</b>
<b>Abstract</b>	<b>6</b>
<b>Impact Statement</b> .....	<b>8</b>
<b>Table of Contents</b> .....	<b>10</b>
<b>List of Tables</b> .....	<b>13</b>
<b>List of Figures</b> .....	<b>15</b>
<b>List of units and abbreviations</b> .....	<b>23</b>
<b>Chapter 1 Introduction and literature review</b> .....	<b>25</b>
1.1 Nanoparticles for biomedical applications.....	26
1.2 Synthesis of NPs in solution .....	26
1.3 Magnetic nanoparticles for hyperthermia therapy .....	30
1.4 Methods for making water dispersible MNPs.....	48
1.5 Conclusion .....	52
1.6 Thesis Outline .....	53
<b>Chapter 2 Characterisation Techniques</b> .....	<b>55</b>
2.1 X-Ray Diffraction (XRD).....	56
2.2 Superconducting quantum interference device – vibrating sample magnetometer (SQUID-VSM).....	59
2.3 Transmission electron microscopy (TEM) .....	63
2.4 X-ray photoelectron spectroscopy .....	69
2.5 Dynamic light scattering.....	72
2.6 Magnetic Hyperthermia .....	74

2.7	Nuclear magnetic resonance spectroscopy .....	77
2.8	Fourier Transformed Infrared Spectroscopy .....	78
2.9	Iron quantification technique.....	80
2.10	Raman Spectroscopy .....	83
2.11	<sup>57</sup> Fe Mössbauer Spectroscopy .....	83
<b>Chapter 3 Synthesis of Fe@Fe<sub>x</sub>O<sub>y</sub> Nanoparticles.....</b>		<b>85</b>
3.1	Introduction.....	86
3.2	Materials and Methods .....	88
3.3	Results and discussion .....	95
3.4	Ligand modification for water-soluble Fe NPs .....	115
3.5	Magnetic Hyperthermia .....	141
3.6	Discussion on oxidation of Fe NPs.....	145
3.7	Conclusion .....	146
<b>Chapter 4 One pot synthesis of iron carbide NPs for magnetic hyperthermia....</b>		<b>148</b>
4.1	Introduction.....	149
4.2	Materials and methods .....	151
4.3	Results and discussion .....	153
4.4	Conclusion .....	187
<b>Chapter 5 Shaped iron oxide nanoparticles for magnetic hyperthermia .....</b>		<b>188</b>
5.1	Introduction.....	189
5.2	Materials and method .....	191
5.3	Results and discussion .....	193
5.4	Conclusion .....	224
<b>Chapter 6 Conclusions and future works .....</b>		<b>225</b>

6.1	Conclusions.....	226
6.2	Future works.....	228
	<b>Appendix: Publications and conferences attended .....</b>	<b>230</b>
	<b>Bibliography .....</b>	<b>232</b>

## List of Tables

Table 1-1 Summary of iron-based material with the highest $M_s$ value. <sup>71</sup> .....	41
Table 3-1 Amount of Fe precursor used for single hot-injection.....	95
Table 3-2 Summary of NPs size and Fe size obtained through TEM and XRD analysis. .....	97
Table 3-3 Conditions used for continuous hot-injections.....	100
Table 3-4 Reaction condition used to obtain different sizes of Fe NPs .....	103
Table 3-5 Summary of size for the four samples obtained through TEM and XRD, magnetic properties and estimated size using magnetic properties. The XRD size values of Fe core were obtained applying the Scherrer formula on the main peak (110) of $\alpha$ -Fe pattern. The diameter, $d$ , of Fe TEM was estimated by measuring the size of the core of the NPs in the TEM micrographs. The thickness of $Fe_xO_y$ phase was estimated by subtracting the average diameter of the core@shell NPs with the average diameter of Fe core, dividing the total by 2.....	114
Table 3-6 Conditions used for the coating of Fe NPs with Silica.....	116
Table 3-7 Hydrodynamic size and Z-potential values for Silica-coated NPs.....	123
Table 3-8 Magnetic Hyperthermia measurements for 18.3 nm NPs (2.0 mmol) and relative conditions used.....	145
Table 4-1 Summary of the different parameters used for the synthesis of IC NPs.	154
Table 4-2 Summary of the reaction conditions used.....	161
Table 4-3 Fit parameters for Fe NPs XPS Fe2p spectrum and calculated proportion of the species present. ....	176
Table 4-4 Fit parameters for $Fe_2C$ NPs XPS Fe2p spectrum and calculated proportion of the species present.....	176
Table 4-5 Best fit parameters for the room temperature Mossbauer spectrum preseted in Figure 4.16 .....	182
Table 4-6 Magnetic hyperthermia measurements for $Fe_2C$ NPs and relative conditions used.....	186
<b>Table 5-1</b> Reaction conditions for the experiments presented in this chapter. ....	192

Table 5-2 Summary of sample' feature for Experiment IV (without SO) and XII (with 0.8 mmol SO).....	217
Table 5-3 Magnetic Hyperthermia measurements for Experiment IV and XII and relative conditions used.....	223
Table 6-1 Summary of heating efficiency of different magnetic NPs.....	228

## List of Figures

Figure 1-1 a) The graph shows three stages in NP synthesis, where (I) corresponds to the increase of monomer concentration due to precursor decomposition, (II) corresponds to the supersaturation and nucleation phase, and (III) the growth. b) The graph shows the effect of concentration of monomers on size and distribution. Figure 1.1a is reproduced from the work of Park et al. <sup>8</sup> and Figure 1.1b is reproduced from the work of Yin et al. <sup>7</sup> .....	27
Figure 1-2 Schematic response of magnetic materials to an applied magnetic field. <sup>50</sup> .....	33
Figure 1-3 M-H curve showing a typical hysteresis loop of a multi-domain magnetic material. The loop arises from the different fields intensity necessary to align different domains. <sup>3</sup> .....	34
Figure 1-4 Schematic representation of the relationship between coercivity and particles size in case of single-domain and multi-domain particles. ....	35
Figure 1-5 Schematic representation of the Néel versus Brownian relaxation. Néel relaxation: the magnetic moment rotates within each particle. Brownian relaxation: the particle rotates as a whole. ....	37
Figure 1-6 Threshold diameters for superparamagnetism ( $d_{sp}$ ) and maximum monodomain ( $d_{cr}$ ) size for spherical nanoparticles, based on bulk material parameters. <sup>66</sup> .....	40
Figure 2-1 Bragg diffraction from a cubic crystal lattice .....	57
<b>Figure 2-2 Josephson union in a SQUID flux sensor</b> .....	60
Figure 2-3 Schematic representation of a magnetic Hysteresis loop. ....	62
Figure 2-4 Schematic representation of TEM and its main components. Image provided by Dr Graham Beards-Wikipedia, Public domain. <a href="https://commons.wikimedia.org/w/index.php?curid=8106664">https://commons.wikimedia.org/w/index.php?curid=8106664</a> .....	64
Figure 2-5 Electron diffraction pattern coming from the interaction of electrons with Fe <sub>2</sub> C nanocrystals. ....	66

Figure 2-6 Schematic representation of X-ray emission and energy loss electron formation after electron bombardment of the sample. As a vacancy in the core is formed, an X-ray is emitted while a higher energy electron drops down to fill the position. The energy loss electron is formed after the inelastic interaction of a coming electron with a core electron.....	67
Figure 2-7 Schematic representation of photoelectron and Auger electron emission after X-ray bombardment of the sample.....	70
Figure 2-8 Representation of the sample holder for magnetic hyperthermia measurement. Picture from the producer. <sup>146</sup> .....	75
Figure 2-9 Example of a typical heating curve obtained during the analysis of NPs performance in Magnetic Hyperthermia.....	76
Figure 3-1 Specific loss power (or specific absorption rate) evolution as a function of size for various nanoparticle systems at 300 kHz and 39.8 kA m <sup>-1</sup> . <sup>67</sup> .....	87
Figure 3-2 Schematic representation of overall synthetic setup and procedures. ...	90
Figure 3-3 TEM pictures for reactions a) Fe_1 using 0.20 ml of Fe(CO) <sub>5</sub> , b) Fe_2 using 0.25 ml of Fe(CO) <sub>5</sub> , c) Fe_3 using 0.30 ml of Fe(CO) <sub>5</sub> , d) Fe_4 using 0.35 ml of Fe(CO) <sub>5</sub> . .....	96
Figure 3-4 XRD patterns for different amount of iron precursor Fe(CO) <sub>5</sub> used: 0.20 ml for Fe_1, 0.25 ml for Fe_2, 0.30 ml for Fe_3 and 0.35 ml for Fe_4. ....	97
Figure 3-5 Extended La-Mer plot configuration.....	99
Figure 3-6 a) TEM micrographs of Fe NPs synthesised with 1.3 ml/h injection rate and XRD pattern of the same sample. b) TEM micrographs of Fe NPs synthesised with 0.4 ml/h injection rate and XRD pattern of the same sample. c) b) TEM micrographs of Fe NPs synthesised with 0.2 ml/h injection rate and XRD pattern of the same sample. Reference pattern in the XRD corresponds to α-Fe (pdf ref. 00-006-0696).....	101
Figure 3-7 TEM images of Fe NPs and relative zoom-in inset of the yellow square, for 1.0 mmol a), 1.3 mmol b), 2.0 mmol c) and 2.4 mmol d) of Fe(CO) <sub>5</sub> used. The scale bars in all four pictures correspond to 50 nm. e) Size distribution for the four reactions with different amount of precursor used. f) The relationship between NP volume and the amount of Fe(CO) <sub>5</sub> injected into the system. ....	105

Figure 3-8 a) HAADF-STEM images of one Fe NP synthesized using 1.3 mmol of Fe(CO) <sub>5</sub> . EDS elemental mapping is also shown where signal intensities coming from b) oxygen and c) iron. d) It shows an overlapping of the signals coming from the two elements.....	106
Figure 3-9 HAADF-STEM images of one Fe NP synthesized using 2.0 mmol of Fe(CO) <sub>5</sub> . EDS elemental mapping is also shown where signal intensities coming from b) oxygen and c) iron. d) It shows an overlapping of the signals coming from the two elements. ....	107
Figure 3-10 a) High-resolution HAADF-STEM image of a core@shell NP, with the lattice spacing of Fe <sub>3</sub> O <sub>4</sub> /γ-Fe <sub>2</sub> O <sub>3</sub> in red, and α-Fe in blue. b) An area of the oxide shell, with c) the corresponding indexed FFT from the dashed white box. ....	108
Figure 3-11 (top) XRD patterns of the Fe NPs synthesised using different amounts of Fe(CO) <sub>5</sub> . The dark grey reference pattern corresponds to Fe <sub>3</sub> O <sub>4</sub> phase and the green one to bcc-Fe phase (JSPC PDF no. 01-079-0418 and 00-006-06969 respectively). (bottom) Fitting of XRD pattern data of Fe NPs synthesised with 1.3 mmol of Fe(CO) <sub>5</sub> . ....	110
Figure 3-12 Fe2p XPS spectrum of Fe NPs synthesised at different injection time.	111
Figure 3-13 Magnetic hysteresis loop taken at 300 K (blue line) and 5 K (red line) with relative zoom in at low fields for the four samples: a) 1.0 mmol b) 1.3 mmol c) 2.0 mmol and d) 2.4 mmol of Fe(CO) <sub>5</sub> used.....	112
Figure 3-14 Igepal-CO-520 molecular structure .....	115
Figure 3-15 TEM pictures of FeSi_1 reaction aliquot at 1.5 h (left) and at the end of the reaction (left). ....	118
Figure 3-16 FTIR measurement of FeSi_1 NP before and after Silica coating (3 h) reaction. ....	119
Figure 3-17 XRD pattern of FeSi_1 NPs with α-Fe (grey) and Fe <sub>3</sub> O <sub>4</sub> (blue) reference patterns. ....	120
Figure 3-18 TEM images of FeSi_2 reaction aliquot at 3 h of reaction (left) and sample at the end of the reaction after 24 h (right). ....	121

Figure 3-19 TEM images of the FeSi_3 sample at the end of the reaction after 3 h. .....	121
Figure 3-20 TEM images of the FeSi_4 sample. In this case, the amount of TEOS added was split into two different aliquots. ....	123
Figure 3-21 Molecular structure of PMAO polymer. ....	124
Figure 3-22 a) High magnification and b) low magnification TEM images for the PMAO encapsulated Fe NPs (2.0 mmol) using a NPs:polymer mass ratio of 12. c) XRD spectrum of the Fe@PMAO nanoparticles where the green reference pattern refer to $\alpha$ -Fe phase and the grey one refer to magnetite.....	126
Figure 3-23 TEM images of Fe NPs after encapsulation with PMAO using a ratio of NPs : polymer equal to 1:40. High magnification image on the left and low magnification on the right.....	127
Figure 3-24 Molecular structure of PIMA (left) and dopamine (right). ....	129
Figure 3-25 $^1\text{H-NMR}$ of dopamine hydrochloride. ....	131
Figure 3-26 $^1\text{H-NMR}$ of PIMA-Dopa polymer. ....	131
Figure 3-27 TEM images at low (left) and high (right) magnification of Fe NPs after ligand exchange process with PIMA-Dopa polymer. ....	133
Figure 3-28 Picture of Fe NPs transferred in water using PIMA-Dopa polymer.....	134
Figure 3-29 $^1\text{H-NMR}$ of Mod-PIMA-Dopa polymer .....	136
Figure 3-30 Characterization of the samples after ligand exchange: TEM picture of Fe NPs synthesised with a) 1.3 mmol and b) 2.0 mmol of $\text{Fe}(\text{CO})_5$ , the scale bar corresponds to 20 nm. c) The XRD patterns are shown with the grey reference pattern corresponding to the $\text{Fe}_3\text{O}_4$ phase and the green one to the Fe phase.....	137
Figure 3-31 DLS measurement of 18.3 nm Fe NPs in Milli-Q water with relative fit of the data using LogNormal function. ....	138
Figure 3-32 Colloidal stability study of the 18.3 nm NPs in different pH solutions. a) Hydrodynamic size in different pH, b) Zeta-potential value in different pH. c) Picture of the dispersion after 24 h.....	140
Figure 3-33 Colloidal stability study of the 18.3 nm NPs in NaCl solutions at various concentrations. a) Hydrodynamic size in different NaCl concentrations, b) Zeta-	

potential value in different NaCl concentrations. c) Picture of the dispersion after 24 h.....	141
Figure 3-34 Heating profile of 18.3 nm NPs at 303 KHz and 308 Gauss (top). Fitting of the first heating curve for the calculation of dT/dt (bottom).....	143
Figure 3-35 TEM picture of Fe NPs (2.0 mmol) dispersed in water, 2 months after ligand exchange with Mod-PIMA-Dopa. ....	144
Figure 4-1 Schematic representation of the synthetic procedure for the formation of iron carbide NPs. ....	152
Figure 4-2 TEM images of the samples FeC_1 to FeC_6 with the mmol of OAm (red) and HDA-Cl (blue) used in the reaction. ....	155
Figure 4-3 XRD patterns of samples FeC_1 to FeC_6 with the mmol of OAm (grey) and chloride source (blue) used in the reactions. ....	157
Figure 4-4 TEM for carbide at different temperature 220 °C (FeC_7), 260 °C (FeC_4) and 300 °C (FeC_8). ....	159
Figure 4-5 XRD patterns of IC NPs synthesised at different temperature 220 °C (FeC_7), 260 °C (FeC_4) and 300 °C (FeC_8). ....	160
Figure 4-6 Tem images at different magnification (top) and XRD pattern of FeC_9 (bottom), obtained using HDA. ....	162
Figure 4-7 a) XRD pattern of FeC_9 after centrifugation where the sample from the supernatant and the precipitate where analysed. b) TEM and ED pattern of the sample from precipitate and c) TEM and EM pattern of the sample from supernatant. ....	163
Figure 4-8 a)TEM images of FeC_10 sample using 3 mmol of ODA, and b) relative size distribution plot. c) XRD pattern of the same sample with relative fitting of the spetra matching the pattern of Fe <sub>2</sub> C phase(JSPC PDF No. 00-036-1249).....	165
Figure 4-9 TEM images with the relative ED pattern of Fe NPs (top), Fe <sub>2</sub> C NPs after 5 min at 260 °C (middle) and Fe <sub>2</sub> C NPs after 15 min at 260 °C (bottom). ....	168
Figure 4-10 Integrated ED patterns of Fe and Fe <sub>2</sub> C NPs and plotted in terms of d-spacing.....	169

Figure 4-11 HR-TEM image (top) with lattice spacing of Fe <sub>3</sub> O <sub>4</sub> /Fe <sub>2</sub> O <sub>3</sub> in blue and Fe <sub>2</sub> C in red and STEM-HAADF image(bottom) of IC NPs.....	171
Figure 4-12 EELS spectrum of the Fe edge on Fe <sub>2</sub> C NPs with relative area analysed underlined in yellow. The signal comes from the core (top) and from the shell area (bottom). .....	173
Figure 4-13 Fe2p core level XPS for Fe NPs (top) and Fe <sub>2</sub> C NPs (bottom). Black, yellow, blue, and red curves represent raw data, Shirley background, deconvoluted peaks and the sum of the components, respectively. ....	175
Figure 4-14 C1s core level XPS spectra for Fe NPs (grey) and Fe <sub>2</sub> C NPs (black). ....	178
Figure 4-15 a) Raman spectrum of Fe NPs and Fe <sub>2</sub> C NPs. b) Best fit of the Raman spectrum for Fe <sub>2</sub> C NPs. ....	179
Figure 4-16 Room temperature Mossbauer spectrum for Fe <sub>2</sub> C NPs. The best fit was obtained using a superposition of two Voigtian doublets and four Voigtian sextets. The residual to the measured data is indicated. ....	181
Figure 4-17 a) Magnetic hysteresis loop taken at 300 K (blue line) and 5 K (red line) with relative zoom in at low fields; b) ZFC-FC curve taken with H = 100 Oe.....	183
Figure 4-18 FTIR spectrum of Fe <sub>2</sub> C NPs with grey line indicating the as-synthesised NPs and the blue line indicating the NPs after ligand exchange. ....	184
Figure 4-19 a)TEM images of Fe <sub>2</sub> C NPs after ligand exchange at lower b) and higher magnification. c) Electron diffraction pattern is shown and d) the relative plot in terms of d-spacing is compared with α-Fe (blue), Fe <sub>2</sub> C (green) and Fe <sub>3</sub> O <sub>4</sub> (grey) patterns. ....	185
Figure 5-1 TEM image (left) and XRD pattern (right) of the sample obtained through the decomposition of Fe(acac) <sub>3</sub> at high temperature in OAm with HDA-Cl. The grey reference pattern corresponds to Fe <sub>3</sub> O <sub>4</sub> phase and the blue one to bcc-Fe phase (JSPC PDF no. 01-079-0418 and 00-006-06969 respectively). ....	195
Figure 5-2 High magnification TEM image for Experiment I sample. ....	195
Figure 5-3 TEM images taken by tilting the sample holder at different angles from 0 to 60 degrees. ....	197

Figure 5-4 TEM images and relative electron diffraction of different areas of the same sample (Experiment I) containing magnetite nanoparticles (top) and large material made of $\alpha$ -Fe (bottom).....	199
Figure 5-5 XRD pattern and TEM image of the sample obtained without purging $N_2$ inside reaction solution (Experiment II).....	201
Figure 5-6 TEM images of samples obtained using a) 0 mmol, b) 0.5 mmol, c)1.0 mmol and d) 2.0 mmol HDA-Cl.....	202
Figure 5-7 Graph showing the size and percentage of plate-like NPs obtained according to the amount of HAD-Cl used. ....	203
Figure 5-8 XRD pattern (left) of sample synthesised with 0.5, 1.0 and 2.0 mmol of HDA-Cl and ED pattern (right) of the sample synthesised without HDA-Cl.....	204
Figure 5-9 TEM images and ED patterns for the sample obtained using 0.6 mmol (a & b) and 2.5 mmol (c & d). ....	206
Figure 5-10 Reaction pathways that lead to fcc metal nanocrystals with different shapes. First, a precursor is reduced or decomposed to form the nuclei (small clusters). After a certain size is reached, seeds are formed and they can have a single-crystal, singly twinned, or multiply twinned structure. The green, orange, and purple colors represent the {100}, {111}, and {110} facets, respectively. <sup>190</sup> .....	208
Figure 5-11 Representation of a silver halide model for a single twin plane. Alternating sides contain A-type and B-type faces. The structure promotes faster growth of the A-type faces, leading to a triangular prism. <sup>202</sup> .....	209
Figure 5-12 TEM images and ED pattern of the sample obtained when 0.4 mmol of extra ligand was added. a) & b) corresponds to the sample obtained using OA. c) & d) corresponds to the sample formed with SO and e) & f) was formed using TOPO. .	211
Figure 5-13 TEM images and ED pattern of the sample obtained when a) 0.2 mmol of SO, b) 0.8 mmol of SO & c) 1.0 mmol of SO were added. ....	214
Figure 5-14 TEM images of NPs obtained with 0.8 mmol of SO, taken by tilting the sample holder at different angles from 0 to 60 degrees. ....	216

Figure 5-15 Magnetic hysteresis loop taken at 300 K for 24.4 nanoplates dark blue and 15.6 nm nanoplates light blue (left). Zoom-in of the magnetic hysteresis for both samples at low fields (right) .....	218
Figure 5-16 DLS measurements in water after ligand exchange of NPs from a) Experiment XII and NPs from b) Experiment IV .....	219
Figure 5-17 Colloidal stability study of the Experiment XII (15.6 nm NPs) in different pH solutions: a) hydrodynamic diameter in different pH, b) zeta-potential value at different pH, c) picture of the dispersion at 0 and 4 d. ....	221
Figure 5-18 Colloidal stability study of the Experiment XII (15.6 nm NPs) in NaCl solutions at various concentrations: a) zeta-potential value in different NaCl concentrations, b) hydrodynamic diameter in different NaCl concentrations, c) picture of the dispersion at 0 and 4 d. ....	222

## List of units and abbreviations

A	ampere
Å	angstrom
AC	alternating current
AMF	alternating magnetic field
ATR	attenuated total reflectance
D <sub>H</sub>	hydrodynamic diameter
DLS	dynamic light scattering
DMSO	dimethyl sulphoxide
D <sub>TEM</sub>	particle core size determined by TEM
D <sub>XRD</sub>	crystallite size determined by XRD
ED	electron diffraction
EtOH	ethanol
f	frequency
FTIR	Fourier transform infra-red spectroscopy
g	gram
h	hour
H	amplitude of the magnetic field
H <sub>c</sub>	coercive field or coercivity
HCl	hydrochloric acid
HDA	hexadecylamine
HDA-HCl	hexadecylammonium chloride
IC	iron carbide
ILP	intrinsic loss power
IO	iron oxide
IR	infrared
K	kelvin
kg	kilogram
L	litre
M	magnetic moment
m	metre
min	minute
mL	millilitre
mmol	millimole
M <sub>n</sub>	number average molecular weight
Mol	mole
MRI	magnetic resonance imaging
M <sub>s</sub>	saturation magnetisation
M <sub>w</sub>	weight average molecular weight
MWCO	molecular weight cut-off
nH	nanoHenry
nm	nanometre

NMR	nuclear magnetic resonance
NP	nanoparticle
OA	oleic acid
OAm	oleylamine
ODA	octadecylamine
ODE	1-ocadecene
Oe	oersted
pdf	powder data file
PEG	polyethylene glycol
Pima-Dopa	dopamine-functionalised Poly (isobutylene- <i>alt</i> -maleic anhydride)
rpm	revolutions per minute
RT	room temperature
s	second
SAR	specific absorption rate
SPION	superparamagnetic iron oxide nanoparticle
SQUID	superconducting quantum interference device
t	time
T	temperature
T	tesla
T <sub>B</sub>	blocking temperature
T <sub>C</sub>	Curie temperature
TEM	transmission electron microscope
TGA	thermogravimetric analysis
THF	tetrahydrofuran
V	volume
VSM	vibrating sample magnetometer
W	watt
XRD	X-ray diffraction
ZFC/FC	zero field cooled/field cooled

# Chapter 1 Introduction and literature review

## 1.1 Nanoparticles for biomedical applications

Recent advances in nanotechnology have allowed the production of new tools with great potentials in medical research and healthcare. Nanoparticles (NPs) possess at least one physical dimension under 100 nm and this makes their size comparable to the sub-cellular environment of living animals, allowing them to interact with cells parts and organelles which otherwise are difficult to reach. Moreover, NPs could be easily tailored according to the needs they have to fulfil, and this has been driving the application of nanotechnology into biomedical fields. Among the most interesting inorganic nanoparticles for biomedicine we can easily underline the family made of magnetic material. Their intrinsic magnetic moment present in metals, alloys and oxides (Fe, Co, Ni, FeCo, FePt, CoFe<sub>2</sub>O<sub>4</sub>, Fe<sub>3</sub>O<sub>4</sub>, Fe<sub>2</sub>C, Fe<sub>2</sub>O<sub>3</sub>) can be exploited for magnetic delivery,<sup>1</sup> where the magnetic moment of NPs is used to accumulate and concentrate the particles in a narrower area of the body; MNP can be used for sensing,<sup>2</sup> like in MRI analysis where MNPs can act as contrasting agents, and heat generation in magnetic hyperthermia.<sup>3</sup> The use of such materials have proved to hold great potentials in treatment of cancer, which remains one of the leading causes of death.<sup>4</sup>

In this chapter, first, an overview on the strategies used for the synthesis of NPs will be discussed. Secondly, the magnetic properties of NPs and the recent advances in the development of MNPs for hyperthermia will be described, focusing also on the different parameters influencing the heating performances. Lastly, the chapter focus on different strategies used to functionalise magnetic nanocomposites and provide them with the colloidal stability needed for biomedical applications.

## 1.2 Synthesis of NPs in solution

In nanoparticle chemistry, small (1 – 20 nm) monodisperse NPs are sought<sup>5</sup> due to their high surface area to volume ratio, and size dependent properties. Controlled

shape has also shown to further tailor the physical properties of NPs, allowing to tune them for different applications. In this thesis, one of the goals is to form iron-based NPs with monodisperse size and shape. Here are presented the factors to consider and strategies utilized in the literature for forming size and shape-controlled NPs.

The synthesis of NPs in solution is generally described starting from the decomposition of a metal precursor leading to metal monomers dispersed in solution. Once the monomers' concentration in solution reaches the critical solubility, the monomers nucleate and eventually grow into nanoparticles (Figure 1.1a).<sup>6</sup> The initial concentration of the monomers in solution will ultimately affect the critical size of the NPs and the size distribution of the NPs (Figure 1.1b).<sup>7</sup> During the growth stage, NPs below the critical size keep growing while NPs above the critical size undergo dissolution.<sup>8</sup> This process decreases the size distribution as smaller NPs grow and larger ones decrease in size.

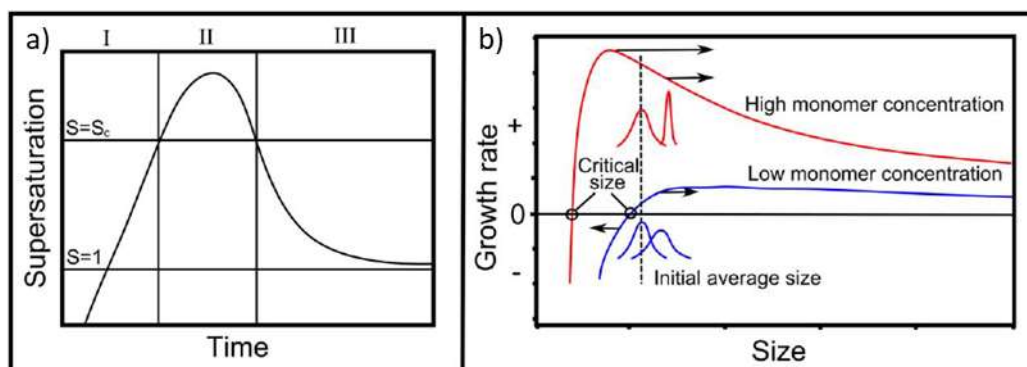


*Figure 1-1 a) The graph shows three stages in NP synthesis, where (I) corresponds to the increase of monomer concentration due to precursor decomposition, (II) corresponds to the supersaturation and nucleation phase, and (III) the growth. b) The graph shows the effect of concentration of monomers on size and distribution. Figure 1.1a is reproduced from the work of Park et al.<sup>8</sup> and Figure 1.1b is reproduced from the work of Yin et al.<sup>7</sup>*

Ideally, during the synthesis of NPs, nucleation and growth would occur at a different time. However, nucleation and growth can also happen at the same stage, leading to

polydisperse NPs in size.<sup>9</sup> One of the first solution to this problem came in 1993, when Murray *et al.* pioneered the hot-injection method where the NPs precursor was injected into a boiling solution set above the decomposition temperature of the precursor.<sup>10</sup> This leads to a sudden nucleation and afterward just the growth is favoured by decreasing the reaction temperature and the concentration of monomer available in solution.

In 2001 Heyon *et al.* reported the formation of uniform iron oxide nanocrystals via a heat-up approach.<sup>11</sup> The accumulation of the monomer in solution takes place via the decomposition of the precursor while the temperature (T) is slowly raised, and the nucleation is suppressed by a high energy barrier. The nucleation is then promoted once a critical concentration of the monomer is reached. The methods showed also great potential to produce large-scale amount of NPs.<sup>12</sup> The difference between the heat-up and hot injection processes is the way in which the critical concentration level is reached before the nanocrystal formation process. In the hot-injection approach, it is achieved by an external operation, being the quick injection of precursors. In the heat-up approach, the high energy barrier for the homogeneous nucleation suppresses the nanocrystal formation process during the formation of the monomers until the concentration is high enough for burst nucleation.<sup>13</sup>

The NPs growth generally takes place *via* addition of monomer on the surface of the growing particles. This results in a faster growth of smaller NPs compared to bigger ones, as the addition of monomers to smaller NPs surface has a larger impact on the size.<sup>14</sup>

### 1.2.1 Ostwald ripening

Another process happening during the NPs growth is Ostwald ripening. As larger NPs grow, they consume smaller NPs which have the tendency to dissolve because they are below the critical solubility limit of the solution. The first part of Ostwald ripening

process leads to a broadening of the size distribution of the NPs in solution because the bigger NPs keep growing while the smaller NPs are reduced in size.<sup>8</sup> As Ostwald ripening continues, NPs will eventually all tend towards the large particle size, thus leading to a narrow size distribution of the NPs and form larger nanoparticles.<sup>15</sup> Usually, in the synthetic methods, NPs growth is stopped before the Ostwald ripening process starts taking place, to avoid a polydisperse population. One strategy to avoid Ostwald ripening process is to use a second or more injections of precursor to shift the critical size and narrow the size distribution again.<sup>6,16,17</sup>

### 1.2.2 Stabilising Agents

Surfactants are often used in NPs growth to stabilise the NPs colloids by interacting with the surface of the NPs and preventing aggregation.<sup>18</sup> At the same time, stabilising agents have been exploited to affect size<sup>19</sup> of the NPs, this is due to their binding strength.<sup>20</sup> When the surfactant has a weak interaction with the NPs surface it allows easy access for the monomer to attach onto the surface. Instead, if the interaction is strong the monomer addition will be hindered and, thus, the growth of NPs limited. This means that varying the concentration of surfactant used, especially in the case of strongly binding ligands, allows control of the size of the final NPs.<sup>21</sup> It has also been reported that the size of the surfactant can affect the final dimension of NPs: stabilising agents with bigger tail groups form nanoparticles of smaller sizes because of the limited access of the monomer to the surface of the NPs.<sup>22</sup>

Stabilising agents can also play a role in controlling the NPs shape<sup>23</sup> thanks to the preferential binding of the surfactants on different crystal facets of the NPs. As nanocrystals grow, their crystal structure will affect the shape of the seed and particles, leading to the appearance of facets. Some ligand may show more affinity towards some facets rather than others, and this may be used to control the shape of the final NPs.<sup>24</sup> Often a mixture of a strong and a weakly binding surfactant is used.

While the weakly binding surfactant is mainly used to prevent aggregation, the strong-binding one is used to bind specific facets and stabilise them.<sup>25</sup>

### 1.2.3 Ions stabilizing crystal facets

A common strategy used to improve the control of the synthesis of NPs involves also the utilisation of ions which get adsorbed to the growing nuclei, leading to the stabilization of a crystal facet. For example, bromide ions have been reported to stabilize the {100} facet of face centred cubic (*fcc*) metals forming cubic NPs of palladium,<sup>26,27</sup> platinum<sup>28</sup> and rhodium.<sup>26</sup> Similarly, in the case of Fe NPs, bromide and chloride ions have been shown to drastically improve the crystallinity of Fe NPs by interacting with the forming nanocrystals when Fe(CO)<sub>5</sub> was used as precursor.<sup>29–31</sup> Moreover, Ag<sup>+</sup> ions have been reported to promote anisotropic growth in gold nanoparticles by preferentially inhibiting the {110} facets by underpotential deposition of silver on the gold's surface, and favouring the growth from the uninhibited facets, either the {100} or {111} facet, thus forming gold nanorods.<sup>32,33</sup> A mix of bromide and Hofmeister salts series can be used for fine-tuning gold nanorods aspect ratio.<sup>34</sup>

## 1.3 Magnetic nanoparticles for hyperthermia therapy

### 1.3.1 Introduction to hyperthermia

The first reports of hyperthermia as treatment can be traced back to the Greeks, Egyptians and Romans.<sup>35,36</sup> In 1970, after the observation that whole body hyperthermia caused by fever could induce tumour regression, the first clinical trials on hyperthermia started.<sup>35</sup> It was observed that cancer cells are more sensitive to heat than healthy cells. When cancer cells are exposed to a temperature between 42° and 45° C, they go through the process called apoptosis,<sup>37</sup> which is a kind of cell death where cells trigger their self-destruction in response to a signal.<sup>38</sup> On the other hand, healthy cells can withstand such temperatures with no effects. If the

temperature of the treatment goes above 46 °C, it is defined as thermal ablation.<sup>39</sup> This can affect also healthy cells, and it usually leads to death of the treated tissue for necrosis. The necrosis is able to start an inflammatory reaction in the surrounding environment, leading to potentially more side effects than the apoptosis process.<sup>40</sup>

The higher sensitivity to heat of cancer cells compared to healthy ones is due to the nature of the disease. Cancer cells grow in a faster and more chaotic manner, leading to a more disorganised architecture of the vascular vessels.<sup>41</sup> As a consequence, when hyperthermia is applied, the blood flow surrounding the tumour is less efficient to dissipate heat, causing the temperature in a tumour to rise faster and trigger apoptosis or necrosis earlier than in normal tissues.<sup>42</sup> Hyperthermia has also shown promising results when combined with chemotherapy or radiotherapy, as cell becomes more sensitive towards drugs if heat is delivered first.<sup>3,43</sup>

Hyperthermia treatment can be divided into three kinds: i) local, ii) regional and iii) whole-body. In the whole-body hyperthermia the temperature of the body is increased using heating chambers or warm blanket.<sup>44</sup> In this case, the general and unspecific heat increase can stimulate the blood flow and the efficiency of drugs and radio therapy. The regional and local treatment, instead, is used for localised tumours. Local hyperthermia is the least invasive technique and allows to treat tumours located superficially or in accessible body cavities. Several techniques like radiofrequency,<sup>45</sup> microwave radiation,<sup>46</sup> laser ablation<sup>47</sup> can be used to deliver heat. One of the most promising technique uses magnetic NPs as a vector to deliver heat and it is therefore called Magnetic Hyperthermia (MH).<sup>48</sup>

### 1.3.2 Magnetic properties

In any material, the magnetic properties originate from the electrons in the atoms. Two factors contribute to the magnetic behaviour: the movement of electrons that orbit around the nuclei, defined as the orbital magnetic moment, and the spin of electrons defined as spin magnetic moment. The interaction between the spin of the

electron and its motion produces the spin-orbit coupling. Just valence electrons contribute to the magnetic moment as core electrons from filled orbitals have a zero net magnetic moment as they are combined into pairs with opposite spin. The overall interaction of the electrons in a material leads to distinctive magnetic properties, depending on the electronic configuration of the material itself, and ultimately two scenarios are formed, one where the interaction couples the spins parallel (ferromagnetic interaction,  $\uparrow\uparrow$ ), and another where the spins are coupled antiparallel (antiferromagnetic interaction,  $\uparrow\downarrow$ ). The possible configurations originate different types of magnetic materials which can be classified as diamagnetic, paramagnetic, ferromagnetic, ferrimagnetic and anti-ferromagnetic substances.<sup>49</sup>

Diamagnetic and paramagnetic materials do not show a net magnetisation moment ( $M$ ) when no external magnetic field is applied. In the case of diamagnetic materials, all electrons are paired, and they respond to an external magnetic field generating an induced opposite magnetic moment (Figure 1.2). In the presence of unpaired electrons paramagnetism is observed and when an external magnetic field is applied, the moments of the atoms tend to align to it. Due to thermal motion, those moments are randomly oriented, and the net moment goes back to zero once the external field is removed. In the field of materials showing net magnetisation moment, we find ferromagnetic, ferrimagnetic and antiferromagnetic materials. The difference among them depends on the crystal lattice of the material which affects the final magnetic properties. In the case of ferromagnetic materials, all the magnetic domains present (regions in which the magnetisation is in a uniform direction) are parallel to each other. In some cases, magnetic domains can organise in two antiparallel magnetic domains, forming ferrimagnetic and antiferromagnetic materials. In the first case, the lattices are not equivalent, and a net moment is observed while in the latter the lattices are equivalent with no resulting magnetization. Ferro- and ferrimagnetic materials behave as paramagnet above a certain temperature (called Curie

temperature,  $T_c$ ) because the thermal motion randomly orientates the magnetic moment resulting in a zero-net moment.<sup>49</sup>

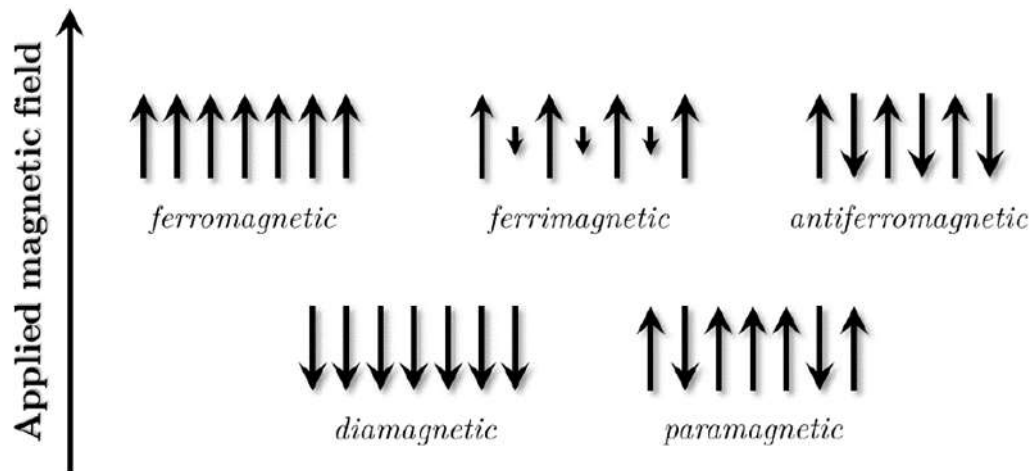


*Figure 1-2 Schematic response of magnetic materials to an applied magnetic field.<sup>50</sup>*

### 1.3.2.1 Superparamagnetism

Bulk ferro- and ferrimagnetic materials are made of magnetic domains that lower the energy state of a crystal. At the border between different domains (domain walls) defects generally are present, causing a difference in the magnetic moment.<sup>51</sup> When the material's features are analysed through the measurement of their magnetic moment in response to an external magnetic field (M-H curve), the classical curve observed is a loop due to the flipping of the magnetic domains trying to align to the magnetic field applied (Figure 1.3).<sup>52</sup> The saturation magnetization ( $M_s$ ) is observed once every moment of all the domain in the material is aligned towards the applied magnetic field direction. Once the field is removed, the material retains some extent of the magnetic moment and an opposite field needs to be applied to obtain a moment equal to zero. This field is called coercive field or coercivity ( $H_c$ ). When the size of the particles is reduced, small enough NPs becomes single-domain particles. There exists a critical size ( $D_c$ ) for each material under which the transition from multi-

domain to single-domain happens. The coercivity field reach a maximum at the critical size, and if the size is reduced further the coercivity decreases due to thermal effects.<sup>53</sup> When the size goes below  $D_p$  the thermal effects are able to completely demagnetise the material after the removal of an external magnetic field (Figure 1.4). This state is called superparamagnetic state. In such state, the material is magnetised in a similar manner to a paramagnet, with a much larger magnetic susceptibility. As this state is thermally activated, there is a temperature below which superparamagnetic particles have a ferromagnetic behaviour because they cannot be demagnetised by the thermal motion and particles result as “blocked”. The temperature is called blocking temperature ( $T_B$ ).

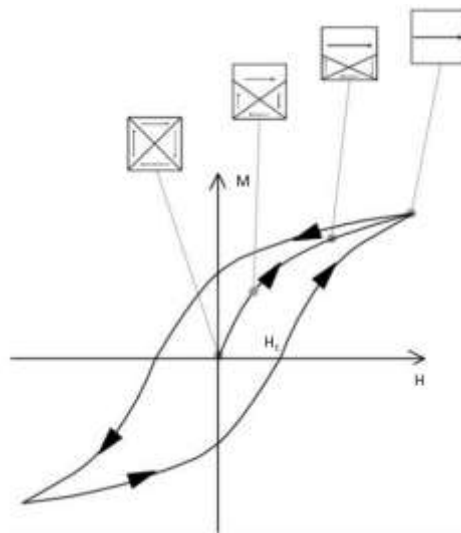


*Figure 1-3 M-H curve showing a typical hysteresis loop of a multi-domain magnetic material. The loop arises from the different fields intensity necessary to align different domains.<sup>3</sup>*

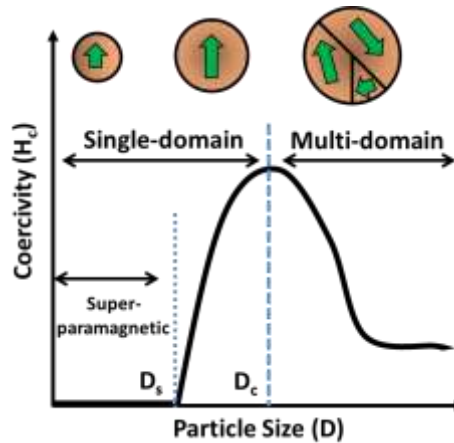


*Figure 1-4 Schematic representation of the relationship between coercivity and particles size in case of single-domain and multi-domain particles.*

### 1.3.3 Magnetic Hyperthermia

MNPs have proved to be promising in converting magnetic energy into thermal energy when they are exposed to an external oscillating magnetic field. This process is called Magnetic Hyperthermia (MH).

#### 1.3.3.1 Heat generation mechanism

To convert the magnetic energy to thermal energy, MNPs are exposed to an alternating current (AC) magnetic field. Different mechanisms of heating are in place depending on the magnetic properties of the NPs.

In ferri- and ferromagnetic materials, in multi-domain configuration, the production of heat is proportional to the hysteresis behaviour observed in such material under AC magnetic field. The cycle of alignment of the domains to the varying uniaxial magnetic field generate hysteresis losses.<sup>54</sup> For each cycle the heat produced,  $P$ , can be estimated from the area of the hysteresis loop according to the following equation:

$$P = \mu_0 f \oint H dM \quad (\text{Eq. 1-1})$$

where  $\mu_0$  is the magnetic permeability,  $f$  is the frequency of the applied field,  $H$  is the strength of the field and  $M$  the magnetisation.<sup>55</sup>

In the case of superparamagnetic particles, when an AC magnetic field is applied, no hysteretic behaviour is observed, therefore no heat lost is generated *via* this process. Instead heat lost is generated *via* two relaxations modes called Neel and Brownian relaxation. Neel relaxation is produced by the alignment of the magnetic moment of the NPs towards the direction of the oscillating magnetic field. When the magnetic moment relaxes to its equilibrium orientation, energy is lost. The rotation time of the magnetic moment is described by the Neel relaxation time in the following equation:

$$\tau_N = \tau_0 \exp\left(\frac{KV}{k_B T}\right) \quad (\text{Eq. 1-2})$$

Where  $\tau_0 \sim 10^{-9}$  s,  $K$  is the anisotropy constant of the material,  $V$  the volume of magnetic particle,  $k_B$  the Boltzmann constant and  $T$  the temperature.

Brownian relaxation arises from the physical rotation of the particles interacting with the applied AC magnetic field. The particles, rotating in the carrier liquid, attempt to re-orientate with the direction of the magnetic field, producing a friction. The rotation is defined by Brownian relaxation time,  $\tau_B$  with the following equation:

$$\tau_B = \frac{3\eta V_B}{kT} \quad (\text{Eq. 1-3})$$

where  $\eta$  represents the viscosity of the surrounding medium,  $V_H$  the hydrodynamic volume of the particles,  $k_B$  the Boltzmann constant and  $T$  the temperature. Neel and Brownian relaxation mechanism are represented in Figure 1.5.

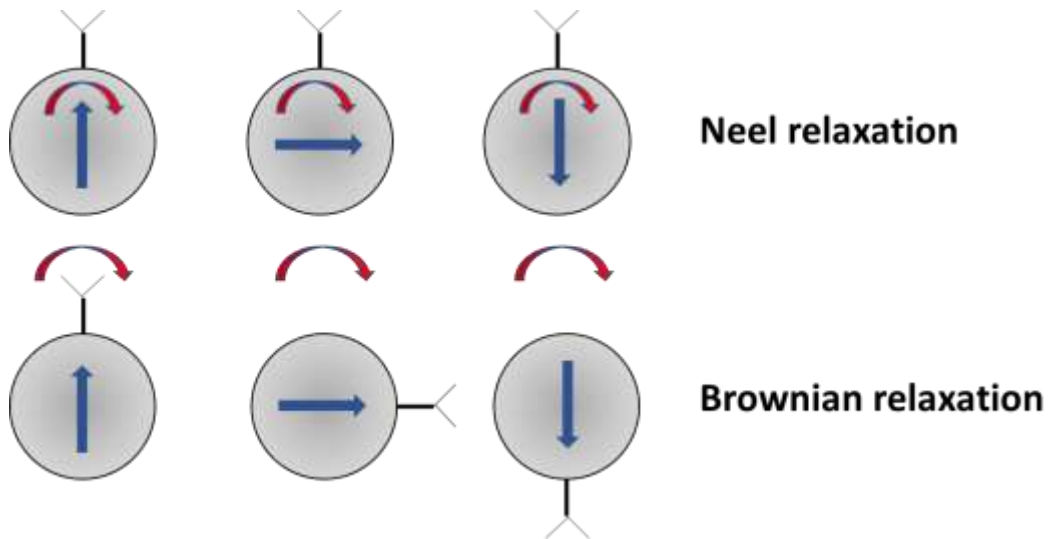


*Figure 1-5 Schematic representation of the Néel versus Brownian relaxation. Néel relaxation: the magnetic moment rotates within each particle. Brownian relaxation: the particle rotates as a whole.*

The two processes greatly depend on the size of the NPs and the nature of the magnetic material through its magnetic anisotropy constant.<sup>56,57</sup> In general Néel relaxation is predominant in smaller NPs as less energy is required to reorient the magnetic moment. Conversely, Brownian relaxation will dominate in the case of bigger NPs (also present in the case of ferromagnetic NPs). However, in this case the surrounding environment can also affect the relaxation process, as highly viscous media can hinder the rotation of the particles. Indeed, NPs internalised in cells often show a reduction in heating performance compared to “free” NPs in solution due to the lack of Brownian relaxation contribute.<sup>58</sup>

Both relaxations are not independent from one to another and the relaxation process in NPs is the result of the two relaxation phenomena combined as described:

$$\tau_{eff} = \frac{\tau_B \tau_N}{\tau_B + \tau_N} \quad (Eq. 1-4)$$

### 1.3.3.2 Quantification of heat loss

To quantify the heating power of MNP in a varying magnetic field, the specific absorption rate (SAR) is usually used. It is defined as:

$$SAR = \frac{\Delta T}{\Delta t} \frac{C}{m_{Fe}} \quad (Eq. 1-5)$$

where  $C$  is the heat capacity of the solvent where the measurement takes place,  $T$  is the temperature, and  $t$  is the time, and  $m_{Fe}$  is the iron concentration in solution. Importantly, SAR does not measure an intrinsic property of a system because it is strongly dependent on the strength and frequency of the magnetic field applied.<sup>59</sup> To overcome this issue, it was proposed to use a different parameter to quantify the heating power of a given system, called intrinsic loss power (ILP)<sup>60</sup>. This is defined as:

$$ILP = \frac{SAR}{(f \cdot H^2)} \quad (Eq. 1-6)$$

This parameter helps to compare results coming from different laboratories as it normalises the SAR parameter by the field strength and frequency used during the measurement.

### 1.3.4 Nanoparticles for magnetic hyperthermia

Having NPs with a high heating output is fundamental for the clinical use of MH for two main reasons. Firstly, it would allow to introduce in the body just the minimum amount of foreign material, reducing any possible issues concerning the toxicity of the material. Secondly, it would allow to work within safe doses of delivered electromagnetic field. The SAR output of a system increases with the frequency and the strength of the applied field used, but it was estimated that the product of strength and frequency ( $H \times f$ ) of the field used should not exceed the threshold of  $5 \times 10^9 \text{ Am}^{-1}\text{s}^{-1}$  to be considered safe for the human body.<sup>61</sup> Above this limit, the formation of Eddie currents could result in inductive heating of healthy tissues, and other harmful side effects like muscular stimulation or heart arrhythmias.<sup>62</sup>

Several parameters can play a role in the optimisation of SAR values. Regarding the material's properties, high SAR requires high  $M_s$  value and low magnetocrystalline anisotropy.<sup>63</sup> Moreover, the NPs size (NPs diameter,  $d_{NP}$ ) also affects the final properties. Indeed, ferromagnetic (and ferri-magnetic) nanomaterials below a critical size ( $d_{cr}$ ) form particles with single magnetic domain, whereas above the critical size particles have multiple magnetic domains. As the size of a monodomain particle is reduced, the superparamagnetic limit ( $d_{SP}$ ) is achieved, and the particle is in a superparamagnetic state. Hergt *et al.* suggested that the optimal size for MNPs with high SAR value should be close to the size at the transition from superparamagnetic to ferromagnetic behaviour ( $d_{NP} \approx d_{SP}$ ).<sup>64</sup> Medaloui *et al.* also highlighted that SAR abruptly drops, along with coercivity, after the transition toward multidomain MNPs, ( $d_{NP} > d_{cr}$ ) suggesting that such MNPs are not the most efficient for MH, with the optimized particles being single-domain MNPs.<sup>65</sup> As the specific transition diameters ( $d_{cr}$  and  $d_{SP}$ ) depends on the material used, different optimal size also depends on the NPs' composition; hence the size of the particles should be carefully controlled to meet the needs of a given application. Figure 1.6 shows the estimated value of the threshold diameters for superparamagnetic ( $d_{SP}$ ) and monodomain ( $d_{cr}$ ) spherical nanoparticles of the most common magnetic materials.<sup>66</sup>

Among several materials, Habib *et al.* calculated that NPs with the highest power loss output would be FeCo NPs of 35 nm and  $\alpha$ -Fe NPs of 11 nm, with the field amplitude and frequency taken to be 50 mT and 300 kHz.<sup>67</sup> However metallic NPs have been less studied due to their poor stability and toxicity concerns.

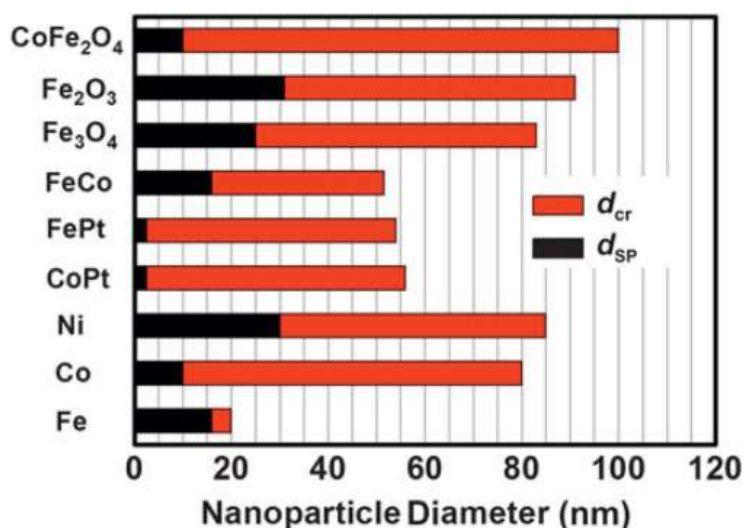


Figure 1-6 Threshold diameters for superparamagnetism ( $d_{SP}$ ) and maximum monodomain ( $d_{cr}$ ) size for spherical nanoparticles, based on bulk material parameters.<sup>66</sup>

Conversely, metal-doped ferrites ( $Fe_2Fe_{1-x}M_xO_4$  where  $M = Co^{2+}$ ,  $Zn^{2+}$  or  $Mn^{2+}$ ) have been widely investigated for their potential use in magnetic hyperthermia. The effects of  $Co^{2+}$ ,  $Zn^{2+}$  or  $Mn^{2+}$  doping have been tested in magnetic hyperthermia with mixed results.<sup>25,56,68</sup> In particular,  $Zn^{2+}$  and  $Mn^{2+}$  were used to increase the  $M_s$  value in ferrite-doped NPs, but while the doping of magnetite NPs with  $Mn^{2+}$  ions led to an increase in heat loss in magnetic hyperthermia applications,<sup>69</sup> Zn-doped NPs showed little to no SAR increase in the final performances.<sup>70</sup> Conversely, doping magnetite NPs with  $Co^{2+}$  led to a reduction of  $M_s$  value but it was shown to improve the performance of NPs in magnetic hyperthermia compared to the non-doped NPs thanks to the optimisation of the magneto-crystalline anisotropy of the material.<sup>25</sup> One of the most successful example in the use of doped ferrite NPs was provided by combining different magnetic ferrite core/shell particles with the core made of Co-doped ferrite and the shell made of Mn-doped ferrite. Thanks to the interaction between the soft-magnetic shell and the hard-magnetic core, 15 nm  $CoFe_2O_4@MnFe_2O_4$  core@shell NPs showed an ILP of  $5.8 \text{ nHm}^2\text{Kg}^{-1}$  ( $SAR = 2280 \text{ Wg}^{-1}$ ), among the highest ever reported.<sup>71,72</sup> Changing the dopants concentration allowed to tune the anisotropy and the  $M_s$  of the NPs with effect on the final SAR.<sup>70,73</sup>

However, the insertion of dopants inside the crystal structure can be challenging to control and reproduce and the presence of  $\text{Co}^{2+}$  and  $\text{Mn}^{2+}$  raises toxicity concern for biomedical applications. In this work, only Fe-based materials have been investigated as potential heating tools because of their high  $M_s$  and lower toxicity. The magnetic moments of iron-based materials are summarised in Table 1.1.

*Table 1-1 Summary of iron-based material with the highest  $M_s$  value.<sup>71</sup>*

Material	$M_s$ (emu/g)
Metallic iron ( $\alpha$ -Fe phase)	210
Iron carbide ( $\text{Fe}_2\text{C}$ ) <sup>74</sup>	140
Iron oxide ( $\text{Fe}_3\text{O}_4$ )	98
Iron oxide ( $\text{Fe}_3\text{O}_4$ )	70

#### 1.3.4.1 Iron nanoparticles

Pure metals like Fe, Co or FeCo alloys have the highest saturation magnetisation among the naturally occurring materials.<sup>71</sup> Among them, Fe is the most reactive and quickly oxidises in air, forming a protective iron oxide layer which makes the NPs more biocompatible.<sup>75</sup> The synthesis of Fe NPs requires special handling compared to iron oxide, and Fe NPs are mainly prepared in organic solvents. Typically,  $\text{Fe}(\text{CO})_5$  is used as precursor and decomposed at high temperature in the presence of long-chain amines.<sup>76-80</sup> This procedure benefits from Fe atoms being already reduced (zero-valent iron), thus no reducing agents are required. In early studies, the use of Pt seeds proved to enhance crystallinity, and thus magnetic properties of the Fe NPs formed.<sup>76</sup> In a recent work, monodisperse amorphous Fe NPs were made by thermal decomposition of  $\text{Fe}(\text{CO})_5$  in 1-octadecene (ODE) and oleylamine (OAm).<sup>81</sup> To stabilize the Fe NPs, a dense shell of crystalline  $\text{Fe}_3\text{O}_4$  was formed around the Fe core *via* controlled oxidation with  $(\text{CH}_3)_3\text{NO}$ . The resultant Fe/ $\text{Fe}_3\text{O}_4$  NPs show an enhanced stability after 24 h of exposure to air. Recently, Lacroix *et al.* showed that

a body centred cubic (bcc) Fe phase is obtained if  $\text{Fe}(\text{CO})_5$  is decomposed in the presence of hexadecylammonium chloride (HDA).<sup>29,31</sup> bcc-Fe NPs exhibit increased chemical stability and higher  $M_s$  value than amorphous Fe NPs and showed also increased SAR output.<sup>29</sup> However, Chaudret *et al.* pointed out that the magnetic properties of the obtained NPs were generally lower than the bulk value because of the presence of the CO of the precursor which forms carbonaceous traces in the final product.<sup>82</sup> To prevent such process,  $\text{Fe}(\text{CO})_5$  has been replaced by iron salts or organometallic compounds, whose decomposition do not yield any interfering carbon species and are also less toxic. However, for the decomposition and reduction of iron salts, harsh conditions are required.  $\text{FeCl}_2$  could be reduced in water by sodium borohydride, but boron contamination has also been found in the final NPs, leading to a decrease of the magnetic moment.<sup>83</sup> The decomposition of organometallic compounds such as  $\text{Fe}(\text{C}_5\text{H}_5)(\text{C}_6\text{H}_7)$ <sup>84–86</sup> or  $[\text{Fe}[\text{N}(\text{SiMe}_3)_2]_2]_2$ <sup>79</sup> under dihydrogen atmosphere has been proposed as alternative way to yield Fe NPs in mild conditions with final magnetic properties close to Fe bulk value. In particular, the use of  $[\text{Fe}[\text{N}(\text{SiMe}_3)_2]_2]_2$  precursor, allowed for slow and controlled nucleation and growth steps leading to greater size and shape control of Fe NPs. Indeed, with such precursors cubic-shaped Fe NPs are obtained.<sup>87</sup> These shaped NPs have great potential for magnetic hyperthermia since it has been shown that shape anisotropy can actually enhance the heat generation under an alternating an AC magnetic field.<sup>88</sup> However,  $\text{Fe}(\text{C}_5\text{H}_5)(\text{C}_6\text{H}_7)$  and  $[\text{Fe}[\text{N}(\text{SiMe}_3)_2]_2]_2$  are not commercially available and a complex chemistry is involved in their preparation, thus limiting their use. Finally, Fe NPs can be prepared *via* the reduction of iron oxide NPs. If coated with  $\text{SiO}_2$  shell, iron oxide cores can be reduced to  $\alpha$ -Fe using  $\text{CaH}_2$  as reducing agent forming  $\text{Fe}@\text{SiO}_2$  core@shell NPs. The presence of silica prevents the aggregation of the forming Fe phase during the reduction at high temperature.<sup>89,90</sup> As iron oxide ( $\text{Fe}_3\text{O}_4$  or  $\text{Fe}_2\text{O}_3$ ) NPs have been widely studied in the literature, there are plenty of synthetic protocols available that would ease the formation of specific size and shape in comparison with the synthesis of Fe NPs. Moreover many cheap precursors are commercially available for the synthesis of iron oxide NPs.<sup>91</sup> However, even though

the synthesis of iron oxide is relatively simple, coating each and every particles with a silica shell is challenging and so far has not been trivial. The thickness of a silica shell is hard to control,<sup>92</sup> and non-uniform silica shells, along with the formation of clustered magnetic NPs within a silica matrix, can lead to a decrease of the final heating properties.<sup>93</sup>

There is therefore the need to develop a novel and simple synthetic approach that can overcome the previously mentioned limitations such as precursor availability and size tuning capability, and that can form highly crystalline Fe NPs. Furthermore, it is important to also investigate the stability of Fe NPs in an aqueous media because metallic Fe NPs are more reactive towards air and moisture than Fe<sub>3</sub>O<sub>4</sub> NPs and there has been little research on the chemical stability of Fe NPs once they are transferred from organic solvent into aqueous media. Such information is important to evaluate the potential of Fe NPs in clinical hyperthermia.

#### 1.3.4.2 Iron carbide nanoparticles

Iron carbide (IC) nanomaterials have recently been considered as possible tools for biomedical applications. IC NPs consist of Fe and C alloy (Fe<sub>x</sub>C<sub>y</sub>), of different composition, where carbon occupies the interstitial sites within the iron cubic crystal structure. The compound shows interesting magnetic properties thanks to the Fe maintaining its metallic nature, while the presence of carbon in the crystal structure provides the material with enhanced chemical stability, desirable for biomedical applications.

Synthetic protocol for the formation of uniform Fe<sub>x</sub>C<sub>y</sub> NPs are still limited in the literature, especially if compared with the syntheses of Fe or Fe<sub>3</sub>O<sub>4</sub> NPs. Meffr *et al.* reported for the first time the synthesis of monodispersed Fe<sub>3</sub>C NPs by decomposing Fe(CO)<sub>5</sub> in the presence of pre-existing Fe NPs and promoting the formation of carbide phase under 3 bar of H<sub>2</sub> for 24 h of reaction.<sup>82</sup> Ce Yang *et al.* instead, starting

from Fe NPs, produced Fe<sub>5</sub>C<sub>2</sub> phase at 350 °C in a mixture of long-chain amines.<sup>30</sup> Yang *et al.* showed that the presence of halides in solution could affect the final ratio of Fe and C in the alloy. They obtained at least 5 different IC samples with different composition and crystal structure, depending on the amount of halide used.<sup>74</sup>

Other reactions have been reported, such as treatment of ferrocene with high pressure and high temperature in solid state synthesis,<sup>94</sup> through laser ablation of bulk iron with 1064 nm nanosecond pulses in commonly used organic solvents (i.e. tetrahydrofuran, acetonitrile, dimethylformamide, dimethylsulfoxide, toluene, and ethanol) which were acting as carbon source,<sup>95</sup> or via carbothermal reduction of magnetite NPs to Fe<sub>3</sub>C at 650 °C, using a biopolymeric matrix as carbon source.<sup>96</sup> However, the last synthetic protocols showed big limitations in the control of size, size distribution and final phase, making the NPs produced via these methods unsuitable for biomedical applications.

Despite the recent interest on IC NPs, some studies showed the potential of IC NPs as “theranostic” tools where the NPs were able to deliver both therapy and diagnosis at the same time, hence theranostic NPs. Such a multimodality probe, which integrates imaging with therapeutic capabilities, can further achieve early diagnosis and therapy of cancer. Specifically, the presence of carbon in IC NPs made the particles able to absorb Near Infrared (NIR) radiation and release the energy into the surrounding area as heat (photothermal hyperthermia) while the magnetic moment made the NPs suitable to be used as contrast agents in MRI scans for diagnostic purposes.<sup>97–100</sup> Indeed, their high magnetic moment interacts with the external magnetic field applied during MRI scans creating a local magnetic field which in turns modify the magnetic properties of the protons in the surrounding environment. The difference between the area with NPs and without NPs during MRI scans creates a contrast, enhancing the imaging of the area where the NPs are located. The same high magnetic moment of the material could be used for magnetic hyperthermia treatment.

In fact, just two reports on the use of IC NPs in magnetic hyperthermia can be found in the literature, both coming from Prof Chaudret's group.<sup>82,101</sup> Their Fe<sub>3</sub>C/Fe<sub>2</sub>C NPs, had a greater SAR value than the starting Fe NPs. Fe<sub>3</sub>C were used as a heating tool to locally promote a catalytic reaction inside an oxygen-free, sealed reaction vessel and at high field they reached a SAR value of  $\approx 3200$  W/g and an ILP of 14.<sup>101</sup> Even though this study shows the potential of this material in magnetic hyperthermia, it does not evaluate the performances of NPs under biomedically compatible conditions, because in such studies the as-synthesised NPs were collected after the synthesis and tested for hyperthermia under inert atmosphere in a mesitylene dispersion.<sup>82</sup>

Therefore, even though IC NPs possess high magnetic moment and high chemical stability, which are desirable for magnetic hyperthermia, there is the need to develop a robust and reproducible synthesis of IC NPs with defined size and composition. These last two parameters must be controlled in order to obtain homogeneous magnetic properties among the NPs. Also, the stability of such particles in aqueous media should be assessed as no information are available at the moment. Such information would help to further assess the potential of IC NPs in magnetic hyperthermia applications.

#### 1.3.4.3 Iron oxide nanoparticles

Iron oxide NPs (Fe<sub>3</sub>O<sub>4</sub> and Fe<sub>2</sub>O<sub>3</sub>) have been the most studied magnetic material for biomedical applications so far, with a special focus on Fe<sub>3</sub>O<sub>4</sub>. Indeed, magnetite has a moderate M<sub>s</sub> value, it is easy to synthesise and functionalise and shows low toxicity. Products based on iron oxide NPs, e.g. Ferridex, have also received FDA approval as contrast agent for MRI, which has opened the way for such materials to be utilised in biomedical applications.<sup>69</sup> However, there is still a lot of active research going on to improve the reproducibility, scale-up and performances of magnetite NPs in MH.

The most common chemical procedures to form iron oxide NPs are the co-precipitation of  $\text{Fe}^{2+}$  and  $\text{Fe}^{3+}$  aqueous salt in basic solution and the decomposition of organometallic iron precursor at high temperature. A vast range of reaction conditions have been explored for the synthesis of iron oxide NPs. Different precursors, solvents, temperature, reaction time, surfactants have produced almost countless iron oxide NPs with different magnetic properties shape and size distribution.<sup>102–104</sup> In general, the co-precipitation is a fast process and can form NPs even at room temperature.<sup>105</sup> It has few drawbacks though, as it is hard to obtain uniform products and there may be reproducibility issues because the process is hard to control.<sup>3</sup> The decomposition of organometallic precursor, instead, is done in organic solvent and usually requires high temperature. It allows for a greater degree of control and tunability of shape, size and composition which cannot be achieved in the co-precipitation method.<sup>91</sup>

In the decomposition method, the various synthetic procedure reported in the literature are based on the work of Hyeon *et al.*<sup>67</sup> where it was highlighted the importance of the *in situ* formation of an iron-oleate complex for the formation of crystalline and monodisperse iron oxide NPs. The complex formed from the decomposition of  $\text{Fe}(\text{CO})_5$  around 100 °C in the presence of oleic acid and ultimately was responsible for the controlled decomposition around 300 °C, feeding the formation of monodisperse NPs. This led to the introduction of iron-oleate as a starting precursor for  $\text{Fe}_x\text{O}_4$  NPs, avoiding the use of harmful carbonyl-based precursors.<sup>12</sup> However, the use of iron-oleate raised concerns on the reproducibility of the results as the iron-oleate complex were often prepared *in loco* before the synthesis of NPs, and different iron : oleate ratios were formed.<sup>16</sup> The different stoichiometry in the complex causes variations of the decomposition temperature profiles, which, can lead to uneven results.  $\text{Fe}(\text{acac})_3$  was then introduced as non-toxic, cheap, commercially available and high-purity precursor able to produce uniform NPs in a similar manner in the presence of oleic acid and oleylamine.<sup>106,107</sup>

The optimal size of NPs for magnetic hyperthermia is still an open discussion. In early studies, iron oxide NPs close to 10 nm were targeted for biomedical applications because the size was within the superparamagnetic domain. Indeed, superparamagnetic NPs show no residual magnetic moment once the external magnetic field was removed, making the particles less prone to aggregation and more stable in a dispersion, but the heating efficiency was low.<sup>60,108,109</sup> To improve the heating efficiency, recent studies focused on increasing the particles size. For example Huber *et al.* showed that among spherical iron oxide NPs ranging from 12 nm to 25 nm, the peak in SAR output was found at 21 nm.<sup>110</sup> The study showed that in Fe<sub>3</sub>O<sub>4</sub> NPs bigger than 20 nm, the superparamagnetic behaviour was lost, with the particles being still within the single magnetic domain and showing soft-ferromagnetic behaviour. The results suggested that viable NPs for magnetic hyperthermia do not need to be as small as previously thought as long as they form a stable dispersion.

NPs' shape can also affect the heating performances in MH. Shape is a more recent research topic compared to size, however, it has become more evident that shaped NPs can enhance SAR outputs in comparison to spherical NPs of similar volume.<sup>111</sup> One of the first studies was carried out by Guardia *et al.* and showed that 19 nm Fe<sub>3</sub>O<sub>4</sub> nanocubes possessed an outstanding ILP of 5.6 nHm<sup>2</sup>Kg<sup>-1</sup> (SAR = 2453 Wg<sup>-1</sup>).<sup>25,112</sup> Since then, the gain in SAR output with cubic NPs has been explained with mainly two reasons. One of the reasons was associated to the spin-canting phenomenon occurring at the nanoscale. Spin-canting arises from the reduced number of magnetic neighbouring ions around atoms at the particle surface, or around crystal defects in the interior part. Such "defects" cause local magnetic frustration because the spin of the magnetic atoms deviates locally from ideal collinear spin structures. In general, such magnetic behaviour leads to a reduced magnetization and it is responsible for the difference in magnetic properties of nanoparticles respects those of the corresponding bulk materials.<sup>113,114</sup> Compared to spherical NPs, faceted morphology leads to a decrease in spin canting effect on the nanocrystal surface, due to a higher

degree of order of the spin on the surface of shaped NPs, decreasing the magnetically “dead” layer usually found on the surface of spherical NPs.<sup>112</sup> Secondly, some shapes can promote the occurrence of a collective behaviour that can enhance the performances in magnetic hyperthermia. In specific, it was observed that NPs with cubic shape under an external magnetic field can rearrange to form a chain-like arrangement, improving the heating efficiency.<sup>115</sup> Such enhancement is due to the formation of uniaxial anisotropy along the chain promoting a collective behaviour under the external magnetic field. Similar findings were also reported in the case of octahedral iron oxide NPs, showing a SAR value of 2629 Wg<sup>-1</sup>.<sup>116</sup> A huge increase in heating capabilities was also observed for multi-core flower-shaped maghemite NPs of 24 nm made of multiple 11 nm superparamagnetic cores, resulting in a SAR value of 1992 W/g, and it was hypothesised that, also in this case, a collective behaviour of particles within a defined aggregate resulted in enhanced SAR.<sup>117</sup>

However, the synthesis of shaped NPs has been proven very challenging and with no straightforward parameter used to control and form shapes.<sup>112</sup> Most of the parameters used to promote the growth were using a combination of heating rate, ligand to precursor ratio and solvent polarity fine tuning. Such parameters are challenging to reproduce among different laboratories and a more straightforward strategy to form shaped NPs would be highly advantageous.

#### 1.4 Methods for making water dispersible MNPs

The synthetic methods based on organic solvents, allow for the formation of NPs in a water-free environment. This has some benefits like a broad choice of solvents and the possibilities to work within a broad range of temperatures. Indeed, both ‘hot-injection’ and ‘heating-up’ methods require the thermal decomposition to take place in high-boiling point solvent to produce highly monodisperse NPs with superior control on size, shape and composition of the final particles. However, in terms of surface chemistry, these methods produce hydrophobic NPs which are unsuitable to be

used immediately for water-based biomedical applications. Therefore, it is necessary to add post-synthetic surface-modification procedures to prepare suitable NPs. This surface modification step should not only make NPs hydrophilic, but it should also improve NPs' colloidal stability, biocompatibility and, possibly, allow to easily functionalise the system for eventual applications. Among the most used strategies we can find ligand exchange, polymer encapsulation and silica coating approaches.

#### 1.4.1 Ligand Exchange

The ligand exchange method generally involves the direct replacement of the native hydrophobic ligand present on the NPs' surface with another ligand having hydrophilic functional groups; the process renders hydrophobic nanoparticles water soluble. For an effective process, the ligand should bear at least one functional group with high affinity towards the NP's surface to be able to displace the existing ligand, and it should also have functional groups able to provide suitable colloidal stability.

For iron-based NPs, cationic surfactants like tetramethylammonium hydroxide (TMAOH)<sup>118,119</sup> have been used to displace the native ligand and makes NPs water-soluble, however, they easily aggregate in ionic solution, e.g. Phosphate-Buffered Saline solution (PBS), due to the strong interaction with various ions present in solution, leading to aggregation.<sup>120</sup> Catechol functional groups have proved to have a high affinity to iron ions present in the NP's surface, forming a strong complex able to displace the previous ligand and maintain the new one well attached.<sup>121</sup> For the transfer of iron-based NPs in water, many studies have used catechol-based molecules such as dopamine,<sup>121</sup> 3,4-dihydroxyhydrocinnamic acid,<sup>20</sup> dopamine-functionalised polymer,<sup>122</sup> and dopamine-based molecular structure.<sup>123</sup> Also hydrophilic ligands bearing carboxylic acid (–COOH) moieties have been widely utilised to render iron-based NPs water-dispersible thanks to its good affinity towards the surface of iron oxide. For example, dimercapto succinic acid (DMSA),<sup>85</sup> citric

acid,<sup>91</sup> carboxylic acid- functionalised poly ethylene glycol (COOH-PEG)<sup>124</sup> were also proved to successfully displace hydrophobic native ligands.

In general, ligand exchange needs to consider the chemistry of NPs' surface and the affinity of a ligand to it. If the ligand-NPs bonding is too weak, it decreases the success rate of exchange, and consequently it increases the risk of detachment of the new ligand, ultimately favouring aggregation. Finally, ligand exchange process can alter NPs' physical properties of the surface.

#### 1.4.2 Polymeric encapsulation

Polymeric ligands provide a broad range of platforms that can be used to transfer NPs in water *via* the inclusion of the hydrophobic nanoparticle in an amphiphilic polymeric shell. Amphiphilic polymers have both hydrophobic and hydrophilic parts present within the same structure. The NPs are simply wrapped in a polymeric shell due to hydrophobic interaction between the alkyl chains of the surfactant coating and the hydrophobic regions of the polymer, regardless of the type of surfactant and of the specific inorganic material that forms the nanocrystal core. Therefore, such procedure can be used for several type of hydrophobic NPs.

One of the first study showing the suitability of polymer encapsulation to transfer hydrophobic NPs in water was carried out by Pellegrino *et al.*<sup>125</sup> They successfully used Poly(maleic anhydride-alt-1-octadecene), a cheap and commercially available polymer, to transfer several colloidal nanocrystals with various compositions, morphologies, and sizes. The strategy involved the intercalation of hydrophobic octadecene tails from the polymer into the alkyl chains of the NPs ligands. Following the hydrolysis of the anhydride moieties, the NPs then became water-dispersible.

In the literature, different engineered polymeric systems are reported for transferring hydrophobic nanoparticles in water. Indeed polyacrylic acid,<sup>126</sup> poly 2-hydroxyethyl aspartamide graft copolymers,<sup>127</sup> poly acrylic acid and polystyrene

block copolymer,<sup>128</sup> poly isobutylene-*alt*-maleic anhydride (PIMA) modified with alkylamine,<sup>129,130</sup> poly maleic anhydride-*alt*-1-tetradecene,<sup>131</sup> poly maleic anhydride-*alt*-1-octadecene (PMAO),<sup>125,132</sup> poly N-isopropylacrylamide modified PMAO,<sup>133</sup> polyethylene glycol modified PMAO,<sup>134,135</sup> and poly(styrene-*co*-maleic anhydride)<sup>136</sup> are just some of the polymer proved to efficiently encapsulate NPs and transfer them in water. In general, amphiphilic polymers that contain anhydride moieties (such PMAO or PIMA), have been preferred thanks to their ease of functionalization with very common reactive moieties like amines.<sup>137</sup>

This method provides an enhanced steric hindrance to the system thanks to the polymeric backbone, and the presence of functional groups on the polymeric shell allows the resultant hydrophilic nanoparticles to be conveniently functionalised. The method is versatile and can be used for different hydrophobic NPs systems obtained from thermal decomposition in organic solvent. This technique can be also preferred as it will not impair the physical properties of the nanoparticles, as the core crystal does not take part during the encapsulation process.

One of the drawbacks of this method is the control over the number of particles encapsulated within the polymeric structure. Indeed, for highly interacting NPs, the encapsulations of multiple NPs can occur, leading to aggregation.

### 1.4.3 Silica Coating

Silica coating has also been used as a approach to transfer hydrophobic NPs in water *via* sol-gel reaction (Stöber method)<sup>138</sup> or reverse microemulsion.<sup>139</sup> The process allows to encase the hydrophobic nanoparticles with an inert and amorphous silica shell using silica precursors such as tetramethoxysilane<sup>140</sup> and tetraethylorthosilicate.<sup>141</sup> The resulting core/shell particles comes with functional group on the silica surface (i.e. hydroxyls) which makes the particle hydrophilic providing also electrostatic repulsion. The surface moieties can also be used for further functionalisation in reaction with other silane-based molecules, allowing to

further improve the colloidal stability and tailor the final properties of the nanocomposite. For instance, reaction with PEG-modified silane adds enhanced colloidal stability to the system.<sup>142</sup>

Usually, silica coating requires NPs to be surfactant-free for the layer of silane to react with the surface of the hydrophobic NPs. Therefore, hydrophobic nanoparticles need to firstly undergo additional phase transfer step prior to silanization. For example, in the case of iron oxide NPs ligand exchange (*e.g.* with TMAOH)<sup>143</sup> and micelle formation (*e.g.* with Igepal-520) were commonly used in literatures.<sup>92</sup>

Although late silica coating protocols were able to isolate and coat individual nanoparticles,<sup>92</sup> achieving a thin layer of silica coating has proved to be very challenging. Shell of 10–50 nm silica thickness is usually obtained which can be detrimental for biomedical applications, hindering the physical properties of the coated nanoparticles.<sup>93</sup>

## 1.5 Conclusion

In this chapter, the synthesis of different kind of magnetic NPs have been reviewed especially in relation to their magnetic hyperthermia application.

Magnetic NPs have shown great potential for being used as heating probes and this has led to a great deal of research. However, MH is still far from achieving its full clinical potential and there is still the need for magnetic NPs with a high ILP value. Most of the research on NPs for magnetic hyperthermia has been directed towards spherical iron oxide-based NPs (magnetite and/or maghemite), with little investigation on different materials which hold great potential in MH but their use has been often limited by a more challenging synthetic procedure compared to spherical iron oxide NPs.

Moreover, it is important to have good colloidal stability for the NPs in order to use them in biomedical applications. Therefore, prior to testing the NPs for magnetic hyperthermia it is necessary to equip the surface of the NPs with suitable ligands.

This chapter provides the basics and fundamentals on which the following work is based.

## 1.6 Thesis Outline

The thesis focuses on the development of different magnetic Fe-based NPs for application in magnetic hyperthermia. Focusing on highly magnetic materials, NPs made of metallic Fe, Fe-C alloy and anisotropic  $\text{Fe}_x\text{O}_y$  were selected as potential heating probes and different strategies were followed to optimise their performances.

In general, prior to testing them for magnetic hyperthermia, the final NPs need to be: i) high quality NPs with excellent physical properties (high crystallinity and single domain with high MS value); ii) controllable in size and morphology with monodisperse size distribution; iii) hydrophilic with good colloidal stability (pH, ionic solution).

Chapter 2 provides an overview of the techniques and methods used in this work for the characterisation of the synthesised NPs up to the characterisation of the final nanocomposites once the NPs are transferred in water, including the equipment used for the evaluation of MNP performances in magnetic hyperthermia.

In Chapter 3 the study focused on the development of a new synthetic protocol for Fe NPs. Fe NPs are sensitive to oxidation and the final size of NPs was considered as an important parameter used to increase the hyperthermia output. Therefore, the drive of this chapter was to examine whether a synthetic protocol with size-tuning capabilities of Fe NPs could be achieved. This would allow the synthesis and

characterisation of metallic Fe NPs of different sizes and an investigation on the size-related oxidation process, and size-related magnetic hyperthermia output. In this chapter the quest for an easy and optimal process to transfer the synthesised NPs in water was also undertaken.

In Chapter 4, Fe-C alloy NPs were studied as potential tool for magnetic hyperthermia. The focus was to obtain uniform  $\text{Fe}_x\text{C}_y$  NPs so then their potential in magnetic hyperthermia could be examined, after being transferred in water.

In Chapter 5, the pursuit for easily obtaining shaped iron oxide NPs was examined focusing on the use of Hexadecylammonium Chloride to develop a facile synthetic protocol to control size and shape of NPs. The effect on magnetic hyperthermia were also studied.

In Chapter 6 the results from the previous chapters are summarised and the magnetic hyperthermia performances of different NPs are reported along with future perspective and research direction.

# Chapter 2 Characterisation Techniques

Nanoparticles used in biomedical applications require a broad range of techniques to fully assess their properties and structure. In this chapter the basics and principles of the main techniques used is described.

## 2.1 X-Ray Diffraction (XRD)

XRD is a technique used to determine the crystal structure of materials. Crystals are made of ordered arrays of atoms presenting a periodic three-dimensional repetition of an atomic pattern with interatomic distances in the order of Angstrom. X-Rays are electromagnetic radiations in the wavelength range of 0.1 to 100 Å. X-Rays with wavelength smaller than 10 Å are used to interact with the atoms in the crystal structures.

For XRD purposes it is essential to use a monochromatic source therefore filters and monochromators are usually used to filter out unwanted X-rays and make a single wavelength hit the sample. The reason lies on the Braggs' law which constitutes the base of this technique:

$$n\lambda = 2d_{hkl}\sin\theta \quad (2.1)$$

Where  $n$  is a positive integer number,  $\lambda$  is the X-rays wavelength,  $d_{hkl}$  is the distance between diffracting planes and  $\theta$  is the incident angle. According to the equation 2.1 the incident X-rays, hitting parallel lattice planes of a crystal, produce constructive interference when under a glancing angle  $\theta$  the path difference is a positive integer number of wavelengths, as can be seen from Figure 2.1.

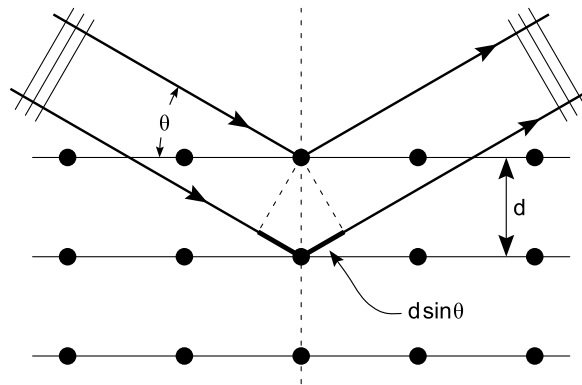


Figure 2-1 Bragg diffraction from a cubic crystal lattice

The diffracted X-ray photons are translated into voltage pulses inside the detector. When the conditions described by the Bragg law are satisfied, the constructive interferences observed at different angles will feature the peaks of the XRD pattern of the material under analysis. These peaks are related to the distance between specific type of crystal planes present within the crystal,  $d_{hkl}$ , therefore the pattern can be related ultimately to the atomic arrangement of the crystal. For instance, crystal systems with *hcp* crystal structure (hexagonally closed pack) will show different series of peak compared to *fcc* (face centred cubic) crystals. The identification of the crystal structure of the material is done by matching the obtained XRD pattern with the library of XRD patterns present in the literature.

### 2.1.1 Sample preparation and analysis

For the work carried out in UCL, XRD diffraction patterns were obtained using an X-ray diffractometer PanAlytical with a cobalt metallic anode as source ( $\lambda = 1.79 \text{ \AA}$ ). For the sample preparation the dry powder of the sample was flattened on a zero-background silicon holder. The analysis and matching of the obtained pattern were carried out with a software provided by PANalytical: X'Pert HighScore Plus.

For the work carried out in JAIST, XRD diffraction patterns were obtained using a Rigaku Miniflex 600, where the source was a Cu metallic anode ( $\lambda = 1.54 \text{ \AA}$ ).

The analysis and interpretation of a diffraction pattern mainly focused on the position, the relative intensity and the full width at half maximum of the peaks (FWHM). The positions and relative intensities of a diffraction pattern is characteristic of a specific crystal structure and the relative powder data files (PDF) for the identification can be retrieved from the International Centre for Diffraction Data (ICDD). The FWHM value of the peaks was used to calculate the mean diameter of the crystalline domains *via* the Scherrer formula. In order to calculate the FWHM value the peaks areas in the XRD patterns were first integrated. The Scherrer formula relates the broadening of the peak, measured with the FWHM value, to the size of the crystal domains. Although a certain degree of caution must be used, Scherrer's equation can be useful to estimate the size of the crystal domain:

$$\tau = \frac{K\lambda}{\beta \cos \theta} \quad (2.2)$$

Where  $\tau$  is the mean diameter of the ordered (crystalline) domains,  $K$  is a dimensionless shape factor (i.e. equal to 1 for spherical),  $\lambda$  is the X-ray wavelength,  $\beta$  is the difference in radians between the FWHM intensity and the instrumental line broadening which depends on the single instrument,  $\theta$  is the Bragg angle. It should be noted that the crystalline domain size can differ from the nanoparticle size because a particle can be made of multiple crystalline domains and therefore the particles can be much larger than the crystal grains they are made of, whereas if the diameter of particles matches the crystalline domain size, the particles are defined as single-crystal particles.

## 2.2 Superconducting quantum interference device – vibrating sample magnetometer (SQUID-VSM)

A SQUID-VSM was used for the measurement of magnetic properties of the synthesised NPs. The equipment used the combination of two different ways of measuring magnetic properties.

To measure subtle magnetic fields in a SQUID, two semi-rings made of superconducting material are put together in a superconducting solenoid. The link between the two is made of an insulating material and it is called Josephson junction (Figure 2.2). The formation of a superconducting current between the two superconducting materials is called Josephson's effect. The current is carried by pairs of electrons bound together, known as Cooper pairs, which travel through the junction by tunnelling effect. The current produced at the junction when an external magnetic field is applied is used to measure the magnetic properties of the sample. In this case, the solenoid is made of niobium-titanium superconductor and given the need to maintain superconductivity in the magnetometer, the device needs to be cooled with liquid helium to operate few degrees above the absolute zero.

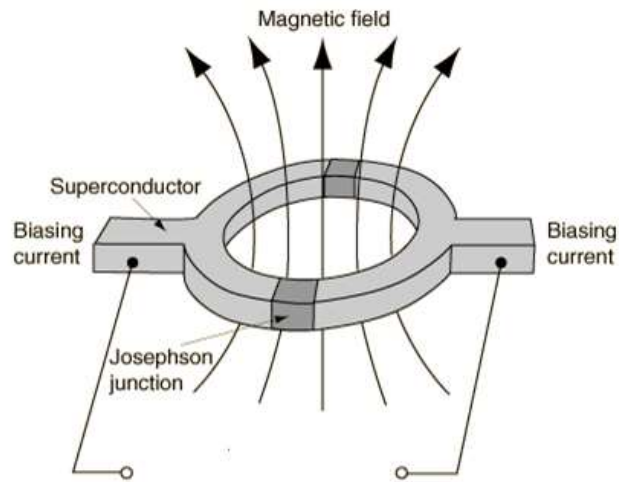


**Figure 2-2** *Josephson union in a SQUID flux sensor*

A vibrating sample magnetometer (VSM) allows quicker measurement of magnetic behaviour of samples without the sensitivity of a SQUID. In general, the sample is located next to a pickup coil and a magnetic field is applied through an external electromagnet. The instrument, then, starts moving quickly the sample up and down within the pick-up coil and the induced voltage in the pickup coil is measured. The signal intensity of the measured voltage is related to the magnetic properties of the sample (magnetic moment) using a palladium calibration standard material with a known magnetic moment.

Therefore, a SQUID-VSM put together the high sensitivity of a SQUID and the measurement speed of a VSM, allowing for rapid measurement of even weak magnetic fields. The instrument can give information on the magnetic saturation, hysteresis and blocking temperature of the nanoparticles.

The main measurements obtained from SQUID-VSM instrument were the  $M(H)$  hysteresis curves. Figure 2.3 shows an example of a hysteretic loop for a ferro(ferri-)magnetic material. Briefly, at the beginning of the measurement the external applied magnetic field,  $H$ , is set to zero and the net magnetic moment of the particles,  $B$ , is measured. When the external magnetic field is increased, the magnetic domains of

the material will gradually align towards the direction of the external magnetic field leading to an increase of the magnetic moment starting from the origin of the axis, as shown in Figure 2.3. Eventually all the magnetic domains will reach a complete alignment to the external field,  $H$ , and the magnetic moment value,  $B$ , reaches a plateau, also called Magnetisation Saturation  $M_s$ , where no change of value of  $B$  is observed with further increment of  $H$ . This first curve from the origin of the axis to the  $M_s$  value is called “virgin curve”. After, the value of  $H$  is first decreased, and an opposite magnetic field ( $-H$ ), increasing in strength, is applied to the sample. As the magnetic domains tend to re-align to the modified magnetic field, the sample’s magnetisation,  $B$ , starts decreasing without following the previous path rather following the curve at higher  $B$  values. This lagging of  $B$  behind  $H$  is called hysteresis. The point *Remanence* in the graph indicates the conditions at  $H = 0$  with a finite value of  $B$ . The remanence shows that after removing the magnetizing force ( $H$ ), a magnetic moment with little value remains in the material and it is known as residual magnetism ( $M_r$ ) and it is due to the retentivity of materials. Incrementing  $-H$  in reverse direction decreases the value of the residual magnetism that eventually gets to zero ( $B = 0$ ) with a certain negative value of  $H$ . This negative value of  $H$  is called *coercivity* or *coercive field* ( $H_c$ ). When  $H$  is further increased in negative direction ( $-H$ ),  $B$  gets reversed, eventually reaching again the magnetic saturation ( $-M_s$ ) but in opposite direction with respect to the previous case.

If the direction of the external field is changed again in the positive direction, the value of  $-H$  decreases and  $B$  decreases following a new path, always due to the retentivity of materials. At  $H = 0$  zero,  $B$  is with finite value, reaching again the *Remanence* value ( $-M_r$ ) but in the opposite direction compared to the previous case. If the  $H$  is increased, the residual magnetism ( $-M_r$ ) again decreases and gets zero at a point reaching again the coercivity value,  $H_c$  but in the opposite direction. Again, with further increment of  $H$ , the value of  $B$  increases from zero to its maximum value or saturation level ( $M_s$ ). The whole path forms the hysteresis loop.

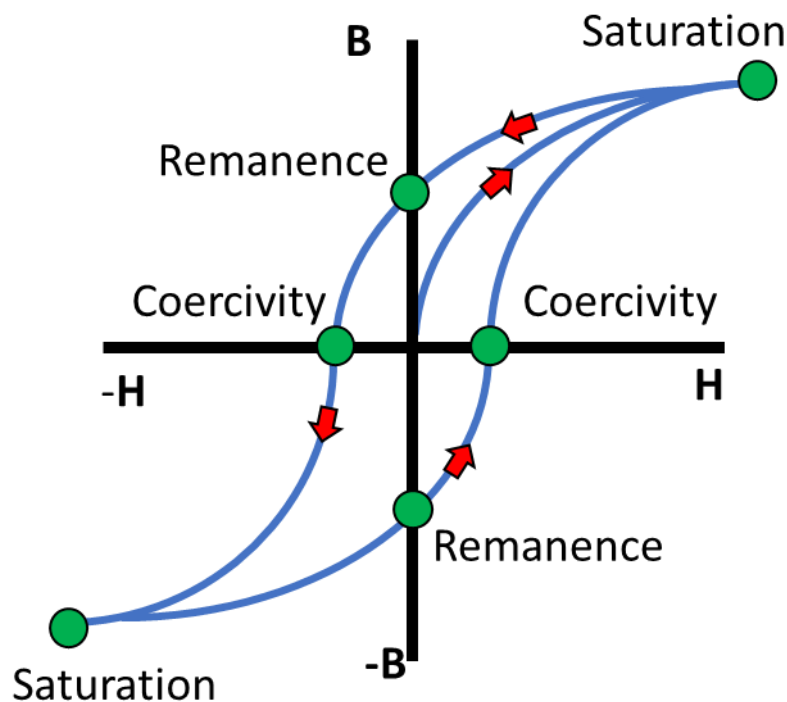


*Figure 2-3 Schematic representation of a magnetic Hysteresis loop.*

In this work, the hysteresis loops of the magnetic nanoparticles were measured at 300 K and 5 K using external magnetic fields ranging from -5 T to 5 T. The samples were demagnetised prior to each measurement in order to suppress any memory effect in terms of magnetic properties.

Zero-field cooled – field cooled (ZFC-FC) measurements were taken to investigate the blocking temperature ( $T_B$ ) of the nanoparticles, which is the temperature below which superparamagnetic NPs are “blocked” and show ferromagnetic behaviour. The ZFC-FC measurements were done by cooling the sample with no external magnetic field applied (zero-field) down to 5 K and then data were recorded while heating it up to 300 K in a 100 Oe field (ZFC curve). Subsequently the sample was cooled down again to 5 K with 100 Oe applied field while data were being recorded. This

constituted the FC curve. The temperature at which two curves converged gives the blocking temperature ( $T_B$ ) of the sample.

### 2.3 Transmission electron microscopy (TEM)

Transmission electron microscopy (TEM) is an imaging technique exploiting electrons shined onto a sample. Compared to light-based microscopy, TEMs can reach significantly higher resolutions. The main reason lies on the theoretical maximum resolution,  $d$  that can be achieved in microscopy. This has generally had its main limitation in the wavelength of the photons,  $\lambda$ , used to image the sample, according to the equation:

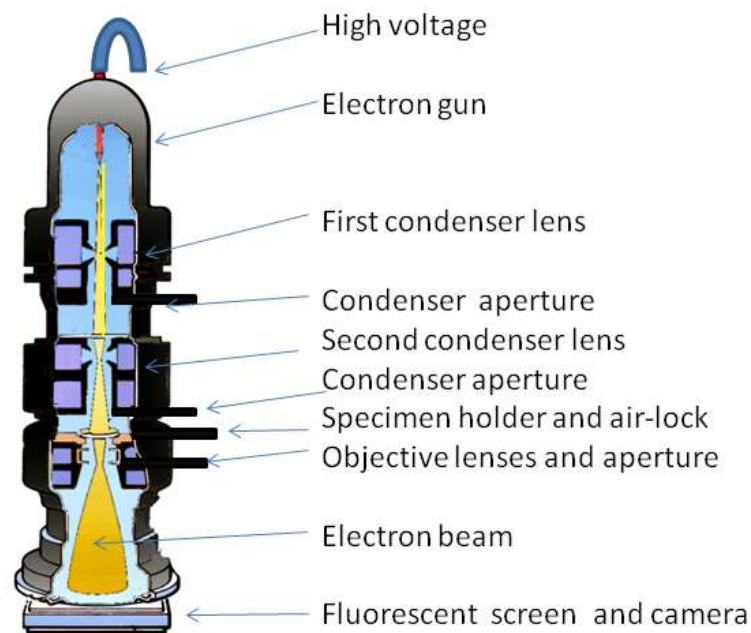
$$d = \frac{\lambda}{2NA} \quad (2.3)$$

where  $NA$  is the numerical aperture related to the system and lens used. At the beginning of the 1900, it was proposed to get around the limitations of using visible light ( $\geq 400$  nm) by using electrons. Electrons can follow both particle and wave behaviour, so a beam of electrons can have the same properties of a beam of electromagnetic waves. In this case the maximum resolution is dependent on the kinetic energy of electrons which determines their wavelength.

The imaging process of a specimen in the electron microscope occurs due to the electron being deflected by passing in proximity of the electrons or the positive nucleus of an atom. Due to spatial variation in the Z-number (related to atomic number) within a sample, a contrast is created in the final image. Areas with a higher Z-number will scatter electrons more strongly and appear darker in the bright-field images. The effect is also proportional to the thickness of the specimen, therefore thicker samples will usually appear darker than thin samples.

The beam of electrons can be generated usually from a tungsten (W) filament or a lanthanum hexaboride ( $LaB_6$ ) source by either applying high difference of potential

or by heating the material and promoting a thermionic emission process. The whole system operates under low pressure values to increase the mean free path of the electrons. The electrons then are focused and guided towards the sample through electromagnets present in the column of the TEM. The first magnetic lenses, condenser, control the region of the sample being illuminated, and allows for the manipulation and focusing of the beam on the sample. After that, the objective lenses enable the magnification of the image and the final image is then projected on a phosphorescent screen or a CDD camera. A schematic representation of TEM components is depicted in Figure 2.4



## Transmission Electron Microscope

*Figure 2-4 Schematic representation of TEM and its main components. Image provided by Dr Graham Beards-Wikipedia, Public domain. <https://commons.wikimedia.org/w/index.php?curid=8106664>.*

By exploiting different setups in an electron microscope, and different phenomena involved in the interaction between electrons and matter, several chemical and

structural information can be obtained. In the following paragraphs a brief explanation of other techniques associated with TEM will be provided.

### 2.3.1 Electron diffraction

In the Electron Diffraction (ED) mode the electron beam can be focussed on a single area and gain a diffraction pattern of a single particle. ED comes from the scattered electrons interacting in a similar manner to what is seen in X-ray diffraction. As the electrons scatter off planes of atoms, their wave functions can interact constructively or destructively displaying the crystals structural of the sample. This would produce a set of spots coming from the single crystal, while with small and densely NPs rings arise due to the randomly oriented crystals as it is shown in Figure 2.5. Each ring relates to a specific atomic spacing that can be indexed to the nanoparticles  $d$ -spacings, similarly to XRD.

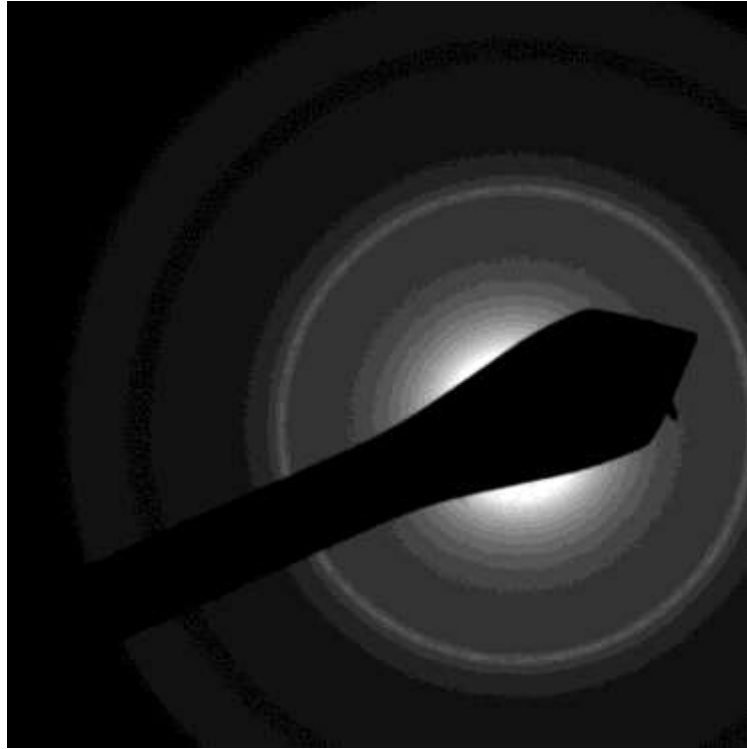


*Figure 2-5 Electron diffraction pattern coming from the interaction of electrons with Fe<sub>2</sub>C nanocrystals.*

The electron diffraction patterns can be used and plotted with the intensity plotted against the  $d$ -spacing in a similar way to how X-ray diffraction patterns are usually displayed. At UCL the electron diffraction patterns were taken after a previous calibration done with a sample with known elemental structure and  $d$ -spacing (e.g. gold). The plug-in PASAD in Gatan Micrograph 2.0 software was used to radially integrate the rings. This would output the data as two columns, one is the intensity and the other is the spacing between diffracting planes within the crystal ( $d$ ).

### 2.3.2 Scanning transmission electron microscopy

Scanning transmission electron microscopy (STEM) differs from conventional TEM as the beam can be focussed into a spot that can be scanned across the sample as a raster. This method can be coupled with other techniques to provide additional information on single particles and specific areas of the particle itself.

Energy Dispersive X-ray Spectroscopy (EDS) can be used along with STEM (STEM-EDS) to detect the elemental composition of a sample. When high energy electrons hit the sample, X-rays are emitted. This process is due to the incoming beam of electrons passing the valence electrons of an element and reaching the core electrons and giving these electrons enough energy to escape the nuclei. The lost electron is then replaced by an electron from the outer shell dropping down to a lower energy position and this transition is accompanied by the emission of an X-ray (Figure 2.6).

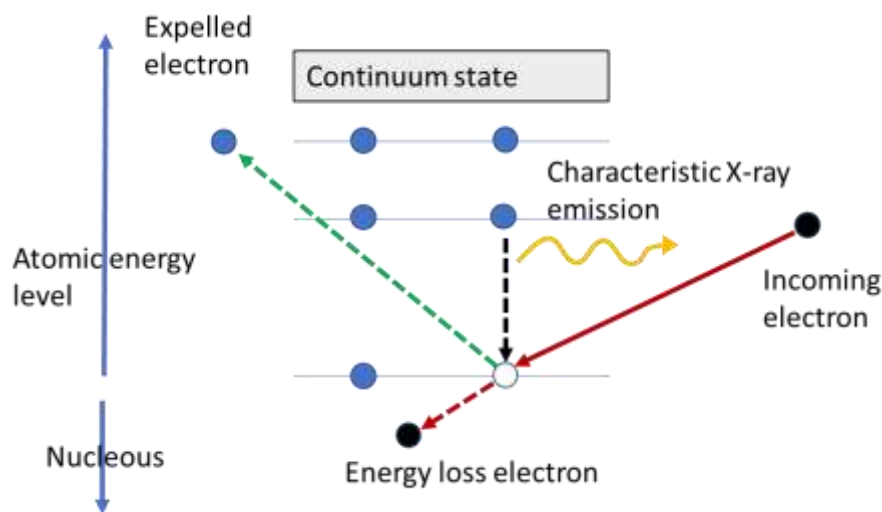


*Figure 2-6 Schematic representation of X-ray emission and energy loss electron formation after electron bombardment of the sample. As a vacancy in the core is formed, an X-ray is emitted while a higher energy electron drops down to fill the position. The energy loss electron is formed after the inelastic interaction of a coming electron with a core electron.*

The energy of the transition process is characteristic for each element and this allows the elemental identification of the sample. One of the limits of this technique is that light elements ( $Z < 11$ ) are hard to detect because in this case the production of X-ray involves valence electrons, therefore the chemical state and surrounding of the material can alter the final energy of the characteristic X-ray. This makes the characterisation more ambiguous for light elements whereas in heavy elements the X-rays are originated from electrons not involved in chemical bonds. The second

limitation is that if the nanoparticles are above 30 nm in size the X-ray emitted can be re-adsorbed by the rest of the crystal, altering the results.

STEM can also be used along with high-angle annular dark-field imaging (STEM-HAADF). An annular dark field detector collects electrons from an annulus around the main transmitted beam. This technique uses the Z value of the atoms to give the contrast. The dark field image is formed only by very high angle, scattered electrons which are scattered from the nuclei of the atoms in the sample. Therefore, the technique is highly sensitive to variations in the atomic number of atoms resulting in brighter contrast when Z is larger.

A STEM coupled with electron energy loss spectroscopy (STEM-EELS) was also used in this work to investigate the chemical composition of the NPs. The beam of electrons generated in the TEM is with a known, narrow range of kinetic energies. When the beam pass through the sample, some of the electrons undergo inelastic scattering and therefore lose energy. The energy lost can be quantified via an electron spectrometer by measuring the zero-loss energy beam (unscattered electrons) with loss energy electrons. Although different phenomena can contribute to this energy loss, the ionizations of inner or core electrons are particularly useful. A specific minimum energy transfer  $E_c$  from the beam electron is required to promote an inner shell electron to an unoccupied higher state therefore each element show characteristic edges at specific energy loss values. EELS can also provide information on the bonding state of the electrons and can be used to determine the oxidation state of an element.

### 2.3.3 Sample preparation and analysis

At UCL, the TEM images and ED patterns of the NPs were acquired with a JEOL JEM-1200EX, with a thermionic electron gun (W filament) working at a voltage of 120 kV. At JAIST the TEM used was a Hitachi H-7650 operating at an acceleration voltage of 100 kV (W filament).

At JAIST, a STEM equipped with HAADF detector, EDS and EELS was also used to further analyse the nanoscale structure of the NPs. HAADF-STEM imaging, EELS and EDS elemental mapping were performed on a JEOL JEM-ARM200F microscope operated at 200 kV with a spherical aberration corrector and a nominal resolution of 0.8 Å.

The TEM was used to investigate the morphology, composition, size and size distribution of the inorganic nanoparticles. Samples were prepared by dropping the nanoparticles dispersion onto a carbon-coated copper grid and allowed to dry in air. *Gatan Micrograph* software was used to process the images obtained from the measurements and *ImageJ* software was used to measure the size of the NPs. A minimum of 100 particles were measured in each TEM size determination (excluding STEM and EELS analyses).<sup>144</sup> The size measurement with *ImageJ* was carried out manually rather than automatically as the intrinsic characteristic of the particles does not allow for an accurate automatic counting. An automated NPs analysis would be less time-consuming and less dependent on the operator, however, contrary to denser materials which possess a high contrast in TEM imaging,  $\text{Fe}_x\text{O}_y$  has a low contrast in TEM micrograph (due to the low  $Z$  value of oxygen), also compared with metallic Fe and  $\text{Fe}_2\text{C}$  phase. Therefore, iron oxide phase can be easily overlooked with a software determination because it gets mixed up with the background of the sample holder. Moreover, if the sample does not disperse well onto the TEM grid, agglomerates counted as unique object lead to measurement errors.<sup>145</sup> Indeed, recent works on Fe-based NPs with similar features to the one studied in this thesis, reported manual size estimation.<sup>17,93</sup>

## 2.4 X-ray photoelectron spectroscopy

X-ray photoelectron spectroscopy (XPS) is a technique able to provide information on the elemental composition of a material, and the binding energies of the elements. It exploits the photo-electric effect occurring when a specimen is bombarded by an

X-ray beam. The incoming X-rays pass the valence electrons of an element to reach the core electron and gives this electron enough energy to escape the nuclei. The lost electron is then replaced by an electron from the outer shell dropping down to a lower energy position and this transition is accompanied by the emission of an Auger electron (Figure 2.7). The energy of the escaped electrons is then measured to give information on the chemical state of the element.

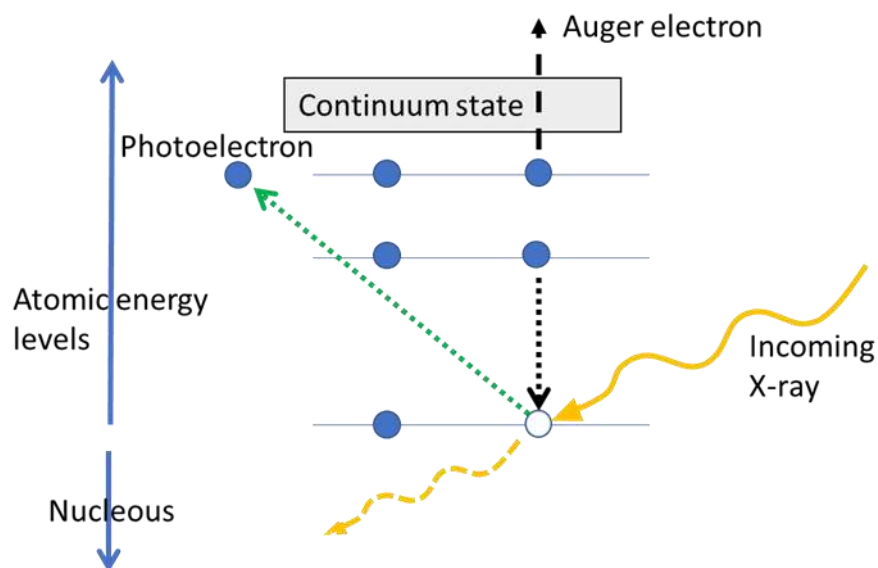


*Figure 2-7 Schematic representation of photoelectron and Auger electron emission after X-ray bombardment of the sample.*

XPS use a beam of monochromatic X-rays to hit the sample, coupled with an electron energy analyser to measure the kinetic energy of the expelled electrons. To maximise the number of electrons detected during the acquisition process, XPS measurement are operated under ultra-high vacuum conditions ( $P < 10^{-9}$  millibar). This setup allows for a longer mean free path of the electrons and avoids any risk of contaminations. Both photoelectrons and Auger electrons can be detected. The emitted photoelectrons have a kinetic energy which is proportional to its binding energy in the atom, as shown in eq. 2.4:

$$E_{binding} = E_{photon} - (E_{kinetic} + \phi) \quad (2.4)$$

where  $E_{binding}$  is the binding energy,  $E_{kinetic}$  is the kinetic energy measured by the detector,  $E_{photon}$  is the energy of the incident photon, and the  $\phi$  is the work function of the spectrometer. The Auger electron possesses kinetic energy equal to the difference between the energy of the initial ion and the doubly charged final ion. The kinetic energy of the Auger electron is independent of the photon energy.

The binding energy of the emitted photoelectrons gives information on the electron shell from which the electron was ejected, as well as the chemical environment of the atom. In this way XPS can give information on the elements present and the binding environment of those atoms.

In theory, XPS can detect all the elements but in practice light elements are harder to observe, and just elements with  $Z > 3$  (Lithium) can be detected. The detection limits for most samples are in the parts per thousand range, and thus the technique is highly sensitive to impurities present in the sample.

In order to be detected, photoelectrons need to travel through the material and escape into the vacuum. The mean-free path of the photoelectron is generally around 5 nm in length, and thus the signals coming from the surface of the sample is more intense than the signals coming from the material deeper below the surface. This makes XPS spectrum highly surface-specific and the reachable depth of analysis is less than 10 nm.

#### 2.4.1 Sample preparation and analysis

The XPS experiments were carried out in Japan at JAIST on a high-performance XPS system (Shimadzu Kratos, Axis-Ultra DLD) using Al  $K\alpha$  radiation. Generally, the sample was positioned on a stainless-steel support and it was fixed on a carbon-based double tape. A carbon spectrum is recorded prior to each measurement to calibrate the final

data. The value used for the calibration was 284.8 eV corresponding to the C-C bond from the tape.

## 2.5 Dynamic light scattering

Dynamic Light Scattering (DLS) is a spectroscopic analysis technique which is used to determine the hydrodynamic size of particles in a liquid dispersion. The technique exploits the Brownian motion of the dispersed particles to extract information over their hydrodynamic size distribution. Bigger particles have slower Brownian motion while smaller particles are moving faster in the liquid. When a laser source is directed towards the sample, the light gets scattered by the moving particles. The rate at which the intensity of the scattered light fluctuates at a given angle is measured, and this provides information on the velocity of the particles. In the case of small particles, the intensity fluctuates more rapidly than for large ones. The analysis is then related to their diffusion coefficient  $D$  and the particles size is calculated using the Stokes-Einstein's equation:

$$D_H = \frac{kT}{3\pi\eta D} \quad (2.5)$$

where  $D_H$  is the hydrodynamic diameter of the particles,  $k$  is the Boltzmann's constant,  $T$  is the temperature,  $\eta$  is the liquid carrier viscosity, and  $D$  is the diffusion coefficient.

DLS is used to evaluate the hydrodynamic diameter of the particles in a dispersion and providing information on the colloidal stability and homogeneity of the dispersion itself. It should be noted that  $D_H$  values come from the sum of NPs diameter plus the surrounding organic ligands on the surface of NPs in a dispersion. The value can significantly differ from TEM measurements as the organic matter is not detected in TEM measurements. The DLS measurements in this work were performed onto aqueous dispersion of NPs after the ligand exchange process, which

allows for the transfer of NPs from organic solvents into aqueous media. Therefore, for a given sample, a close value of hydrodynamic diameter to the TEM diameter meant that the ligand exchange occurred onto a single NP rather than a cluster of NPs.

### 2.5.1 Z-potential

With the same instrument it is possible to measure the zeta potential of particles in a specific solvent. Particles develop a net charge at surface due to the presence of functional groups. This leads to an increasing concentration of counter ions (ions of opposite charge to that of the particle) close to the surface. The liquid layer surrounding the particle can be then divided into two parts. An inner region, closer to the surface of the particles, called the Stern layer where the ions are strongly bound to the particles through electrostatic attraction. Then there is an outer region, diffuse layer, where ions are less firmly attached. This forms an electrical double layer around each particle. Within the diffuse layer there is a notional boundary inside which the ions and particles form a stable entity. This is called slipping plane. When a particle moves, ions within the slipping plane move with it, but any ions beyond it do not follow the particle. The potential that exists at the slipping plane corresponds to the zeta potential ( $\zeta$ ). To quantify the zeta potential value, the velocity of the particles is measured when an electric field is applied to the dispersion. This allows to determine the zeta potential using the Henri equation:

$$UE = 2\varepsilon z f(K_a) 3\eta \quad (2.6)$$

Where  $z$  is zeta potential,  $UE$  is the electrophoretic mobility,  $\varepsilon$  is the dielectric constant,  $\eta$  the viscosity and  $f(K_a)$  is the Henry's function. Zeta potential measurement can be used to evaluate the stability of colloidal systems since a high positive or negative value on the NPs surface leads to a repulsion between the particles, thus avoiding the flocculation process. As the charge of the functional groups on the surface of the NPs can change with the pH of the dispersion, Z-potential

measurements are also affected by the pH of the dispersion and they should be tested in a range of known pH values.

## 2.6 Magnetic Hyperthermia

The heating potential of the synthesised NPs was evaluated using a commercial device G2 driver D5 series calorimetric analyser (nBnanoScale Biomagnetics, Spain). The heating characteristics were measured during exposure to AC magnetic fields of various frequency and field strengths. This analyser used an optical fibre temperature probe immersed inside the magnetic NPs solution, monitoring temperature variations during field exposure. One of the most used parameters to measure the heating capabilities of nanoparticles is the specific absorption rate [SAR ( $\text{W}\cdot\text{g}^{-1}$ )]. The value is defined as

$$SAR = \frac{c}{m} \frac{dT}{dt} \quad (2.7)$$

where  $C$  is the specific heat capacity of water ( $4,185 \text{ J}\cdot\text{L}^{-1}\cdot\text{K}^{-1}$ ) and  $m$  is the concentration ( $\text{g}\cdot\text{L}^{-1}$ ) expressed in magnetic material present in the dispersion. In this work the concentration is expressed in amount of Fe present in the dispersion. For the measurement a volume of 0.5 ml NPs dispersion in a 1 ml glass vial was used. The vial is then inserted inside the sample holder featuring a sealed glass Dewar flask that provides thermal insulation. Within the sample holder box is also located the metallic coil that generates magnetic fields. From the top of the holder the optic fibre is inserted inside the solution to measure variations in temperature (Figure 2.8).

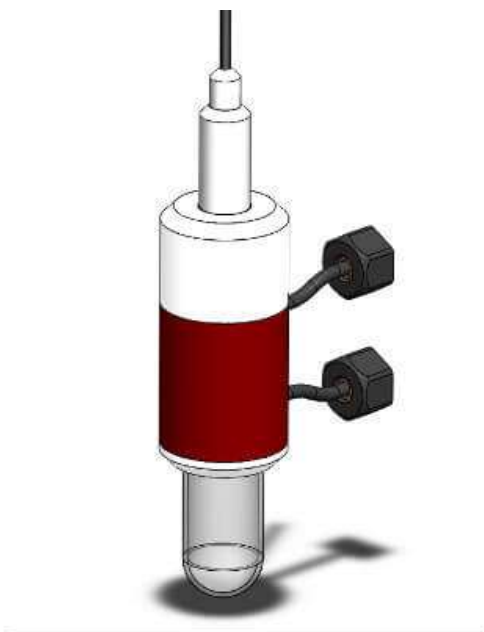


*Figure 2-8 Representation of the sample holder for magnetic hyperthermia measurement. Picture from the producer.<sup>146</sup>*

The data obtained from the measurement represent the temperature profile against the time during which the alternating field is applied. Figure 2.9 provides an example of a typical heating curve obtained during the analysis of NPs performance in Magnetic Hyperthermia. For the quantification of SAR, it is preferred to consider just the initial part of the curve where the heat loss of the sample to the surrounding environment is at minimum. In this case the heating curve follows a linear profile and can be fitted to obtain the  $\Delta T/\Delta t$  value. The value is then used to obtain the maximum heating power of the NPs. The fitting of the data is obtained through a Python script that takes into account the first 10, 20, 30, 40 seconds of measurement and the best fit is then used to extrapolate the SAR value.

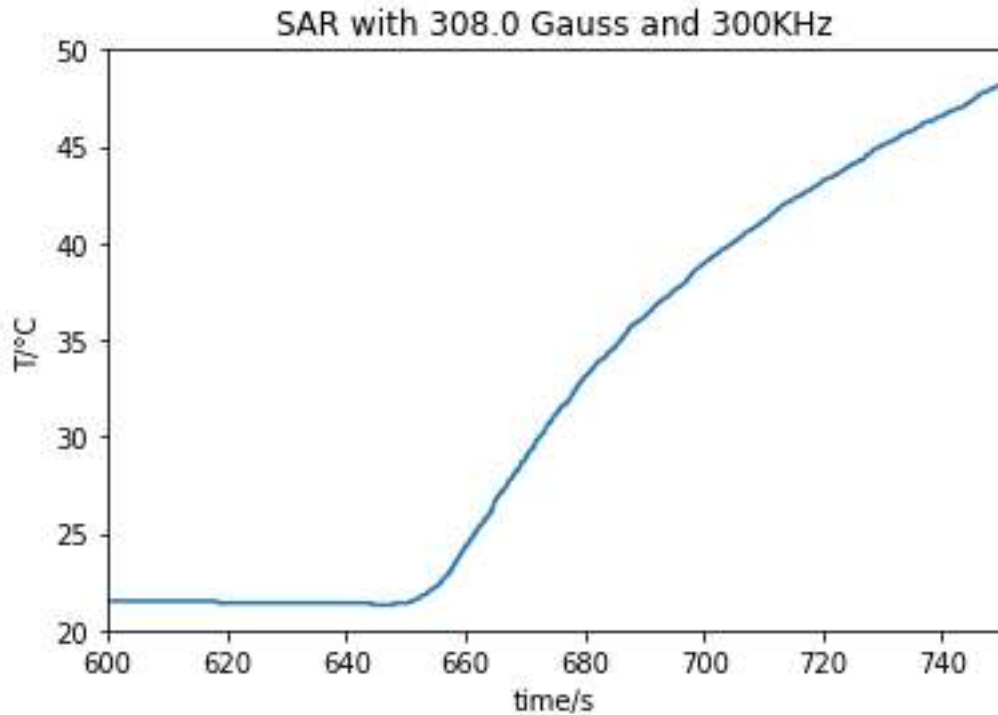


*Figure 2-9 Example of a typical heating curve obtained during the analysis of NPs performance in Magnetic Hyperthermia.*

Since size and composition of NPs affect the magnetic properties of NPs, SAR values highly depend on the value of frequency and field used during the measurement. This makes the comparison of different NPs not trivial. To better compare the results, it was also used the intrinsic loss parameter [ILP ( $\text{nHm}^2 \cdot \text{kg}^{-1}$ )]<sup>60</sup> to characterise the NPs. This parameter is more independent from the conditions used and it is obtained by normalising the SAR values with the fields and frequency amplitudes used in each measurement as follows

$$ILP = \frac{SAR}{(f \cdot H^2)} \quad (2.8)$$

Where f is the frequency of the field and H is the field strength.

## 2.7 Nuclear magnetic resonance spectroscopy

Nuclear magnetic resonance (NMR) is a spectroscopic technique that gives information on the magnetic fields around the atomic nuclei which can be used to determine the chemical structure of certain materials.

Subatomic particles can be considered as spinning on their axes and in the case of some atoms like  $^1\text{H}$  or  $^{13}\text{C}$ , the nuclei possess a nuclear spin. According to quantum mechanics, a spin  $I$  will allow  $2I+1$  possible orientations for the nuclear spin. With no external magnetic field applied, the energy of these possible orientations is equal, whereas when a static magnetic field is applied, the energy is split. In this case, for  $^1\text{H}$  nuclei with a  $I = \frac{1}{2}$ , we have two levels, one at lower and one at higher energy. The level at lower energy will be slightly more populated than the other as described by the Boltzmann distribution. The  $\Delta E$  between the two energies can be given as

$$\Delta E = \frac{\gamma h B}{2\pi} \quad (2.9)$$

where  $\gamma$  is a fundamental constant which depends on the kind of nucleus considered and is defined as magnetogyric ratio;  $h$  is the Planck constant and  $B$  is the external magnetic field. Higher values of  $B$  result in higher  $\Delta E$ . The energy is in the order of radio waves (MHz) and the excitation of the population from the lower energy state to the higher one with an electromagnetic pulse, provides the principles of  $^1\text{H}$ -NMR spectroscopy. The frequency at which this transition occurs is called resonance transition.

The power of this technique relies on the fact that the magnetic field at the proximity of the nucleus differs from the applied magnetic field. Electrons, circulating in the applied field, produce an opposite magnetic field, contributing to a shielding effect. Briefly, if an electron donating group is bonded to the proton, a higher electron

density is present around the nucleus and thus a weaker  $B$  is “felt” by the nucleus. This translates into a decrease of transition energy.

The final NMR spectrum is given in terms of chemical shift ( $\delta_H$ ) vs the intensity of the transition. The chemical shift is determined by the environment of the nucleus. It is usually measured in relationship with a reference compound that in the case of  $^1\text{H}$  NMR, is usually tetramethyl silane,  $\text{Si}(\text{CH}_3)_4$  ( $\delta_H=0$ ). At lower chemical shift values, the nucleus is more shielded from the external magnetic field, whereas at higher chemical shift values the nuclei are the least shielded. This can be associated to the presence of electro-donating and electro-withdrawing groups bounded to the protons in the molecular structure. Moreover, the intensity for each peak can give quantitative information on the groups present as the area of the peak is proportional to the number of protons involved.

$^1\text{H}$ -NMR was used to provide information on the polymeric ligands synthesised in this study. It was used to establish the successful addition of functional groups on the polymer and estimate the number of groups added.  $^1\text{H}$ -NMR spectra were recorded on a Bruker Advance III 400 MHz spectrometer using deuterated dimethyl sulphoxide as solvent. The TopSpin processing software was used to plot and analyse the  $^1\text{H}$ -NMR spectra.

## 2.8 Fourier Transformed Infrared Spectroscopy

Fourier-transform infrared spectroscopy (FTIR) is a technique using infra-red light to analyse the sample. The absorption of the sample in this range of electromagnetic waves provides information on the molecular composition of the studied material and this can be solid, liquid or gaseous.

The technique uses a polychromatic source that usually covers the wavelength range from  $2.5\ \mu\text{m}$  to  $25\ \mu\text{m}$  ( $4000\ \text{cm}^{-1}$  to  $400\ \text{cm}^{-1}$  in wavenumber). To break down the

beam into specific wavelengths a Michelson interferometer is used.<sup>147</sup> This is made of a specific configuration of lenses and mirrors, and one of the mirrors is moving. Briefly, the source of light pass through a beam splitter, and half of the light goes to a fixed mirror and the other half goes towards a moving mirror. Both mirrors then reflect the light, which goes back towards the splitter where it recombines, and it is then directed towards the sample. By changing the position of the moving mirror, the two beams created after the split have to travel different path lengths and this generates wave interference once the two beams recombine, allowing to modulate the final wavelength of light directed to sample. After, a detector measures the amount of light being absorbed by the sample. The absorption of light at each position of the moving mirror is correlated to the absorption at specific wavelength though a mathematical function called Fourier Transform, thus the name FTIR.

Infrared wavelengths are able to excite the vibrational states of molecules. When the energy of the incoming radiation matches the energy level of a vibrational mode, this molecule absorbs the radiation at that specific energy and a reduction in the intensity of the transmitted light is recorded. This absorption is correlated to the molecular structure of the sample. However molecular structures are “active” in the FT-IR spectroscopy only if the absorption of light is accompanied with a change of electric dipole in the molecule; if this does not happen, no absorption is observed in the final spectrum. The presence of electric dipole does not need to be permanent; when infra-red light is absorbed, atoms in the molecules can vibrate in many ways by stretching, scissoring, rocking, wagging and twisting. If during this process a temporary electric dipole is formed, then the absorption is observed. In the case of homonuclear diatomic molecules (e.g. N<sub>2</sub>) the electric dipole moment is always zero even when the molecule vibrates, so no absorption is detected.

The final spectrum is given in energy of the vibration (in cm<sup>-1</sup>) against the intensity of the absorption (in transmittance mode). Usually vibrations tend to be more intense for specific functional groups in the molecular structure and the position of the

absorption band is related to the strength of the bond and the mass of the atoms. FTIR is often used to quickly detect the presence of specific chemical groups.

Attenuated total reflectance (ATR) sampling can be used along with IR spectroscopy. This allows for the analysis of liquid or solid samples without any special preparation. ATR uses a sample holder made of a crystalline material with a high refractive index. An infra-red beam directed onto one side of the crystal gets totally reflected, forming an evanescent IR wave traveling within the crystal and able to reach the sample on the other side of the crystal. The evanescent infra-red waves are then absorbed and attenuated by the sample, leading to the final FTIR spectrum.

In this studies, ATR-FTIR spectroscopy was conducted with a Perkin Elmer Spectrum 100 spectrometer. ATR-FTIR was used to confirm the occurrence of the ligand exchange process. The replacement or modification of the organic ligands on the surface of NPs can be confirmed by comparing the NPs before and after the ligand exchange process. Indeed, the inorganic NPs are not active in FT-IR, whereas the change in the chemical structure of the ligands can be observed *via* FT-IR.

## 2.9 Iron quantification technique

The magnetic characterisation of a sample and the quantification of phenomena deriving from their magnetic properties depends on the determination of the magnetic mass present in a sample. In this study the nanomaterials used are iron based and different techniques were used for the quantification of this element.

### 2.9.1 Inductively coupled plasma atomic emission spectroscopy

Inductively coupled plasma atomic emission spectroscopy (ICP-AES) is a technique used to analyse the presence and quantity of material in the sample and the concentration detected is part per millions. The basic principles rely on the fact that when ionised atoms and electrons produced at high temperature recombine, a

photon is emitted, and the wavelength of the photon is specific of the element involved in the process.

Either liquids or solid samples can be analysed and in the case of solid samples they are dissolved in solution through acid digestion using strong acids. The solution is then directed into a helium or argon plasma at very high temperature (6000-8000 K) where the sample gets broken down in ions by the collision with the charged ions and electrons composing the plasma. During this process, atoms continuously lose electrons and recombine in the plasma and the photon emitted by the recombination of ions and electrons is collected and separated through monochromators and measured via photomultiplier tubes or charge coupled devices. The wavelength detected is specific for each element and the intensity is proportional to the amount of that element present in the sample. Finally, to obtain the concentration of a given element in the sample, the intensity is compared with a calibration curve previously obtained by measuring the intensity of the same element at different known concentrations.

For the measurements, a Varian 720 axial ICP-AES was used to determine the concentration of iron in the synthesised nanoparticles. Usually sample were prepared by digesting a known amount of nanoparticles powder (ca. 1 mg) in 0.5 ml of *aqua regia*, which was then diluted with 49 ml of milli-Q water. The upper limit range of the machine was 10 ppm because after this the detector could get saturated and thus limit the accuracy of the measurement. A series of 5 different concentrations were used to estimate a calibration curve covering the range between 0 to 10 ppm. ICP iron standard solution of 1000 ppm, HCl for atomic mass spectroscopy and HNO<sub>3</sub> for atomic mass spectroscopy were used for this kind of analysis.

### 2.9.2 Colorimetric assay

Colorimetric assay is an analytic technique using reagents which undergo a change of colour in the presence of analytes and the appearance of this new colour is

proportional to the concentration of analytes in solution. This variation can be measured via UV-Vis spectroscopy.

Briefly, for iron quantification, a common method involves the use of 1,10 o-phenanthroline as complexing agent for  $\text{Fe}^{2+}$ . Phenanthroline is a colourless molecule in solution and does not absorb in the visible range of the electromagnetic spectrum. However, in the presence of iron, three molecules of phenanthroline react with one iron ion forming a complex with the maximum of absorption situated at wavelength  $\lambda_{\text{max}} = 520 \text{ nm}$ . To create the optimal conditions for the reaction to happen, the complexation is carried out in mildly acidic environment using sodium acetate to create a buffer solution.  $\text{Fe}^{3+}$  ions form green-blue complex; thus hydroxylamine hydroxide is used as mild reducing agent to reduce any eventual  $\text{Fe}^{3+}$  present in the sample into  $\text{Fe}^{2+}$ .

For the measurements, a protocol optimised for the study of nanomaterials was used to determine the concentration of iron in the synthesised nanoparticles. Usually sample were prepared by digesting nanoparticles in 0.5 ml of HCl 4 M. Appropriate dilutions were made to obtain a final concentration that would lie within the detection limit of the method. After, sodium acetate, hydroxylamine hydroxide and finally phenanthroline were added to the solution and the reaction was let to complete for a couple of hours. A series of 5 different concentrations were used to obtain a calibration curve covering the range between 0.01 mg/ml to 0.2 mg/ml, by applying a similar procedure to the one used for the sample solution. Finally, the absorption values for the standard solutions and the sample were measured at 520 nm with a SpectraMax M2e multi-mode microplate reader.

## 2.10 Raman Spectroscopy

Raman Spectroscopy was used for the characterisation of carbonaceous phase of Fe<sub>2</sub>C NPs. This technique is used to detect vibrational modes similarly to infrared spectroscopy.

A laser beam is shone on a solid sample interacting with molecular vibrations or phonons present in the sample structure. The beam is then scattered both elastically and inelastically. While the elastically scattered photons are filtered out before reaching the detector, the inelastically scattered photons are collected and are used for the analysis of the sample. The inelastic scatter comes from the interaction of the electromagnetic wave from the laser source with the electronic cloud of the sample. This causes an excitation of the vibrational states of the sample to a virtual energy state; the sample then relaxes to a vibrational state which is different than the initial one emitting a photon with either higher or lower energy compared to the incident one. This phenomenon is called Stokes shift or anti-Stokes shift, respectively. The shift in energy provides information on the vibrational modes in the sample and it can be associated to the chemistry of sample.

Raman spectroscopy provides complementary information compared to FTIR. In the latter, a change in the dipole moment must happen for the vibrational mode to be observed, while in Raman is a change in polarizability of a molecule that leads to the final signal. This means that in FTIR just heteronuclear functional group with polar bonds are observed, which is not the case in Raman. This makes Raman a widely used technique for nanosized carbon-based materials like nanotube and graphene.

## 2.11 <sup>57</sup>Fe Mössbauer Spectroscopy

The characterisation of Fe<sub>2</sub>C NPs with Mössbauer was done in collaboration with Dr Lara Bogart at UCL Healthcare Biomagnetics Laboratory. In this technique,  $\gamma$ -rays are

shined onto a solid sample and a detector is used to quantify the intensity of the beam transmitted through the sample. The emitting source and the absorbing atoms in the sample must be of the same isotope, therefore in this case a  $^{57}\text{Fe}$  source was used. The source and the sample have different chemical environment, causing the respective nuclear energy levels to differ slightly (in the order of neV). The  $\gamma$ -ray spectral linewidth emitted by the radioactive  $^{57}\text{Fe}$  isotope is so narrow that the change in the absorbance of the Fe atoms in the sample becomes large and the resonance between source and sample is lost. To find again the energy at which the source and the sample are back into resonance, the source is placed in a linear motor that allows for the change in energy of  $\gamma$ -ray via Doppler effect, providing a range of energies used to scan the sample. The resulting output is a plot of the intensity of  $\gamma$ -rays vs the velocity of the source. When the energy is absorbed by resonant nuclear energy levels, the intensity of the  $\gamma$ -rays has a drop and the dip's features (number, position and intensity) give information on the chemical environment of the absorbing nuclei.

# Chapter 3 Synthesis of Fe@Fe<sub>x</sub>O<sub>y</sub> Nanoparticles

### 3.1 Introduction

Iron (Fe) nanoparticles (NPs) have been gathering much attention in the last few decades due to their intrinsically high magnetic moment.<sup>71</sup> This is known to be beneficial in many biomedical applications such as magnetic hyperthermia, magnetic resonance imaging (MRI), magnetic cell separation and targeted drug delivery.<sup>2,29,63,84,148–151</sup> In the case of magnetic hyperthermia, the higher magnetic moment resulted in better performances compared to relative oxides (magnetite or maghemite) and proof-of-concept demonstrations with Fe NPs showed promising results.<sup>65</sup>

High-quality Fe NPs were typically synthesized in organic solvents where it was easier to control the crystal phase and size.<sup>75</sup> Once formed in solution, the metallic Fe NPs were partially oxidised to form an oxide layer on the surface, by adding oxidising agent<sup>81</sup> or simply exposing the solution to air.<sup>152</sup> This can act as a protective shell for the Fe core to suppress further oxidation. Therefore, the term Fe NPs usually refers to a core@shell structure made of a  $\alpha$ -Fe and an  $\text{Fe}_x\text{O}_y$  shell (magnetite,  $\text{Fe}_3\text{O}_4$  or maghemite,  $\text{Fe}_2\text{O}_3$ ). Before being used in biological conditions, Fe NPs need to be transferred into water, usually via ligand exchange of the surfactants bound to the iron oxide shell surface.<sup>152</sup> However, while there are studies on the chemical stability of  $\text{Fe}@Fe_xO_y$  structure in air there is little information on the effects that aqueous media can have on  $\text{Fe}@Fe_xO_y$  NPs. Such missing information could potentially explain the divergence between hyperthermia outputs of  $\text{Fe}@Fe_xO_y$  reported prior to water-transfer<sup>63</sup> vs the hyperthermia outputs of  $\text{Fe}@Fe_xO_y$  reported after Fe NPs were transferred in water.<sup>29</sup>

Nemati *et al.* analysed a series of different sizes of  $\text{Fe}@Fe_3O_4$  NPs between 8 and 14 nm for magnetic hyperthermia after being ligand-exchanged.<sup>153</sup> They showed that for the bigger core@shell NPs a better magnetic response and heating rate was achieved after the transfer in water. This was due to a hollowing process known as the

Kirkendall effect which they observed was size dependent, and for smaller NPs (8 nm) resulted in completely hollow NPs in a few weeks, while for the larger NPs (14 nm) the process left parts of the core intact. However, in this case, the residual Fe core resulted in poor magnetic hyperthermia outcomes. Therefore, for biomedical applications larger Fe@Fe<sub>3</sub>O<sub>4</sub> NPs are desirable to allow the oxidation to occur without destroying the core@shell structure and retain a Fe core able to induce enhanced heating effects. In addition, theoretical studies found that the optimal size of Fe NPs should be greater than 10 nm to achieve the highest heating efficiency, with a sharp rise in performance at ca. 11-12 nm in size (Figure 3.1).<sup>67</sup>

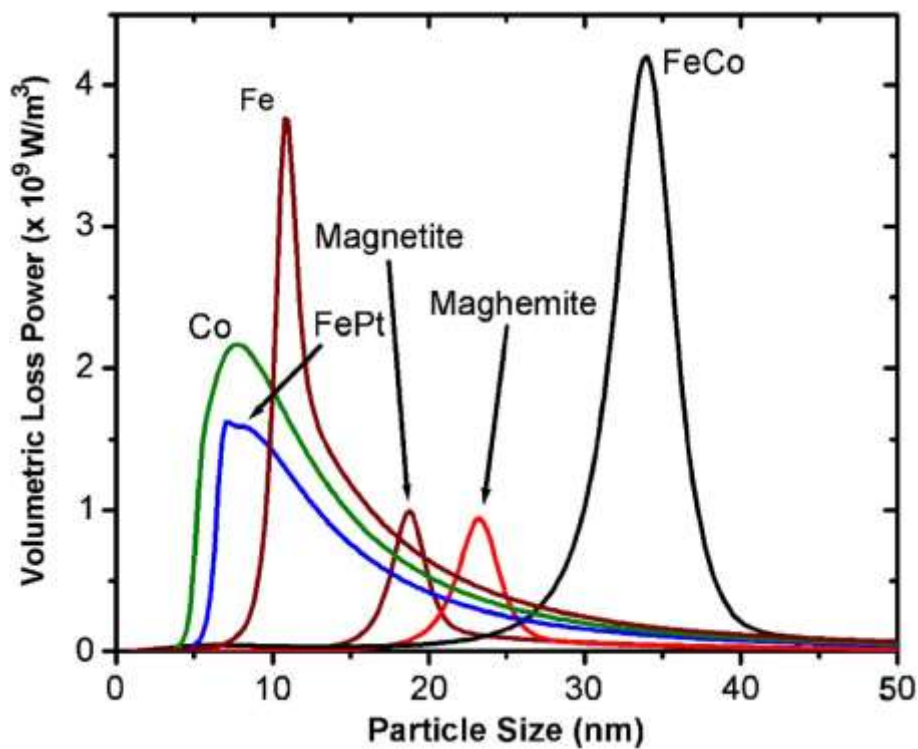


Figure 3-1 Specific loss power (or specific absorption rate) evolution as a function of size for various nanoparticle systems at 300 kHz and 39.8 kA m<sup>-1</sup>.<sup>67</sup>

In Nemati's work, the 14 nm Fe@Fe<sub>3</sub>O<sub>4</sub> NPs were, in fact, made of a 7.2 nm Fe core and 3.2 nm iron oxide shell prior to the ligand exchange. Since the authors attributed the reduction of heating performance to the further reduction of Fe core after the water-transfer, 14 nm Fe@Fe<sub>3</sub>O<sub>4</sub> NPs were still far from the optimal size for

Fe@Fe<sub>3</sub>O<sub>4</sub> NPs for magnetic hyperthermia. A new synthetic protocol allowing for the synthesis of larger Fe@Fe<sub>3</sub>O<sub>4</sub> NPs with a Fe core larger than 10 nm would be highly beneficial.

In this chapter, new methods to produce NPs with different sizes were investigated and the final NPs were then characterised. Moreover, different ways to transfer the Fe NPs in water were studied, covering the most common strategies used in the recent literature. The results from each method are discussed. The best result was then used to evaluate the magnetic hyperthermia efficiency of Fe NPs.

## 3.2 Materials and Methods

### 3.2.1 Reagents

1-Octadecene (ODE, purity 90%), hexadecylamine (HDA, purity 90%), diethyl ether (anhydrous, purity ≥99.7%), hydrochloric acid (HCl, assay 37%), oleylamine (OAm, purity 70%), poly(isobutylene-*alt*-maleic anhydride) (PIMA,  $M_w \approx 6,000$ ), dopamine hydrochloride (DOPA), dimethylformamide (DMF, anhydrous), triethylamine, tetrahydrofuran (THF) and di-sodium tetraborate buffer solution were purchased from Sigma-Aldrich, Japan. Polyoxyethylene (5) nonylphenylether (IGEPAL CO-520), cyclohexane, Tetraethyl orthosilicate (TEOS), ammonium hydroxide (25%–28%), poly (maleic anhydride-*alt*-octadecene) (PMAO) were purchased from Sigma-Aldrich, UK. Ethanol (EtOH, purity 99.5%) was obtained from Nacalai Tesque, Japan. Iron pentacarbonyl [Fe(CO)<sub>5</sub>, purity >95%], hexane and chloroform were obtained from Kanto Chemicals, Japan. All the reagents were used as purchased without any further purification.

### 3.2.2 Synthesis of Hexadecylammonium Chloride

The hexadecylammonium chloride salt (HDA-Cl) was synthesised according to the reported literature<sup>29</sup>. Briefly, 2.44 g of HDA (10 mmol) was dissolved in 100 ml of

hexane and left under vigorous stirring for 10 min to promote the solubilisation of the solid. In the meantime, an ice bath was put below the reaction flask. After, 12 ml of HCl 1 M in diethyl ether freshly prepared was injected in the reaction leading to the immediate formation of a white precipitate (ammonium salt). Then the ice bath was removed, and the reaction was let to complete for 2 h. After that, the precipitate was filtered and washed with hexane. Finally, the product was dried under vacuum to remove any residual hexane and stored in the fridge for further use.

### 3.2.3 Synthesis of Iron NPs through single-shot hot-injection

The iron NPs were prepared by following a slightly modified procedure previously reported in the literature<sup>29</sup>. Typically, OAm (0.160 mL, 0.5 mmol), HDA-HCl (0.138 g, 0.5 mmol) were added to 10 ml of 1-octadecene inside a 50 mL three-neck flask connected to a Schlenk line in one the neck so that the reaction is carried out in inert atmosphere. The solution was heated up at 120°C and degassed for 60 min under an Ar flux bubbled inside the solution through a syringe needle. After, the solution temperature was set at 180 °C and once stable, neat Fe(CO)<sub>5</sub> was loaded into a 1 ml syringe and was injected in a single and quick shot with a syringe. After the addition of iron precursor, Fe(CO)<sub>5</sub>, the solution became orange and turned black within a few minutes, indicating the formation of the NPs. The solution was kept at 180°C temperature for 30 min in total and after that the heating was stopped. Once the reaction reached room temperature, the solution was collected and transferred into two 50 ml centrifuge tubes and 5 ml of chloroform followed by 15 ml of ethanol were added. The solutions were centrifuged at 5000 rpm for 3 min. The supernatant was then discarded, and the precipitated nanoparticles were washed again adding 5 ml of chloroform first to redisperse the NP and 15 ml of ethanol after to promote the precipitation of NPs during the following centrifugation. The process was repeated twice in total and finally the NPs were redispersed in chloroform and stored for further use. The quantity of Fe(CO)<sub>5</sub> used in each reaction is listed in Table 3-1. Figure 3.2 shows a schematic representation of the setup used with a single shot injection.

### 3.2.4 Synthesis of Iron NPs through continuous addition of precursor

The Fe NPs were prepared by using OAm as a ligand and hexadecylammonium chloride (HDA-Cl), as an essential additive, to control the decomposition rate of  $\text{Fe}(\text{CO})_5$  to obtain highly crystalline Fe NPs.<sup>29</sup> HDA-Cl was synthesised following a previously published procedure.<sup>31</sup> Typically, OAm (0.160 mL, 0.5 mmol), HDA-Cl (0.138 g, 0.5 mmol) were added to 10 ml of 1-octadecene inside a 50 mL three-neck flask attached to a Schlenk line in one the neck so that the reaction is carried out in inert atmosphere. The solution was heated up at 120°C and degassed for 60 min under an Ar flux bubbled inside the solution through a needle. After increasing the solution temperature up to 180 °C,  $\text{Fe}(\text{CO})_5$  was added to the flask using a syringe pump (KD Scientific Inc., KDS100) at a rate of addition of 0.4 mL/h. By setting the rate of addition and the specifics of the syringe size (i.e. diameter and total volume) in which  $\text{Fe}(\text{CO})_5$  was charged, the volume of  $\text{Fe}(\text{CO})_5$  injected in the solution was calculated as a function of the injection time. The quantity of  $\text{Fe}(\text{CO})_5$  used in each reaction is listed in Table 3-4

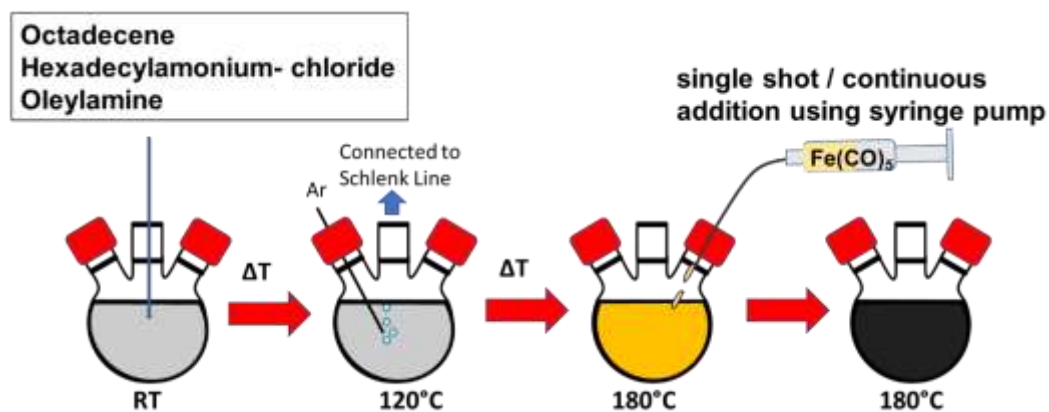


*Figure 3-2 Schematic representation of overall synthetic setup and procedures.*

The start of the reaction,  $t_0$ , was considered when the first drop of precursor was introduced into the reaction solution. The rate of addition of  $\text{Fe}(\text{CO})_5$  and the concentration of both OAm and HDA-Cl were kept constant in all the reactions and different amounts of the iron precursor were added by extending the injection time.

After the addition of  $\text{Fe}(\text{CO})_5$ , the solution typically turned black after about 15 min of injection, indicating the formation of Fe NPs. The longest reaction was run for 45 min, after which the injection and the heating were stopped, and the solution was left to cool down at room temperature. Three other injections times were selected to obtain different sizes of NPs. At the end of each reaction, the solution was collected and transferred into two 50 ml centrifuge tubes and 5 ml of chloroform and 15 ml of ethanol were added. The solutions were centrifuged at 5000 rpm for 3 min. The supernatant was then discarded, and the precipitated nanoparticles were washed again adding 5 ml of chloroform to redisperse the NP and 15 ml of ethanol to promote the precipitation of NPs during the following centrifugation. The process was repeated twice in total and finally the NPs were dispersed in chloroform and stored for further use. Figure 3.2 shows a schematic representation of the setup used with a continuous injection of  $\text{Fe}(\text{CO})_5$  using a syringe pump.

### 3.2.5 Silica coating

The synthesis followed a previously reported protocol used for the coating of iron oxide NPs.<sup>92</sup> Briefly, 0.5 g of Igepal CO-520 was dissolved in 11 mL of cyclohexane and sonicated for 10 min. Then, a known amount of solid Fe NPs was dispersed in 1 ml of cyclohexane and added to the reaction solution with continuous stirring; subsequently, 0.2 mL of ammonium hydroxide (25%–28%) was added to the above mixture solution. Finally, different volumes of TEOS were added and the reaction was left to react for 3 h. The reaction solution was collected and transferred in a centrifuge tube. 5 ml of ethanol was added, and the NPs were centrifuged for 10 min at 8400 rpm and then magnetically separated. The amount of Fe NPs and of TEOS used in each reaction was varied to achieve core@shell@shell  $\text{Fe}@\text{Fe}_x\text{O}_y@\text{SiO}_2$  NPs as described in Table 3.7.

### 3.2.6 Poly (maleic anhydride-*alt*-1-octadecene) coating

For the coating of Fe NPs with poly (maleic anhydride-*alt*-octadecene) (PMAO), it was followed the procedure reported by Moros *et al.* with some modifications.<sup>132</sup> First, 250 mg of PMAO was dissolved in 200 mL of chloroform under magnetic stirring. Secondly, 20 mg of Fe NPs dispersed in few ml of chloroform were added dropwise to the solution and the mixture was let stir for 1 h. To promote the encapsulation of the NPs with PMAO, the flask was placed in a rotary evaporator and a mild vacuum was applied to slowly remove the solvent. This process forms a black film at the bottom of the flask. 20 mL of NaOH 0.05 M solution was added into the flask to react with the maleic anhydride groups and make the nanocomposite water-soluble. The turbid solution was left to shake for at least 24 h adjusting the pH from time to time by adding more NaOH. Once the NPs are fully transferred in water the solution becomes clear, and it was then filtered using syringe filters of 0.45  $\mu\text{m}$ . To remove the excess of the unbound polymer the NPs solution was centrifuged at 40000 rpm for 3 min using an ultracentrifuge. The supernatant, where the excess of polymer remains, was discarded and the precipitate was redispersed in distilled water with the aid of a sonicator. The process was repeated three times. The NPs were finally dispersed in distilled water and stored for further use.

### 3.2.7 Poly (isobutylene-*alt*-maleic anhydride)-dopamine coating

The synthesis of dopamine-functionalised poly (isobutylene-*alt*-maleic anhydride) (PIMA-Dopa) followed a previous procedure with some modifications.<sup>154</sup> The synthesis of the polymer was carried out as follows: 0.385 g of PIMA (2.5 mmol monomer units) was dissolved in 10 mL of DMF in a 50 mL three-necked round-bottomed flask. After purging the solution with nitrogen, the temperature was raised to 70 °C. Separately, in 0.5 mL of DMF, 1.25 mmol of dopamine hydrochloride salt, was activated with 1.25 mmol of triethylamine. The process promoted the formation of triethylammonium chloride which was precipitated by centrifugation of the dispersion for 3 minutes at 5000 rpm. The supernatant (dopamine in DMF) was

sucked with a 1 ml syringe which was placed in a syringe pump (KD Scientific Inc., KDS100) to slowly inject the dopamine solution into the PIMA solution at 70°C. The addition of the dopamine solution was complete within an hour and the reaction was left to react overnight. To collect the polymer, the DMF was removed under vacuum using a rotatory evaporator, leaving a waxy liquid on the walls of the round bottom flask. After, 2 ml of deionized water was added, and a white solid started to precipitate from the waxy liquid. The dispersion was centrifuged for 5 min at 8400 rpm, the supernatant was discarded, and the precipitated polymer was further washed adding 5 ml of 1 M HCl solution following another round of centrifugation. The washing with HCl 1 M and subsequent centrifugation was repeated three times in total to remove any traces of DMF and unreacted dopamine from the sample. Finally, 5 ml of deionized water was used for the last round of centrifugation. Once the water was discarded, the polymer was left to dry under vacuum overnight.

The ligand exchange was carried out as follows: firstly, 25 mg of polymer was added to 1 mL of THF containing few drops of EtOH to improve the solubility of the polymer. The suspension was sonicated for 5 min until a clear solution was obtained. Secondly, about 5 mg of NPs dispersed in 1 mL of THF was added to the polymer solution and left in a rotating shaker for 24 h. Mechanical shaking of the reaction solution was preferred over magnetic stirring as the magnetic NPs tended to stick to the magnetic bar during the ligand exchange process leading to a low efficiency of the process due to the precipitation of particles. The sample was then precipitated adding 3 ml of hexane and the dispersion was transferred in a centrifuge tube and centrifuged for 2 min at 4,000 rpm. After discarding the supernatant 0.5 mL of THF and 0.3 mL of EtOH were added to disperse the precipitate; 2 ml of hexane was further added, and the turbid dispersion was centrifuged again. The supernatant was then discarded, and the precipitate was dried under vacuum leaving a black pellet. This was finally transferred in 5 mL of di-sodium tetraborate buffer solution at pH = 9.2 and allowed to stir for 24 to 48 h in a rotating shaker after few minutes of sonication to help to break down the pellet in smaller pieces. Once the dispersion gets clear, indicating

that water transfer was complete, a 0.45  $\mu\text{m}$  disposable syringe filter with VWR polyethersulfone membrane was used to remove any big aggregates and the excess of ligands was removed through a centrifugal filter (Sartorius, Mw cut-off 50 kDa) by applying three to four rounds of concentration/dilution with Milli-Q water ( $> 18.0 \text{ M}\Omega\cdot\text{cm}^{-1}$ ).

### 3.2.8 Modified poly (isobutylene-*alt*-maleic anhydride)-dopamine coating

To obtain a dopamine-functionalised polymer with a limited number of anchor points (Mod-PIMA-Dopa), the synthesis followed the same procedure of PIMA-Dopa with some modifications: 0.770 g of PIMA (5 mmol monomer units) was dissolved in 10 mL of DMF in a 50 mL three-necked round-bottomed flask. After purging the solution with nitrogen, the temperature was raised to 70  $^{\circ}\text{C}$ . Then, 0.5 mL of DMF containing 0.25 mmol of dopamine, previously activated with triethylamine hydrochloride was slowly injected into the solution using a syringe pump and left to react overnight. The washing procedure followed the same steps as PIMA-Dopa in the previous section.

The ligand exchange was carried out as follows: firstly, 50 mg of polymer was added to 10 mL of THF containing few drops of EtOH. The suspension was sonicated for 5 min until a clear solution was obtained. Secondly, about 10 mg of NPs was precipitated from the original dispersion in chloroform using EtOH and then dispersed in few mL of THF. Subsequently, this nanoparticle dispersion was added to the polymer solution and let in a rotating shaker for 48 h. The sample was then precipitated using 5 ml of hexane and centrifuged for 2 min at 4,000 rpm. After discarding the supernatant 6 mL of THF and 1 mL of EtOH were added to disperse the precipitate; 5 ml of hexane was added, and the turbid dispersion was centrifuged again. The supernatant was then discarded, and the precipitate was dried under vacuum leaving a black pellet. This was finally transferred in 10 mL of di-sodium tetraborate buffer solution at pH = 9.2 and sonicated for few minutes to help to break down the pellet in smaller pieces. The dispersion was then allowed to stir in a rotating

shaker for 48 h. Once the dispersion gets clear, indicating that water transfer was complete, a 0.45  $\mu\text{m}$  disposable syringe filter with VWR polyethersulfone membrane was used to remove any big aggregates and the excess of ligands was removed through a centrifugal filter (Sartorius, Mw cut-off 50 kDa) by applying three to four rounds of concentration/dilution with Milli-Q water ( $> 18.0 \text{ M}\Omega\cdot\text{cm}^{-1}$ ).

### 3.3 Results and discussion

#### 3.3.1 Synthesis of iron NPs through single-shot hot-injection: a study of precursor concentration effect

Usually, in the hot-injection method, the precursor is injected into the reaction solution with a temperature above the decomposition temperature of the precursor. This promotes rapid nucleation consuming most of the monomer in solution. The remnant monomer is then consumed by the growth of the nuclei into nanoparticles. Therefore, the initial amount of precursor used can modify the final size of the NPs.<sup>7</sup> For the synthesis of Fe NPs, four different amounts of precursor were investigated using 0.20, 0.25, 0.30 and 0.35 ml of  $\text{Fe}(\text{CO})_5$  (Table 3.1). The amount of  $\text{Fe}(\text{CO})_5$  used in each reaction was measured by using a 1 ml graduated syringe.

*Table 3-1 Amount of Fe precursor used for single hot-injection*

<b>Name</b>	<b><math>\text{Fe}(\text{CO})_5</math> ml</b>	<b><math>\text{Fe}(\text{CO})_5</math> (mmol)</b>
Fe_1	0.20	1.4
Fe_2	0.25	1.7
Fe_3	0.30	2.1
Fe_4	0.35	2.5

The TEM images (Figure 3.3) showed that in all four samples, NPs have a spherical shape with a darker core, likely made of iron and a brighter shell, possibly iron oxide. At 0.20 ml (Fe\_1) of Fe precursor injected the reaction leads to monodisperse NPs in size with an average size of  $13.5 \pm 1.2 \text{ nm}$  (Figure 3.3 a). Increasing the amount of Fe

precursor to 0.25 ml (Fe\_2), the average size increased as well with NPs of  $16.3 \pm 2.8$  nm (Figure 3.3 b). When 0.30 mL of Fe precursor was used (Fe\_3), the obtained average size was  $14.4 \pm 1.0$  nm (Figure 3.3 c) and finally, when 0.35 ml of  $\text{Fe}(\text{CO})_5$  was used (Fe\_4), the final size was  $16.3 \pm 3.3$  nm (Figure 3.3 d).

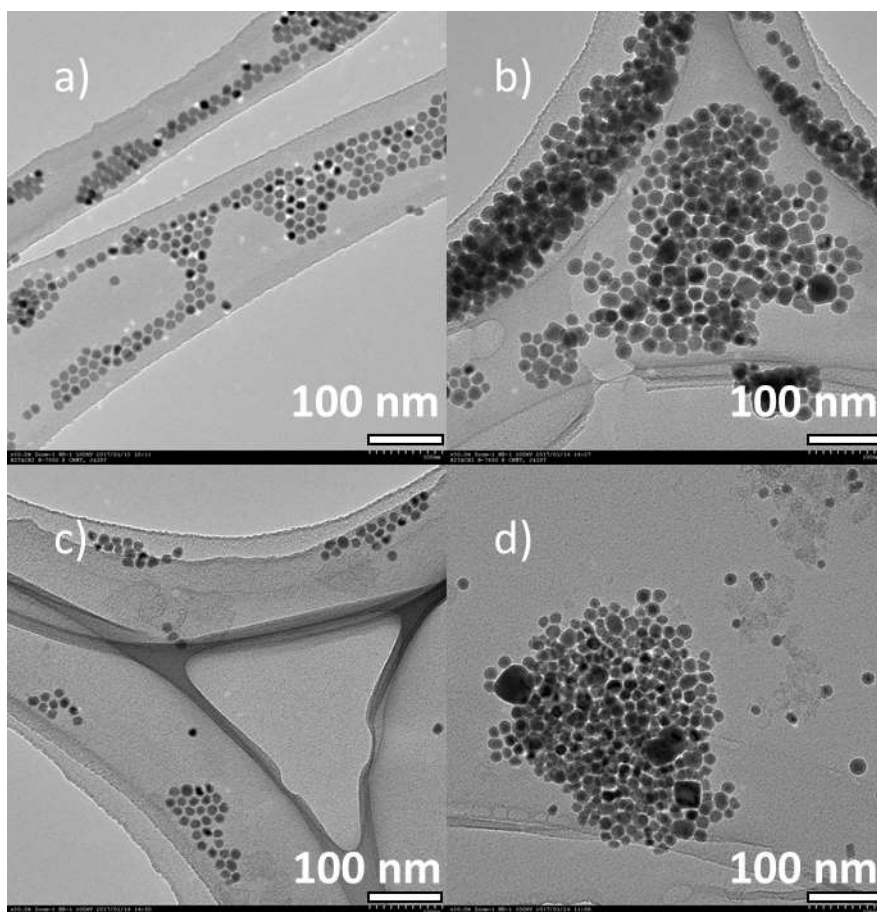


*Figure 3-3 TEM pictures for reactions a) Fe\_1 using 0.20 ml of  $\text{Fe}(\text{CO})_5$ , b) Fe\_2 using 0.25 ml of  $\text{Fe}(\text{CO})_5$ , c) Fe\_3 using 0.30 ml of  $\text{Fe}(\text{CO})_5$ , d) Fe\_4 using 0.35 ml of  $\text{Fe}(\text{CO})_5$ .*

From the XRD patterns, (Figure 3.4) the main phase detected in all four samples matched the pattern of cubic  $\alpha$ -Fe. No evidence of oxide layer was found in the pattern, meaning that the oxide shell was either amorphous or was made of very small crystalline domains which could lead to a weak signal that it was hard to detect in the final pattern. By using the Scherrer equation it was possible to estimate the

crystal size of the  $\alpha$ -Fe phase. The calculation was performed after the integration of the XRD pattern and calculated on the first peak at  $44^\circ$  ( $2\theta$ ) which is the most intense in the pattern. In the case of reaction Fe\_1, the crystal domain size was 8.5 nm. After increasing the amount of precursor, Fe\_2, the size increased to 11.2 nm. In the case of Fe\_3, the obtained value was 10.5 nm and finally, for Fe\_4 the estimated size was 13.1 nm.

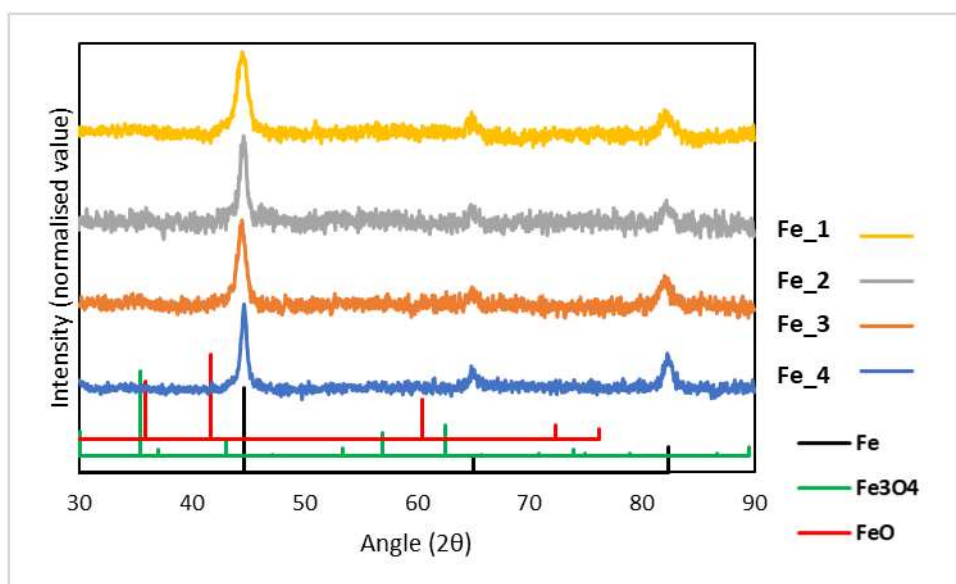


Figure 3-4 XRD patterns for different amount of iron precursor  $Fe(CO)_5$  used: 0.20 ml for Fe\_1, 0.25 ml for Fe\_2, 0.30 ml for Fe\_3 and 0.35 ml for Fe\_4.

Table 3-2 Summary of NPs size and Fe size obtained through TEM and XRD analysis.

Name	NPs Size nm (TEM)	Fe Size nm (XRD)
Fe_1	$13.5 \pm 1.2$	8.5
Fe_2	$16.3 \pm 2.8$	11.1
Fe_3	$14.4 \pm 1.0$	10.5
Fe_4	$16.3 \pm 3.3$	13.1

The TEM values and the estimated crystal size of the Fe phase are summarised in Table 3.2. By increasing the amount of precursor used, the size of NPs (and the size of Fe crystallite) initially increased from 13.5 nm to 16.3 nm. However, after further

increasing the amount of precursor, the size of NPs decreased to 14.4 nm and eventually increased again when more precursor was used. The XRD values followed a similar trend.

It was also observed that the polydispersity values for the size of the NPs (defined as the standard deviation divided by the average diameter times 100) for the four reactions changed considerably from a value around 10 %, in the case of Fe\_1 and Fe\_3, to a value almost double ( $\approx 20$  %) for Fe\_2 and Fe\_4. Higher values in polydispersity corresponded to a broader size distribution of the size of NPs. The polydispersity can be used as a mean to roughly determine how controlled the reaction conditions are. For example, if during the synthesis a single nucleation step takes place, the following growth of nanoparticles usually leads to monodispersed NPs (polydispersity value  $\leq 10$  %).<sup>16</sup> On the other hand if multiple nucleation steps take place at different times, the following growth is not homogeneous within the whole sample and usually NPs with higher size polydispersity are obtained.<sup>75</sup>

However, in this case, the polydispersity values did not follow a straightforward trend and few considerations were done. The size-tuning capability of the reaction protocol was very limited. Changing the amount of precursor led to particles with bigger size but also with larger size distribution. It was hypothesised that when a larger volume of the precursor was used, this did not decompose homogeneously once injected, causing multiple nucleation steps during the reaction which eventually led to a broad size distribution. Possibly, the irregularity of the results was associated with the hot-injection procedure itself, because the injection was performed manually and thus an identical injection time was hard to replicate from batch to batch.

### 3.3.2 Synthesis of Iron NPs through continuous addition of precursor

Good size tunability with a narrow size distribution can be obtained through a sequential injection of precursor.<sup>16</sup> This can prevent the process of Ostwald ripening

(or size defocusing) from taking place when the monomer is depleting. As more monomer is added in a later stage of the reaction, a process of refocusing of the NP size can be promoted.<sup>6,155</sup> In addition, one of the most recognised theories to describe the growth evolution of a colloidal system was proposed by LaMer.<sup>156</sup> Using this model, it is possible to predict that the excessive addition of monomer in a later stage can lead to a second nucleation process if the concentration raises above the nucleation threshold ( $C_{min}$ ). This is undesirable as the growth of two populations would lead to a broadening of the size distribution. By controlling the rate of addition, it is possible to prevent a second nucleation stage and promote just the growth of the crystals (Figure 3.5).

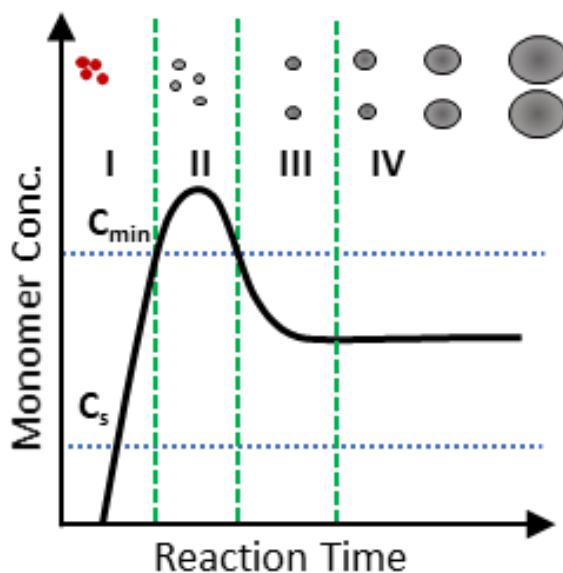


*Figure 3-5 Extended La-Mer plot configuration.*

To tune the final size and polydispersity of Fe NPs, a novel approach was investigated using a continuous injection of precursor instead of a single injection. Moreover, in this case, a syringe pump was used to have a reproducible injection of precursor and to control the rate of addition.

### 3.3.2.1 Control over the injection rate

As a first step, it was evaluated whether a syringe pump could be used to continuously inject the precursor in the reaction solution. Tests were carried out using different rates of addition of the precursor to evaluate which rate of injection would not promote any secondary nucleation step but just growth of the pre-formed particles. (Table 3.4) No changes in the other parameters were made and the concentration of chemicals was left unchanged: 10 ml ODE was used as a solvent, 0.5 mmol of OY was used as a ligand, 0.5 mmol of HDA-Cl and 2.0 mmol of  $\text{Fe}(\text{CO})_5$  (0.27 ml) were used as a necessary chemical for the formation of crystalline Fe NPs.

*Table 3-3 Conditions used for continuous hot-injections.*

<b>Sample</b>	<b>Rate of injection <math>\text{Fe}(\text{CO})_5</math> (ml/h)</b>	<b><math>\text{Fe}(\text{CO})_5</math> (mmol)</b>	<b>HDA-Cl (mmol)</b>	<b>OAm (mmol)</b>
Fe_5	1.3	2.0	0.5	0.5
Fe_6	0.4	2.0	0.5	0.5
Fe_7	0.2	2.0	0.5	0.5

In general, as the precursor was injected into the reaction solution, the colour of the reaction became bright yellow. After some minutes the solution turned brown and then quickly black. This indicated the formation of NPs, which became big enough to scatter light. This step can be related to the nucleation event.<sup>110</sup> A faster colour change was observed with increasing the rate of injection.

When using 1.3 ml/h rate of injection, (Fe\_5 sample) Fe NPs appeared to be highly polydisperse in size with particles over 50 nm with cubic structures also appearing (Figure 3.6 a). This indicates that multiple nucleation events occurred, and the growth was not controlled due to the fast rate of injection of the precursor. The XRD pattern for the same sample showed that the main phase was  $\alpha$ -Fe with a crystallite size of 16.7 nm.

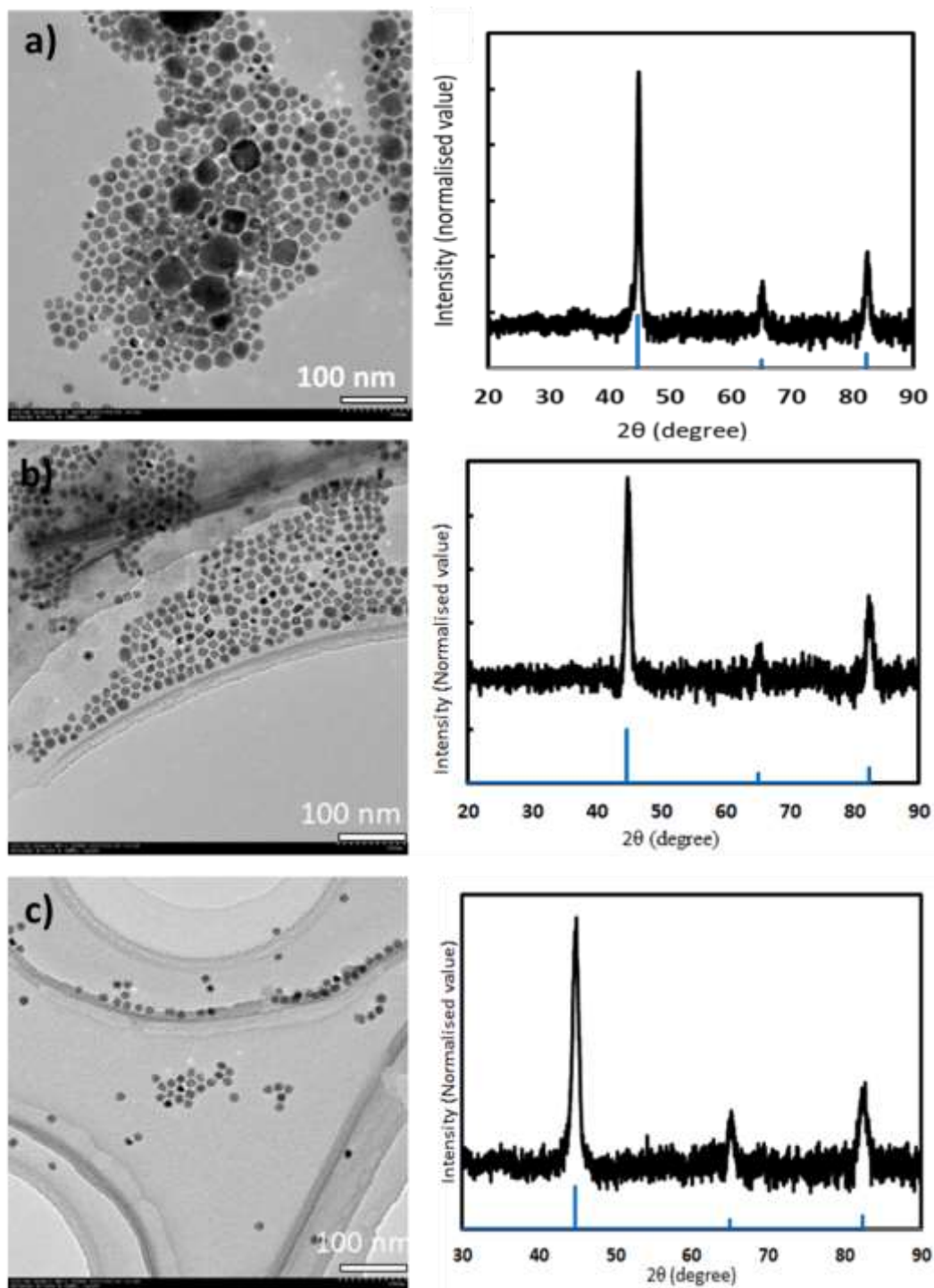


Figure 3-6 a) TEM micrographs of Fe NPs synthesised with 1.3 ml/h injection rate and XRD pattern of the same sample. b) TEM micrographs of Fe NPs synthesised with 0.4 ml/h injection rate and XRD pattern of the same sample. c) TEM micrographs of Fe NPs synthesised with 0.2 ml/h injection rate and XRD pattern of the same sample. Reference pattern in the XRD corresponds to  $\alpha$ -Fe (pdf ref. 00-006-0696).

The rate of injection was then reduced to 0.4 ml/h to avoid multiple nucleation steps. In this case, the particle size appeared to be homogeneous with an average value of  $17.7 \pm 1.9$  nm (Figure 3.6 b). The XRD pattern showed that the phase corresponded to  $\alpha$ -Fe with a mean crystallite size of 10.3 nm. This showed that by decreasing the rate of addition, the formation of NPs resulted in a more controlled fashion, indicating that multiple nucleation steps were avoided. Also, some shaped NPs were present in the sample and this may come from slower growth of the NPs compared to the single hot-injection. This could favour an anisotropic growth guided by the cubic crystal structure of  $\alpha$ -Fe instead of an isotropic growth.

The rate of injection was then further slowed down to 0.2 ml/h to confirm the hypothesis that controlled growth is achieved with a slow injection of the precursor. Moreover, it would help to investigate whether the rate of addition of precursor can also affect the final cubic morphology of the NPs.

From Figure 3.6 c, the TEM micrograph shows core@shell nanoparticles with an average size of  $14.4 \pm 0.8$  nm. The sample also showed some shaped and cubic-like NPs along with spherical NPs. However, no clear difference was detected in the overall shape of the NPs compared to the sample obtained with 0.4 ml/h injection rate. The XRD pattern showed that the phase corresponds to  $\alpha$ -Fe with a mean crystallite size of 9.4 nm.

We concluded that the 0.4 mL/h rate is slow enough to obtain a controlled synthesis without multiple nucleation events. With a faster rate of injection, the obtained NPs were polydisperse and multiple nucleation events occurred. Slowing down the rate to 0.2 mL/h still produced highly monodispersed NPs but required longer reaction times and did not significantly affect the final shape of the NPs. Therefore 0.4 ml/h was selected as the optimal injection rate for further experiments.

### 3.3.2.2 Control over amount of precursor injected.

After investigating the optimal conditions required for the formation of Fe NPs with the continuous injection of the precursor, it was important to evaluate the tuning capabilities of this method. The conditions used were 10 ml of octadecene, 0.5 mmol of OAm and 0.5 mmol of HDA-Cl. The injection rate for the addition of  $\text{Fe}(\text{CO})_5$  was set at 0.4 ml/h. Fe NPs of different size were produced by adding a different amount of precursor (see Table 3.5), after which the reaction was stopped, and the product was fully characterised.

*Table 3-4 Reaction condition used to obtain different sizes of Fe NPs*

<i>Sample</i>	<i>Rate of injection (ml/h)</i>	<i>Fe(CO)<sub>5</sub> injected (mmol)</i>	<i>Injection time (min)</i>	<i>HDA-Cl (mmol)</i>	<i>OAm (mmol)</i>
Fe_8	0.4	1.0	20	0.5	0.5
Fe_9	0.4	1.3	25	0.5	0.5
Fe_10	0.4	2.0	38	0.5	0.5
Fe_11	0.4	2.4	45	0.5	0.5

The TEM images of the four samples show how the size of NPs increased with increasing the amount of Fe precursor added in the reaction solution (Figure 3.7 a-d). The NPs synthesised using 1.0 mmol of  $\text{Fe}(\text{CO})_5$ , which corresponded to 20 min injection time, had a mean diameter of  $12.6 \pm 0.6$  nm as shown in Figure 3.7 a. No core was observed, and the NPs appeared to be fully oxidised after being exposed to air. When 1.3 mmol of  $\text{Fe}(\text{CO})_5$  was used (25 min of injection time), the NPs size increased to  $15.9 \pm 0.9$  nm and the NPs deposited onto the grid forming a superlattice (Figures 3.7 b and 3.7 c), indicating a high uniformity in size. In this case, a distinct core@shell structure is observed. With a higher amount of precursor, i.e. 2.0 mmol of  $\text{Fe}(\text{CO})_5$ , corresponding to 38 min of injection time, the NP size increased up to  $18.3 \pm 1.1$  nm. When the amount of Fe precursor was further increased to 2.4 mmol, corresponding to 45 min of injection time, bigger NPs with a diameter of  $20.7 \pm 3.9$

nm were obtained (Figures 3.7 d). The polydispersity values remained almost constant for the first three samples (standard deviation below 10%), while the standard deviation of the 20.7 nm NP size reached a value close to 20% (Figure 3.8 e). The volume of the NPs was calculated from the diameter of the NPs obtained in the TEM analysis and the value was plotted against the amount of  $\text{Fe}(\text{CO})_5$  injected in the reaction, as shown in Figure 3.7 f. The graph shows a linear trend with the size increasing with the amount of  $\text{Fe}(\text{CO})_5$  injected, showing that the size of  $\alpha\text{-Fe@Fe}_x\text{O}_y$  NPs can be systematically tuned by controlling the amount of precursor used. However, the NP growth tended to lose control due to a stronger inter-particle magnetic dipole interaction when the NP size approaches 20 nm, causing them to aggregate and precipitate. This ultimately led to a broader size distribution, similarly to previous reports with ferromagnetic metals.<sup>17,157</sup>

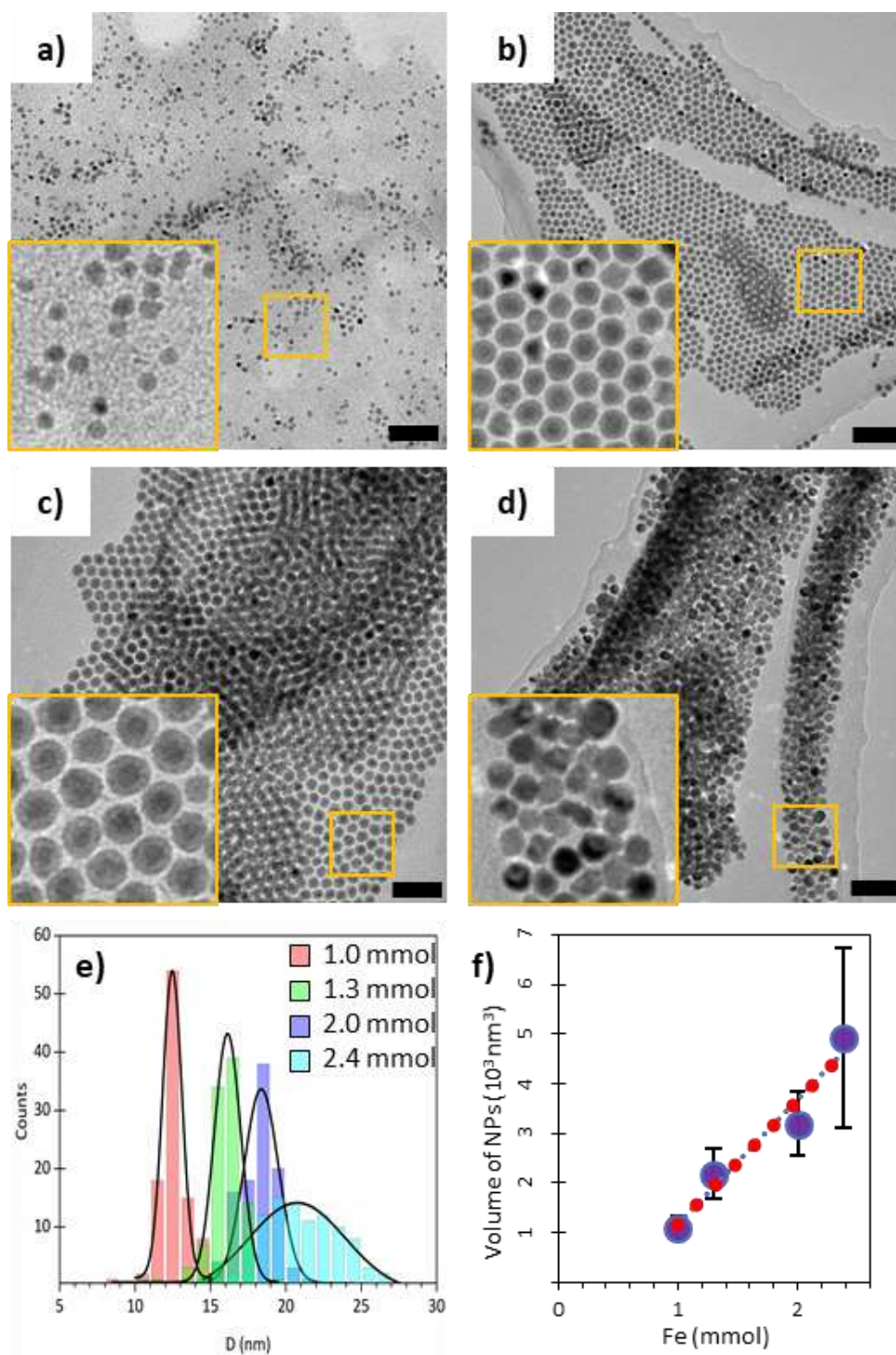
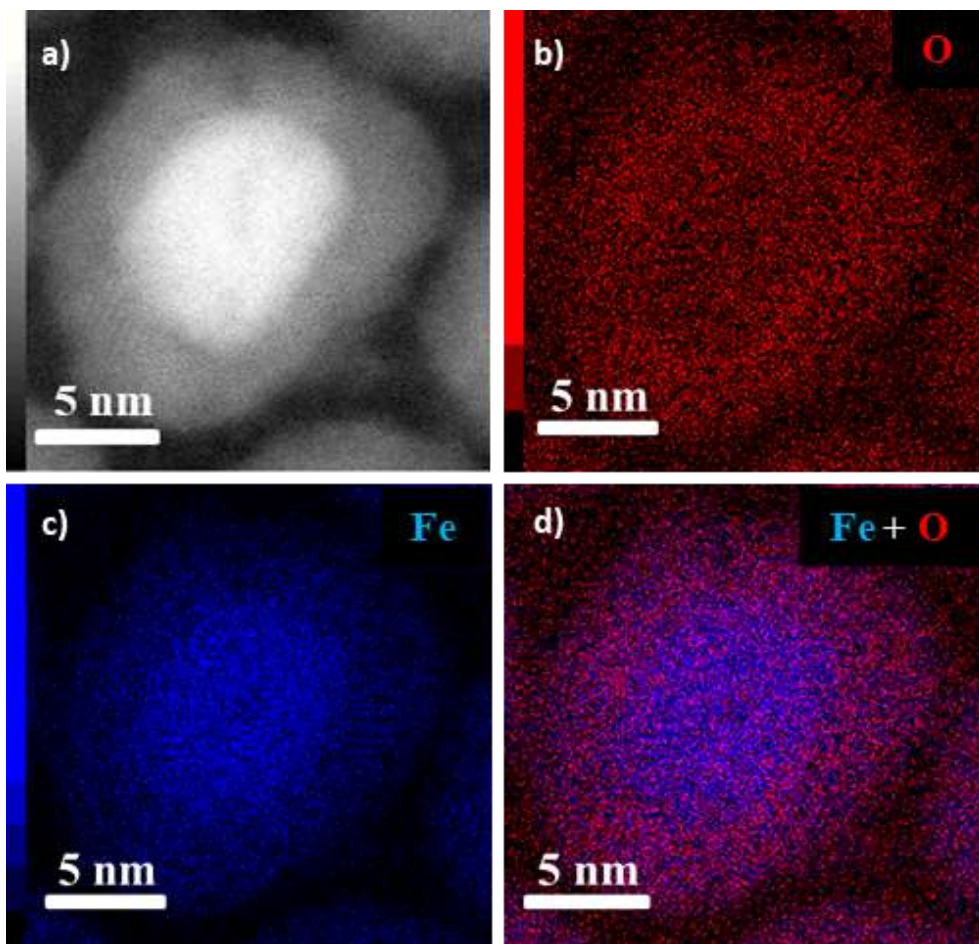
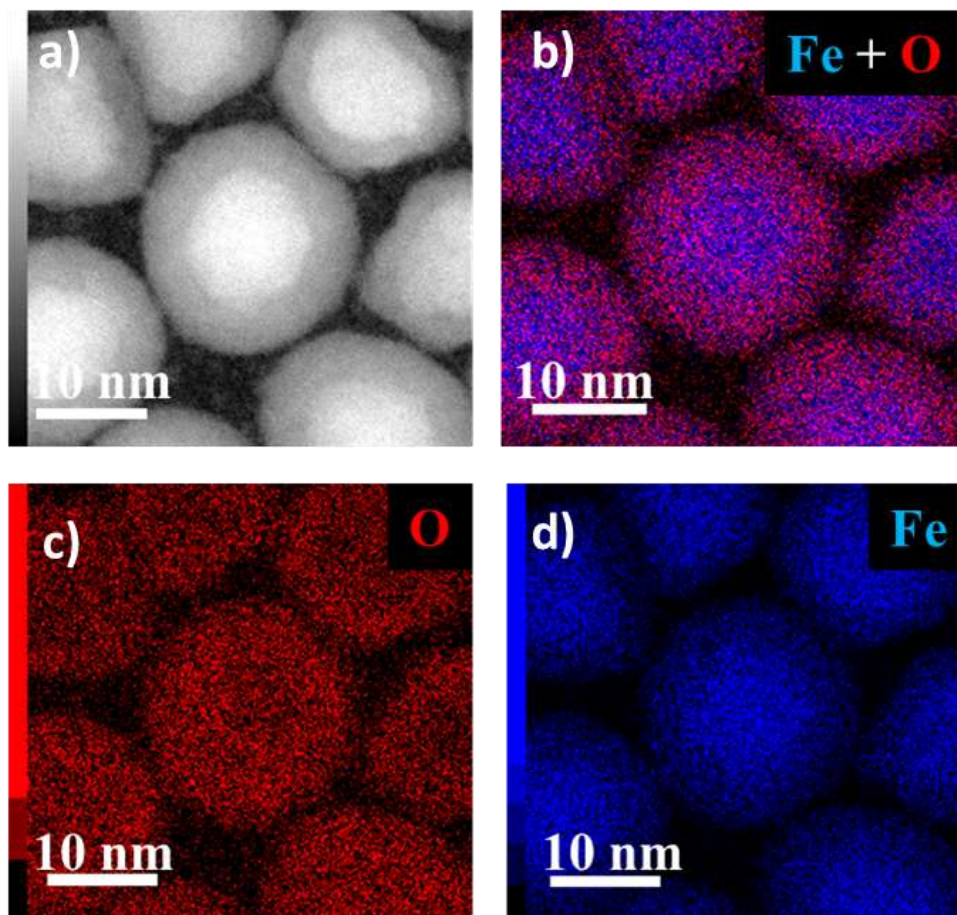


Figure 3-7 TEM images of Fe NPs and relative zoom-in inset of the yellow square, for 1.0 mmol a), 1.3 mmol b), 2.0 mmol c) and 2.4 mmol d) of  $\text{Fe}(\text{CO})_5$  used. The scale bars in all four pictures correspond to 50 nm. e) Size distribution for the four reactions with different amount of precursor used. f) The relationship between NP volume and the amount of  $\text{Fe}(\text{CO})_5$  injected into the system.



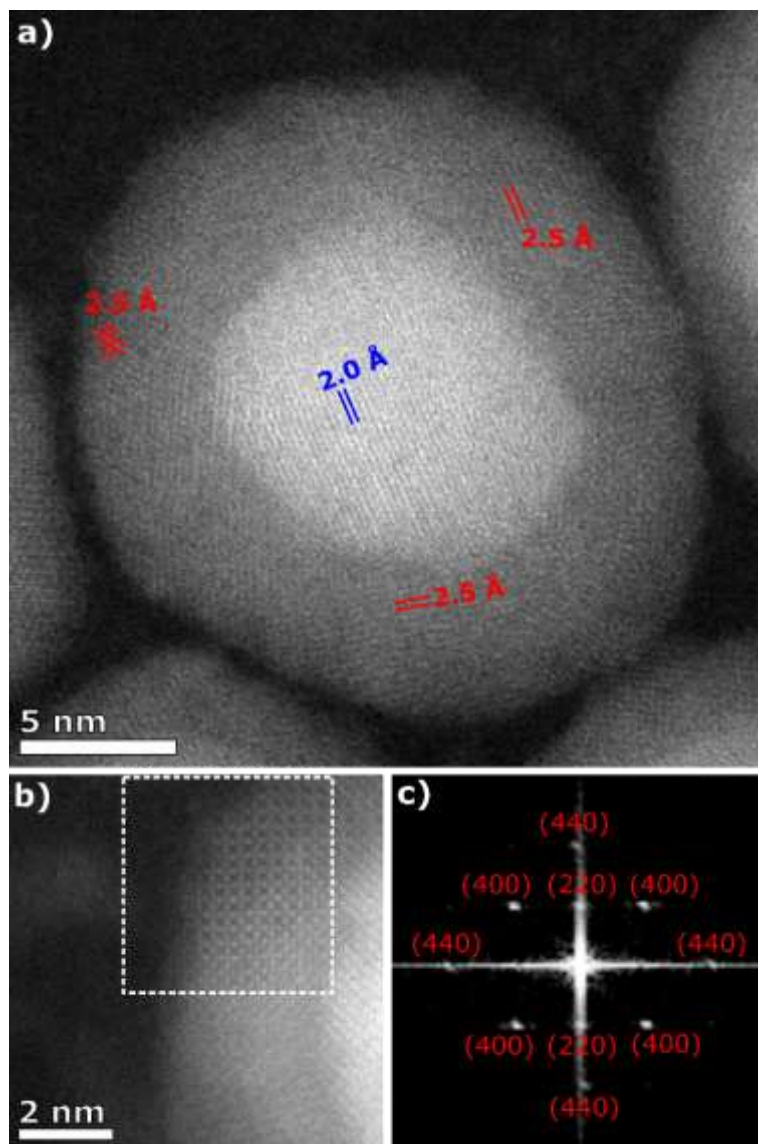
*Figure 3-8 a) HAADF-STEM images of one Fe NP synthesized using 1.3 mmol of Fe(CO)<sub>5</sub>. EDS elemental mapping is also shown where signal intensities coming from b) oxygen and c) iron. d) It shows an overlapping of the signals coming from the two elements.*

Figure 3.8 shows the HAADF-STEM and EDS elemental mapping images of the NPs synthesized using 1.3 mmol of Fe(CO)<sub>5</sub> (25 min of injection time). The HAADF-STEM image confirmed the NPs had a distinct core@shell structure with a darker shell surrounding a brighter core as shown in Figure 3.8 a. Oxygen seemed to be localized at the shell region, while Fe was rich in the core region (Figure 3.8 b-d). The same structural feature can be observed in the NPs synthesized using 2.0 mmol of Fe precursor as shown in Figure 3.9.



*Figure 3-9 HAADF-STEM images of one Fe NP synthesized using 2.0 mmol of  $Fe(CO)_5$ . EDS elemental mapping is also shown where signal intensities coming from b) oxygen and c) iron. d) It shows an overlapping of the signals coming from the two elements.*

Figure 3.10 (a) showed the high-resolution HAADF-STEM image of a single NP. The lattice spacing of 2.0 Å was clearly observed in the core region, which corresponded to the (110) spacing of bcc Fe ( $\alpha$ -Fe) phase. On the other hand, a lattice spacing of 2.5 Å was observed in the shell region corresponding to the (311) spacing of iron oxides



*Figure 3-10 a) High-resolution HAADF-STEM image of a core@shell NP, with the lattice spacing of  $\text{Fe}_3\text{O}_4/\gamma\text{-Fe}_2\text{O}_3$  in red, and  $\alpha\text{-Fe}$  in blue. b) An area of the oxide shell, with c) the corresponding indexed FFT from the dashed white box.*

such as  $\text{Fe}_3\text{O}_4$  or  $\gamma\text{-Fe}_2\text{O}_3$ . In addition, the shell was found to be polycrystalline in nature. Full analysis of the HAADF-STEM image at the shell region revealed the existence of an  $\sim 4$  nm crystalline domain viewed down the [100] zone axis of the inverse spinel crystal structure (Figure 3.10 b and 3.10 c). Analysis of the crystallite sizes in the oxide shell showed that the crystallite size was approximately of the same size as the shell thickness. The shell was made of small polycrystalline oxidised domains formed via the lattice expansion that occurred upon oxidation from  $\alpha\text{-Fe}$  to

the inverse spinel structure of  $\text{Fe}_3\text{O}_4/\gamma\text{-Fe}_2\text{O}_3$ . Figure 3.11 shows the XRD patterns of the four samples. The sample synthesized with the lowest amount of Fe precursor (shortest injection time) had no peak corresponding to  $\alpha\text{-Fe}$ , while one the peaks originating from iron oxides was observed.

The primary peak at  $35^\circ$  was attributed to the (311) plane of  $\text{Fe}_3\text{O}_4/\gamma\text{-Fe}_2\text{O}_3$ . Although it is difficult to assign the rest of the peaks present in the XRD pattern because the pattern is quite noisy, the absence of any peak corresponding to metallic Fe phases including  $\alpha\text{-Fe}$ ,  $\gamma\text{-Fe}$  and  $\delta\text{-Fe}$  confirms the complete oxidation of the NPs. In the cases of other samples, the peaks of the  $\alpha\text{-Fe}$  phase became dominant and peaks related to oxides became negligibly weak. This was due to the small size of the  $\text{Fe}_x\text{O}_y$  grains, which translated into broader and less intense peaks in the XRD pattern compared to the peaks coming from  $\alpha\text{-Fe}$ .

The mean crystallite sizes of  $\alpha\text{-Fe}$  phase for NPs synthesized using 1.3, 2.0 and 2.4 mmol of  $\text{Fe}(\text{CO})_5$  (corresponding to 25, 38 and 45 min of injection time) were estimated using the (110) peak as shown in Figure 3.11 (bottom). The values for each sample were calculated to be 11.0, 11.4 and 13.2 nm, respectively. Those values were in good agreement with the average core sizes determined from the TEM analysis (see Table 3.7) suggesting that the Fe core was monocrystalline. From both XRD and TEM analysis, the mean size values of the Fe core followed an increasing trend along the four reactions, indicating that after the nucleation event the formed seeds acted as primary sites for the growth of Fe NPs as single crystal while more Fe precursor was added.

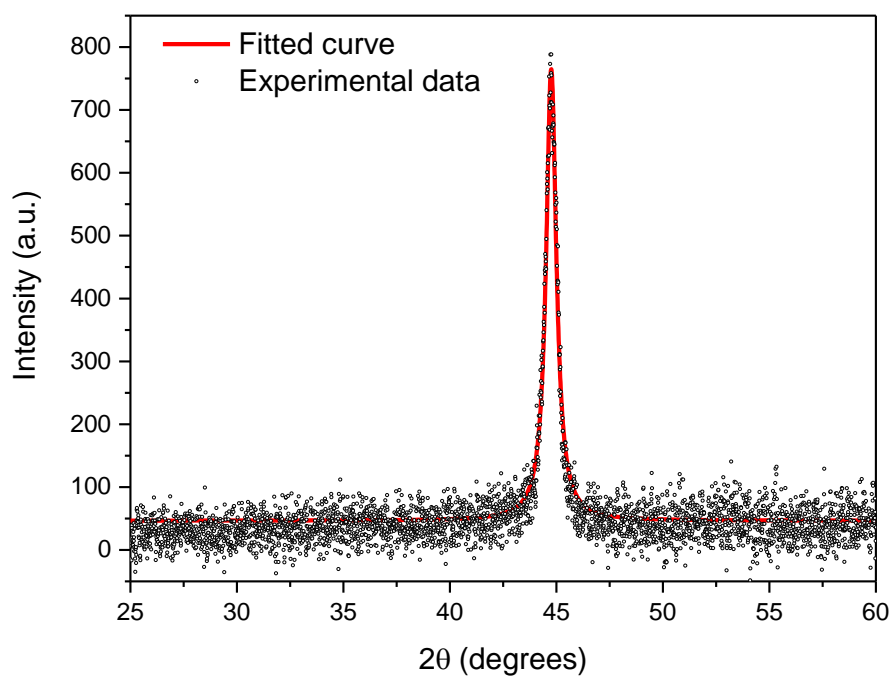
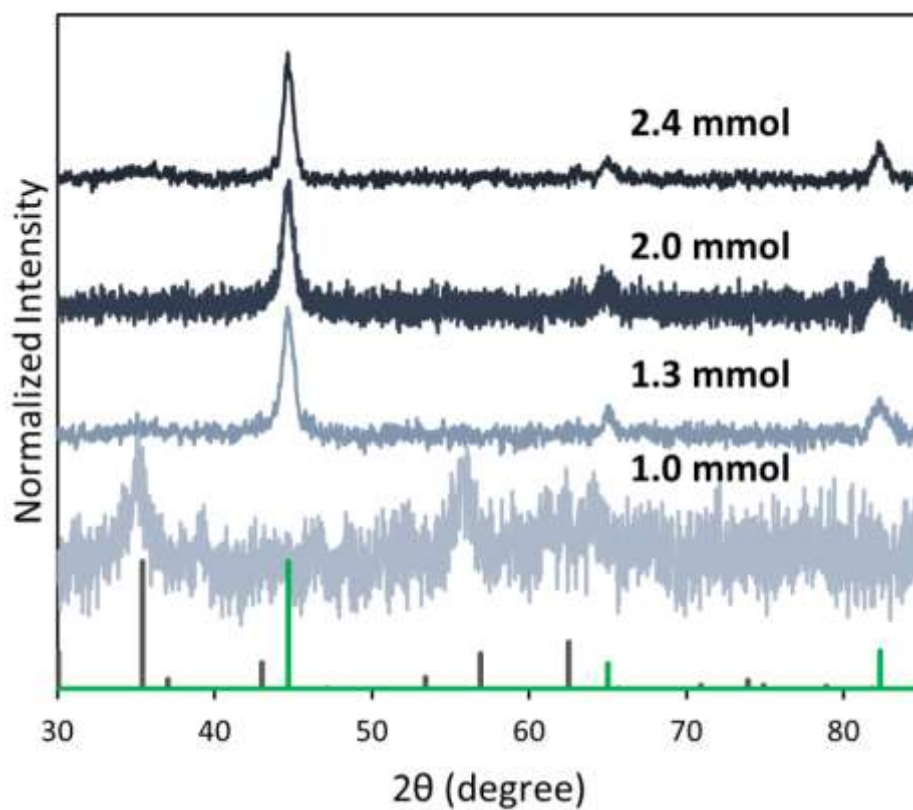
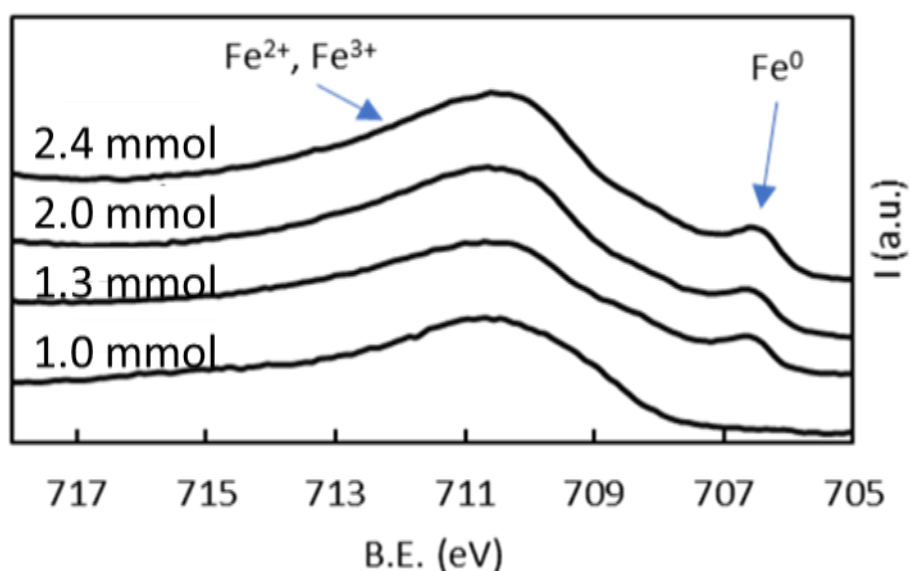


Figure 3-11 (top) XRD patterns of the Fe NPs synthesised using different amounts of  $\text{Fe}(\text{CO})_5$ . The dark grey reference pattern corresponds to  $\text{Fe}_3\text{O}_4$  phase and the green one to bcc-Fe phase (JSPC PDF no. 01-079-0418 and 00-006-06969 respectively). (bottom) Fitting of XRD pattern data of Fe NPs synthesised with 1.3 mmol of  $\text{Fe}(\text{CO})_5$ .

XPS analyses were also performed to confirm the chemical structure of the sample. Figure 3.12 shows the Fe 2p XPS spectra of the four samples obtained varying the amount of Fe precursor. XPS is very sensitive to the chemical state and environment in which Fe atoms are. Fe<sup>0</sup> has a sharp peak at around 707 eV, while Fe<sup>2+</sup> and Fe<sup>3+</sup> lies at higher energy of the spectrum, around 711 eV. The two oxidised species usually overlap as the difference in energy between the two species is very narrow (< 1 eV).<sup>2</sup> The NPs synthesized with the lowest amount of Fe precursor (1.0 mmol) exhibited no peak corresponding to Fe<sup>0</sup> but just the peak at 711 eV coming from Fe<sup>2+</sup> and Fe<sup>3+</sup>, while all the other samples clearly showed the presence of Fe<sup>0</sup> supporting the fact that the NPs obtained with 1.0 mmol of Fe(CO)<sub>5</sub> were completely oxidised.



*Figure 3-12 Fe2p XPS spectrum of Fe NPs synthesised at different injection time.*

The magnetic properties of the four samples were analysed via SQUID-VSM. Figure 3.13 shows the hysteresis loops at 300 K and the main magnetic parameter are summarised in Table 3.6.

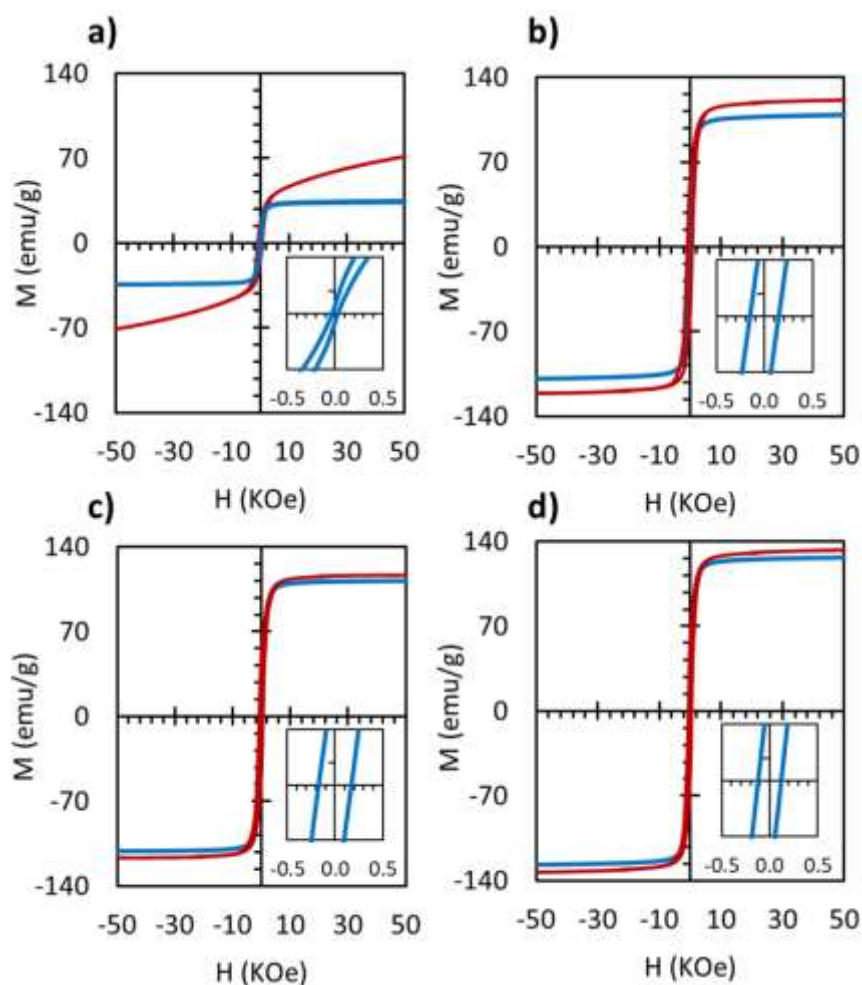


*Figure 3-13 Magnetic hysteresis loop taken at 300 K (blue line) and 5 K (red line) with relative zoom in at low fields for the four samples: a) 1.0 mmol b) 1.3 mmol c) 2.0 mmol and d) 2.4 mmol of Fe(CO)<sub>5</sub> used.*

An increasing trend for the value of  $M_s$  was related to the increase in the size of the NPs. The smallest NPs (12.6 nm) showed a value of 35 emu/g, which was the lowest of the series (Figure 3.13 a). When the size of NPs increased from 12.6 to 15.9 nm, the  $M_s$  value jumped from 35 to 109 emu/g (Figure 3.13 b), while for magnetite NPs one of the highest saturation magnetisation was 88 emu/g.<sup>20</sup> For the NPs of mean size of 18.3 nm, the NPs gave a similar  $M_s$  value of 112 emu/g (Figure 3.13 c). In the case of the largest NPs (20.7 nm), the  $M_s$  value reached 127 emu/g (Figure 3.13 d). The behaviour can be explained by considering that in the first case, the NPs were completely oxidised, hence the lower  $M_s$  value. However, this value was much

smaller than the value reported for NPs of similar size composed of monocrystalline magnetite phase.<sup>158</sup> This was probably due to the rapid oxidation process and the subsequent formation of multi-grains of small iron oxide nanocrystals leading to the low  $M_s$  value. When the size increased,  $M_s$  value went up due to the presence of highly crystalline  $\alpha$ -Fe core. While the 15.9 and 18.3 nm NPs showed similar  $M_s$  values, the largest NPs (20.7 nm) showed the highest  $M_s$  value due to the presence of larger ferromagnetic cores.<sup>159</sup>

The measured  $M_s$  values were used to estimate the volumes of  $\alpha$ -Fe phase and oxide phases as reported from Sun *et al.*<sup>29</sup>:

$$M_{sTot} = M_{sFe}w_{Fe} + M_{sFe_3O_4}w_{Fe_3O_4} \quad (Eq\ 3.1)$$

$$w_{Fe} + w_{Fe_3O_4} = 1; \quad (Eq\ 3.2)$$

$$v_{Fe} = \frac{w_{Fe}}{\rho_{Fe}} \quad v_{Fe_3O_4} = \frac{w_{Fe_3O_4}}{\rho_{Fe_3O_4}}; \quad (Eq\ 3.3)$$

$$V_{Fe} = \frac{v_{Fe}}{(v_{Fe} + v_{Fe_3O_4})} * V_{Tot}; \quad (Eq\ 3.4)$$

$$d_{Fe} = \sqrt[3]{\frac{V_{Fe} * 6}{\pi}} \quad (Eq\ 3.5)$$

where  $M_{sTot}$  is the experimental magnetization saturation,  $M_{sFe}$  and  $M_{sFe_3O_4}$  correspond to the bulk magnetization values,  $w$  is the weight fraction,  $v$  is the volume fraction and  $V$  indicates the volume.

The iron oxide shell thickness remained almost constant along the whole series, being around 4-5 nm, while the Fe core diameter gradually increased, similarly to the values reported in the TEM analysis (Table 3.6). The slight difference in obtained values

between two different techniques can be explained by the spin canting effects present on the surface of the NPs which impairs the  $M_s$  in nanosized materials compared to the bulk counterparts,<sup>160</sup> leading to smaller estimated size. The coercivity of 12.6 nm NPs of 30 Oe indicated extensive oxidation, while in the case of bigger particles where the core@shell structure was maintained, the coercivity increased to around 150 Oe, in agreement with values reported in previous work.<sup>29,161</sup>

### 3.3.2.3 Summary

The synthesis of Fe@Fe<sub>3</sub>O<sub>4</sub> NPs via continuous injection of precursor was optimised studying the optimal injection rate necessary to deliver controlled and tunable Fe NPs. Setting the injection rate at 0.4 ml/h, the synthetic procedure allowed to achieve four different size of Fe NPs varying the amount of Fe(CO)<sub>5</sub> injected into the reaction solution via a syringe pump. The size of the four Fe NPs samples follows a linear increasing trend with the increase of Fe precursor. The characterisation results are summarised in Table 3.6

*Table 3-5 Summary of size for the four samples obtained through TEM and XRD, magnetic properties and estimated size using magnetic properties. The XRD size values of Fe core were obtained applying the Scherrer formula on the main peak (110) of  $\alpha$ -Fe pattern. The diameter,  $d$ , of Fe TEM was estimated by measuring the size of the core of the NPs in the TEM micrographs. The thickness of Fe<sub>x</sub>O<sub>y</sub> phase was estimated by subtracting the average diameter of the core@shell NPs with the average diameter of Fe core, dividing the total by 2.*

Fe inj. (mmol)	$M_s$	$M_s$	$H_c$	$H_c$	$d_{Fe}$	$d_{Fe}$	$t_{Fe_3O_4}$	$d_{Fe}$	$t_{Fe_3O_4}$
	300K (emu/ g)	5K (emu/ g)	300 K (Oe)	5K (Oe)	XRD (nm)	TEM (nm)	TEM (nm)	SQUID (nm)	SQUID (nm)
1.0	35	71	30	195	-	-	-	-	-
1.3	109	121	150	760	11.0	10.3	2.8	7.1	4.3
2.0	112	117	180	580	11.4	11.5	3.4	8.7	4.7
2.4	127	133	120	480	13.2	15.6	2.5	12.1	4.3

### 3.4 Ligand modification for water-soluble Fe NPs

While the Fe NPs synthesised in this work have hydrophobic ligands on the surface, Fe NPs need to be dispersible in water to be used for magnetic hyperthermia. In the following section, several strategies used to make Fe NPs water-dispersible are reported. The strategies were based on previously published protocols used for iron oxide NPs because the as-synthesised Fe NPs have an iron oxide shell. However, adapting the protocols for the water transfer of  $\text{Fe}_x\text{O}_y$  NPs into Fe NPs is not trivial because Fe NPs are more magnetic, hence more prone to aggregation, and the chemical stability of the Fe core must be considered as it is more prone to oxidation.

#### 3.4.1 Silica coating

To make Fe NPs soluble in water and protect the Fe core from further oxidation, silica coating was attempted. Silica comes as a negatively charged material on the outer surface due to the presence of free silanol (Si-O-H) moieties, making the material hydrophilic. Moreover, silica is biocompatible<sup>162</sup> and numerous silane-functionalised reagents are commercially available and can be easily added to the silica substrate, making silica an attractive and versatile coating material.

The synthesis chosen was reported in the literature for the coating of iron oxide NPs.<sup>92</sup> In our experiment, we used the iron oxide phase of the shell of the NPs to grow a silica layer through the formation of Si-O-Fe bonds.

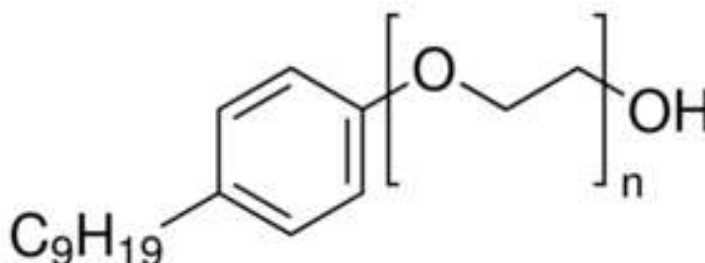


*Figure 3-14 Igepal-CO-520 molecular structure*

For the formation of the silica layer, first, NPs were dispersed in cyclohexane with Igepal CO-520 and the first step of ligand exchange occurred. The alcohol group at one end of the molecule (Figure 3.14) interacted with the iron oxide phase displacing the native ligand (Oleylamine). After the ammonia was added, the amphiphilic nature of Igepal CO-520 led to the formation of a microemulsion, because of the hydrophilic head and hydrophobic tail of the molecule, thus Igepal CO-520 was used both as ligand exchanger and surfactant to form aqueous micelles in cyclohexane. According to Ding *et al.* the exchanged NPs were subsequently transferred into the aqueous micelles, which acted as a reactor where the silica coating occurs once the TEOS was added.<sup>92</sup>

*Table 3-6 Conditions used for the coating of Fe NPs with Silica*

<b>Sample</b>	<b>Fe NPs</b>	<b>Ammonia</b>	<b>Igepal-CO-520</b>	<b>TEOS</b>
FeSi_1	1.3 mg	0.1 mL	0.5 g	75 $\mu$ L
FeSi_2	3 mg	0.1 mL	0.5 g	75 $\mu$ L
FeSi_3	5 mg	0.1 ml	0.5 g	75 $\mu$ L
FeSi_4	2.1 mg	0.1 ml	0.5 g	2 x 37 $\mu$ L

The authors reported that one of the challenges of this protocol was to promote the growth of a silica coating on the surface of Fe NPs rather than the formation of free silica NPs. A key parameter to avoid free silica NPs was to adjust the amount of Fe NPs with the number of aqueous micelles formed in solution, so that all the Fe NPs can be transferred from the organic phase to the aqueous micelles where the silica coating happens.<sup>92</sup> Indeed, if not enough Fe NPs are transferred inside the micelles just silica NPs are formed. The ratio of ammonia to Igepal CO-520 affects the size and

number of aqueous micelles, and while keeping the ratio constant, the amount of NPs should be adjusted according to the NPs size. If all the aqueous domains are filled with Fe NPs, this would reduce the chance to form free silica NPs. Therefore, the first reactions were carried out varying the amount of Fe NPs used in the coating reaction, keeping the ammonia to Igepal-52 ratio constant. During the reaction, different aliquots were taken and analysed with TEM to monitor the evolution of the reaction.

In Figure 3.15 TEM images for FeSi\_1 are shown. An aliquot of the reaction solution was taken to monitor the evolution of the reaction at 1.5 h. In the sample, free silica NPs were the predominant species. Si NPs appeared brighter in the TEM because of the lower atomic number of Si compared to Fe atoms. Some Fe NPs were also observed, having a thin brighter shell which may suggest that the particles were coated with silica. In the TEM image of the final sample (Figure 3.15 right), after 3 h of reaction, no free silica NPs were observed. Indeed, during the washing of the final sample, Si NPs were removed *via* magnetic separation step. Fe NPs appeared aggregated, and a clear analysis of the final structure was not easy. However, a brighter shell can be observed on the particles at the edges of the agglomerate, which could be associated with the successful formation of Si coating on top of Fe NPs.

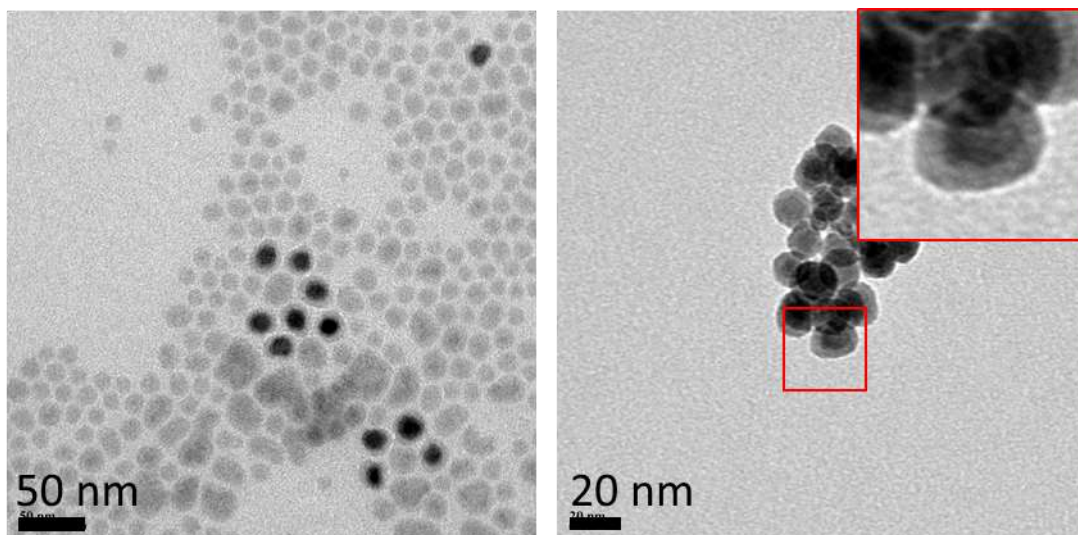


*Figure 3-15 TEM pictures of FeSi\_1 reaction aliquot at 1.5 h (left) and at the end of the reaction (right).*

FTIR spectra of as synthesised NPs and FeSi\_1 NPs are shown in Figure 3.16. The as synthesised Fe NPs have a characteristic peak at  $2924\text{ cm}^{-1}$  (green arrow) coming from the  $-\text{CH}_2-$  group of the oleylamine present on the surface of the NPs. This peak decreased drastically in the case of silica coated Fe NPs and a more intense peak appeared at  $1098\text{ cm}^{-1}$  (blue arrow), which was associated to Si-O-Si vibration. This vibration mode confirmed the coating of Fe NPs with silica because no free silica NPs were detected in the sample after magnetic separation in the TEM analysis. However, a weak signal coming from the  $-\text{CH}_2-$  vibration mode can still be observed, suggesting that a complete coating with silica was not achieved.

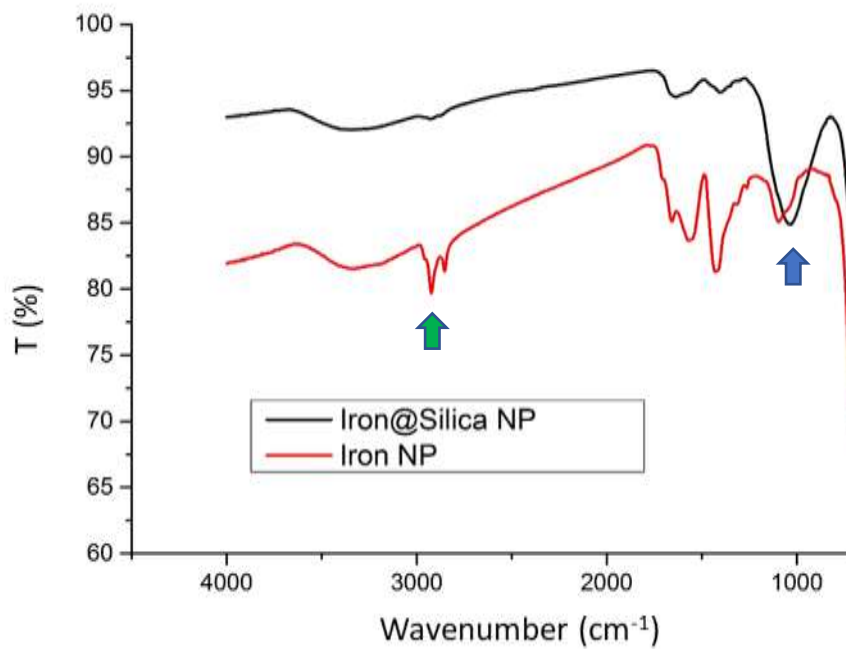


*Figure 3-16 FTIR measurement of FeSi<sub>1</sub> NP before and after Silica coating (3 h) reaction.*

The XRD pattern of FeSi<sub>1</sub> in Figure 3.17 showed that the  $\alpha$ -Fe was the main phase in the sample, indicating that the coating procedure did not affect the structure of the Fe NPs. A broad peak appeared around 20° and this was attributed to amorphous silica coming from the silica shell on the Fe NPs or from pure Si NPs.

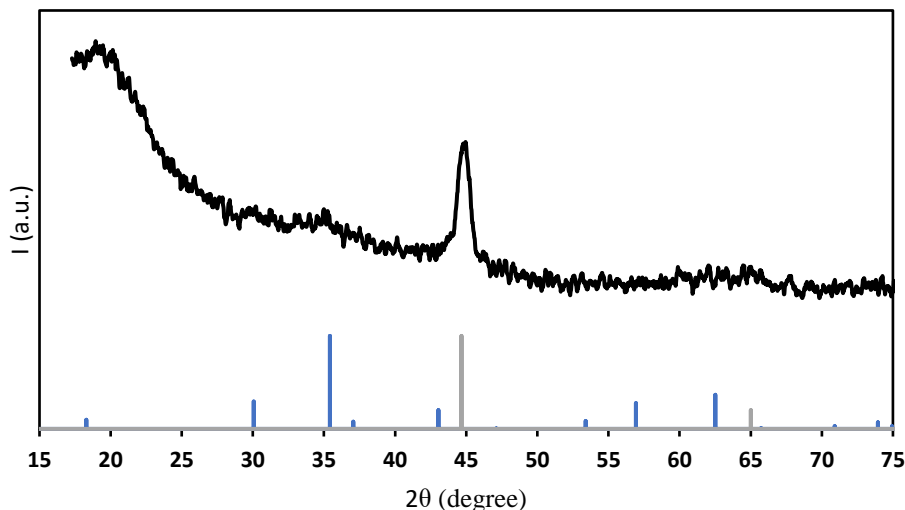


*Figure 3-17 XRD pattern of FeSi\_1 NPs with  $\alpha$ -Fe (grey) and  $Fe_3O_4$  (blue) reference patterns.*

In FeSi\_2 and FeSi\_3, the amount of NPs was increased to 3 mg and 5 mg respectively, to attempt to reduce the formation of free silica NPs. In the case of FeSi\_2, the reaction was also let to react for 24 h to evaluate the effect of time on the overall reaction. However, to compare the results with the previous reactions, an aliquot was taken after 3 h of reaction, which was the time used in all the other silica coating experiments. Figure 3.18 shows TEM images of the aliquot taken at 3 h and at the end of the reaction (after 24 h). In the aliquot micrograph, the formation of Si-coated Fe nanoparticles was observed, however, most of the sample was made of Si NPs, indicating that the increase in the amount of Fe NPs did not stop the formation of Si NPs. When the reaction was left to react for a longer time (24 h), the coating thickness increased as shown in Figure 3.20 (right), showing that the reaction proceeded after 3 h. Along with silica-coated Fe NPs, the sample showed also aggregated Si NPs. A possible explanation for this phenomenon was that both Si NPs and Si-coated Fe NPs have a reactive surface due to the presence of unreacted Si-O<sup>-</sup> bonds which caused inter-particles cross-linking. This phenomenon was favoured by the longer reaction time.

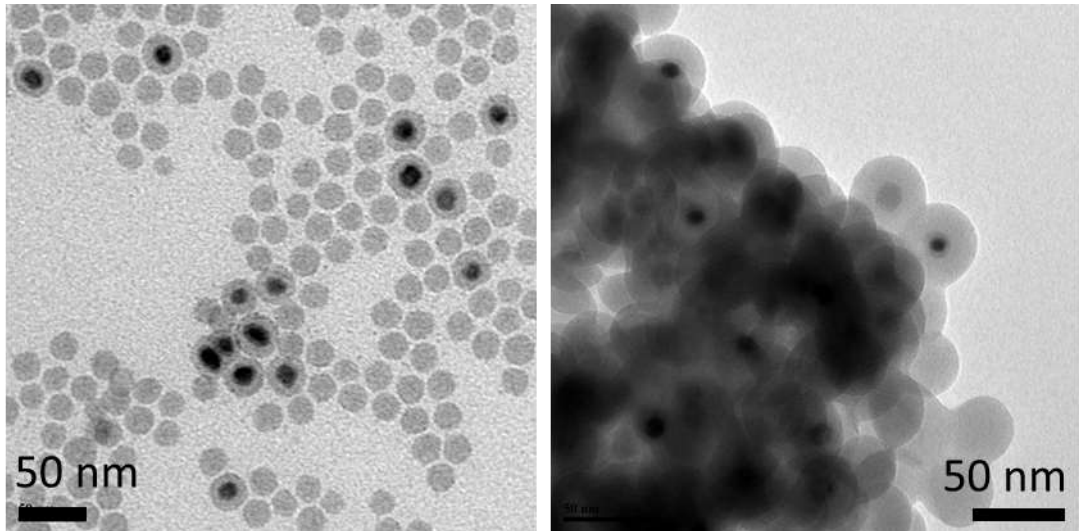


*Figure 3-18 TEM images of FeSi<sub>2</sub> reaction aliquot at 3 h of reaction (left) and sample at the end of the reaction after 24 h (right).*

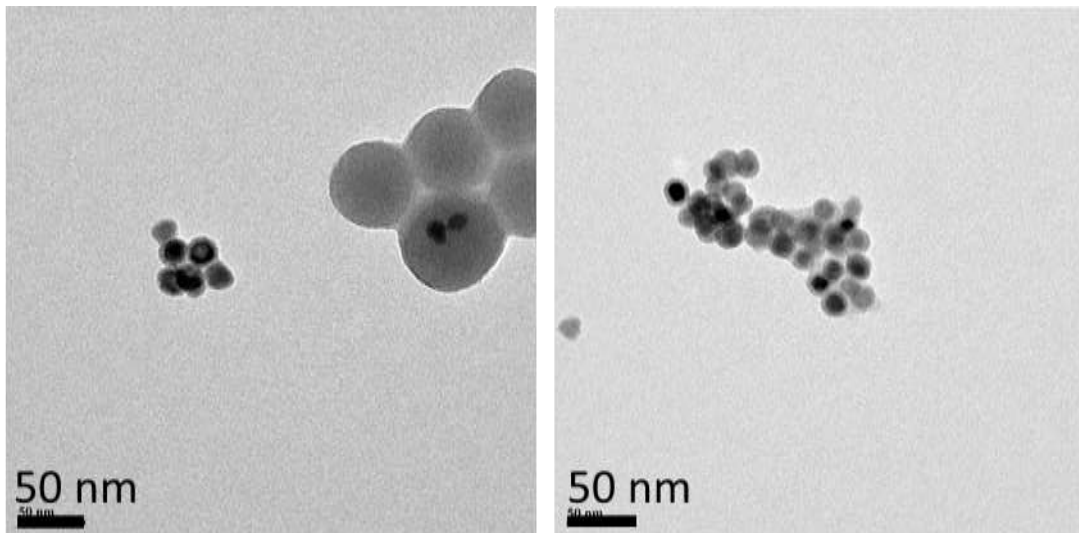


*Figure 3-19 TEM images of the FeSi<sub>3</sub> sample at the end of the reaction after 3 h.*

Figure 3.19 shows TEM images of the sample FeSi<sub>3</sub> obtained with 5 mg of initial Fe NPs. The sample appeared very similar to FeSi<sub>1</sub> with NPs being aggregated; this limits the chance to clearly observe the final structure and determine whether the coating was successful or not. Free Si NPs were also observed and increasing the amount of Fe NPs used did not improve the reaction' results.

After the analysis of these results, it was concluded that Si-coated Fe NPs could be formed but the process was hard to control. Trying to match the number of Fe NPs with the aqueous domains by increasing the amount of initial iron NP, still produces core-free Si NPs. Furthermore, when diluted aliquots were taken from the reaction solution, Si-coated Fe NP can be clearly detected via TEM, but when the final product was analysed, the silica coating was hard to distinguish due to the aggregation of NPs. Instead when the reaction was let for long hours (24 h) the thickness of the silica coating increased, showing more clearly a core@shell structure.

In order to gain more control over the silica layer growth and to decrease the presence of free-silica NPs, the same amount of TEOS used for the reaction was split into two aliquots added separately. After the first 37  $\mu\text{L}$  of TEOS were added, the solution was let react for 30 min before adding other 37  $\mu\text{L}$  of silica precursor. Figure 3.20 shows the TEM images of the final sample obtained with sequential addition of the silica precursor. TEM images suggested that Fe NPs were coated with a silica shell. This was also confirmed by the diameter being 25 nm for the found core@shell NPs, which was larger than the starting Fe NPs (18.9 nm). However, the formation of Si NPs was not stopped, and the sample looked highly aggregated.

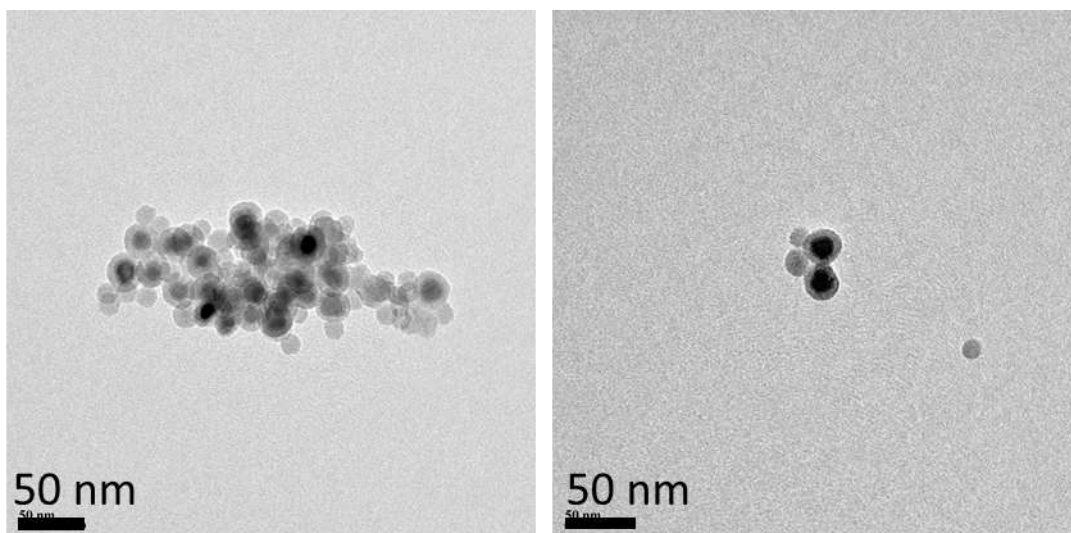


*Figure 3-20 TEM images of the FeSi<sub>4</sub> sample. In this case, the amount of TEOS added was split into two different aliquots.*

*Table 3-7 Hydrodynamic size and Z-potential values for Silica-coated NPs.*

	<b>FeSi_1</b>	<b>FeSi_2</b>	<b>FeSi_3</b>	<b>FeSi_4</b>
D <sub>H</sub> (nm)	191	337	280	290
Z (mV)	-20.3	-42.4	-20.5	-22.3

The colloidal stability of the samples was analysed via DLS. In Table 3-8 the hydrodynamic diameter (D<sub>H</sub>) and the z-potential of the four different reactions are reported. The samples showed a D<sub>H</sub> value of 191 nm for FeSi<sub>1</sub>, around 300 nm for the FeSi<sub>3</sub> and FeSi<sub>4</sub>, and up to 337 nm for the FeSi<sub>2</sub> sample, where the reaction was left to react for 24 h instead of 3 h. The trend seems to agree with the TEM analysis where the bigger D<sub>H</sub> is associated with FeSi<sub>2</sub>, where Fe NPs were coated with a thicker silica layer compared to other samples. Also, the formation of aggregates in solution plays a role in the D<sub>H</sub> value, and in the TEM images, all the sample showed a high extent of aggregation. The Z-potential values for all the four sample were negative and this was due to the presence of Si-O<sup>-</sup> groups on the surface of silica. Interestingly, the Z-potential values were around -20 mV for all the sample except for FeSi<sub>2</sub>, suggesting that with longer reaction time, a better coating was

achieved, leading to more negative Z-potential value. Furthermore, for all the samples, the dispersion was not stable in water and particles precipitated within one day.

#### 3.4.1.1 Summary on silica coating

The results showed that the protocol of coating Fe NPs with silica was partially achieved. TEM, FTIR and XRD analysis showed that Fe NPs could be coated without modifying the initial structure of Fe NPs. However, the coating was not uniform, and many SiO<sub>2</sub> NPs were also formed during the syntheses. It also appeared that the final NPs easily aggregated, and silica did not provide sufficient colloidal stability to the NPs in solution. One possible reason was that ferromagnetic Fe NPs were more prone to inter-particle interactions and this impaired the whole coating process, from the initial transfer in water to the final silica coating, leading to the formation of clusters of NPs with poor colloidal stability. For these reasons, the silica coating was not suitable to transfer Fe NPs in water and protect them from further oxidation.

#### 3.4.2 Encapsulation with poly maleic anhydride alt octadecene

In order to transfer iron NPs in water, a second strategy was investigated using the polymeric encapsulation protocol with PMAO. Each monomer in the polymer has a hydrophobic part having an 18-carbon chain, and a maleic anhydride group which becomes hydrophilic once hydrolysed (Figure 3.21). The hydrophobic part can intercalate and interact hydrophobically with the oleylamine tails that covered the

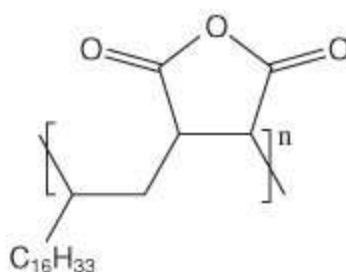


*Figure 3-21 Molecular structure of PMAO polymer.*

as-synthesised nanoparticles' surface. This would allow the maleic anhydride moieties to be exposed to the NPs outermost part. When hydrolysed, the maleic anhydride renders two carboxylic groups which make the nanocomposite water-soluble. At the same time, the maleic moieties can be easily functionalised via nucleophilic substitution with molecules containing nucleophiles (amines, alcohols, thiols etc.) allowing for the tailoring of the system according to the desired application. Finally, the polymer has also been proved to be biocompatible.<sup>132</sup>

The transfer of Fe NPs was first analysed via TEM. The TEM images (Figure 4.22) show some dispersed single particles along with some aggregated areas. These areas can be formed during the evaporation of the solvent from the grid used to deposit the sample, which drives the particles to cluster together. However, also the encapsulation process can be responsible for that if one polymer chain interacts with more than one NP, forming a cluster of NPs. The latter could be favoured by the large size of the polymer itself which has a number average molecular weight,  $M_n$ , of 30.000 - 50.000 g/mol according to the manufacturer. Interestingly, the transfer in water does not seem to compromise the core@shell structure of the NPs with an iron core still clearly visible and no sign of oxidation. To confirm this observation, the sample was analysed using XRD and the resulting pattern clearly showed that the main phase was  $\alpha$ -Fe. Other small peaks can be detected, and they can be attributed to the magnetite/maghemite phase, possibly coming from the iron oxide shell or from some oxidised particles. However, this phase can be considered negligible compared to the  $\alpha$ -Fe. This is important because it shows that no "hard" coating (e.g. silica, gold, etc.) is necessary to stop the oxidation of Fe NPs once when they are transferred in water.

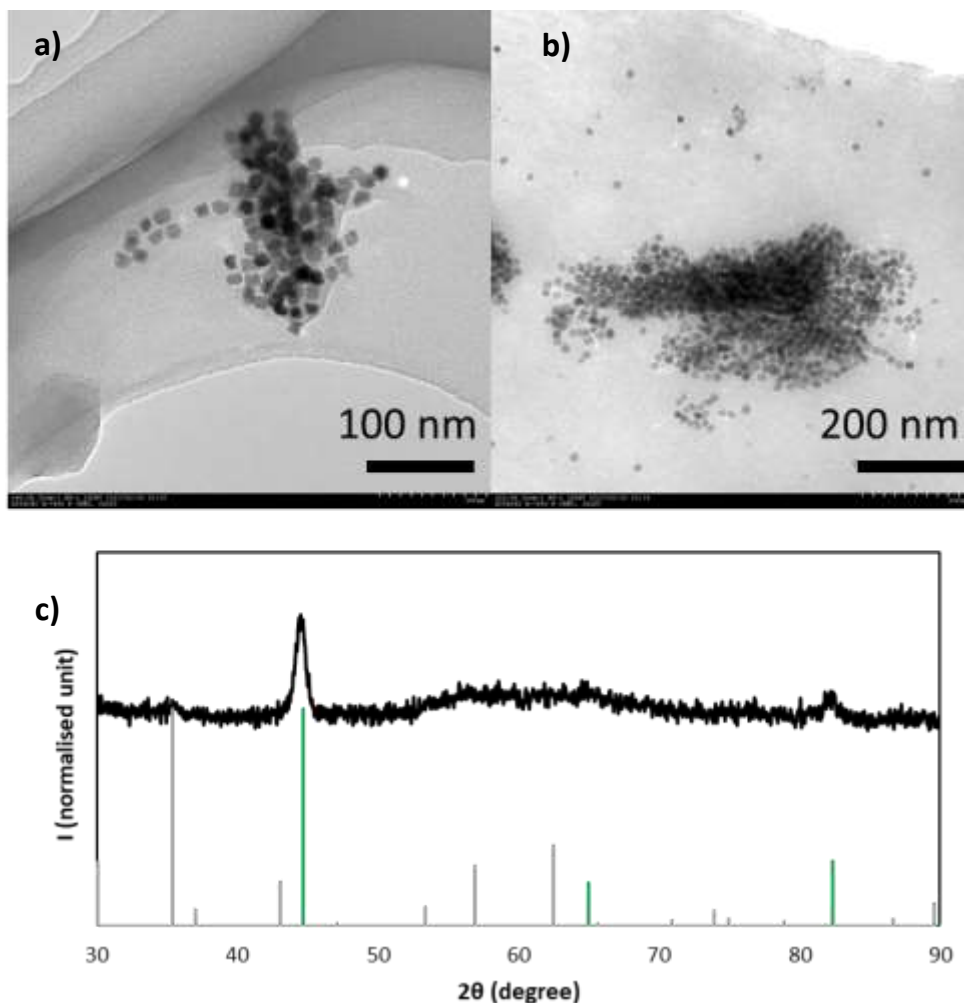
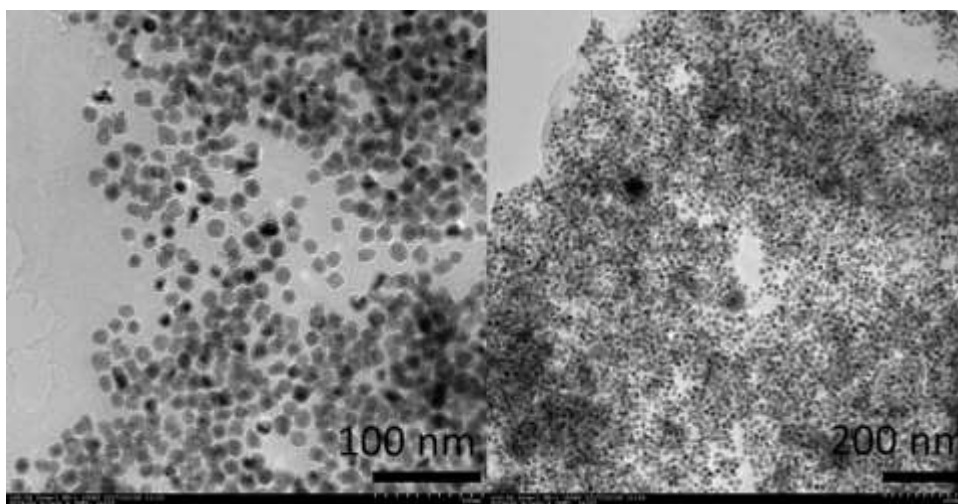


Figure 3-22 a) High magnification and b) low magnification TEM images for the PMAO encapsulated Fe NPs (2.0 mmol) using a NPs:polymer mass ratio of 12. c) XRD spectrum of the Fe@PMAO nanoparticles where the green reference pattern refer to  $\alpha$ -Fe phase and the grey one refer to magnetite.

The TEM and XRD measurements proved that Fe NPs were transferred in water without a change in structural properties and this was highly desirable for their application in magnetic hyperthermia. Another important parameter to assess was their colloidal stability in solution. Analyses with DLS showed an average hydrodynamic diameter ( $D_H$ ) of 370 nm, which was higher than the desirable hydrodynamic diameter (< 100 nm) suitable for biomedical applications.<sup>163</sup> Within a few days, the solution starts to flocculate and NPs sediment at the bottom of the vial.

To improve the encapsulation process, it was attempted to increase the amount of polymer using a ratio of NP : polymer equal to 1 : 40 in mass. Using a higher concentration of polymer would decrease the probability of encapsulating more NPs together. TEM images (Figure 3.23) show NPs transferred in water. The core@shell structure was retained and increasing the concentration of polymer did not affect the final structural properties of NPs. The colloidal properties were investigated using DLS and in this case, the  $D_H$  was 230 nm, which was smaller than the NPs previously encapsulated with less polymer but still far from the optimal hydrodynamic diameter ( $\leq 100$  nm). Furthermore, within a few days, the NPs still crashed out of solution.



*Figure 3-23 TEM images of Fe NPs after encapsulation with PMAO using a ratio of NPs : polymer equal to 1:40. High magnification image on the left and low magnification on the right.*

#### 3.4.2.1 Summary on PMAO coating

Fe@Fe<sub>x</sub>O<sub>y</sub> were successfully transferred in water using an encapsulation strategy with PMAO polymer. The hydrophobic chain of PMAO intercalates between the carbon tails of the native ligand on the surface of Fe NPs, allowing for the transfer of NPs in water. Fe NPs retain the same structural properties once transferred in water with the  $\alpha$ -Fe of the core being still the main phase detected. Although promising, this method showed several drawbacks. Firstly, this method gives the best results

with small non-interacting NPs while in this case, Fe NPs are highly magnetic and ferromagnetic, which promote inter-particle interactions. When the solvent is slowly evaporated during the encapsulation process, the aggregation of NPs is promoted as well, and ultimately the final colloidal stability is impaired. Secondly, the protocol requires to work with very diluted concentrations, hence big volumes, and it is hard to scale up the process to obtain enough NPs for further studies.

### 3.4.3 Ligand exchange with PIMA-Dopa

A different approach was tested relying on the exchange of the native ligand with a new one that would allow for the transfer of NPs in water while also conferring biocompatibility and colloidal stability. This approach would solve the issues faced in the previous section: *i*) it would displace the native ligand, *ii*) it would not require the evaporation of solvent as a mean to encapsulate the NPs and thus it would limit aggregation and *iii*) it would be easier to scale up for larger amounts of NPs.

Poly(isobutylene-*alt*-maleic anhydride) (PIMA) is a linear polymer with maleic anhydrides in each monomer and two methyl groups, (Figure 3.24) instead of the 16-carbon chain present in PMAO. Dopamine has been broadly investigated for the transfer of NPs in water via replacement of the native ligand. Indeed, the catechol group present in the molecular structure can strongly bind on the surface of Fe NPs through coordination bonds.<sup>121</sup> However, dopamine is a small molecule and may not be enough to provide colloidal stability in the case of Fe NPs. The functionalisation of PIMA with dopamine could provide a strong binding polymer, biocompatible and with good colloidal stability.

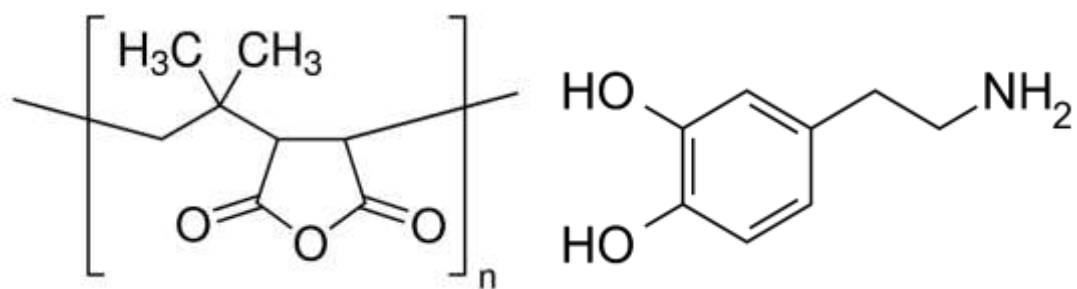


*Figure 3-24 Molecular structure of PIMA (left) and dopamine (right).*

The method takes advantage of some features of PIMA. The polymer is easy to functionalise through the nucleophilic substitution of its anhydride moieties with amines or other nucleophiles. This addition can be achieved in organic media with no need for further chemicals in solution, facilitating the purification step and reducing the presence of undesirable impurities. Furthermore, the polymer can be potentially functionalised with different chemicals thanks to the presence of many maleic anhydride rings. Importantly, PIMA is a copolymer made of alternate anhydride rings next to dimethylpropane groups and this decrease the steric constraints during the addition reaction leading to a higher reaction yield. The addition of dopamine in the PIMA structure forms an amidic bond which is stable in biological conditions over a broad range of pH.<sup>164</sup> Other methods for the formation of the same bond in mild conditions involves the use of N,N'-dicyclohexylcarbodiimide and 1-Ethyl-3-(3-dimethylaminopropyl)carbodiimide (DCC and EDC respectively) condensation between a carboxylic group and an amine group which generates side products like urea, requiring more purification step, along with low efficiency.<sup>165</sup> The use of PIMA as a precursor can overcome many issues related to the other methods.

#### 3.4.3.1 Synthesis of PIMA-Dopa and ligand exchange

PIMA is commercially available with  $M_w \approx 6000$  g/mol, according to the manufacturer. Considering a mass of 154 g/mol for each monomer, it was considered that each polymer has an average number of 39 monomers. For the synthesis of PIMA-Dopa,

50% of the monomers were reacted with dopamine, leaving half of the number of anhydride rings intact. When the maleic anhydride rings react with dopamine, a carboxylic group is also freed for each anhydride ring reacted.

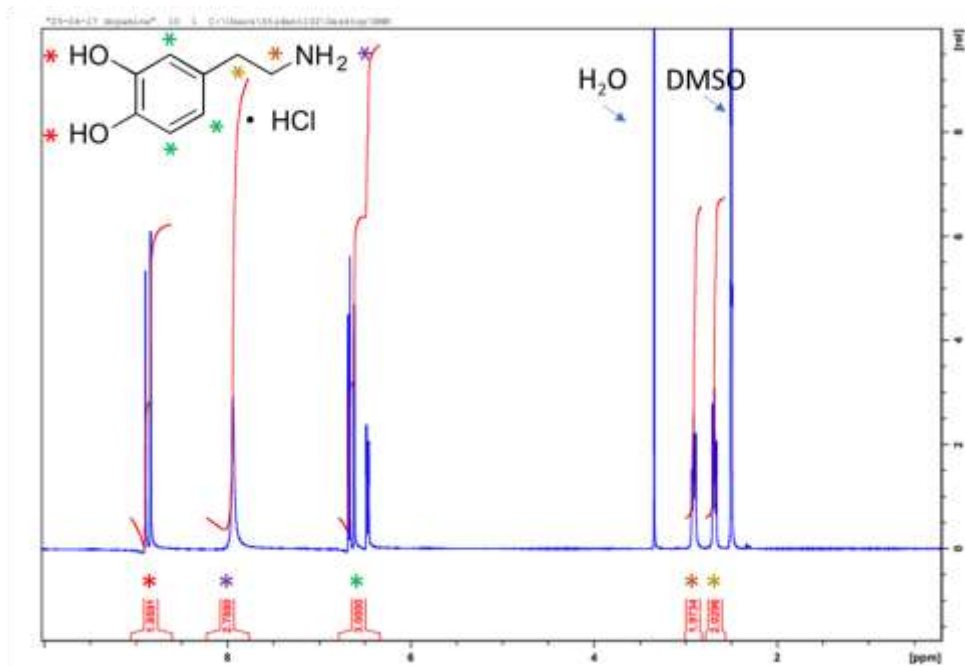


Figure 3-25 <sup>1</sup>H-NMR of dopamine hydrochloride.

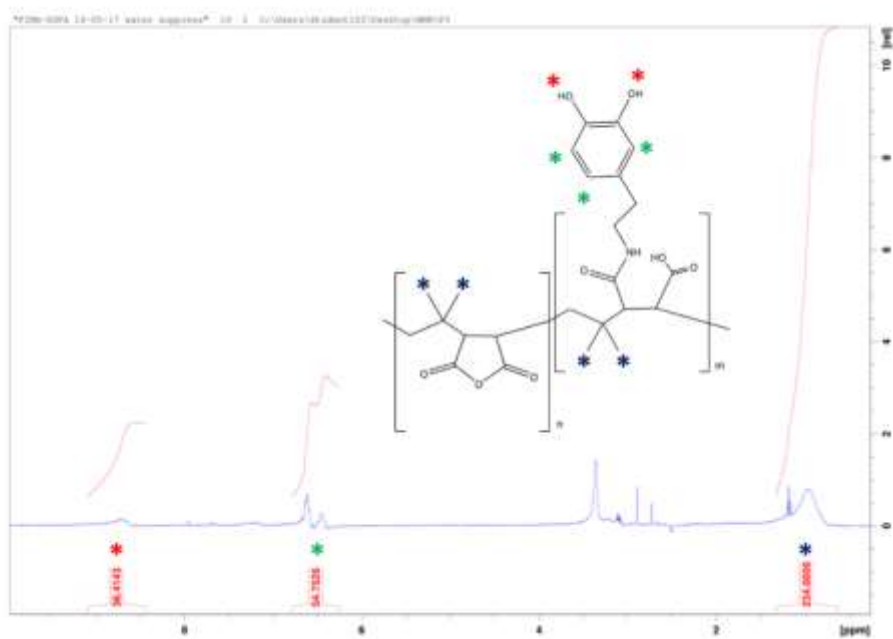
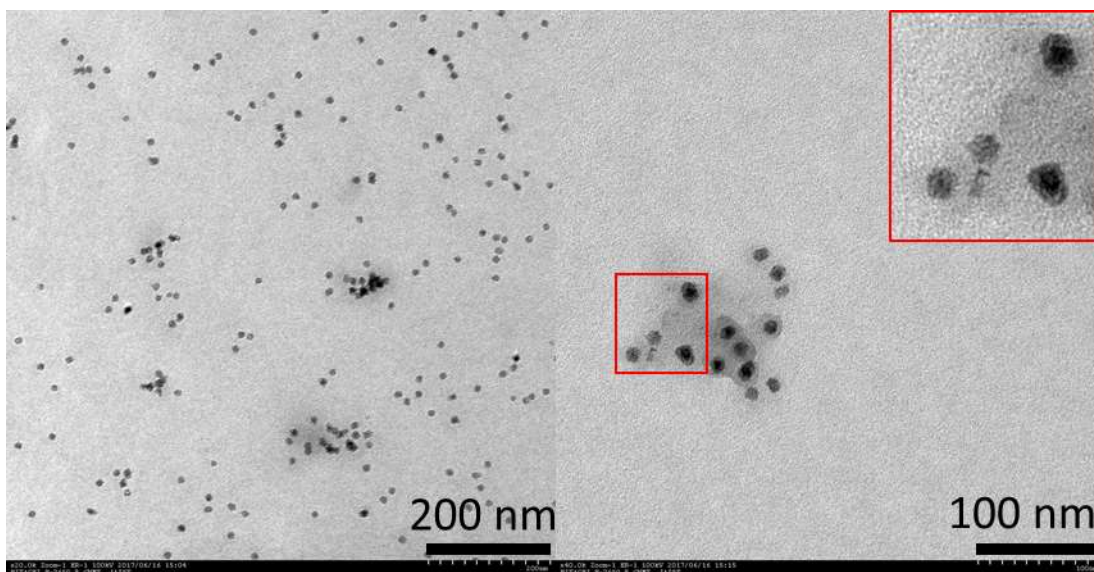


Figure 3-26 <sup>1</sup>H-NMR of PIMA-Dopa polymer.

The yield of the reaction was 91% and  $^1\text{H-NMR}$  was used to control the functionalisation of PIMA with dopamine. The solvent used was deuterated DMSO. Figure 3.25 shows the  $^1\text{H-NMR}$  spectrum for only dopamine hydrochloride with the peaks assigned to the relative protons. The peaks at  $\delta \sim 6.4\text{-}6.7$  ppm were assigned to the 3 aromatic protons in the dopamine molecule, the peaks at  $\delta \sim 2.7 - 2.9$  ppm were assigned to the 4 protons of the methylene groups. The peaks at  $\delta \sim 8.9$  ppm were assigned to the 2 protons in the catechol moiety and finally the peak at  $\delta \sim 7.9$  ppm was assigned to the protons of the amine group where the value of protons resulted close to 3, meaning that the dopamine is still in the form of hydrochloride salt. Figure 3.26 shows the  $^1\text{H-NMR}$  spectrum for PIMA-Dopa with the molecular structure of the final polymer. The multiplet peak at 6.4–6.7 ppm was attributed to the aromatic protons from the catechol functionalities (green stars in the Figure). The broad peak at 8.7 ppm was attributed to the protons on the two alcohols composing the catechol (red stars in the figure). There was also a broad peak around 0.9 ppm coming from the protons of the methyl groups in the polymer which was absent in the case of only dopamine. The stoichiometry of the final product was estimated from the  $^1\text{H-NMR}$  spectrum by integrating the hydrogen peaks from the methyl groups in the polymer ( $\delta \approx 0.9$  ppm, 6 in each monomer with 39 monomers in total) corresponding to 234 H, the three aromatic protons per catechol ( $\delta = 6.4\text{-}6.7$  ppm) and the 2 protons from the alcohol groups. With this procedure, we quantified  $\sim 18$  dopamine moieties ( $54.72/3 = 18.2$  and  $36.4/2 = 18.2$ ;  $m = 18$  and  $n = 21$  in Figure 3.27) per unit of the polymer, which was consistent with the 50% mole fraction of dopamine used to functionalise the polymer.

#### 3.4.3.2 Ligand exchange

After the synthesis of PIMA-Dopa, the polymer was used for the ligand exchange of Fe NPs. The particles used for this experiment were the particles synthesised with 1.3 mmol of precursor (15.9 nm in diameter).



*Figure 3-27 TEM images at low (left) and high (right) magnification of Fe NPs after ligand exchange process with PIMA-Dopa polymer.*

Figure 3.27 shows the TEM images at a high and low magnification of the NPs after ligand exchange. The NPs looked partially oxidised, featuring the formation of voids between the core and the shell, which can be seen in the zoom-in inset in the TEM images. The oxidation appears to be size dependent with smaller particles more affected than bigger ones. Moreover, the NPs are well separated from each other throughout the TEM grid, suggesting that the polymer grafting acted on a single particle rather than forming clusters of NPs. This was also confirmed by DLS analysis where the  $D_H$  value observed was lower than 100 nm ( $D_H = 95$  nm). However, the purification of the NPs was challenging because most of the particles were precipitated out leading to only a small proportion of the iron nanoparticles being dispersible in water.

The NPs in water (Figure 3.28) did not aggregate over time, and it suggested that this strategy allowed for a better transfer of NPs in water, providing also a better final colloidal stability compared to the encapsulation method using PMAO.



*Figure 3-28 Picture of Fe NPs transferred in water using PIMA-Dopa polymer.*

However, the number of NPs successfully transferred in water was very low because most of the particles remained trapped in the syringe filter used during the washing step (0.45  $\mu\text{m}$  cut-off size). This suggests that most of the NPs aggregated during the ligand exchange process, forming structure bigger than 450 nm. Avoiding the use of syringe filters would just translate into the precipitation of NPs within few days.

#### 3.4.3.3 Summary on ligand exchange with PIMA-Dopa

Fe NPs were successfully transferred in water using PIMA-Dopa polymer. The final NPs were highly monodispersed, and the sample showed a  $D_H$  value lower than 100 nm. Although promising, the protocol did not fully address the tendency for Fe NPs to aggregate during the ligand exchange, impairing the transfer of NPs in water. The method here attempted was first reported for the ligand exchange of superparamagnetic iron oxide NPs with a diameter  $\leq 10$  nm. In our case, Fe NPs are larger than 15 nm and their  $M_s$  value was higher than in the case of iron oxide NPs. Being Fe NPs soft ferromagnetic, they are more prone to inter-particles magnetic interactions. Moreover, the presence of many dopamine moieties in the polymer, acting as anchoring for the polymer to the NPs, could increase the probability of interlinking between NPs leading to aggregation.

### 3.4.4 Ligand exchange with modified PIMA-Dopa

In order to increase the ligand exchange efficiency, using dopamine-functionalised polymer to transfer NPs in water, the protocol was modified to overcome some of the issues faced using Fe NPs. The polymer synthesis was designed to have just one or two anchoring points in each polymer chain to avoid any interlinking among NPs during the ligand exchange. For the synthesis of modified PIMA-DOPA (Mod-PIMA-Dopa), 5% of the monomers were reacted with dopamine, leaving the rest of anhydride rings intact.

Figure 3.29 shows the  $^1\text{H}$  NMR spectra for Mod-PIMA-Dopa with the molecular structure of the compound. The weak multiplet peaks at 6.4–6.7 ppm were attributed to the aromatic protons from the catechol functionalities (green stars in the figure). Also, a broad peak around 0.9 ppm was observed, coming from the protons of the methyl groups in the polymer. The peak at around 1.2 ppm was attributed to some residual triethylamine which was used for the activation of dopamine during the synthesis. To estimate the stoichiometry of the final product the  $^1\text{H}$  NMR peaks from the methyl groups in the polymer and the aromatic protons from the catechol were integrated. The value of 234  $^1\text{H}$  coming from the methyl groups in the polymer ( $\delta \approx 0.9$  ppm, 6 in each monomer with 39 monomers in total) corresponded to 9.8 H, ( $\delta = 6.4\text{--}6.7$  ppm) for catechol groups. We quantified  $\sim 3$  dopamines ( $9.8/3 = 3.2$  thus  $m = 3$  and  $n = 36$  in molecular structure of Fig 3.29) per ligand, which is consistent with the 5% mole fraction of dopamine used to functionalise the polymer.

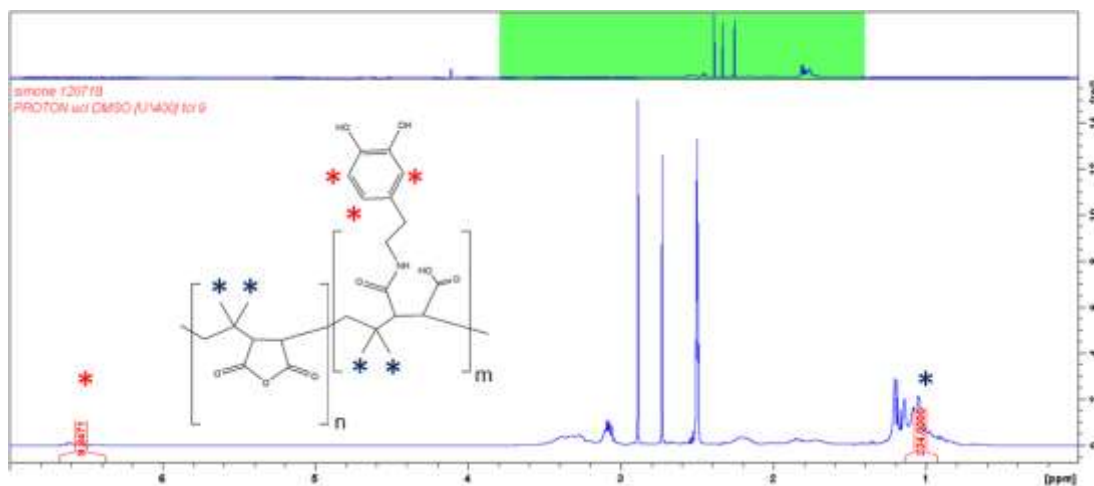
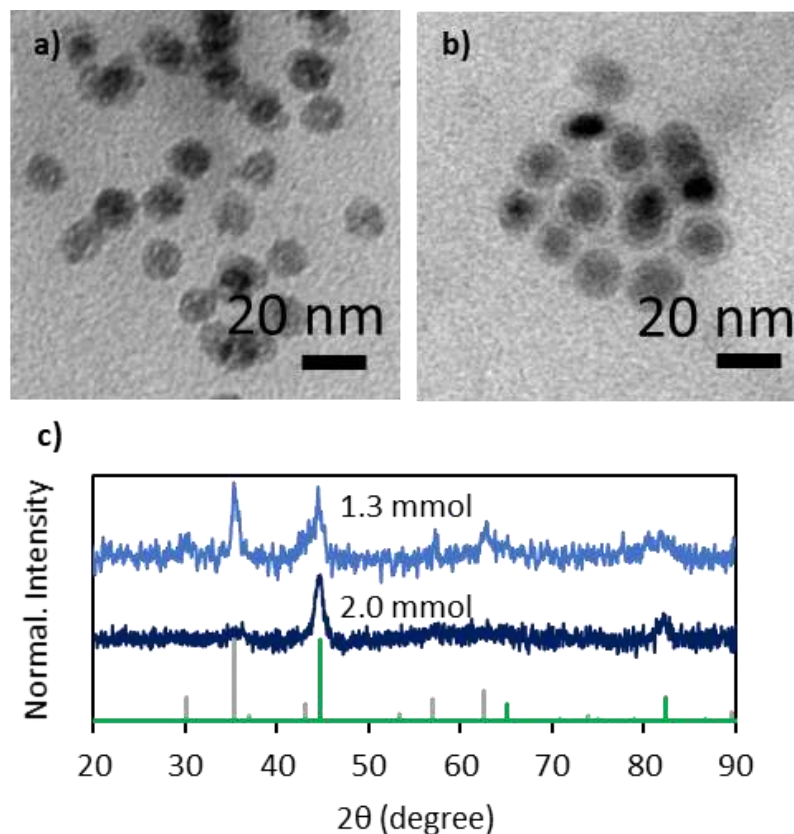


Figure 3-29  $^1\text{H-NMR}$  of Mod-PIMA-Dopa polymer

The ligand exchange reaction was carried out under low concentration conditions. Once the ligand exchange takes place, the remaining anhydride moieties were hydrolysed with  $\text{OH}^-$  in borate buffer solution. This process makes the system water-dispersible and converts each maleic anhydride unit in two carboxylic acid groups, allowing the stabilization of the NPs in water by steric and electrostatic repulsion. Two kinds of NPs (15.9 nm and 18.3 nm NPs) were chosen, which were respectively synthesized using 1.3 and 2.0 mmol of  $\text{Fe}(\text{CO})_5$ . Those NPs have similar magnetic properties ( $M_s$  and coercivity), structural properties, oxide shell thickness and similar polydispersity, except for the Fe core size. Other NPs (12.6 and 20.7 nm NPs, obtained using respectively 1.0 mmol and 2.4 mmol of the precursor) were not studied because the former was heavily oxidized (no Fe core), and the latter was polydisperse in size and colloiddally unstable.

Figure 3.30 a and 3.30 b show TEM images of 15.9 nm and 18.3 nm NPs after the ligand exchange, respectively. In the case of the 15.9 nm NPs (1.3 mmol of the precursor), significantly shrunk cores and some hollow NPs were observed, in contrast to the core@shell structure shown in Figure 3.7. For the 18.3 nm NPs, a distinct core@shell structure was retained, and the formation of voids was observed.



*Figure 3-30 Characterization of the samples after ligand exchange: TEM picture of Fe NPs synthesised with a) 1.3 mmol and b) 2.0 mmol of  $\text{Fe}(\text{CO})_5$ , the scale bar corresponds to 20 nm. c) The XRD patterns are shown with the grey reference pattern corresponding to the  $\text{Fe}_3\text{O}_4$  phase and the green one to the Fe phase.*

To confirm this observation, the XRD patterns of 15.9 nm and 18.3 nm NPs after the ligand exchange were recorded. As shown in Figure 3.31c, the XRD pattern of 15.9 nm NPs showed two different phases present being metal ( $\alpha$ -Fe) and oxide ( $\text{Fe}_3\text{O}_4/\gamma$ - $\text{Fe}_2\text{O}_3$ ) indicating that the NPs further oxidised during the ligand exchange reaction, while no iron oxide peak was detected on the XRD pattern before ligand exchange. The 18.3 nm NPs showed no sign of significant oxidation with  $\alpha$ -Fe still being the main phase present. However, the (110) peak of  $\alpha$ -Fe becomes broader after the ligand exchange. The Fe core sizes estimated from TEM images and the XRD peak are both around 10 nm which is smaller than the core size before ligand exchange, indicating that a certain extent of oxidation occurred.

The resulting aqueous dispersion of 18.3 nm Fe NPs was analysed by DLS and the  $D_H$  value observed in Milli-Q water was  $80 \pm 52$  nm as shown in the Figure 3.31. The data showed a unimodal distribution, confirming the homogeneity of the sample.

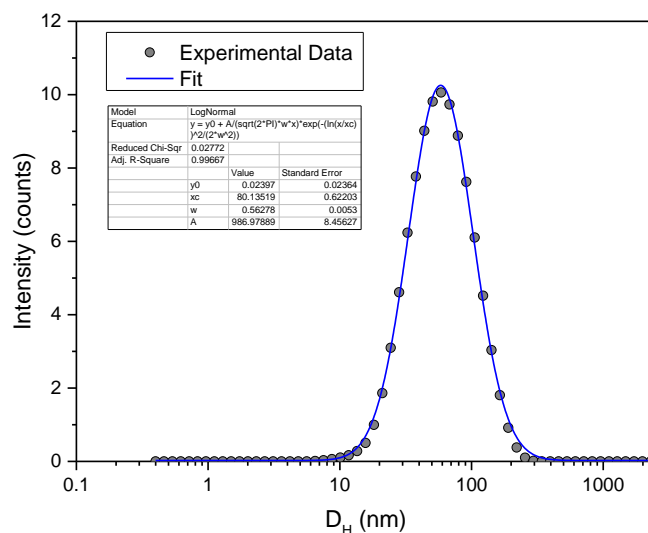


*Figure 3-31 DLS measurement of 18.3 nm Fe NPs in Milli-Q water with relative fit of the data using LogNormal function.*

The colloidal stability of the system at different pH values was investigated as shown in Figure 3.32. At pH = 3.2 the  $D_H$  was over 1000 nm, indicating aggregation of NPs. At pH = 4.5 the  $D_H$  decreased to  $155 \pm 90$  nm while at higher pH value the  $D_H$  reached a constant value of  $64 \pm 43$  nm (at pH 6.2) and remained constant at higher pH. For the Z-potential values, at low pH (3.2) the value was -17 mV and progressively becomes more negative when the pH is increased, reaching a maximum of -59 mV at pH 8.5. This agrees with the fact that the surface of the nanocomposites is surrounded by carboxylic acid moieties. At low pH (< 4.5), they are mostly protonated, thus the electrostatic stabilisation due to carboxylate anions disappear, and the particles start to aggregate. At pH  $\geq$  4.5 enough moieties are deprotonated to guarantee electrostatic stabilisation, hence better colloidal stability, with a  $D_H$  value lower than the one in deionised water. This suggests that electrostatic repulsion is the main factor contributing to the NPs colloidal stability. Furthermore,

stability tests were carried out at different NaCl concentrations (Figure 3.33). Initially, the  $D_H$  increases slightly when the concentration of NaCl is increased, reaching the value of 168 nm in 150 mM NaCl solution. When the NaCl concentration was increased to 300 mM, the  $D_H$  measured was 1093 nm, and the sample aggregated within minutes. The Z-potential passed from -46 mV in ddH<sub>2</sub>O to -26 mV in NaCl solution 75 mM. The Z-potential value remained similar when NaCl concentration was increased. The less negative value observed in NaCl solution can be explained by the Na<sup>+</sup> ions interacting with the negative carboxylate moieties present on the surface of the NPs. The system was found to be stable over a broad range of pH (pH 4 to pH 10) and up to 150 mM of NaCl solution which makes the system suitable for use in biomedical applications.

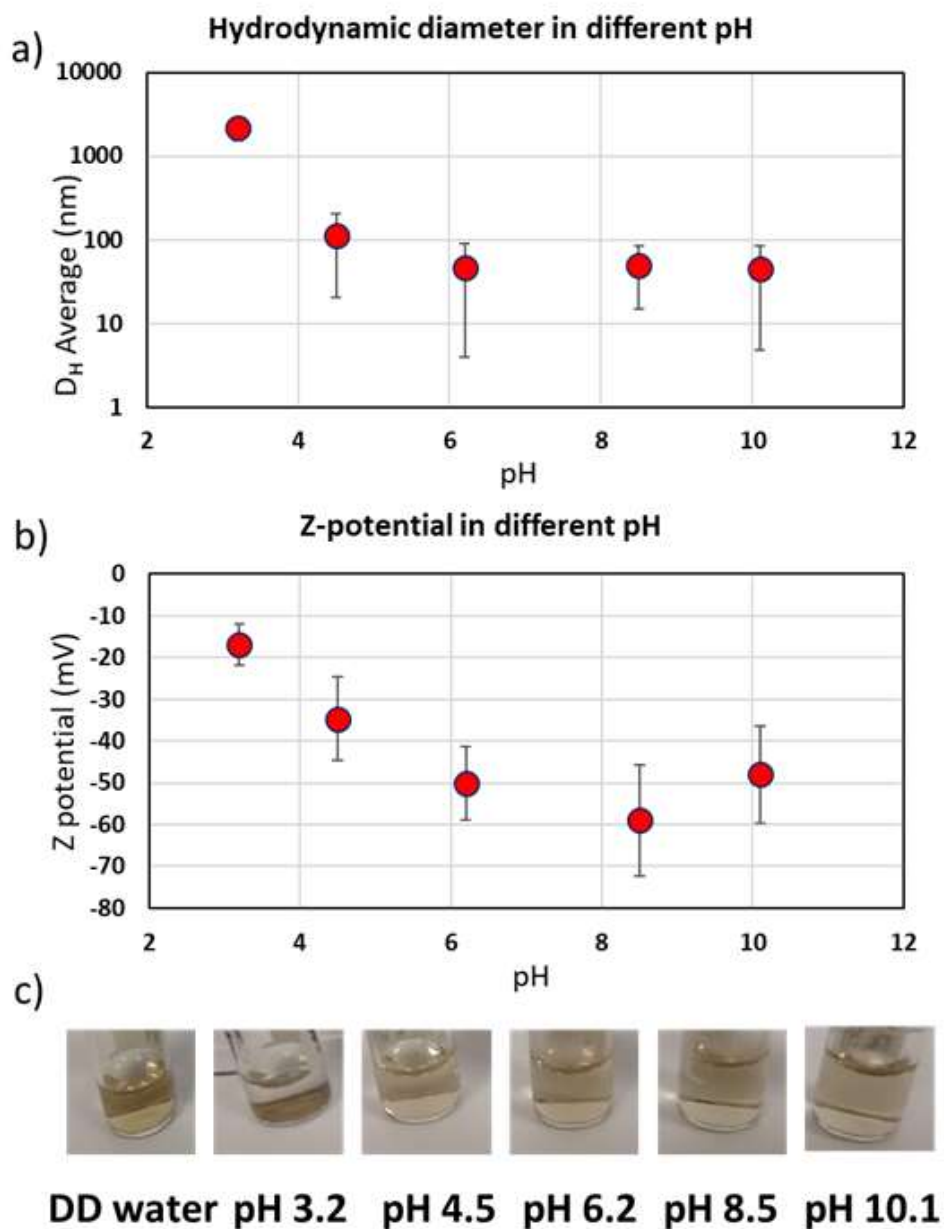


*Figure 3-32 Colloidal stability study of the 18.3 nm NPs in different pH solutions. a) Hydrodynamic size in different pH, b) Zeta-potential value in different pH. c) Picture of the dispersion after 24 h.*

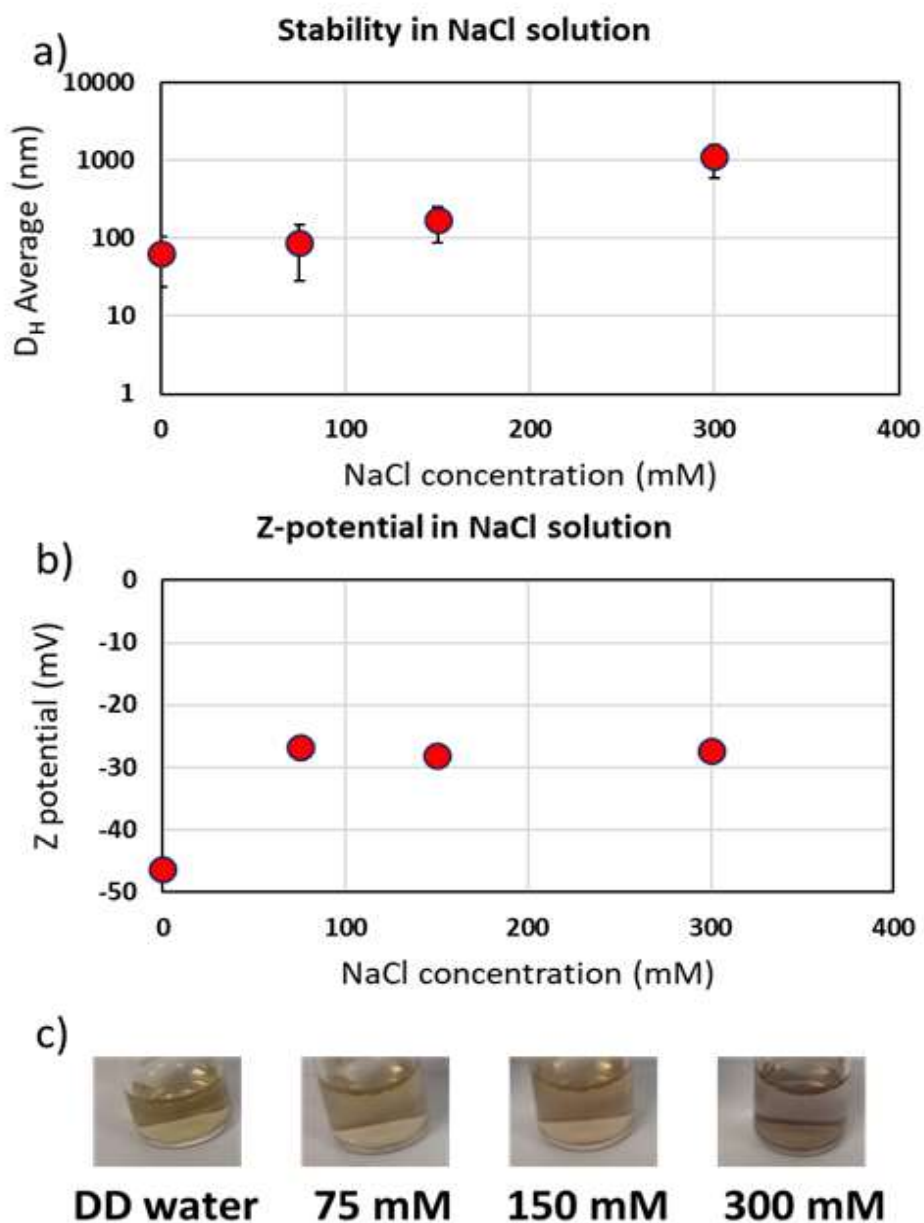


*Figure 3-33 Colloidal stability study of the 18.3 nm NPs in NaCl solutions at various concentrations. a) Hydrodynamic size in different NaCl concentrations, b) Zeta-potential value in different NaCl concentrations. c) Picture of the dispersion after 24 h.*

### 3.5 Magnetic Hyperthermia

Finally, the heating efficiency of the particles was evaluated by magnetic hyperthermia measurement. For the quantification of SAR, the temperature of the

sample was recorded during the application of an alternating magnetic field. Figure 3.34 represents a typical data profile for the magnetic hyperthermia measurement. The temperature showed a dramatic increase when an external alternating magnetic field (303 KHz and 308 Gauss) was applied. As soon as the field was removed, the heating stopped, and the sample started to cool down. The measurement was repeated another time and the same heating curve was obtained, confirming that no changes occurred in the sample like aggregation and/or precipitation, after being exposed to an external magnetic field (Figure 3.34 top). In a perfectly adiabatic set-up, the heating curve would show a linear increase of the temperature. However, in a non-ideal adiabatic system the curve just initially follows a linear trend and it eventually deviate from a linear temperature increase because the solution starts to exchange heat with the environment. Therefore, the fitting of the curve was carried considering just the first seconds of the measurement (e.g. 10, 20, 30 and 40 seconds) to estimate the  $dT/dt$  value, needed for SAR quantification. Figure 3.33 (bottom) shows the fitting of the first part of the heating curve with the relative  $R^2$  parameter. The result showed that at 40 and 30 seconds the heating profile started to deviate from a linear trend while the 20 seconds fit was the longest range which showed also the best  $R^2$  value for a linear fitting. Similar analyses were carried out prior to every SAR value estimation.

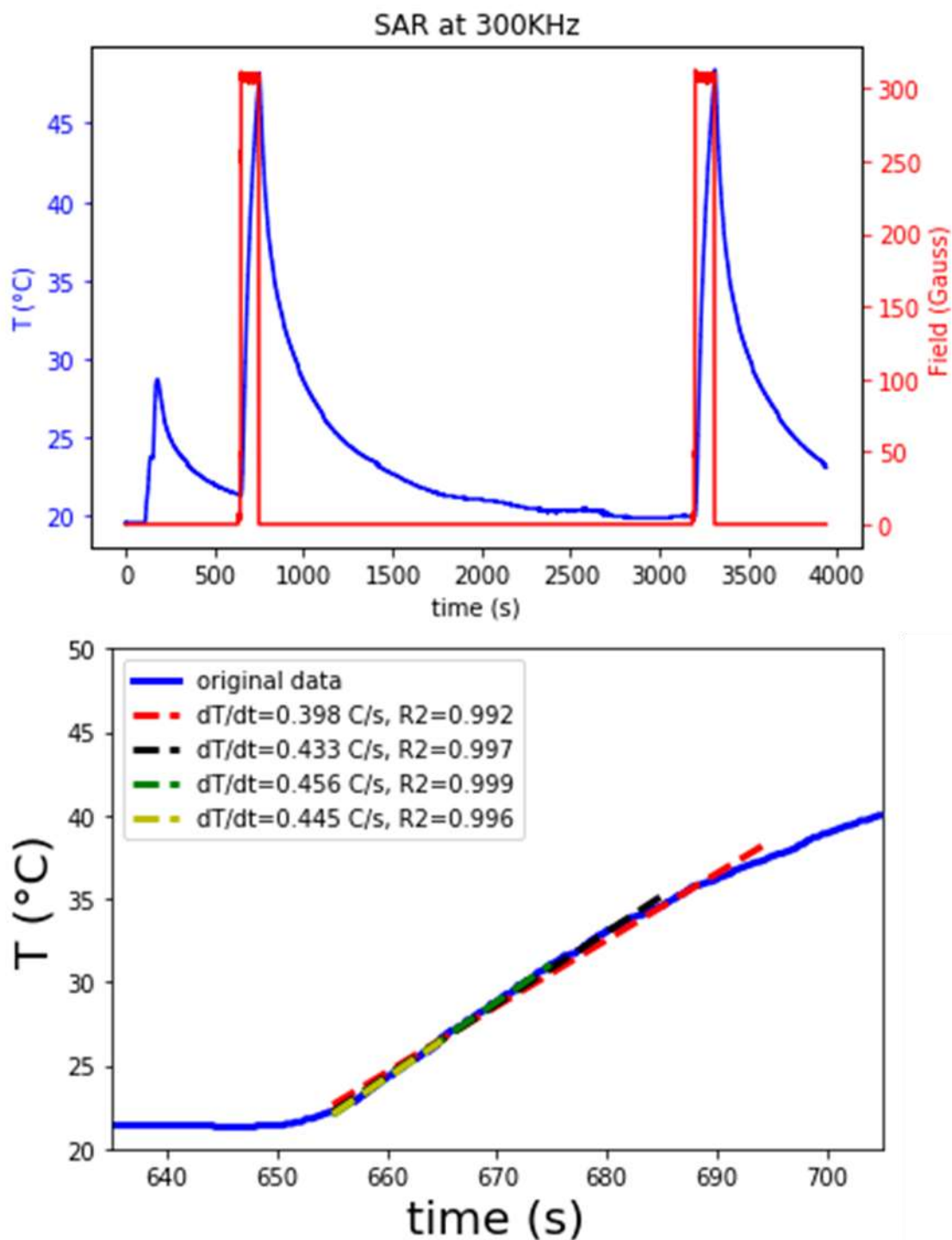
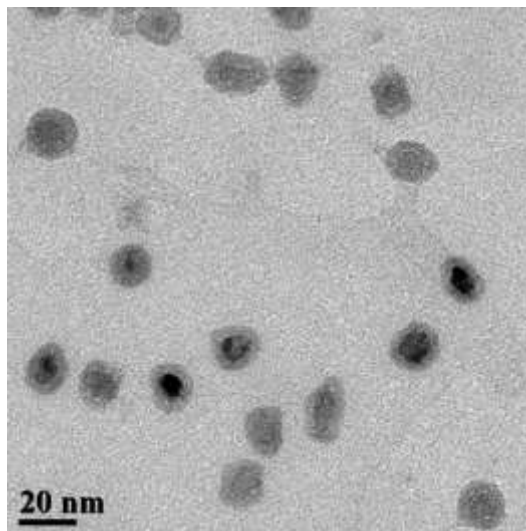


Figure 3-34 Heating profile of 18.3 nm NPs at 303 KHz and 308 Gauss (top). Fitting of the first heating curve for the calculation of  $dT/dt$  (bottom).

For the 15.9 nm NPs it was observed a SAR value of 135 W/g<sub>Fe</sub>, while the 18.3 nm NPs showed a significant increase of SAR value at 660 W/g<sub>Fe</sub>, ILP = 3.6, Table 3.9). The SAR

value for the 15.9 nm NPs is similar to reported values for Fe NPs dispersed in water.<sup>3,14</sup> For the 18.3 nm NPs in water, on the other hand, the SAR output value was found to be 4 times higher than that of 15.9 nm NPs.



*Figure 3-35 TEM picture of Fe NPs (2.0 mmol) dispersed in water, 2 months after ligand exchange with Mod-PIMA-Dopa.*

This behaviour can be explained by the different composition of the NPs. Indeed the 18.3 nm NPs are big enough to retain  $\alpha$ -Fe core even after ligand exchange. From theoretical studies done by Habib *et al.* it was found that a diameter around 10 nm would maximise the hyperthermic effect of Fe NPs.<sup>30</sup> This size is very close to the size of Fe cores (10 nm) in our 18.3 nm NPs. Further to investigate the stability of the system, we repeated the experiment after 2 months, and no clear difference was detected in the ILP value (3.8). Indeed, TEM images confirmed the presence of core@shell structure (Figure 3.35)

It is important for clinical applications that the field and frequency used is within the safe limit.<sup>31</sup> Various fields and frequencies were chosen so that the product ( $Hxf$ ) was lower than  $5 \times 10^9 \text{ A} \cdot \text{m}^{-1}$ . The SAR and ILP values were obtained for 18.3 nm NPs as shown in Table 3.10. Our Fe NPs produce high heating efficiency with ILP of 3.2 to 3.8

which is one of the highest values reported so far for this type of materials in similar conditions.<sup>7,32</sup>

*Table 3-8 Magnetic Hyperthermia measurements for 18.3 nm NPs (2.0 mmol) and relative conditions used.*

Measurement	Frequency (KHz)	Field (KA m <sup>-2</sup> )	SAR (W g <sup>-1</sup> )	ILP (nHm <sup>2</sup> kg <sup>-1</sup> )
1	303	24.5	660	3.6
2 (after two months)	303	24.5	696	3.8
3	150	33.3	583	3.5
4	150	24.5	343	3.8
5	163	31.1	498	3.2

### 3.6 Discussion on oxidation of Fe NPs

After the synthesis, Fe NPs are exposed to ambient environment and they quickly oxidized to form a Fe<sub>x</sub>O<sub>y</sub> layer with a thickness of around 3-4 nm. This value showed no significant dependence on NPs size. Similar values have been reported for both crystalline<sup>3</sup> and amorphous<sup>12</sup> Fe NPs and oxygen diffusion can be responsible for the formation of the first few monolayers of oxide.<sup>33</sup> However concentration of oxygen decreases with depth and a further thickening process of the oxide layer is associated with the Kirkendall effect where the outward diffusion rate of Fe ions in the oxide layer becomes much larger than the inward diffusion rate of oxygen.<sup>34</sup> In an attempt to quantify this phenomenon, Sun *et al.* showed that the formation of the first oxide layers is rapid (below 1 ns) and in the presence of a Fe-Fe<sub>x</sub>O<sub>y</sub> interface the oxidation proceeds via formation of cationic vacancies in the α-Fe crystal. Once enough vacancies are generated, they start to coalesce and ultimately they form a void at the interface while the oxide layer thickens outward. The diffusion rate of Fe atoms is dependent on the temperature and the area of the Fe/Fe<sub>x</sub>O<sub>y</sub> interface so then when

the voids start to form, the interfacial area starts to decrease and the rate of oxidation also decreases simultaneously.<sup>35</sup> In our study, no clear voids formation was observed for the as synthesised Fe NPs while after the ligand exchange step a reduction of Fe core was detected in both samples with brighter gaps between Fe and Fe<sub>x</sub>O<sub>y</sub> interface. Herman *et al.* showed that the removal of the native ligand on the surface of Fe@Fe<sub>3</sub>O<sub>4</sub> facilitates the oxidation of the core/shell structures in air, favouring the Kirkendall effect.<sup>4</sup> The destabilisation of the structure due to ligand displacement and possibly the change of the surrounding environment could explain the deeper oxidation in the case of water-dispersed NPs. However, the 18.3 nm Fe NPs can undergo the aforementioned process and still retain a Fe core because of the initial larger volume of  $\alpha$ -Fe crystal compared to the smaller sample (15.9 nm). Combined with the high crystallinity of  $\alpha$ -Fe, the larger residual core leads to significantly higher magnetic hyperthermia outcomes.

### 3.7 Conclusion

In this chapter, Fe@FexOy NPs of different sizes were synthesised. By changing the amount through a single-shot hot-injection method, it was not possible to control the final size and size distribution of nanoparticles and only by using less than 0.2 mmol of precursor it was possible to achieve a narrow size distribution but no control on the final size of the NPs. Using a continuous injection of the precursor, this synthetic strategy can produce different sizes of NPs by tuning the amount of precursor injected. The nanocrystals formed are made of single crystals with a good size distribution and once open to the air, the formation of an iron oxide shell occurs. When the NPs are as small as 12 nm, mainly iron oxide NPs are obtained, whereas with bigger size a polycrystalline iron oxide shell is formed retaining a single crystalline iron core. An upper limit for the size is reached around 20 nm after which the system starts losing colloidal stability during the reaction and subsequently the size distribution broadens. Different strategies were attempted to transfer the NPs in water such as silica coating and polymer encapsulation. Silica coating was hard to

achieve, and the reaction led mainly to the formation of free Si NPs and highly aggregated Fe NPs. The encapsulation of Fe NPs with PMAO successfully transferred the NPs in water, however, the process promotes aggregation and the final colloidal stability is impaired. Considering the high tendency of Fe NPs to aggregate, a new strategy was proposed by using Mod-Dopa-Pima. Two sets of NPs (15.9 and 18.3 nm) were functionalized with a dopamine-functionalised polymer resulting in an efficient transfer of the NPs into water. Moreover, the NPs dispersed in water were colloidally stable in a wide range of pH and ionic strength that can be found in physiological conditions. The 18 nm NPs possess excellent heating capabilities, being also stable in solution for 2 months with no sign of chemical deterioration. These results indicate a new avenue for producing stable and high heating efficiency nanoparticles that is much needed for hyperthermia and many other biomedical applications.

Chapter 4 One pot  
synthesis of iron carbide  
NPs for magnetic  
hyperthermia.

## 4.1 Introduction

Iron carbides (IC) are a class of materials with various composition and they have been recently reported to hold great potential for several applications when the material is reduced to the nanoscale. For example, it has been shown that IC can play a key role in the Fischer–Tropsch process, a widely studied technology used to produce liquid fuels from syngas (CO and H<sub>2</sub> mix) using a heterogeneous catalysis.<sup>30,166–168</sup> IC NPs as catalysts, have proved to increase the yield of the reaction while also lowering the cost of the process which is traditionally reliant on noble metal catalysts.<sup>30,166–168</sup> On the other hand, iron carbide has recently attracted much attention thanks to its magnetic properties and potential biocompatibility. Indeed, being IC an iron and carbon alloy (Fe<sub>x</sub>C<sub>y</sub>), where carbon occupies the interstitial sites within the iron cubic crystal structure, it brings together many of the benefits of the two components alone. The compound possesses appealing magnetic properties thanks to fact the iron maintains its metallic nature. For example Fe<sub>5</sub>C<sub>2</sub> has a magnetic moment of ~ 140 emu/g,<sup>169</sup> which is comparable with the value of magnetic metallic NPs like Co ( ~ 160 emu/g) and higher than that of Fe<sub>3</sub>O<sub>4</sub>.<sup>71</sup> The presence of carbon in the crystal structure provides the material with good chemical stability, minimizing the drop in magnetisation caused by the oxidation of Fe atoms.

Their high magnetic moment means that IC NPs could act as an effective heating probe under an applied external magnetic field. A recent study on that has been carried by Chaudret *et al.* where they synthesised Fe<sub>3</sub>C/Fe<sub>2</sub>C NPs under elevated pressure, showing that the carbidization of Fe NPs leads to magnetic NPs with greater SAR than the starting Fe NPs. Fe<sub>3</sub>C were then used as a heating tool to locally promote a catalytic reaction inside an oxygen-free, sealed reaction vessel.<sup>101</sup> Even though this study shows the potential of this material in magnetic hyperthermia, it does not evaluate the performances of NPs under biomedically compatible conditions, and in general, studies of iron carbide for magnetic hyperthermia in aqueous media are lacking in the literature. One possible reason is the lack of facile synthetic procedures

to form monodispersed iron carbide NPs compared to more commonly studied magnetic NPs (e.g.  $\text{Fe}_2\text{O}_3$ ,  $\text{Fe}_3\text{O}_4$ , Co, Fe etc.). Meffr *et al.* reported for the first time the synthesis of monodispersed  $\text{Fe}_3\text{C}$  NPs with excellent heating properties by performing the reaction under 3 bar of  $\text{H}_2$  for 24 h.<sup>82</sup> Ce Yang *et al.* instead, starting from Fe NPs, produced  $\text{Fe}_5\text{C}_2$  phase at 350 °C in a mixture of long-chain amines.<sup>30</sup> Indeed, it was reported that at high temperature, Fe NPs act as catalysts promoting the decomposition of long-chain amines and this process provides the carbon species that react to form the iron carbide phase. Yang *et al.* showed that the presence of halides in solution affects the formation of the carbide phase leading to at least 5 different phases with different Fe : C composition and crystal structure, depending on the amount of halide used.<sup>74</sup> They showed that halides interact with the surface of the previously formed  $\alpha$ -Fe NPs and when the concentration of halides increases, it can interfere with the carbon penetration process in the  $\alpha$ -Fe crystal structure, changing, therefore, the final IC NPs composition or blocking the carbidization process altogether. Despite the recent achievements, the synthetic protocols developed can only prepare few kinds of pure IC NPs. The carbidization process may lead to non-uniform carbide phase, which are hard to characterise and standardise. As the performance of IC NPs in many applications depends on dispersion, composition and nanostructure, the synthesis of monodisperse IC NPs with specific compositions, sizes and structures needs more attention.

To approach the synthesis of IC NPs, the process must involve the formation of bcc-Fe phase first, followed by the penetration of C atoms into the crystal lattice.<sup>30</sup> Therefore, here, IC NPs were synthesised starting from the synthesis of crystalline Fe NPs. Subsequently, the effect of different parameters on the final structure were evaluated. After the synthesis, the particles were transferred in water via ligand exchange and their potential as heating probes for magnetic hyperthermia was tested.

## 4.2 Materials and methods

### 4.2.1 Materials

1-Octadecene ( $C_{18}H_{36}$ , 90%), hexadecylamine ( $C_{16}H_{35}N$ , HDA, 90%), diethyl ether ( $Et_2O$ , anhydrous,  $\geq 99.7\%$ ), hydrochloric acid (HCl, 37%) and octadecylamine ( $C_{18}H_{37}N$ , ODA, 70%) were purchased from Sigma Aldrich, Japan. Ethanol (EtOH, 99.5%) was obtained from Nacalai Tesque, Japan. Iron pentacarbonyl ( $Fe(CO)_5$ ,  $>95\%$ ), hexane ( $C_6H_{14}$ ,  $>96\%$ ), chloroform ( $CHCl_3$ ) and were obtained from Kanto Chemicals, Japan. All the reagents were used as purchased without any further purification. For the synthesis of Mod-PIMA-Dopa and subsequent ligand exchange step, the same chemicals listed in Chapter 3 were used.

### 4.2.2 Methods

#### 4.2.2.1 Synthesis of Iron Carbide NPs

For the synthesis of IC NPs, a varying amount of Hexadecylammonium Chloride (halide source) and long-chain amines were added into 10 ml of octadecene (as summarised in Table 4.1) inside a 50 mL three-neck flask connected to a Schlenk line in one the neck so that the reaction was carried out under inert atmosphere. The solution was heated up at  $120^\circ C$  and degassed for 60 min under an Ar flux bubbled inside the solution through a syringe needle. After, the solution temperature was set at  $180^\circ C$  and once stable, 0.2 ml of neat  $Fe(CO)_5$  was loaded into a 1 ml syringe and was injected in a single and quick shot with a syringe. After the addition of iron precursor,  $Fe(CO)_5$ , the solution was kept at  $180^\circ C$  temperature for 30 min in total and subsequently the temperature was raised at  $260^\circ C$  to promote the formation of iron carbide phase and left to react for 15 min, after which the heating mantle was removed and the solution let to cool down.

Once the solution reached room temperature, it was collected and transferred into two 50 ml centrifuge tubes and 5 ml of chloroform followed by 15 ml of ethanol were added. The solutions were centrifuged at 5000 rpm for 3 min. The supernatant was then discarded, and the precipitated nanoparticles were washed again adding 5 ml of chloroform first to redisperse the NP and 15 ml of ethanol after to promote the precipitation of NPs during the following centrifugation. The process was repeated twice in total and finally the NPs were redispersed in chloroform and stored for further use. Figure 4.1 shows a schematic representation of the synthetic protocol.

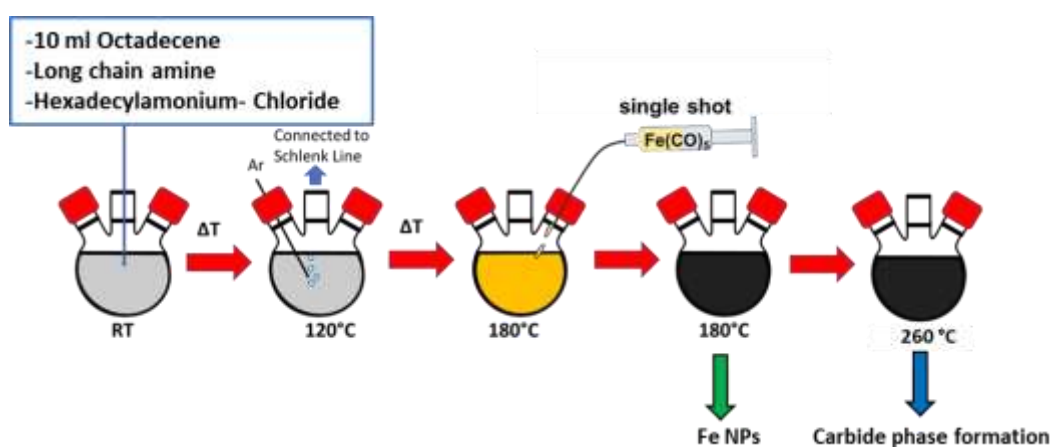


Figure 4-1 Schematic representation of the synthetic procedure for the formation of iron carbide NPs.

#### 4.2.2.2 $^{57}\text{Fe}$ Mössbauer Spectroscopy

$^{57}\text{Fe}$  Mossbauer analysis was carried out to confirm the chemical structure of the iron carbide particles. Briefly, 58 mg of powdered sample was placed in a mortar, to which  $\sim 100$  mg pure sucrose powder was added. The sample and sucrose were mixed using the pestle to form a solid dispersion, which was then sandwiched between two plastic disks to form a coin-shaped absorber of 2.1 cm diameter. Transmission  $^{57}\text{Fe}$  Mössbauer spectra were recorded at room temperature with a time-mode spectrometer using a constant acceleration drive with a triangular reference signal.

Measurements were performed at room temperature using a SeeCo W302 constant acceleration drive with a triangular reference signal. The source was driven at a velocity scale of 12 mm/s. Data were accumulated in 1024 channels and folded relative to a 10  $\mu\text{m}$  thick  $\alpha\text{-Fe}$  foil. The spectra were fitted using Recoil software, where it was folded relative to a 10  $\mu\text{m}$  thick  $\alpha\text{-Fe}$  foil.

## 4.3 Results and discussion

### 4.3.1 Parametric studies on the synthesis of $\text{Fe}_2\text{C}$

#### 4.3.1.1 Effect on ligands concentration and temperature

To form Fe NPs, necessary for the subsequent formation of IC NPs, the single hot-injection of the precursor ( $\text{Fe}(\text{CO})_5$ ) was preferred over the continuous injection approach tested in the previous chapter. This choice would allow higher degree of freedom in tuning the reaction conditions, as slight variations of concentration of ligands (chloride source and/or amines) can significantly change the kinetics of the formation of Fe NPs when the continuous injection setup is used.<sup>170</sup> The amount of iron precursor ( $\text{Fe}(\text{CO})_5$ ) was kept constant through all the experiments reported in this chapter, and 0.2 ml (1.5 mmol) were used because it resulted in monodisperse NPs (Paragraph 3.3.1). Halides have been proved to be vital for the formation of crystalline Fe NPs, but at the same time it can affect the final composition of carbides. Indeed, Yang *et al.* showed that although the presence of halides contributes to the formation of IC NPs through the formation of crystalline Fe phase in the initial steps of the reaction, it can also interfere during the carbidization process by limiting the carbon penetration in the  $\alpha\text{-Fe}$  crystal structure when halide concentration is increased.<sup>74</sup> Therefore it is important to investigate the effect of  $\text{Cl}^-$  on the IC formation. At the same time OAm plays a key role in the synthesis of IC NPs, because it acts as both ligand and carbon source for the carbide formation, so it was important

to also investigate its role. The time in which the solution was heated at high temperature for the formation of the carbide phase was set at 15 min.

*Table 4-1 Summary of the different parameters used for the synthesis of IC NPs.*

<i>Sample</i>	<i>Annealing T (°C)</i>	<i>OAm (mmol)</i>	<i>HDA-Cl (mmol)</i>
FeC_1	260	0.5	0.1
FeC_2	260	3	0.1
FeC_3	260	0.5	0.05
FeC_4	260	3	0.05
FeC_5	260	0.5	0.03
FeC_6	260	0.5	0.01
FeC_7	220	3	0.05
FeC_8	300	3	0.05

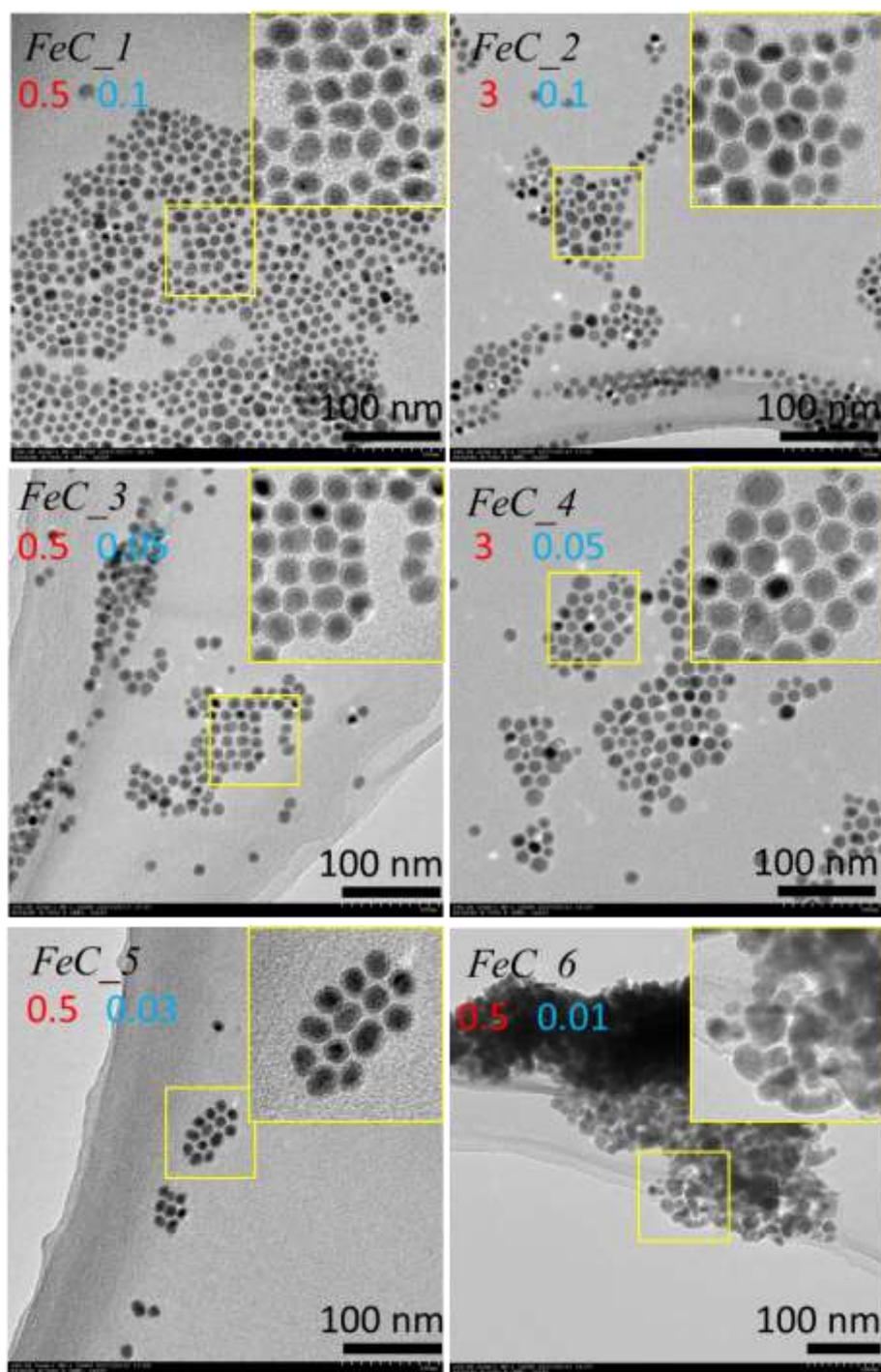


Figure 4-2 TEM images of the samples FeC\_1 to FeC\_6 with the mmol of OAm (red) and HDA-Cl (blue) used in the reaction.

The amount of HDA-Cl and OAm were varied independently to assess the effect on the formation of the IC NPs and Table 4.1 shows the reaction conditions used. The concentration of HDA-Cl in solution were changed to determine the effect on the

formation of IC phase and determine which is the minimum concentration required for the formation of crystalline Fe NPs and consequently IC NPs. At the same time different amounts of OAm were used (0.5 mmol and 3 mmol). 0.5 mmol, was the same amount used for the formation of Fe NPs in previous chapter and 3 mmol was selected to evaluate the effect of excess of amine on the carbide formation. For the samples FeC\_1 to FeC\_6, the amount of chloride source in solution was varied (0.1, 0.05, 0.03, 0.01 mmol) and different amount of OAm (0.5, 3 mmol) were used. Figure 4.2 shows the TEM images of samples FeC\_1 to FeC\_6. The images show spherical core@shell NPs that can be observed in all the samples but FeC\_6, where the final material was highly aggregated, and no clear shape was detected. The average NPs size in the sample was  $11.2\pm 1.7$  nm for FeC\_1,  $11.9\pm 1.9$  nm for FeC\_2,  $12.3\pm 1.8$  nm for FeC\_3,  $14.7\pm 2.3$  nm for FeC\_4 and  $12.2\pm 2.3$  nm for FeC\_5. In the case of FeC\_6 the size was not possible to determine due to the lack of defined NPs.

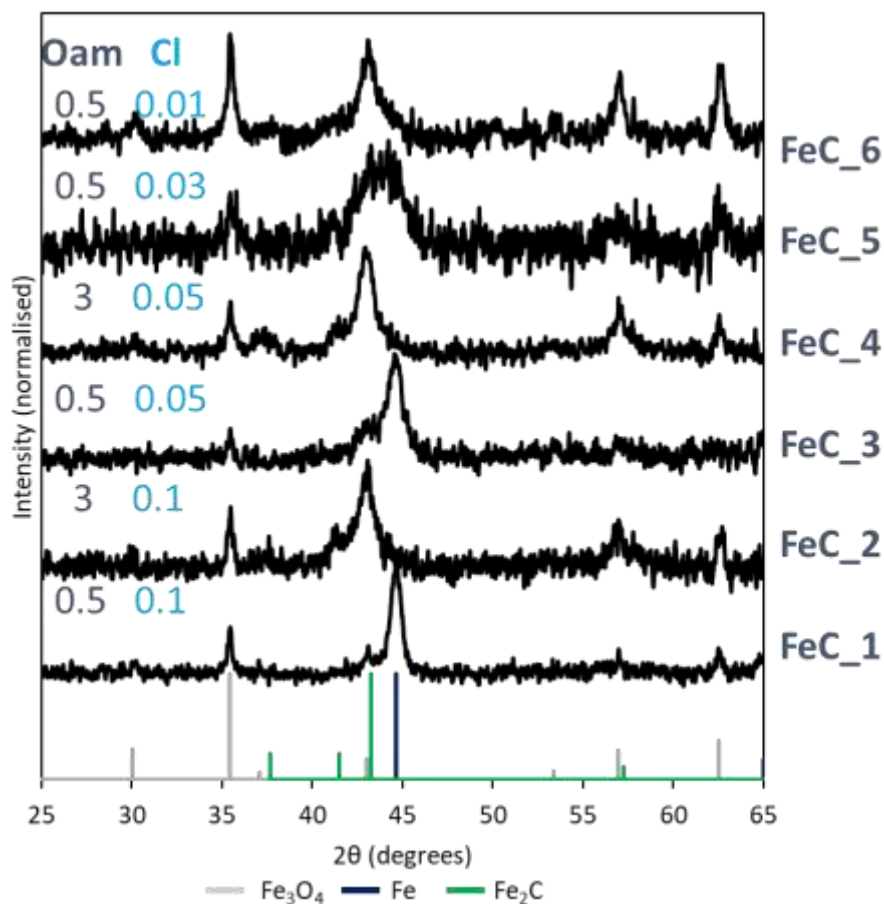


Figure 4-3 XRD patterns of samples FeC\_1 to FeC\_6 with the mmol of OAm (grey) and chloride source (blue) used in the reactions.

Figure 4.3 shows the XRD patterns of sample FeC\_1 to FeC\_6. The diffraction patterns show more clearly the effect of the single parameters on the NPs structure. Regarding the role of OAm, whenever the amount used was 0.5 mmol, there was no formation of the carbide phase, like in the case of FeC\_1 and FeC\_3. In these cases,  $\alpha$ -Fe (JSPC PDF No. 00-006-0696) was the main phase, which was retained even after the annealing step at 260 °C. When the amount of OAm used was 3 mmol (FeC\_2 and FeC\_4)  $\alpha$ -Fe is replaced by the Fe<sub>2</sub>C phase (JSPC PDF No. 00-036-1249). This points out the key role of OAm in acting as a carbon source for the formation of IC NPs.<sup>171</sup> Varying the amount of chloride source did not affect the final composition when the amount was  $\geq 0.05$  mmol. When the amount of HDA-Cl was 0.03 mmol (FeC\_5) the XRD pattern results noisy and a broad peak was detected in the area where the main

peaks of  $\alpha$ -Fe and Fe<sub>2</sub>C usually lie, thus it was not possible to unequivocally match the pattern to the reference. In FeC\_6 (0.01 mmol of HDA-Cl used) the main phase detected becomes iron oxide (Fe<sub>3</sub>O<sub>4</sub>/Fe<sub>2</sub>O<sub>3</sub>). A possible explanation is that a low amount of chloride in solution (0.03 mmol and 0.01 mmol) impairs the formation of crystalline Fe NPs, which are necessary to form subsequently IC NPs.

In FeC\_5 the low amount of chloride (0.03) may facilitate the formation of carbide even if the amine present is just 0.5 mmol, possibly leading to a mix of Fe and Fe<sub>2</sub>C phase. When the chloride was reduced to 0.01, no crystalline Fe NPs are produced before the annealing step, thus the carbide phase cannot be formed, leading to aggregation (TEM micrograph of FeC\_6 in Figure 4.2). This was consistent with previously reported work where the annealing of amorphous Fe NPs at high temperature led to the formation of iron oxide particles.<sup>30</sup> Iron oxide phase was also detected as secondary phase (JSPC PDF No. 01-079-0418) in all the other patterns which needed to be addressed. From now on, 3 mmol of OAm and 0.5 mmol of HDA-Cl was used as an optimal concentration of ligands for the formation of IC NPs.

The role of the annealing temperature on the formation of the carbide phase was studied by annealing Fe NPs at 220 °C (FeC\_7) and 300 °C (FeC\_8); the results were compared with the IC annealed at 260 °C (FeC\_4). In Figure 4.4, TEM images are shown. The particles show a core@shell structure present in all the samples. When 220 °C was used as annealing temperature the NPs showed a pronounced void between the core and the shell. The oxidation looks more pronounced than in the case of FeC\_4 (260 °C annealing T) and the high extent of aggregation hinders the size estimation. When the T used was 300 °C (FeC\_8) the particles were well dispersed on to the grid showing a core@shell structure, with no clear void formation observed between the core and the shell like in the case of the particles carbidized at 260 °C (FeC\_4). In FeC\_8 sample (carbide at 300 °C) multi-shaped NPs with rod- and hexagonal-like NPs appeared along with less defined shaped-NPs. The heating at 300

°C may induce some shape rearrangement in the particles and some coalescence between different particles as the sample show large size variations.

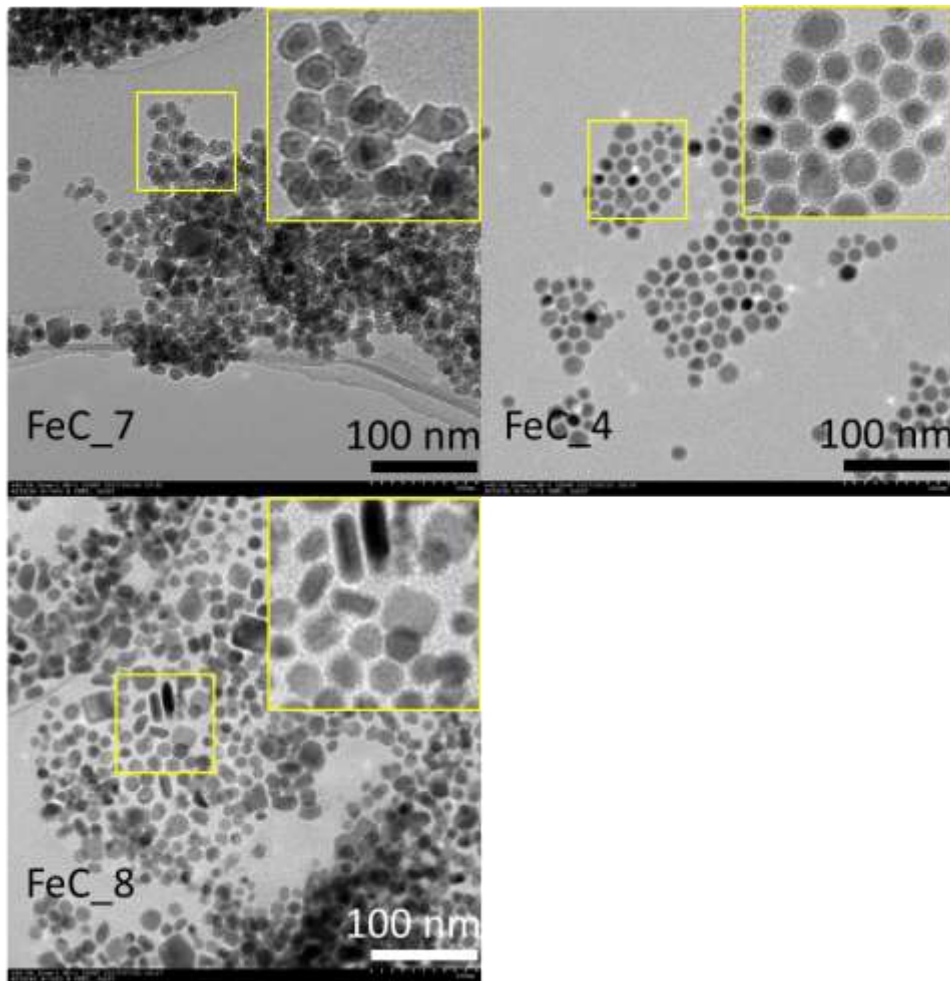


*Figure 4-4 TEM for carbide at different temperature 220 °C (FeC\_7), 260 °C (FeC\_4) and 300 °C (FeC\_8).*

Figure 4.5 shows the XRD patterns for the three samples. When annealed at 220 °C the phases detected corresponded to a mix of Fe and Fe<sub>2</sub>C phases, with Fe still being the main one, along with some secondary impurities of iron oxide. This shows that 220 °C was not high enough to promote fully the formation of carbide NPs. While at 260 °C mainly Fe<sub>2</sub>C was detected, at 300 °C a new phase appears, whose peak lies next to the main peak of Fe<sub>2</sub>C, around 40° – 45° of the XRD pattern. This is matched with a different iron carbide phase which has been reported to be formed at higher

temperature ( $\geq 300$  °C).<sup>97</sup> From the analysis it was concluded that while 300 °C forms a mixed carbide phase, 260 °C was the optimal temperature required for the formation of IC NPs uniform in shape and composition.

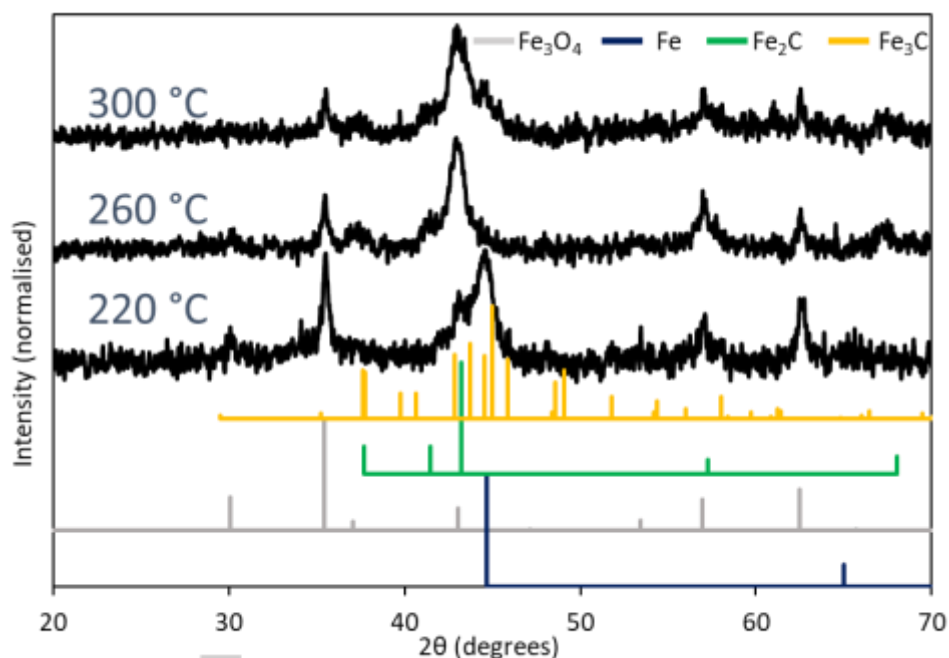


*Figure 4-5 XRD patterns of IC NPs synthesised at different temperature 220 °C (FeC\_7), 260 °C (FeC\_4) and 300 °C (FeC\_8).*

The iron oxide phase, whose origin was still unclear, was detected throughout the whole series. The lower intensity compared to the Fe<sub>2</sub>C phase, suggested that it was formed as impurity during the annealing process and it needed further investigation to suppress its formation.

#### 4.3.1.2 Replacing oleylamine with hexadecylamine and octadecylamine

To resolve the issue of iron oxide presence in the final product the role of different ligands was investigated for the formation of IC NPs. The iron oxides phase appeared during the carbidisation process; in this step, amines were actively taking part in the

reaction, by decomposing and acting as carbon source for the formation of carbide phase, thus amines may be also responsible for the formation of the oxide phase. OAm is commercially available with a 70% purity grade which could make the reaction conditions harder to control. Also, OAm has a double bond between the carbons 9 and 10 of the chain, which makes the molecule more reactive at high temperature. For this reason, hexadecylamine (HDA) and octadecylamine (ODA) were used to replace OAm as surfactant and carbon source. HDA is an amine with a 16-carbon chain, while ODA has an 18-carbon chain and they are both available with a purity grade  $\geq 90\%$ . This is important to have more control over the synthesis and minimise the eventual role that impurities may play. Moreover, ODA and HDA are linear and this will remove any uncontrolled reaction that the double bond in the carbon chain may undergo at high temperature, potentially affecting the final product.<sup>107</sup>

*Table 4-2 Summary of the reaction conditions used.*

<i>Sample</i>	<i>Anneal. T (°C)</i>	<i>Amine (mmol)</i>	<i>HDA-Cl (mmol)</i>
FeC_9	260	3 (HDA)	0.05
FeC_10	260	3 (ODA)	0.05

Figure 4.6 shows the TEM images and XRD patterns of the NPs synthesised using HDA instead of OAm. The NPs have a spherical shape and core@shell structure similar to the particles synthesised with OAm. The average size of NPs was  $15.5 \pm 2.2$  nm, which was close to the size obtained for NPs synthesised with OAm. The XRD pattern shows that the main phases present into the sample were iron oxide and iron carbide.

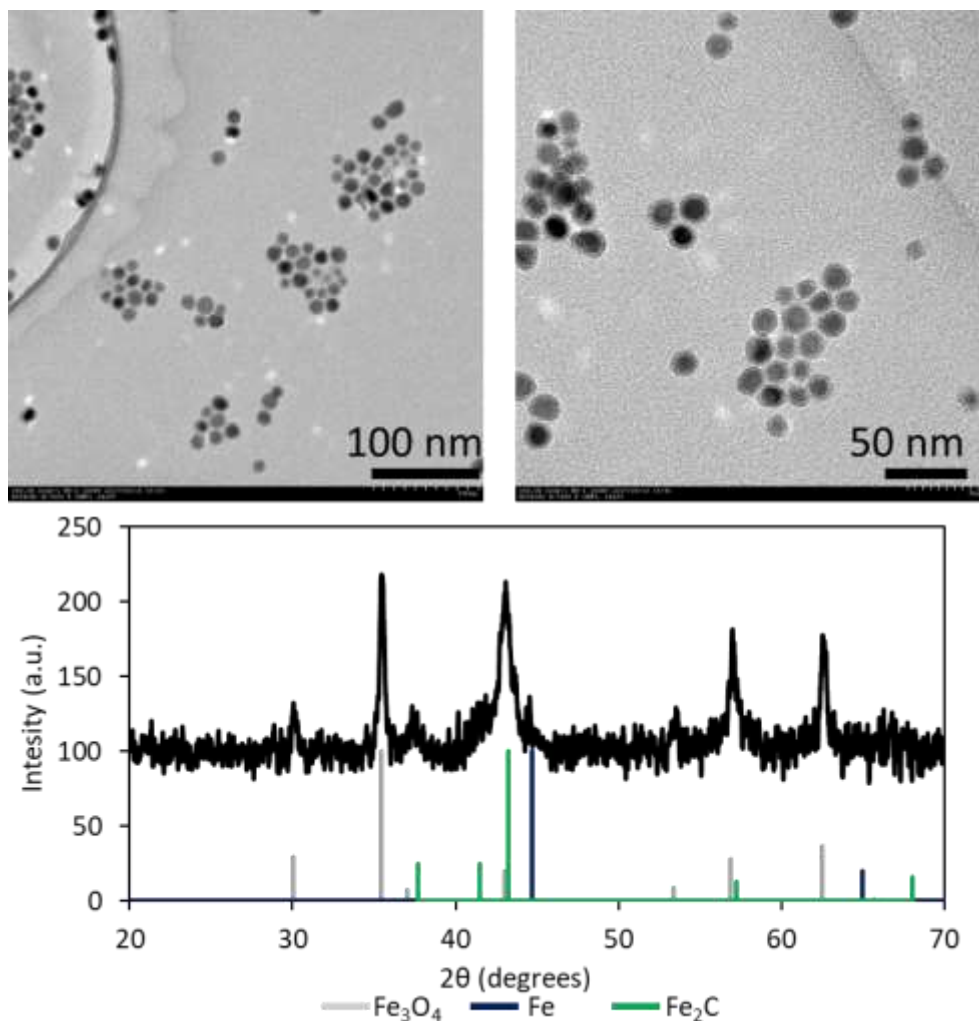


*Figure 4-6 Tem images at different magnification (top) and XRD pattern of FeC\_9 (bottom), obtained using HDA.*

The final sample, dispersed in chloroform, was centrifuged for 2 min at 3000 rpm. The black supernatant was separated from the black precipitate and in both cases XRD and TEM analysis were performed (Figure 4.7). A similar experiment was attempted also with samples obtained with OAm, however the amount of sample recovered from the supernatant was never enough to produce a clear XRD pattern. In this case, instead, the XRD shows that material recovered in the supernatant was made solely of Fe<sub>2</sub>C, while the precipitate was composed of big particles made of iron oxide. The size of the Fe<sub>2</sub>O<sub>3</sub>/Fe<sub>3</sub>O<sub>4</sub> crystallite was estimated to be 25 nm, considering the most intense peak at  $2\theta = 35.5^\circ$  (311), while in the case of Fe<sub>2</sub>C the crystallite size

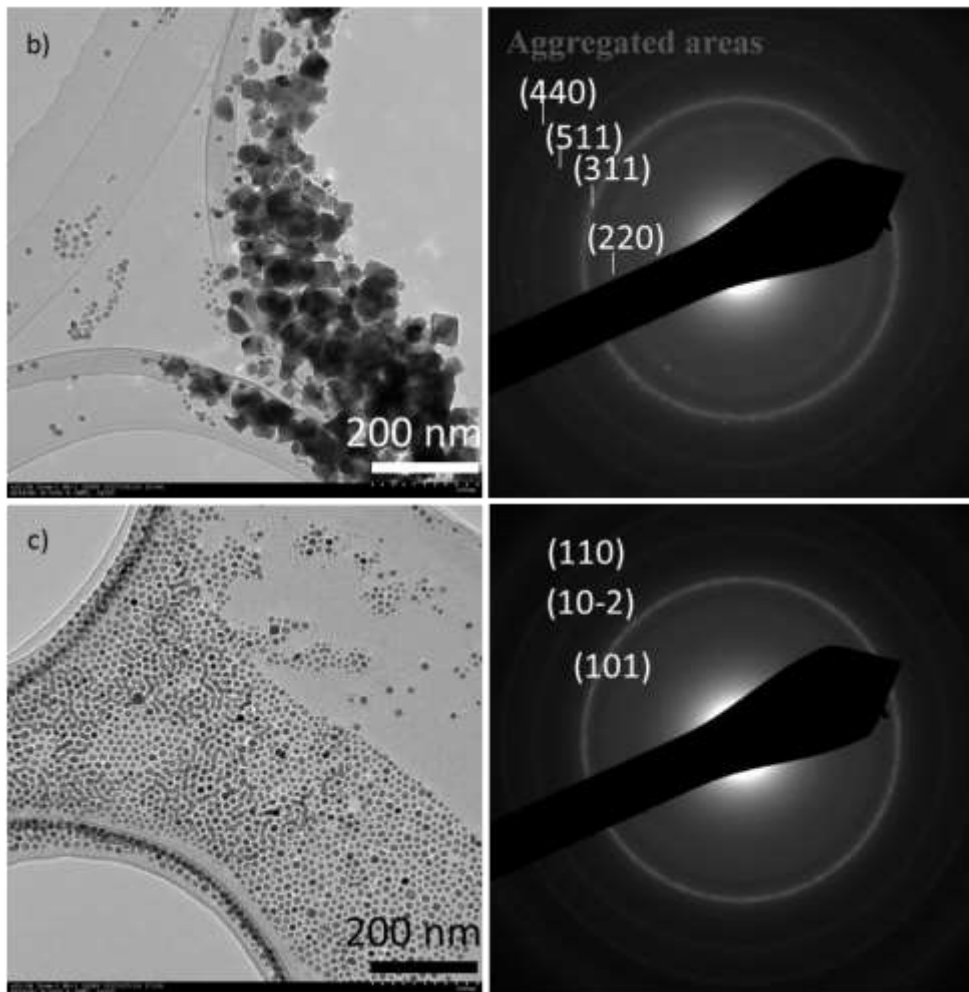
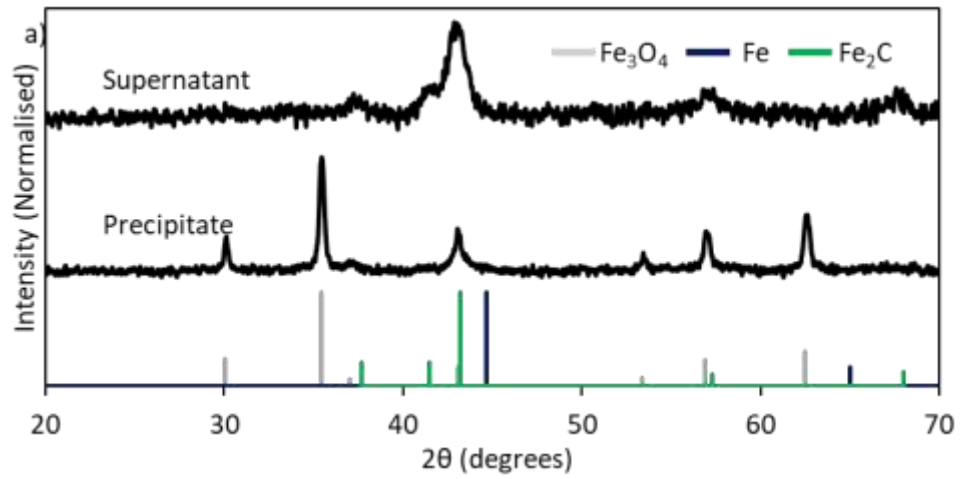


Figure 4-7 a) XRD pattern of FeC<sub>9</sub> after centrifugation where the sample from the supernatant and the precipitate were analysed. b) TEM and ED pattern of the sample from precipitate and c) TEM and ED pattern of the sample from supernatant.

was estimated to be 7.2 nm by fitting the two peaks at  $2\theta = 43.2^\circ$  (101) and  $2\theta = 41.5^\circ$  (002). Similarly, the TEM analysis shows that the precipitate sample was made of aggregated material with irregular shape, next to some small core@shell NPs. The electron diffraction pattern confirms that the phase of the material was iron oxide ( $\text{Fe}_3\text{O}_4/\text{Fe}_2\text{O}_3$ ). The TEM image and the relative electron diffraction pattern of the supernatant (Figure 4.7 c) confirmed that the NPs were made of  $\text{Fe}_2\text{C}$  phase.

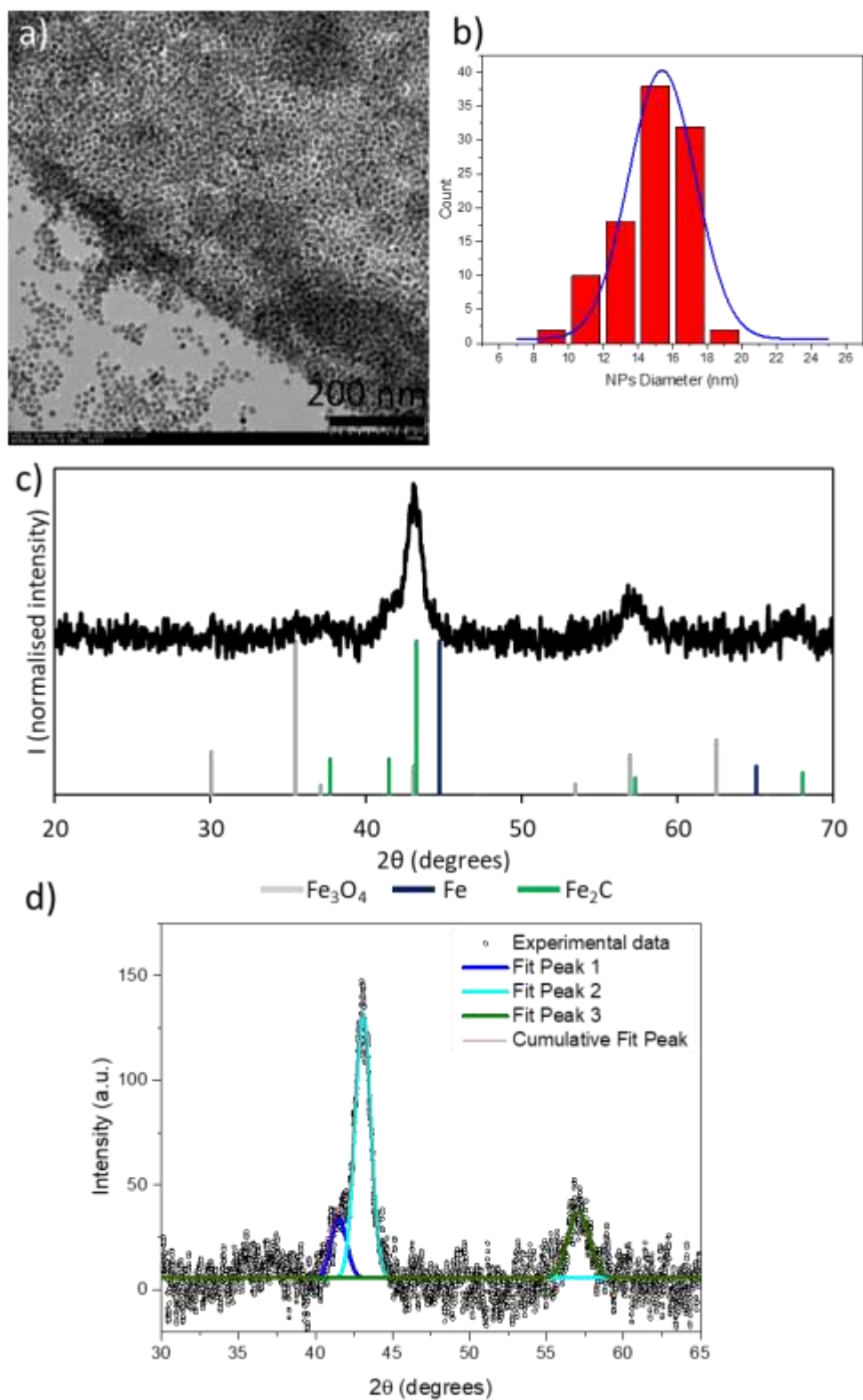


Figure 4-8 a) TEM images of Fe<sub>3</sub>C<sub>10</sub> sample using 3 mmol of ODA, and b) relative size distribution plot. c) XRD pattern of the same sample with relative fitting of the spectra matching the pattern of Fe<sub>2</sub>C phase (JSPC PDF No. 00-036-1249)

Figure 4.8 shows the TEM images and XRD pattern of FeC\_10 sample, when NPs were obtained by replacing HDA with ODA. The TEM images show spherical NPs with a core@shell structure. The average size was  $14.8 \pm 2.2$  nm, with a core diameter of  $9.4 \pm 1.5$  nm. The XRD pattern shows that the NPs phase was Fe<sub>2</sub>C, with the main peaks observed attributed to IC NPs and no iron oxide structure was detected. The average size of Fe<sub>2</sub>C crystallites were found to be 7.6 nm by fitting the two peaks at  $2\theta = 43.2^\circ$  (101) and  $2\theta = 41.5^\circ$  (002). The value is close to the diameter of the core for the core@shell structure measured via TEM, suggesting that the carbide phase was single-crystalline.

The results showed that ODA was the most suitable surfactant for the synthesis of pure IC NPs, among the other amines tested here, leading to IC NPs with no sign of aggregation and presence of undesired iron oxide secondary phase. A possible explanation is that OAm, having the double bond may be more prone towards degradation process when the temperature is increased compared to linear amine like HDA or ODA, leading to an inferior control. Also, longer the chain and more thermally stable amines are,<sup>172</sup> therefore ODA was chosen as ligand to produce uniform Fe<sub>2</sub>C NPs.

#### 4.3.1.3 Tracking the phase transformation

The phase transformation of  $\alpha$ -Fe into Fe<sub>2</sub>C was monitored through ED and TEM characterisation. Three reactions were repeated, where one was stopped at 180 °C, and the other two were stopped after 5 min and 15 min of the carbidization process at 260 °C. Figure 4.9 shows the TEM images and the relative ED patterns of the sample at different temperatures and time. After 30 min at 180 °C the NPs have round and irregular shape, with an average diameter of  $14.6 \pm 1.0$  nm (4.19 top). Five minutes after the solution reaches 260 °C, the NPs have a more regular shape, and an average diameter of  $14.2 \pm 1.5$  (Figure 4.9 middle). Also, the ED pattern differs significantly from the previous one related to the NPs at 180 °C. The NPs at 260 °C after 15 min

show a similar diffraction pattern to the one after 5 min, with an average diameter of  $14.8 \pm 2.2$  nm (Figure 4.9 bottom). This suggests that the NPs underwent quickly a phase rearrangement once the solution reached 260 °C. In Figure 4.10 the electron diffraction patterns were converted in terms of d-spacing (Å) using PASAD software, able to integrate the circular electron diffraction pattern and convert it into 2D pattern. This allows for the matching of the experimental phase profile with the reference patterns from the literature, which were also converted in terms of d-spacing. The data show the transition from  $\alpha$ -Fe to Fe<sub>2</sub>C within 5 min of annealing of NPs at 260°C. Interestingly, in Fe NPs electron diffraction pattern, a broad peak can be detected around 2.5 Å which could be matched with the iron oxide phase present in the shell, formed once the NPs are exposed to the air. The same peak is not detected in the electron diffraction profile of NPs annealed at 260 °C.

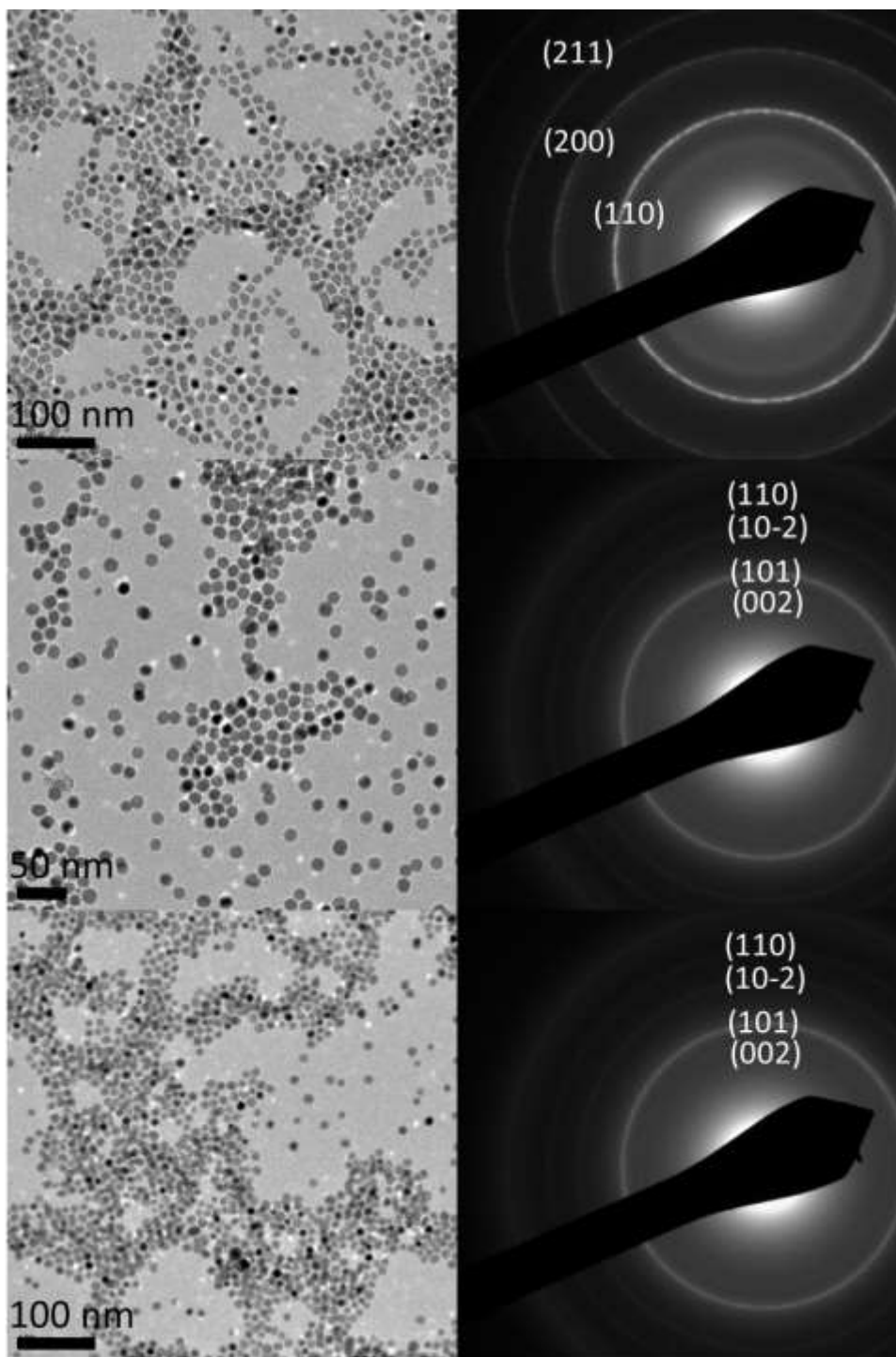


*Figure 4-9 TEM images with the relative ED pattern of Fe NPs (top), Fe<sub>2</sub>C NPs after 5 min at 260 °C (middle) and Fe<sub>2</sub>C NPs after 15 min at 260 °C (bottom).*

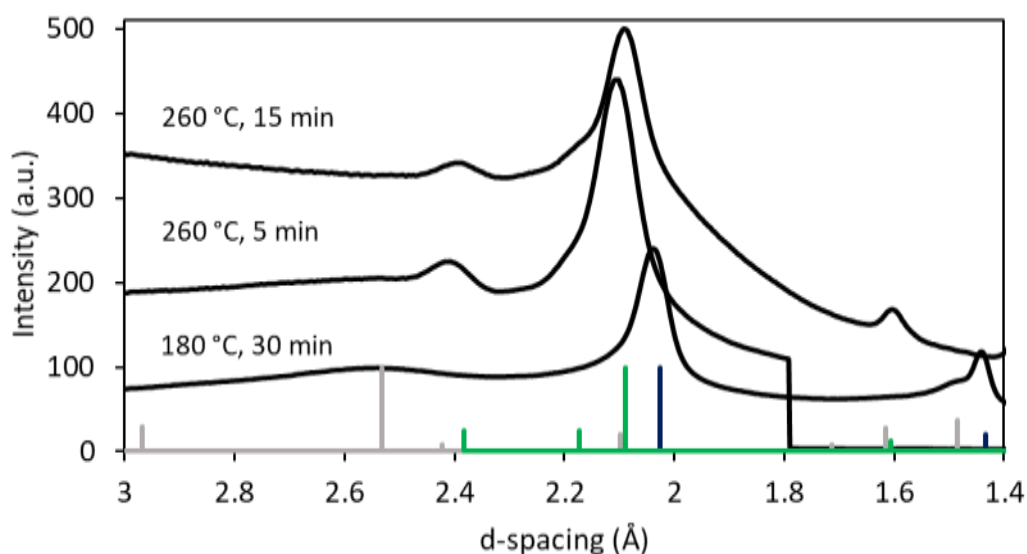


*Figure 4-10 Integrated ED patterns of Fe and Fe<sub>2</sub>C NPs and plotted in terms of d-spacing.*

In conclusions, the best conditions used were 0.05 mmol of chloride and 3 mmol of ODA, in 10 ml of ODE with a reaction time of 15 min at 260 °C. They were able to fully transform Fe NPs into Fe<sub>2</sub>C without the formation of secondary iron oxide phase.

#### 4.3.2 Characterisation of Fe<sub>2</sub>C nanoparticles

The best conditions used to form IC NPs were 0.05 mmol of chloride and 3 mmol of ODA, in 10 ml of ODE (sample FeC\_10). At 180 °C Fe(CO)<sub>5</sub> is injected and the solution was kept at this temperature to allow for the formation of Fe NPs. After, the solution was heated for 15 min at 260 °C to promote the formation of carbide phase. The IC NPs are here fully characterised.

Figure 4.11 (top) shows the high-resolution HAADF-STEM image of the sample and it confirms the NPs have a distinct core@shell structure with a darker shell surrounding a brighter core. The brighter contrast in the shell confirms that there is a denser phase in the core and it can be associated to the Fe<sub>2</sub>C crystal structure. The NPs feature a clear void between the core and the shell, which was not detected in the case of

Fe@Fe<sub>x</sub>O<sub>y</sub> NPs. In Figure 4.11 (bottom), lattice spacings of 2.4 Å, 2.0 Å and 1.5 Å was measured in the core region, which corresponds

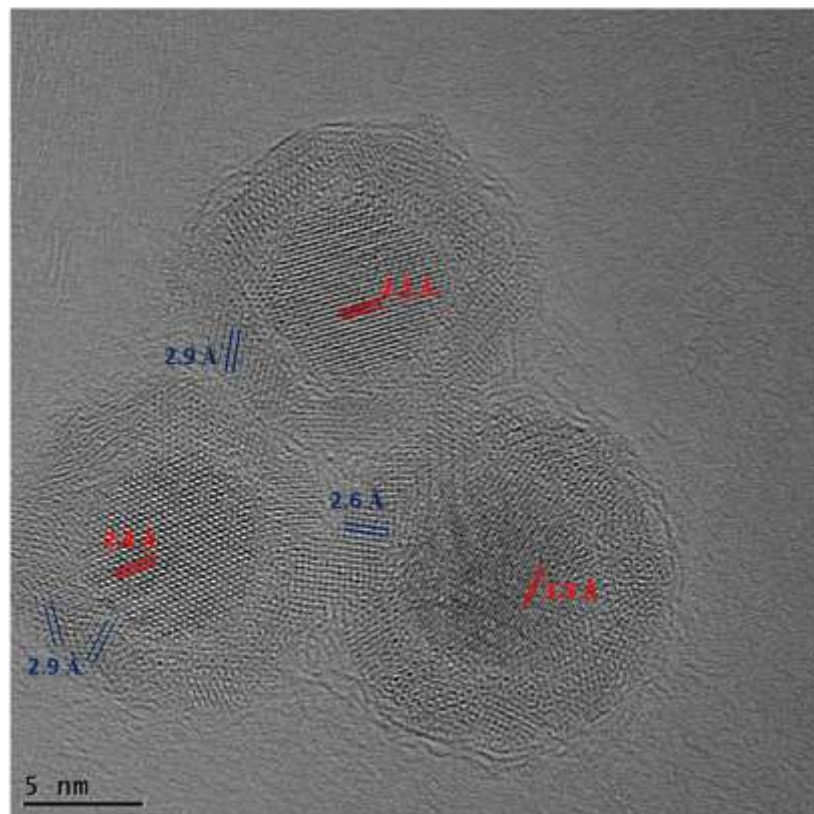
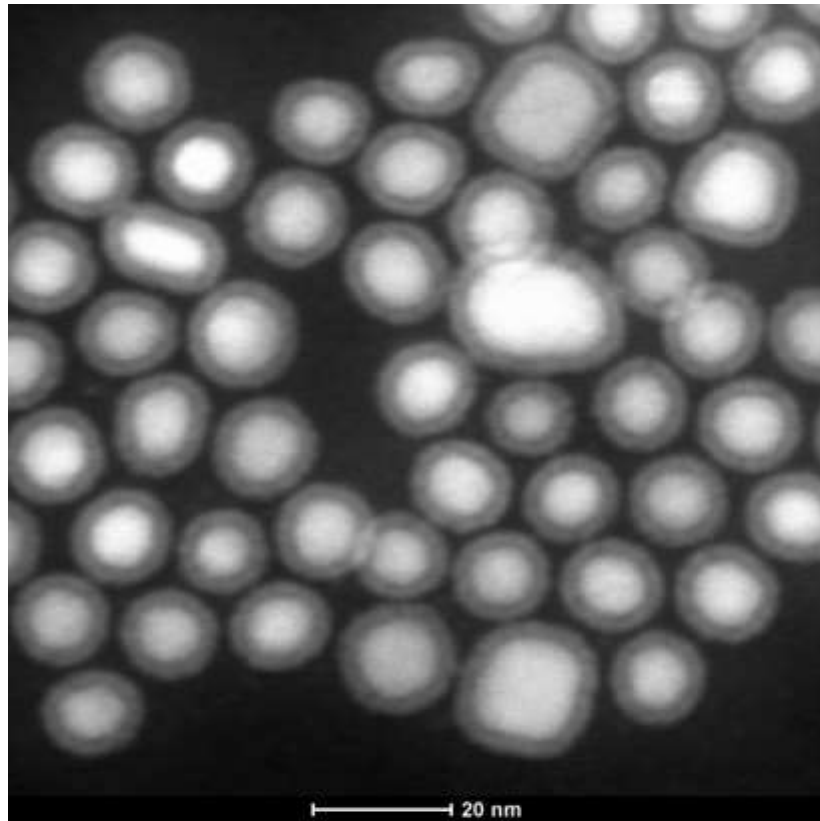


*Figure 4-11 HR-TEM image (top) with lattice spacing of  $\text{Fe}_3\text{O}_4/\text{Fe}_2\text{O}_3$  in blue and  $\text{Fe}_2\text{C}$  in red and STEM-HAADF image (bottom) of IC NPs.*

to the (101), (100) and (110) spacings of the  $\text{Fe}_2\text{C}$  phase, respectively. Moreover, the core area was found to be monocrystalline. On the other hand, the shell region appeared heterogeneous and attempts to measure the lattice spacing of some of the areas within the shell region led to the values 2.9 Å and 2.6 Å. These values match the (220) and (311) spacings of iron oxide phases like  $\text{Fe}_3\text{O}_4$  or  $\gamma\text{-Fe}_2\text{O}_3$ . It is likely that the shell is made of small polycrystalline oxidised domains formed via the lattice expansion that occurs upon oxidation from  $\text{Fe}_2\text{C}$  to the inverse spinel structure of  $\text{Fe}_3\text{O}_4/\gamma\text{-Fe}_2\text{O}_3$ . In addition, the shell was found to be polycrystalline in nature. Amorphous material was also detected in the shell area and therefore could not be matched with any phase.

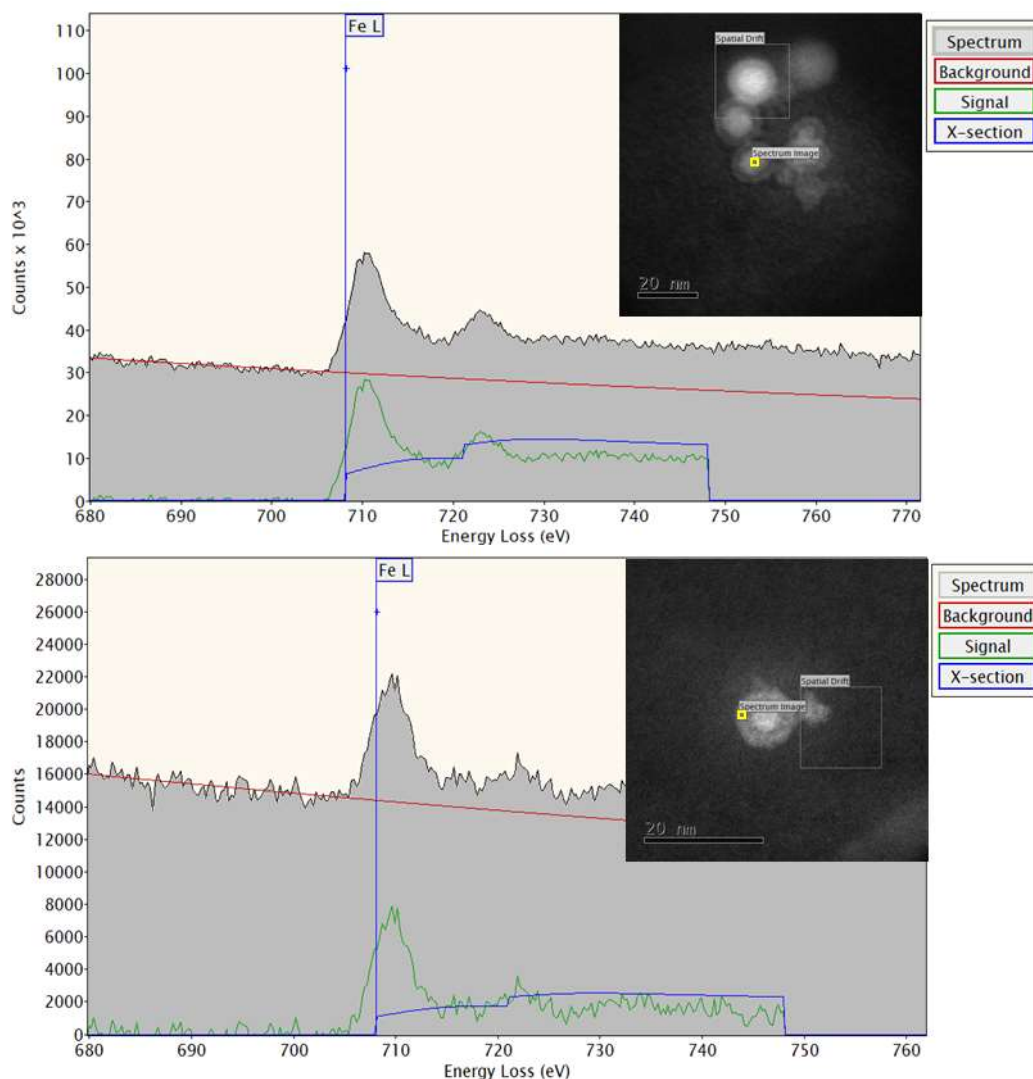


*Figure 4-12 EELS spectrum of the Fe edge on Fe<sub>2</sub>C NPs with relative area analysed underlined in yellow. The signal comes from the core (top) and from the shell area (bottom).*

EELS spectrum of the core and shell portions of NPs were taken, focusing on the Fe edge in the EELS spectrum (Figure 4.12). The Fe signal is usually characterised by two peaks, next to each other with about 12 eV difference, where the peak at lower energy (~710 eV) has a higher intensity compared to the other at higher eV (~722).<sup>173</sup> Both peaks can be detected in the core and the shell area, confirming the presence of Fe species in both NPs portions. Moreover, EELS provides information on the chemistry of the species in the sample. From [www.eelsdb.eu](http://www.eelsdb.eu) (web database of EELS spectra of several materials) it was possible to retrieve reference spectra to compare

with the experimental data. In the case of metallic Fe ( $\alpha$ -Fe used as reference), the ratio of the intensity between the first peak at 210 eV and the second one at 722 eV is 1.8 while, in the case of oxidised Fe atoms the value is 3 ( $\text{Fe}_2\text{O}_3$  used as reference). The measured value for the intensity ratio coming from the core of the NPs was 1.9, which was very close to the value from the literature. The state of Fe in  $\text{Fe}_2\text{C}$  is still in its metallic state, thus the value is expected to be close to the one of  $\alpha$ -Fe. On the other hand, the value obtained from the shell was 2.6, which is close to the value reported for oxidised Fe species confirming the formation of a shell made of iron oxide. Attempts of measuring the carbon signal from the carbon-rich areas were performed, however when the sample holder was switched from the carbon-based grid to the boron nitride one, the stability of the sample under the electron beam was greatly affected, with the sample quickly degrading during the analysis. Therefore, no information on the Carbon species could be obtained from the EELS analysis.

The IC NPs were further characterised *via* XPS, analysing the signal coming from Fe and C atoms in the NPs. As comparison, the measurement was also performed on  $\text{Fe}@\text{Fe}_x\text{O}_y$  NPs. In Figure 4.13, the spectra coming from the Fe 2p orbital of Fe atoms in both samples are shown. Typically, in XPS experiments, due to the symmetry of the orbital, the signal from Fe 2p is split in Fe 2p  $\frac{1}{2}$ , located at higher energies, and Fe 2p  $\frac{3}{4}$  at lower energies. Both states provide the same kind of information on the chemical state of Fe atoms in the sample. However, the 2p  $\frac{1}{2}$  state has a double probability of being occupied by electrons compared to the Fe 2p  $\frac{3}{4}$  and this translates into the signal from Fe 2p  $\frac{1}{2}$  state to be double the one from Fe 2p  $\frac{3}{4}$ . Moreover, the difference in energy between the two states is known to be  $\sim 13.2$  eV.<sup>2</sup> The ratio between areas and the energy delta are used to deconvolute the spectrum obtained from XPS analysis into the different chemical species present in the NPs. For the deconvolution of  $\text{Fe}@\text{Fe}_x\text{O}_y$  NPs spectrum, five different Fe species such as  $\text{Fe}^0$ ,  $\text{Fe}^{2+}$ ,  $\text{Fe}^{3+}$ , high-binding energy surface structures, and satellite peaks were used for both Fe 2p  $\frac{1}{2}$  and Fe 2p  $\frac{3}{4}$ .<sup>174</sup>

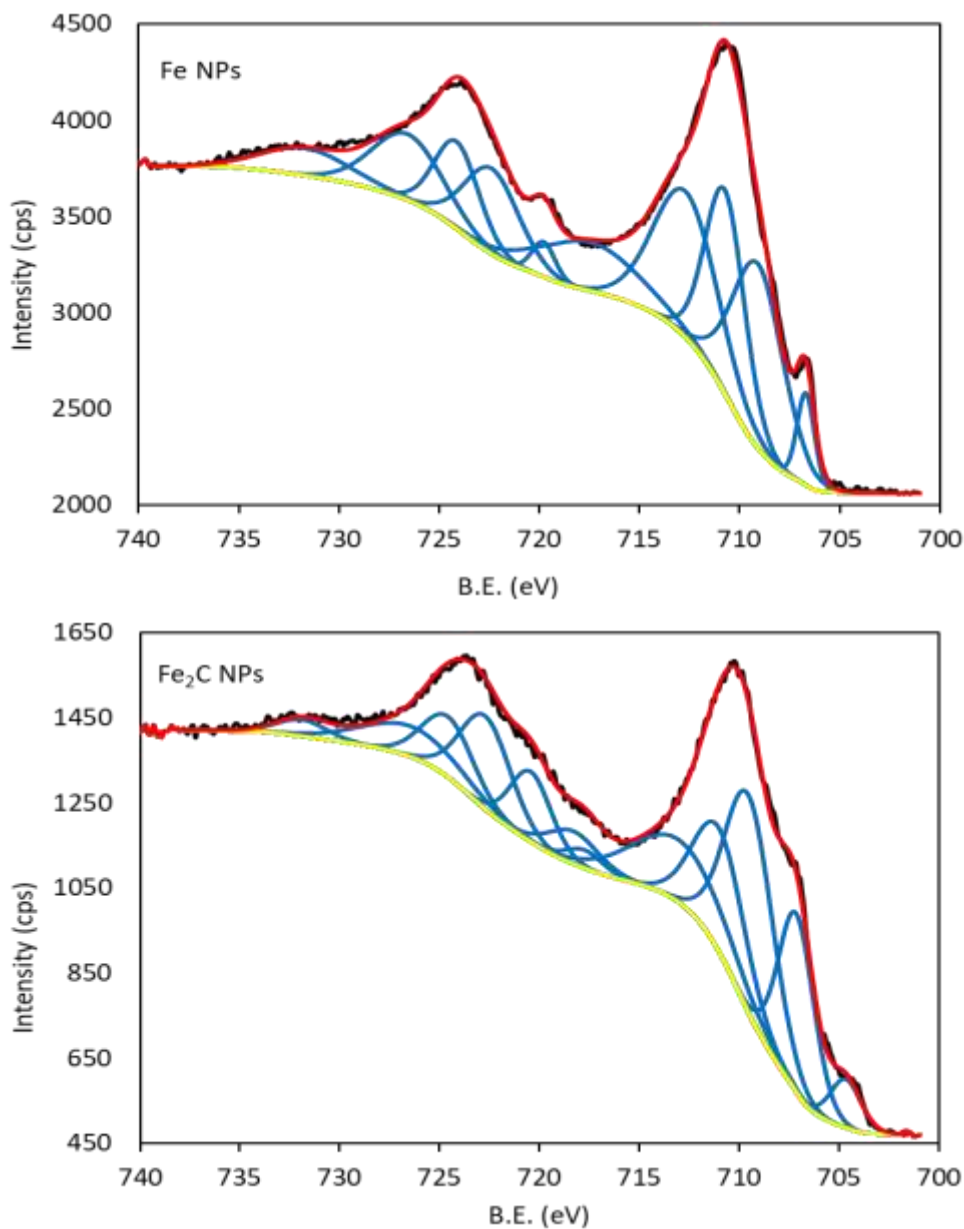


*Figure 4-13 Fe2p core level XPS for Fe NPs (top) and Fe<sub>2</sub>C NPs (bottom). Black, yellow, blue, and red curves represent raw data, Shirley background, deconvoluted peaks and the sum of the components, respectively.*

The IC NPs were fitted using the same species plus an extra species appearing in the spectrum at around 704 eV was added. Therefore, in the case of Fe<sub>2</sub>C nanoparticles a sixth couple of peaks were added to fit the spectrum. For Fe NPs the parameters

used for the fit of the Fe 2p spectrum are shown in Table 4.3. From the area of each peak the percentage of each component ( $\text{Fe}^0$ ,  $\text{Fe}^{2+}$  and  $\text{Fe}^{3+}$ ) was estimated.

*Table 4-3 Fit parameters for Fe NPs XPS Fe2p spectrum and calculated proportion of the species present.*

Component	BE $2p_{3/2}$ [eV] (FWHM)	BE $2p_{1/2}$ [eV] (FWHM)	BE ( $2p_{1/2}$ - $2p_{3/2}$ ) [eV]	Spin-orbit intensity ratio	Proportion (%)
$\text{Fe}^0$	706.7 (1.0)	719.8 (1.3)	13.1	2.0	8.5
$\text{Fe}^{2+}$	709.1 (3.0)	722.4 (3.2)	13.3	2.0	49.4
$\text{Fe}^{3+}$	710.7 (2.3)	724.1 (2.6)	13.4	2.1	42.1
Fe surface	712.7 (3.7)	726.6 (4.1)	13.9	2.0	-
Fe satellite	717.5 (5.8)	731.7 (5.1)	14.2	2.0	-

*Table 4-4 Fit parameters for  $\text{Fe}_2\text{C}$  NPs XPS Fe2p spectrum and calculated proportion of the species present.*

Component	BE $2p_{3/2}$ [eV] (FWHM)	BE $2p_{1/2}$ [eV] (FWHM)	BE ( $2p_{1/2}$ - $2p_{3/2}$ ) [eV]	Spin-orbit intensity ratio	Proportion (%)
Fe-C	704.6 (1.8)	717.7 (2.2)	13.1	2.2	6.1
$\text{Fe}^0$	707.1 (2.1)	720.4 (2.4)	13.3	2.2	25.7
$\text{Fe}^{2+}$	709.5 (2.8)	722.7 (2.9)	13.2	2.2	42.0
$\text{Fe}^{3+}$	711.0 (3.0)	724.6 (3.0)	13.6	2.0	26.2
Fe surface	713.0 (5.5)	726.5 (5.7)	13.5	2.0	-
Fe satellite	718.3 (3.0)	731.9 (3.0)	13.6	2.0	-

For Fe NPs, the  $\text{Fe}^0$  component was associated with the  $\alpha$ -Fe phase present in the core of NPs and it accounted for the 8.5% of the sample. The rest was made of iron oxide species and the presence of both  $\text{Fe}^{2+}$  and  $\text{Fe}^{3+}$  species was associated to a

mixture of magnetite ( $\text{Fe}_3\text{O}_4$ ) and maghemite ( $\text{Fe}_2\text{O}_3$ ) phase located in the shell area. The high percentage of  $\text{Fe}^{2+}$  suggested that other iron oxides phases like wurtzite ( $\text{FeO}$ ) may be present. In the case of IC NPs, Table 4.4 shows the parameter used for the fitting of the spectrum. The peak coming from  $\text{Fe}^0$  species accounts for almost 26 % of the whole sample. In  $\text{Fe}_2\text{C}$  the Fe atoms retain a metallic state, and no  $\alpha$ -Fe phase was detected from the XRD analysis of  $\text{Fe}_2\text{C}$  NPs, thus the  $\text{Fe}^0$  from the XPS analysis of IC was attributed to the  $\text{Fe}_2\text{C}$  phase located in the core of the NPs.<sup>74</sup> The peak at 704.6 eV was harder to index because no similar values were reported in the literature for Fe species. However, the binding energy was lower than  $\text{Fe}^0$  suggesting that the species was closer to the metallic state rather than the oxide one, and it possibly differed from the  $\text{Fe}^0$  species because of a different C-Fe composition or a different crystallinity.<sup>175</sup> If also the latter component (called "Fe-C" in Table 4.4) was considered in the estimation of the iron carbide phase, the percentage reaches 32 %, which is more than three times the percentage of metallic Fe present in the  $\text{Fe}@Fe_xO_y$  NPs. This proved that the  $\text{Fe}_2\text{C}@Fe_xO_y\text{-C}$ , were more resilient to oxidation than  $\text{Fe}@Fe_xO_y$ , which is highly desirable for their use in biomedical applications.

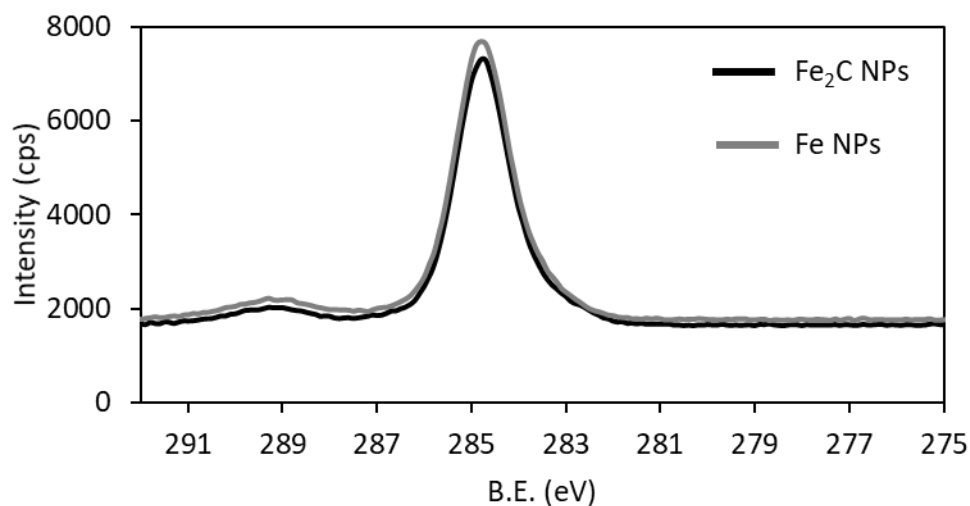


*Figure 4-14 C1s core level XPS spectra for Fe NPs (grey) and Fe<sub>2</sub>C NPs (black).*

On Figure 4.14 the 1s Carbon spectra for the two samples are shown. The spectra were recorded using an Al foil substrate to enhance the Carbon signal coming from the sample. No difference was observed between the two samples. A possible explanation was that C spectra on XPS are always affected by adventitious carbon contaminations that get adsorbed on the surface of the sample. Being XPS a surface-sensitive technique, the contaminations may hide the weaker signal coming from the carbon present in the inner part of the sample.

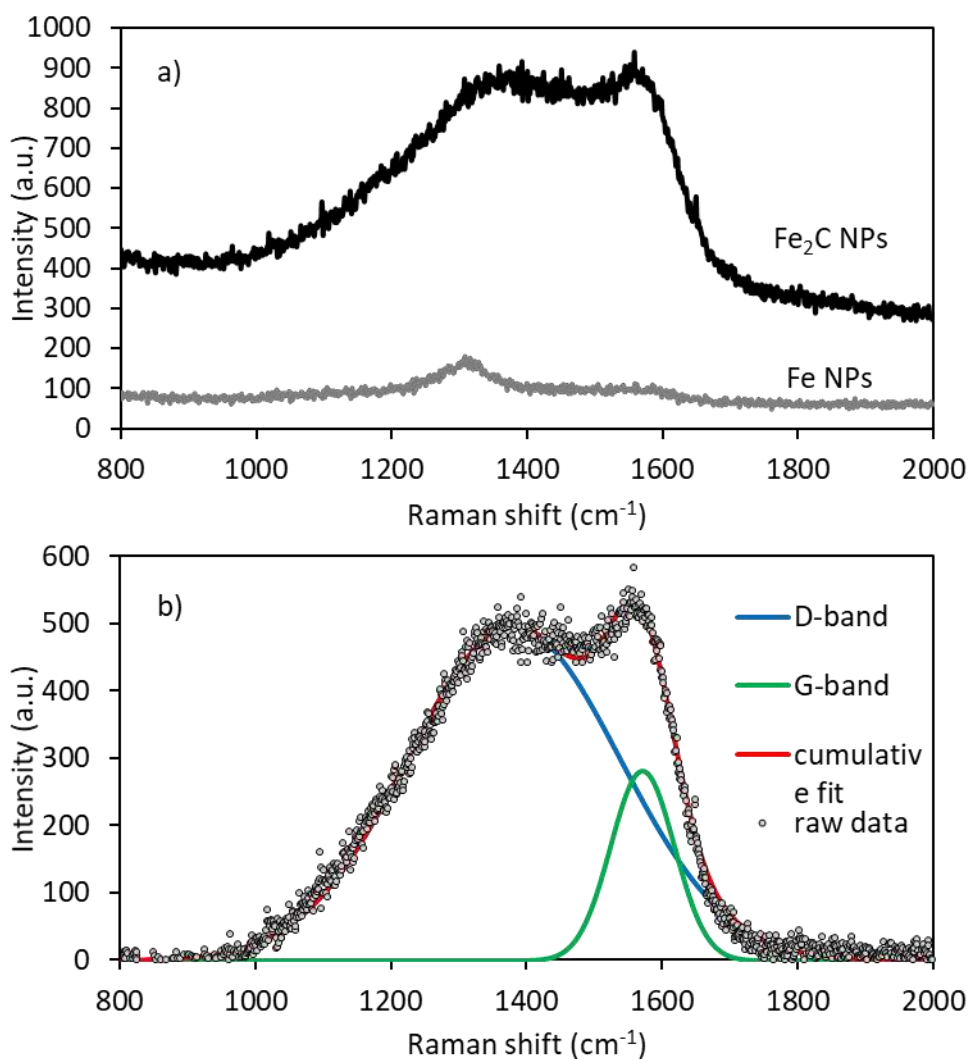


Figure 4-15 a) Raman spectrum of Fe NPs and Fe<sub>2</sub>C NPs. b) Best fit of the Raman spectrum for Fe<sub>2</sub>C NPs.

To investigate further the carbon component of the Fe<sub>2</sub>C@Fe<sub>x</sub>O<sub>y</sub>, Raman spectroscopy was used due to the high sensitivity of this technique to carbon-based materials. In Figure 4.15 a, the Raman spectra of Fe and Fe<sub>2</sub>C NPs are shown.

The Fe<sub>2</sub>C spectrum was characterised by a broad peak area which was distinctly more intense than the Fe spectrum, confirming the presence of C in the Fe<sub>2</sub>C structure. Figure 4.15 b shows the best fit of the data coming from Fe<sub>2</sub>C NPs. The sample was characterised by two peaks, one at 1571 cm<sup>-1</sup> (corresponding to G-band) and the other at 1378 cm<sup>-1</sup> (D-band). The D-band relates to the disordered structure of sp<sup>2</sup>-

hybridised carbon system; it is usually associated to the presence of defects in the graphitic structure and the broadness of the peak suggests that the phase was amorphous<sup>30,176</sup>. The G-band, instead, arises from the stretching of the C-C bond in graphitic materials. The spectrum showed the coexistence of both crystalline and amorphous carbon in the structure. If also the results from the HR-TEM analysis are taken into account, where amorphous material was detected in the shell area, it was hypothesised that the amorphous carbon detected in Raman spectroscopy could be located in the shell while the signal of the crystalline carbon structure arises from the core of the NPs.

To determine and confirm which iron phases are present in the final structure, Mossbauer spectroscopy was performed on Fe<sub>2</sub>C NPs. The technique is based on the Mossbauer effect which consists in the resonant absorption and emission of  $\gamma$ -ray in solids. Mossbauer is very sensitive to the chemical environment of each atom, potentially allowing to detect all the different iron-based phases present in the NPs. The measurement and the fitting were carried out by Dr Lara Bogart from UCL, Department of Chemistry. Figure 4.16 shows the <sup>57</sup>Fe Mossbauer Spectrum on the Fe<sub>2</sub>C and the relative fit. The parameters used for the fitting are listed in Table 4.5.

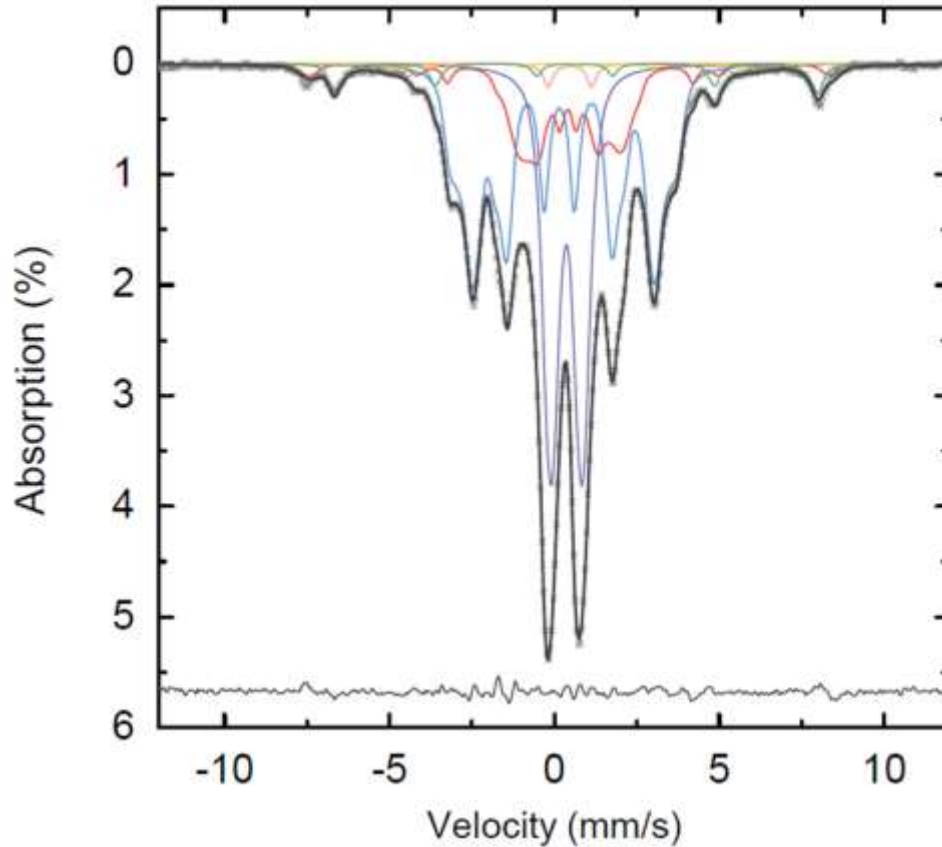


*Figure 4-16 Room temperature Mossbauer spectrum for Fe<sub>2</sub>C NPs. The best fit was obtained using a superposition of two Voigtian doublets and four Voigtian sextets. The residual to the measured data is indicated.*

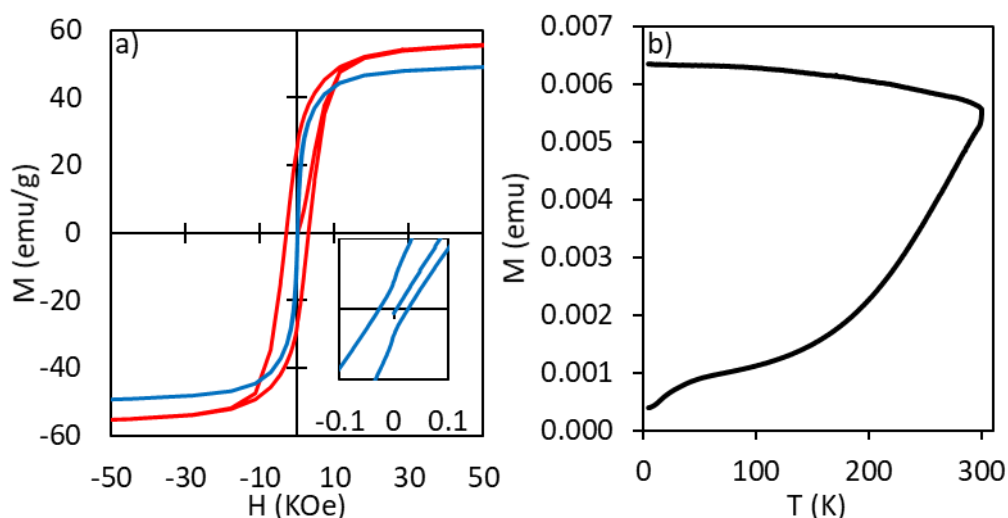
The spectrum is a superposition of at least 4 sextets and a quadrupole doublet which was indicative of a range of chemical composition. A range of different particles size can also originate multiple fitting curves but, given the previous characterisation, this was excluded. Voigtian line shapes have been used to represent a Gaussian distribution of Lorentzian lines, which physically arises from a range in size, shape, chemical composition and crystallinity within the sample.

Table 4-5 Best fit parameters for the room temperature Mossbauer spectrum presented in Figure 4.16

$\delta$ (mm/s)	Q (mm/s)	$\epsilon$ (mm/s)	H (kOe)	w3 (mm/s)	Relative area (%)	Assigned species	
0.366 ± 0.002	0.9443 ± 0.0007	-	-	0.17	30.3	Amorphous Fe <sup>3+</sup>	
0.47 ± 0.03	1.31 ± 0.05	-	-		1.2		
0.217 ± 0.002	-	0.065 ± 0.002	170; $\sigma=10$		70.6	44.5	Fe <sub>2</sub> C
			197; $\sigma=2$		7.2		
			213; $\sigma=6$		22.2		
0.447 ± 0.006	-	0.03 ± 0.03	96; $\sigma=16$		80.0	19.1	Mixture of ferric oxide and Fe-C alloy
			230; $\sigma=0.1$		9.2		
			490; $\sigma=13$	10.8			
0.64 ± 0.01	-	0.02 ± 0.02	442; $\sigma=9$	30.0	3.8	Ferric oxide	
			455; $\sigma=3$	70.0			
0.2 ± 0.1	-	0.4 ± 0.1	335; $\sigma=30$		1.1	$\alpha$ -Fe	

The best fit to the spectrum showed that the sample comprises amorphous paramagnetic Fe<sup>3+</sup> (~30 %) and iron carbide alloy (~45 %), iron carbide-oxide (~19 %) and trace amounts of iron oxide and  $\alpha$ -Fe. Combining these results with the other techniques we can conclude that the core was made of iron carbide (Fe<sub>2</sub>C), with

traces of  $\alpha$ -Fe left unreacted. Moving from the core towards the outer layers, a mixture of ferric oxide and Fe-C alloy appears, possibly at the interface between the core and the shell. Finally, the shell is composed of amorphous areas along with some small crystalline iron oxide smaller portions which is consistent with the HRTEM images of Fe<sub>2</sub>C NPs.



*Figure 4-17 a) Magnetic hysteresis loop taken at 300 K (blue line) and 5 K (red line) with relative zoom in at low fields; b) ZFC-FC curve taken with  $H = 100$  Oe.*

The magnetic properties of the IC NPs were analysed via SQUID-VSM. Figure 4.17 a shows the hysteresis loops at 300 K and 5 K. The  $M_s$  value at 5 K is 57 emu/g while at 300 K is 50 emu/g. The  $M_s$  is lower than Fe NPs of similar size (109 emu/g). When the  $M_s$  was normalised for the amount of Fe in the sample, the value increased to 105 emu/g<sub>Fe</sub> which was closer to the one of Fe NPs and higher than magnetite-based NPs.<sup>20</sup> The coercivity of IC NPs of 30 Oe at 300 K indicates that the NPs are in a quasi-superparamagnetic state and the coercivity values is smaller than the coercivity found for Fe NPs (around 150 Oe). Figure 4.17 b shows the ZFC-FC curves of the IC NPs. The two curves confirm that the NPs are blocked at room temperature, with the curves meeting after 300 K. The curve shows no sign of polydispersity in size or phase present in the sample.

### 4.3.3 Ligand exchange and magnetic hyperthermia

The as-synthesised NPs are coated with octadecylamine, which makes them insoluble in polar solution. To make the Fe<sub>2</sub>C NPs soluble in water, the native ligand on the surface was exchanged with the dopamine-functionalised PIMA polymer developed in the previous chapter. Once exchanged, the polymer would make the particles water-soluble and provide the colloidal stability necessary for the use of NPs in biomedical applications. The procedure followed was the same used in the case of Fe NPs in Chapter 3.4.4 (Ligand exchange with Mod PIMA-Dopa).

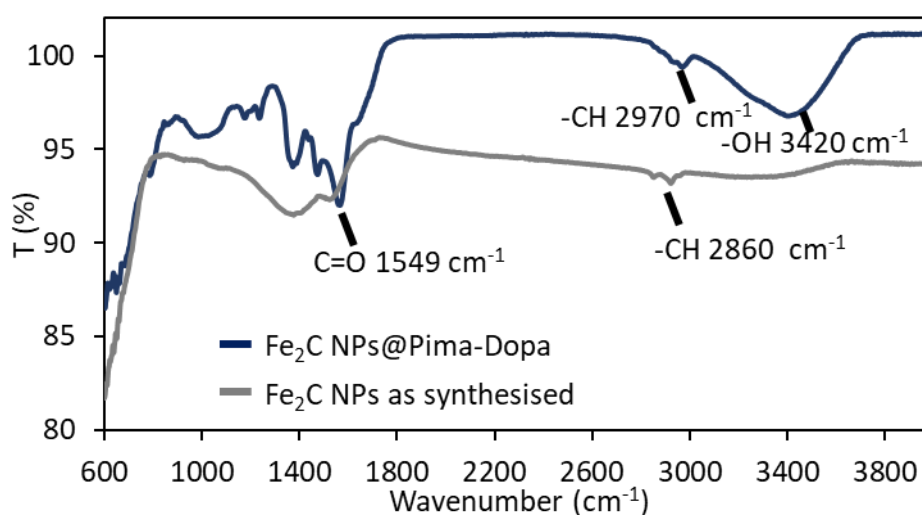


*Figure 4-18 FTIR spectrum of Fe<sub>2</sub>C NPs with grey line indicating the as-synthesised NPs and the blue line indicating the NPs after ligand exchange.*

Figure 4.18 shows the FTIR spectra of Fe<sub>2</sub>C NPs before and after the ligand exchange process. In the curve of the as-synthesised NPs, the most distinctive peak is at 2860 cm<sup>-1</sup> corresponding to the -CH- stretching from the ODA chains present on the surface of the NPs. After the ligand exchange process, different peaks appeared such as the one at 1550 cm<sup>-1</sup>, assigned to C=O stretching, and the one at 3420 cm<sup>-1</sup>, assigned to -O-H vibration. This was consistent with the final structure of the polymer which consists of several carboxylic groups. The peak at 2970 cm<sup>-1</sup>, corresponding to -CH

vibration, was associated with the two methyl groups present in each monomer of the polymer.

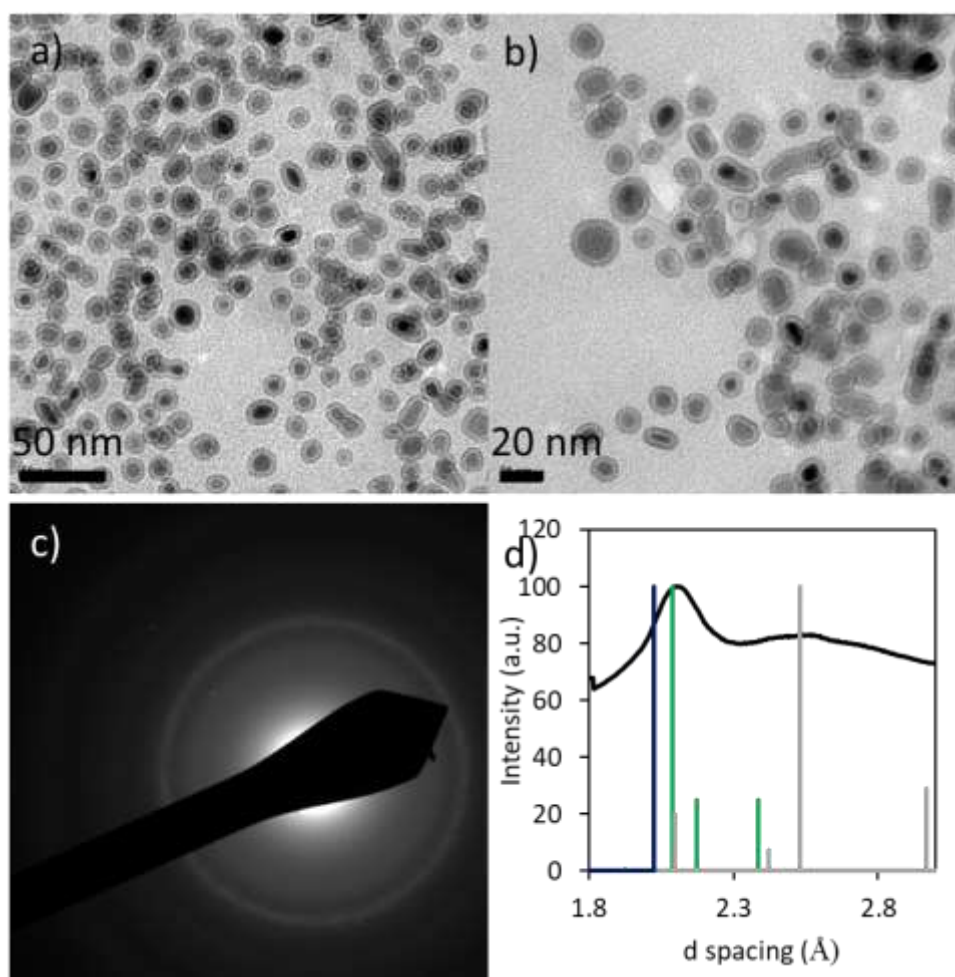


*Figure 4-19 a) TEM images of Fe<sub>2</sub>C NPs after ligand exchange at lower b) and higher magnification. c) Electron diffraction pattern is shown and d) the relative plot in terms of d-spacing is compared with  $\alpha$ -Fe (blue), Fe<sub>2</sub>C (green) and Fe<sub>3</sub>O<sub>4</sub> (grey) patterns.*

Figure 4.19 a and b show the TEM images of the sample after the ligand exchange process with modified-PIMA-Dopa at low and high magnification respectively. The core-shell structure was retained, showing that the particles are more resilient to oxidation in water/ligand exchange compared to Fe NPs of similar size (Chapter 3, Figure 3.31). Figure 4.19 c and d show the ED pattern and relative plot in terms of d-spacing confirming the presence of Fe<sub>2</sub>C phase in the core of the particle.

Finally, to test the heating potential of Fe<sub>2</sub>C, hyperthermia measurements were performed. Table 4.6 shows the measurement done at different frequency and field amplitude and the performance measured in terms of SAR and ILP. Although a value of SAR = 161 Wg<sup>-1</sup> was obtained, the relative ILP was of 0.6, which is lower than the value obtained with Fe NPs in the previous chapter. The ILP value obtained here for Fe<sub>2</sub>C NPs was also far from the value reported in the literature by Chaudret *et al.* for IC NPs which showed an ILP greater than 20 nHm<sup>2</sup> kg<sup>-1</sup>. The difference in heating performances may arise from the different conditions in which the two sets of NPs were tested. Indeed, Chaudret *et al.* reached such value under vacuum condition, using as-synthesised IC NPs not exposed to oxidative agents such as air or water.<sup>101</sup> In a study published after the completion of this work, however, the same group published the performance in magnetic hyperthermia of the same IC NPs after being transferred in water. The ILP value obtained in this case also dropped significantly from 20 to 8 nHm<sup>2</sup> kg<sup>-1</sup>, but still retaining optimal heating performances.<sup>177</sup> The difference between their result and the ones here presented may be explained with another very recent work of the same group where they investigated how within the same reaction protocol, the washing of the NPs had a big impact on the final heating properties. When the nanoparticles surface was depleted of its ligands after extended washing, the particles were strongly and irreversibly agglomerated and, ultimately, cannot align in an alternating magnetic field, resulting in the absence of heating properties for these nanomaterials.<sup>178</sup> Control over the ligand's concentration on the surface of the NPs is therefore an important variable to investigate further in the future works to prepare IC NPs displaying a controllable and large heating power.

*Table 4-6 Magnetic hyperthermia measurements for Fe<sub>2</sub>C NPs and relative conditions used.*

Measurement	Freq (KHz)	Field (KA m <sup>-2</sup> )	SAR (W g <sup>-1</sup> )	ILP (nHm <sup>2</sup> kg <sup>-1</sup> )
1	488	24.2	161	0.6

---

2	303	24.2	106	0.6
---	-----	------	-----	-----

---

#### 4.4 Conclusion

In this chapter,  $\text{Fe}_2\text{C}@Fe_x\text{O}_y/\text{C}$  NPs were synthesised from Fe NPs following a carbidization process at high T and the optimal reaction conditions to produce uniform IC NPs were investigated. By using OAm as capping ligand and carbon source, a mixture of IC NPs and bulk-like iron oxide material was initially produced. By replacing the OAm with ODA, the formation of larger iron oxide particles was stopped. The nanocrystals formed are made of single crystals iron carbide phase with a good size distribution and once open to the air, the formation of an iron oxide/amorphous carbon shell occurred. The NPs were transferred in water using Mod-Dopa-PIMA without showing any sign of further oxidation, proving that the IC NPs are more resilient to oxidation compared to Fe NPs. The IC NPs were then tested as heating probes for magnetic hyperthermia. These results indicate a new avenue for producing stable nanoparticles with potential use in biomedical applications.

# Chapter 5 Shaped iron oxide nanoparticles for magnetic hyperthermia

## 5.1 Introduction

Anisotropic iron oxide-based NPs have shown great potential as heating probes in magnetic hyperthermia.<sup>56</sup> Several reasons have been accounted for that, among them is the fact that faceted morphology leads to a decrease in spin canting effect on the surface, compared to spherical particles of the same volume, leading to a larger magnetically active material.<sup>112</sup> Moreover, it has been shown both theoretically and experimentally that the arrangement of magnetic nanoparticles into 3D linear chains affects magnetic particle hyperthermia efficiency. In a recent work, compared to the non-aligned samples, magnetically aligned ones presented enhanced heating efficiency, increasing specific loss power value by a factor of two.<sup>179</sup> Dipolar interactions are responsible for the chain formation and these structures show uniaxial anisotropy along the chain promoting a collective behaviour under the external magnetic field, leading to an enhanced heating power.<sup>115</sup> Shaped NPs promote the formation of chain-like arrangements of NPs under a magnetic field.<sup>88</sup>

Syntheses of iron based NPs with different shapes such as spheres,<sup>180</sup> cubes,<sup>181</sup> worms,<sup>182</sup> stars,<sup>183</sup> rods,<sup>184</sup> octahedrons,<sup>185</sup> diamonds and prisms<sup>186</sup> have been already reported in the literature to date, especially for Fe<sub>3</sub>O<sub>4</sub> NPs. The degree of control on the NPs shape was often achieved through the decomposition of Fe(acac)<sub>3</sub> along with tuning of ratio of different ligands most commonly being oleic acid and sodium oleate.<sup>187</sup> Pellegrino *et al* found that in order to tune the shape and size of the desired nanocubes, many parameters had to be accurately controlled such the ratio of ligand to precursor, initial degassing step and heating rate of the reaction with their modification being not straightforward.<sup>24,112</sup> Zhao *et al* reported the formation of highly-magnetic octapod-shaped Fe<sub>3</sub>O<sub>4</sub> NPs adding NaCl in the reaction solution to shape the decomposition of iron-oleate in 1-Octadecene at 330°C.<sup>188</sup> While using NaOH and Na oleate instead of NaCl, they mainly formed a mixture of spherical and cubic iron oxide NPs, the octapod structure were also not obtained after using either NaF or KBr. They found that the chloride ions in the solution

reaction were critical for the formation of octapod iron oxide nanoparticles because possibly the chloride ions were selectively bound to iron ions exposed on the high-index facets (probably [311]) of iron oxide during the particle growth. Interestingly, they were also able to control the sizes of octapod nanoparticles by varying the reaction time in the presence of NaCl, which was a more straightforward aspect compared to the Pellegrino and potentially more reproducible. In the previous chapter the chloride source (i.e. Hexadecylammonium chloride) was used to form crystalline  $\alpha$ -Fe phase<sup>31</sup> but it only led to spherical NPs, possibly because a different iron precursor ( $\text{Fe}(\text{CO})_5$ ) was used. The use of different precursor should be evaluated.

Among the most common precursor for the synthesis of iron-based NPs,  $\text{Fe}(\text{acac})_3$  is a very stable and non-toxic precursor. In this molecule the Fe ion is in its oxidised state, thus a reducing agent is needed in the reaction solution to obtain Fe-based NPs. The double bond present in the molecular structure of OAm can act as a mild reducing agent.<sup>107</sup> Mohan *et al.* reported the production of metallic FePt alloys NPs using OAm as solvent, ligand and reducing agent with  $\text{Fe}(\text{acac})_3$  as precursor.<sup>174</sup> OAm is a weakly binding ligand and it does not prevent the formation of NPs if it is used in strong excess.<sup>189</sup> Therefore to attempt the formation of shaped Fe-based NPs,  $\text{Fe}(\text{acac})_3$  was decomposed in OAm, and in the presence of HDA-Cl which is investigated to promote the formation of shaped like NPs.

In this chapter, plate-like NPs made of iron oxide were synthesised using a novel synthetic procedure through the decomposition of  $\text{Fe}(\text{acac})_3$  in the presence of HDA-Cl. Finally, the NPs were transferred in water using the strategy developed in the 3<sup>rd</sup> chapter (with Mod-Dopa-PIMA), and the heating properties were evaluated.

## 5.2 Materials and method

### 5.2.1 Materials

1-Octadecene ( $C_{18}H_{36}$ , 90%), hexadecylamine ( $C_{16}H_{35}N$ , HDA, 90%), diethyl ether ( $Et_2O$ , anhydrous,  $\geq 99.7\%$ ), hydrochloric acid (HCl, 37%), oleylamine ( $C_{18}H_{37}N$ , OAm, 70%), iron(III) acetylacetonate ( $Fe(acac)_3$ , 99.9%), oleic acid ( $C_{18}H_{34}O_2$ , OA, 90%), sodium oleate (SO,  $Na C_{18}H_{33}O_2$ ,  $\geq 82\%$ ), trioctylphosphine oxide ( $C_{24}H_{51}PO$ , TOPO, 90%) were purchased from Sigma-Aldrich. Ethanol (EtOH, 99.5%), hexane ( $C_6H_{14}$ ,  $>96\%$ ), chloroform ( $CHCl_3$ ) were obtained from VWR Chemicals. All the reagents were used as purchased without any further purification. For the ligand exchange step, the same chemicals listed in chapter 3 were used.

### 5.2.2 Synthetic method

The synthesis of nanoplates was carried out via the thermal decomposition of  $Fe(acac)_3$  in Oleylamine. Oleylamine (OAm) here was used as i) solvent for the reaction ii) capping ligand for the formation of NPs, iii) reducing agent to form  $Fe_3O_4$  phase.<sup>107</sup> In some reactions, different strongly-bonding ligands were also added to investigate their effect on the final shape and size, as reported in Table 5.1. The reaction was kept under constant nitrogen flow to create an inert atmosphere.

In a typical synthesis, 1.2 mmol of  $Fe(acac)_3$  was placed in a 50 ml round bottom flask with 20 ml of OAm and 1.2 mmol of Hexadecylammonium Chloride. Eventually the addition of other surfactants was tested. The mixture was heated at 120 °C under vigorous magnetic stirring. The solution was left at this temperature for 30 min to homogenise the solution. The temperature of 120 °C was not high enough to promote the decomposition of Fe precursor, but it was able to remove traces of water in solution. After, the solution was heated up to 270 °C and left to react for 15 min before removing the heating source and let the solution to cool down at room temperature. The solution was then collected and transferred into two 50 ml

centrifuge tubes and 5 ml of chloroform first, and 15 ml of ethanol after, were added. The solutions were centrifuged at 5000 rpm for 5 min. The supernatant was then discarded, and the precipitated nanoparticles were washed again adding 5 ml of chloroform first to redisperse the NP and 15 ml of ethanol after, to promote the precipitation of NPs during the following centrifugation. The process was repeated twice in total. The final precipitate is collected by dispersing the material in 2 ml of chloroform and stored as solution for further use and characterisation. In Table 5.1 the parameter used for the reaction in this chapter are summarised.

*Table 5-1 Reaction conditions for the experiments presented in this chapter.*

<b>Experiment</b>	<b>Precursor (mmol)</b>	<b>OAm (ml)</b>	<b>HDA-Cl (mmol)</b>	<b>Other Ligand (mmol)</b>	<b>Bubbling</b>
<b>I</b>	1.2	20	0.5	No	Yes
<b>II</b>	1.2	20	0.5	No	No
<b>III</b>	1.2	20	0	No	No
<b>IV</b>	1.2	20	1.0	No	No
<b>V</b>	1.2	20	2.0	No	No
<b>VI</b>	0.6	20	1.0	No	No
<b>VII</b>	2.5	20	1.0	No	No
<b>VIII</b>	1.2	20	1.0	0.4 (OA)	No
<b>IX</b>	1.2	20	1.0	0.4 (SO)	No
<b>X</b>	1.2	20	1.0	0.4 (TOPO)	No

<b>XI</b>	1.2	20	1.0	0.2 (SO)	No
<b>XII</b>	1.2	20	1.0	0.8 (SO)	No
<b>XIII</b>	1.2	20	1.0	1.0 (SO)	No

### 5.3 Results and discussion

#### 5.3.1 Preliminary results

The synthesis was first performed to investigate the potential formation of metallic Fe NPs with a non-toxic and easy-to-handle precursor. Indeed, apart from being highly sensitive towards oxidation and degradation, Fe(CO)<sub>5</sub> easily releases CO species, which is highly toxic. Among the most common precursor for the synthesis of iron-based NPs, Fe(acac)<sub>3</sub> is a very versatile, stable, cheap, non-toxic and easy-to-handle precursor. In this molecule the Fe ion is in its oxidised state, thus a reducing agent is needed in the reaction solution to obtain metallic Fe NPs. The double bond present in the molecular structure of OAm can act as a mild reducing agent.<sup>107</sup> Mohan *et al.* reported the production of metallic FePt alloys NPs using OAm as solvent, ligand and reducing agent with Fe(acac)<sub>3</sub> as precursor.<sup>174</sup> OAm is a weakly binding ligand and it does not prevent the formation of NPs if it is used in strong excess.<sup>189</sup> Therefore to attempt the formation of metallic Fe NPs, Fe(acac)<sub>3</sub> was decomposed in OAm, and in the presence of HDA-Cl which is necessary to promote the formation of a crystalline phase.

In Experiment I, the synthesis was carried out using 1.2 mmol of Fe(acac)<sub>3</sub>, 0.5 mmol of HDA-Cl in 20 ml of OAm. The reaction solution was purged with N<sub>2</sub> at 120 °C by flowing nitrogen inside the solution with a needle for 30 min and then the temperature was raised up to 270 °C and left at this temperature for 15 min.

After being collected, the product was washed and characterised via TEM and XRD. In Figure 5.1, the TEM image shows that the sample is made of NPs with unexpected morphologies. At a first glance, several shapes coexist in the same sample, with rounded, triangular (red arrow) and square (blue arrows) shaped NPs observed. The XRD pattern shows the presence of two phases in the sample with one matching  $\text{Fe}_3\text{O}_4$  pattern (magnetite, although maghemite cannot be excluded<sup>158</sup>) and the other matching  $\alpha\text{-Fe}$ . The peaks relative to  $\text{Fe}_3\text{O}_4$  oxide phase appears broader than the ones relative to metallic Fe, which instead appear very sharp, suggesting a stark difference in size for the two phases. Using the main peak from each pattern in the Scherrer equation it was calculated that the iron oxide phase is made of crystalline grains with an average size of 11.3 nm, (311) peak at  $35.4^\circ$ , while for  $\alpha\text{-Fe}$  the crystal grains are at least 42 nm large, (110) peak, at  $44.5^\circ$ . The analysis suggests that the NPs observed in the TEM images are made of magnetite.

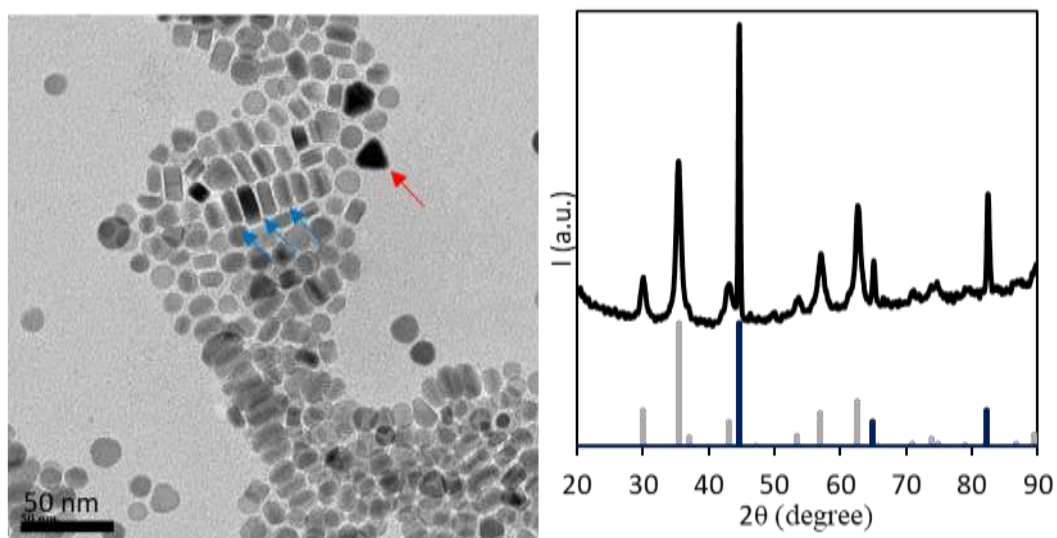


*Figure 5-1 TEM image (left) and XRD pattern (right) of the sample obtained through the decomposition of  $\text{Fe}(\text{acac})_3$  at high temperature in OAm with HDA-Cl. The grey reference pattern corresponds to  $\text{Fe}_3\text{O}_4$  phase and the blue one to bcc-Fe phase (JSPC PDF no. 01-079-0418 and 00-006-06969 respectively).*

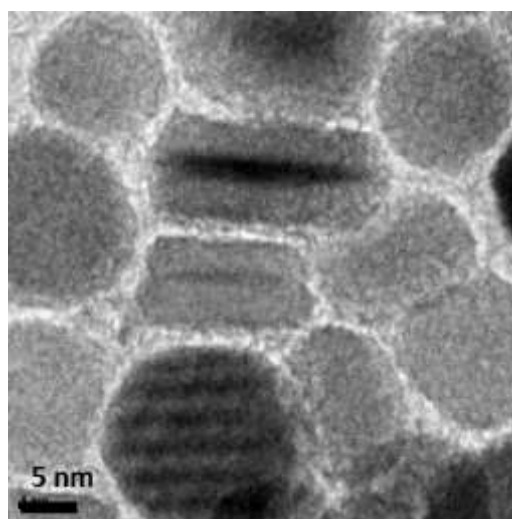


*Figure 5-2 High magnification TEM image for Experiment I sample.*

The TEM image at high magnification (Figure 5.2) highlighted the presence of squared NPs with a darker plane in the middle. The plane appeared to be a twinned plane. Usually a twinned plane is the surface along which the lattice points of two crystals are shared during the growth. This feature, along with the presence of triangular, hexagonal and rounded morphology of the NPs suggested that the NPs have a plate-like morphology. In such case, the several shapes observed may be the result of plate-

like NPs sitting on the sample holder either on their face (triangular, hexagonal and rounded NPs) or on their sides (squared and rectangular NPs).<sup>190</sup>

To confirm the hypothesis of plate formation, TEM pictures of the sample were taken at different tilting angles of the sample holder. When the TEM electron beam hit the sample, a 2D image is observed and no depth can be perceived. Therefore, spherical NPs and disc-like NPs lying on its top or bottom face, with similar diameter, would appear of the same shape. By tilting the sample, different areas of the sample can be observed and while no change would be observed in a spherical NP, a plate-shaped NP would show its side. Figure 5.3 shows a series of images taken between 0° and 60° of the tilting angle of the sample holder during TEM analysis. The range was the maximum rotation of the sample holder allowed by the instrument.

The red circle highlights NPs showing different orientation with varying angles. At 0° many areas are observed with aligned rectangular-shaped NPs. As the sample is tilted, the rectangular shape starts disappearing, showing instead rounded-shape NPs once the sample reaches 60° of tilting. This is consistent with the fact that the NPs have a plate-like morphology. Indeed, when they are sitting on their side face, the NPs look like a rectangular/small rod-shaped NPs, while they resemble spherical NPs when they are sitting on their top or bottom surface.

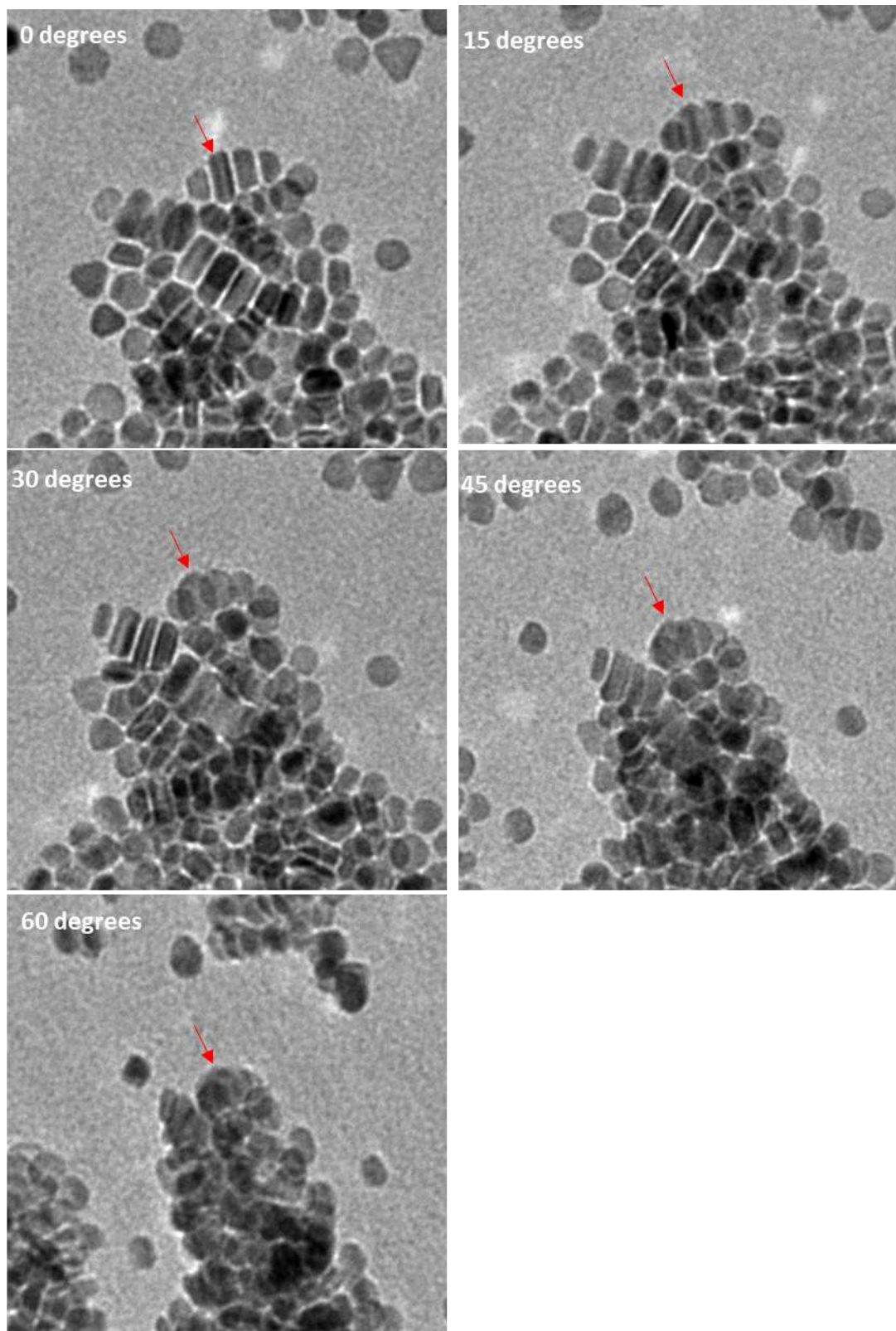


*Figure 5-3 TEM images taken by tilting the sample holder at different angles from 0 to 60 degrees.*

Figure 5.4 shows the electron diffraction pattern recorded for different areas of the TEM grid with NPs obtained from Experiment I, allowing to study locally any variation in the phase of the sample. The top part shows an area with only NPs present, and the only phase detected from the electron diffraction analysis corresponds to the  $\text{Fe}_3\text{O}_4$  reference pattern. On the other hand, the bottom part shows an area of the grid where the main phase detected was  $\alpha\text{-Fe}$ . To measure the size of the particles and be able to compare the size of the different shaped NPs, the diameter was measured for rounded NPs, and the height was measured for triangular and hexagonal NPs. The iron oxide NPs showed a size of  $13.4 \pm 3.0$  nm while the metallic Fe signal originated from aggregated material with no defined shape and size. This suggested that OAm reduced some Fe ions from the precursor into metallic Fe, however, it was not strong enough to reduce the whole sample. Moreover, the formed metallic phase grew into large aggregates, probably due to the high reaction temperature and the weakly binding properties of OAm which cannot prevent the coalescence of  $\alpha\text{-Fe}$  phase.<sup>191</sup>

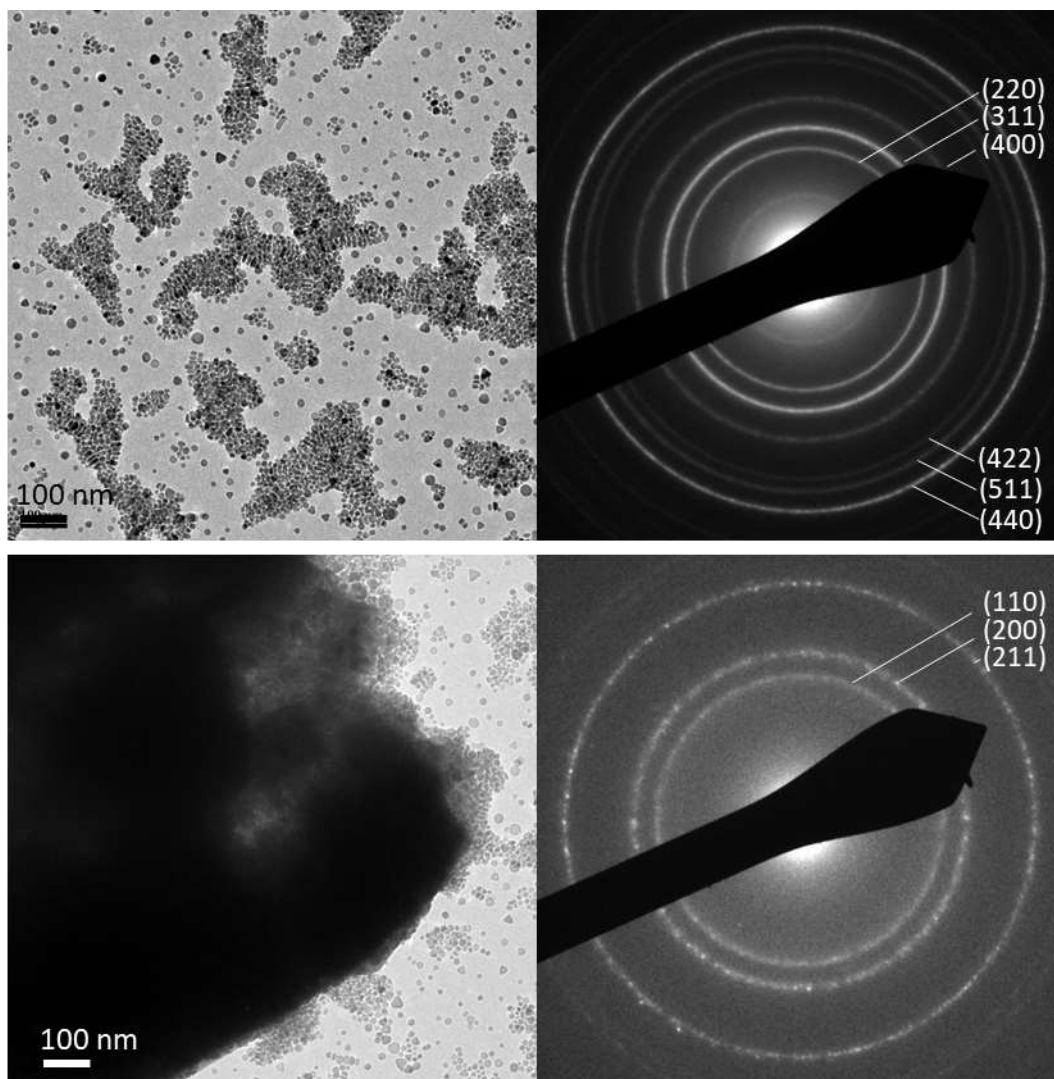


*Figure 5-4 TEM images and relative electron diffraction of different areas of the same sample (Experiment I) containing magnetite nanoparticles (top) and large material made of  $\alpha$ -Fe (bottom).*

With this synthetic method, a mix of  $\alpha$ -Fe material and anisotropic iron oxide NPs with plates shape were formed. Although  $\alpha$ -Fe based materials are suitable candidates for magnetic hyperthermia, this synthetic approach did not allow for enough control of its size. On the other hand, shaped  $\text{Fe}_3\text{O}_4$  NPs can potentially have significant performances in magnetic hyperthermia, thus the parameters and conditions affecting the shape and size of the iron oxide phase were further investigated.

### 5.3.2 Study on single-phase anisotropic NPs.

In order to optimise the synthesis of shaped iron oxide NPs, it was first investigated how to obtain NPs made of uniform phase, with no  $\alpha$ -Fe aggregates.

In Experiment II, the initial purging phase was modified by removing the flowing of  $N_2$  inside the solution at the beginning of the reaction protocol. The synthetic procedure is modified to prevent the formation of the  $\alpha$ -Fe aggregates and promote just the formation of anisotropic iron oxide NPs. Without  $N_2$  purge, oxygen would remain inside the reaction solution and hinder the formation of  $\alpha$ -Fe. Therefore, in this case, instead of purging  $N_2$  inside the solution, the reaction was just left at 120 °C for 30 min under  $N_2$  atmosphere before bringing the solution to the reaction temperature of 270°C.

Figure 5.5 shows the XRD and TEM of the sample obtained without the degassing procedure. The XRD pattern showed no evidence of  $\alpha$ -Fe phase with the main phase being  $Fe_3O_4$ . The crystallite size estimated through Scherrer equation was 11.4 nm which is close to the previous reaction with the degassing step. The TEM image shows that the sample is made of NPs with different shapes ranging from triangular to hexagonal and rounded shape. A series of NPs piled on each other and sitting on one side face of the NPs is clearly detected on the left side of the image suggesting that also in this case nanoplates are formed. The size of the NPs is  $16.1 \pm 3.2$  nm which is also close to the value obtained for NPs synthesised with the degassing step.

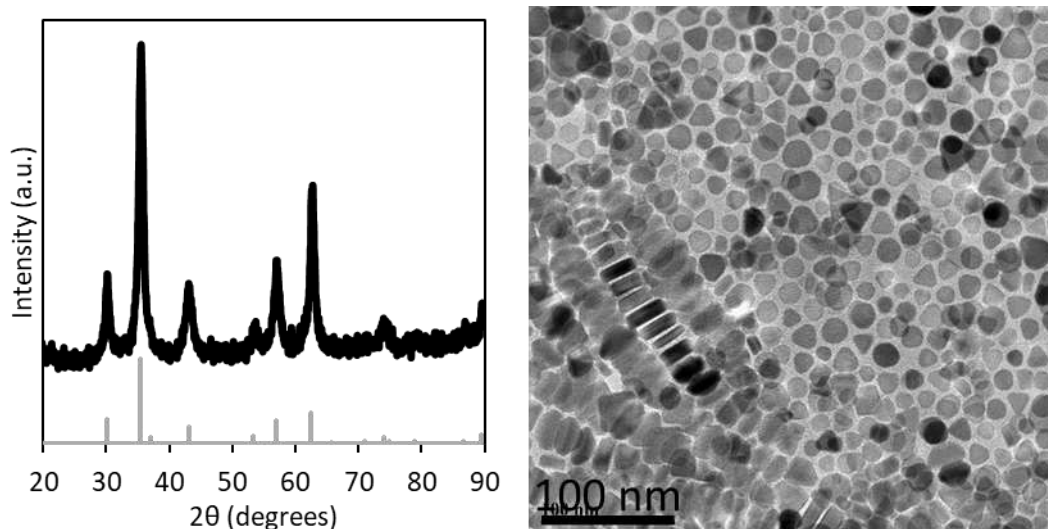
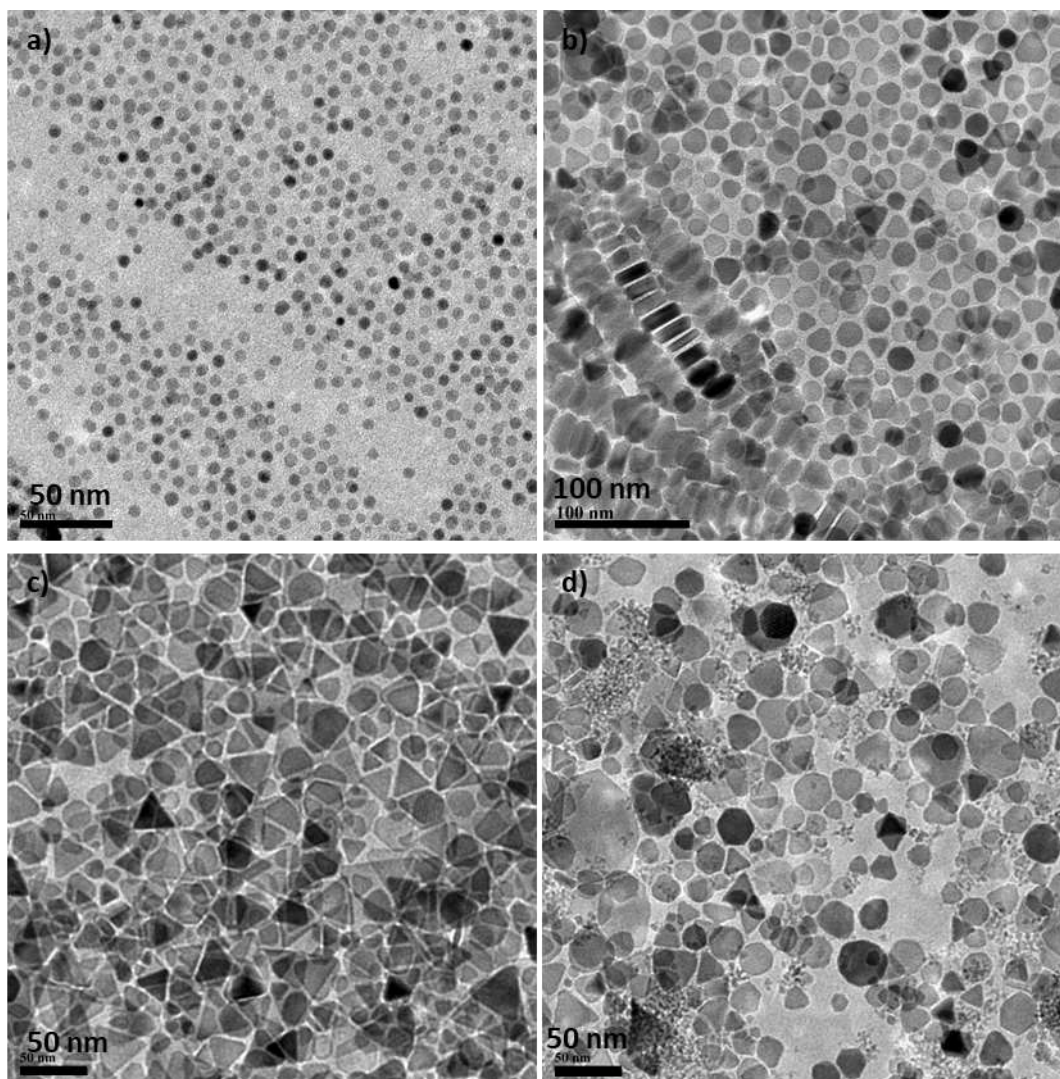


*Figure 5-5 XRD pattern and TEM image of the sample obtained without purging  $N_2$  inside reaction solution (Experiment II).*

Changing the initial purging step prevents the formation of uncontrolled  $\alpha$ -Fe bulk material without affecting the formation of shaped plate-like  $Fe_3O_4$  NPs which are now the only product of the reaction.

### 5.3.3 Study on the effect of chloride in solution

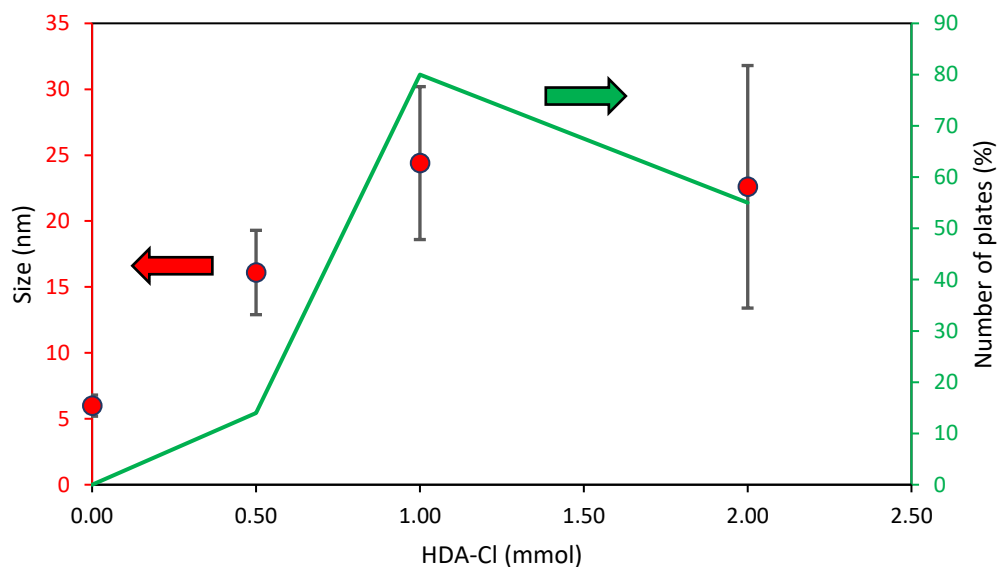
As halides can play a big role in the formation of NPs,<sup>31,74,192</sup> the effect on the variation of the concentration of the chloride source was investigated. Table 5.1 shows the reaction conditions used in the Experiment II, III, IV and V where the amount of chloride source, HDA-Cl, was varied from 0.5 mmol to 0, 1.0 and 2.0 mmol, respectively.



*Figure 5-6 TEM images of samples obtained using a) 0 mmol, b) 0.5 mmol, c) 1.0 mmol and d) 2.0 mmol HDA-Cl.*

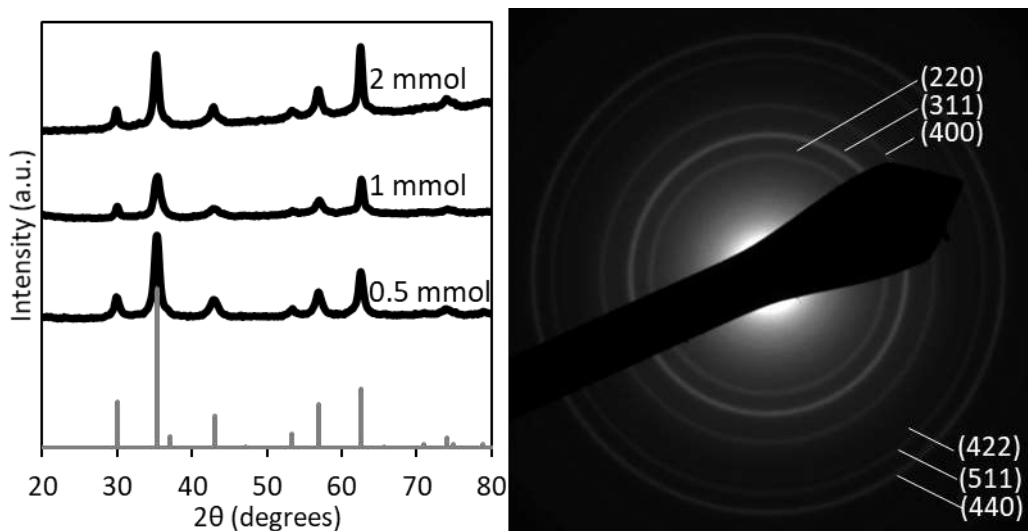
Figure 5.6 shows the TEM images of the four reactions where several amounts of chloride was used. When no HDA-Cl was used (Fig 5.6 a), the reaction formed small spherical NPs with an average diameter of  $6.0 \pm 0.8$  nm. When the chloride source was 0.5 mmol, (Fig 5.6 b) plate-like NPs are formed with an average height of  $16.1 \pm 3.2$  nm. The plates possess a heterogeneous morphology ranging from rounded disk to more edged plates resembling hexagonal and triangular shaped plates (14%). When the chloride source is instead raised to 1.0 mmol (Fig 5.6 c), larger plates-like NPs are formed, having an average height of  $24.4 \pm 5.8$  nm with triangular plates appearing to be the dominant shape (80%). Finally, when the amount of HDA-Cl used

is 2.0 mmol (Fig 5.6 d), a highly polydisperse sample in size and shape is obtained. Indeed, plates with an average height of  $22.6 \pm 9.2$  nm are observed along with clusters of smaller and irregular material.



*Figure 5-7 Graph showing the size and percentage of plate-like NPs obtained according to the amount of HAD-Cl used.*

The phase of the sample was investigated via XRD for the samples obtained with 0.5, 1.0 and 2.0 mmol of HDA-Cl, while in the case of NPs obtained with no Cl source, the amount obtained was not sufficient to carry out XRD analysis and ED was used instead.



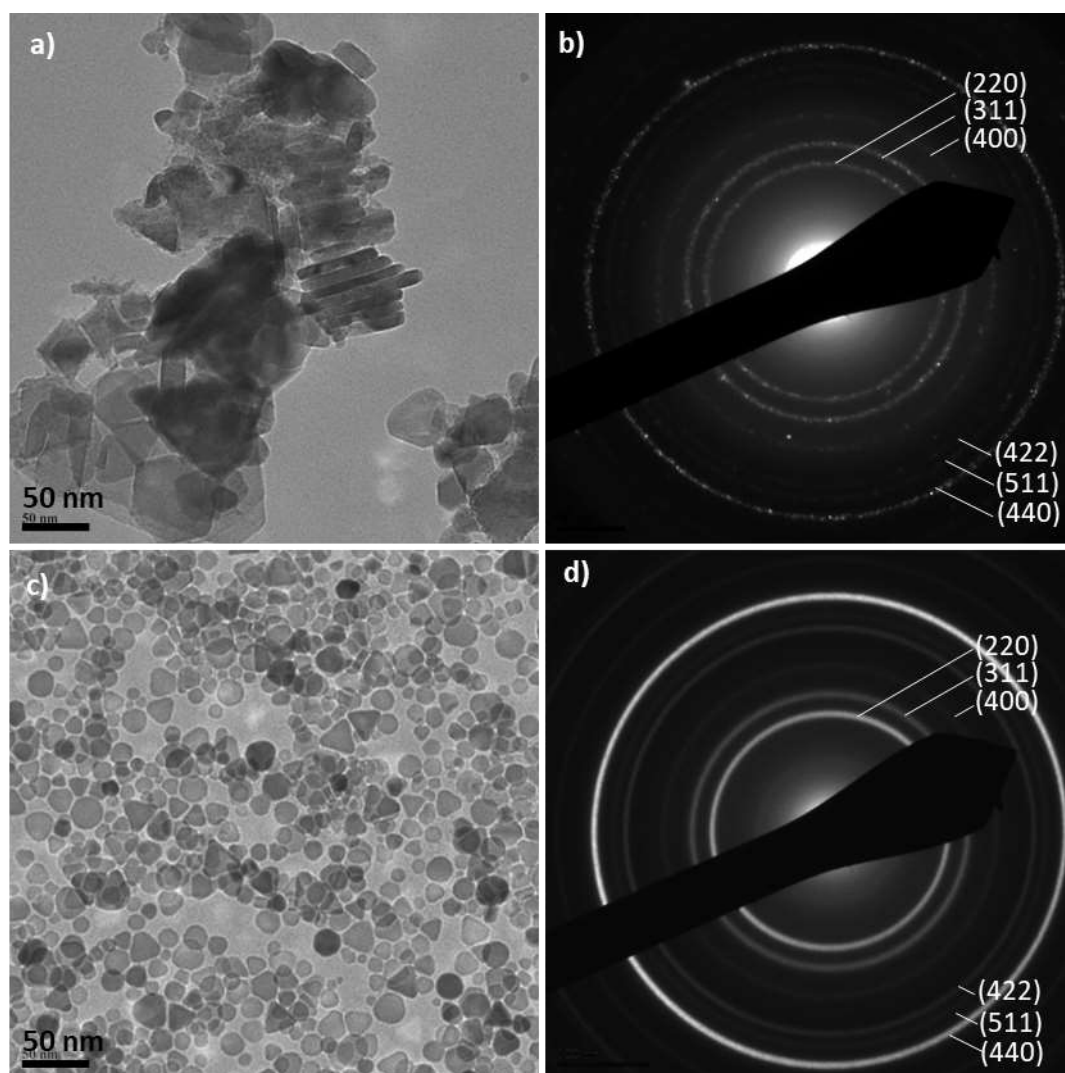
*Figure 5-8 XRD pattern (left) of sample synthesised with 0.5, 1.0 and 2.0 mmol of HDA-Cl and ED pattern (right) of the sample synthesised without HDA-Cl.*

Figure 5.8 shows that the phase obtained in all four samples matches the  $\text{Fe}_3\text{O}_4$  reference pattern. This shows that the HDA-Cl did not play any role in the formation of the final phase, but HDA-Cl played an important role in the final shape of the NPs. If no HDA-Cl is present, the decomposition of Fe precursor in OAm led to small spherical NPs with a low yield. In all the cases where chloride source is used, a certain extent of anisotropy in the shape of NPs was observed, with the most common shape being plate-like. Increasing the amount of chloride in the reaction from 0.5 mmol to 1 mmol led to a more uniform sample regarding the shape of the plate. Indeed, the proportion of triangularly shaped nanoplates passes from 14% in the case of 0.5 mmol HDA-Cl to 80% for 1 mmol. When the amount of chloride was further increased to 2.0 mmol, the majority of the nanoplates still showed a triangular shape (65%), even though the sample became very polydisperse in size. It was therefore concluded that 1.0 mmol of HDA-Cl led to the most uniform results and this amount was used for the rest of the study.

### 5.3.4 The effect of iron precursor amount

The effect of the initial precursor on the NPs was also investigated by varying the amount of  $\text{Fe}(\text{acac})_3$  to half and double the amount used in the previous reaction. The amount of OAm was kept constant and 1.0 mmol of HDA-Cl was used, so then the  $\text{Fe}(\text{acac})_3$  to HAD-Cl ratio was changing. Table 5.1 shows the reaction conditions used in the Experiment VI and VII where the amount of iron precursor was 0.6 and 1.2 mmol respectively.

Figure 5.9 a) and b) show respectively the TEM image and ED pattern of the sample obtained when 0.6 mmol of  $\text{Fe}(\text{acac})_3$  was used. The sample appeared very aggregated and this impeded an accurate size estimation of the particles. In general, it can be observed that nanoplates were still formed and this was confirmed by the presence of NPs clustered together and sitting on their side face. The plates showed hexagonal, triangular and irregular shape, and the particles were larger than 50 nm, which is bigger than particles obtained in previous reactions where 1.2 mmol of Fe precursor was used (Fig 5.6c). The phase detected via ED matched the  $\text{Fe}_3\text{O}_4$  pattern. When the amount of Fe precursor was increased to 2.5 mmol, NPs with an average height of  $22.0 \pm 5.8$  nm were formed (Figure 5.9 c). The size was similar to NPs obtained with 1.2 mmol of  $\text{Fe}(\text{acac})_3$ , (Fig 5.6 c), however, in this case, NPs shape appeared more rounded resembling a disc with a smaller proportion of triangles ( $\approx 30\%$ ). ED pattern (Fig 5.9 d) showed that the NPs are made of crystalline  $\text{Fe}_3\text{O}_4$ .



*Figure 5-9 TEM images and ED patterns for the sample obtained using 0.6 mmol (a & b) and 2.5 mmol (c & d).*

Changing the amount of precursor mainly affected the size of the NPs. The results suggested that when 0.6 mmol of  $\text{Fe}(\text{acac})_3$  is used, the precursor is consumed mainly for the growth of the particles. It must be considered that when 0.6 mmol of  $\text{Fe}(\text{acac})_3$  was used, the amount of chloride source present in solution (1.0 mmol) was nearly double the amount of Fe precursor and this affected the nucleation steps, producing fewer nuclei at the beginning of the reaction hence the remaining Fe precursor in solution promoted the growth of large NPs (< 50 nm).

It was observed that the presence of chloride affects the final morphology of the Fe<sub>3</sub>O<sub>4</sub> NPs. To explain the role of chloride in the reaction it can be useful to understand the formation process of nanoplates first. Xia *et al.* reported an extensive review explaining the different NPs shapes that can be obtained starting from seeds with specific structure (Figure 5.10).<sup>190</sup> In general, it was observed that when the feed of atoms in solution is considerably slow (e.g. slow decomposition of the precursor), the nuclei and the seeds are formed following a random hexagonal close packing (*rhcp*) configuration with the formation of a twinned plane which can also present stacking faults.<sup>193</sup> If the sequence of stacking of different atoms layers should be ABCABCABC, stacking faults are introduced when the stacking sequence is modified and a different order of layer is obtained (e.g., ABCABABC). When the stacking fault forms a mirror image, a twin plane is introduced in the structure.<sup>194</sup> This kind of growth has been defined as kinetically controlled because it promotes the formation of non-thermodynamically stable shapes.

The presence of stacking faults and/or twin planes can promote the formation of a plate-like seed where {111} facets are both at the top and bottom surfaces.<sup>195</sup> The formation of such shapes are obtained when both the nucleation and growth of the seeds deviate from thermodynamically controlled pathways and this has been achieved experimentally through substantially slowing down the precursor decomposition,<sup>196</sup> limiting the availability of atoms for nucleation and growth.<sup>197,198</sup>

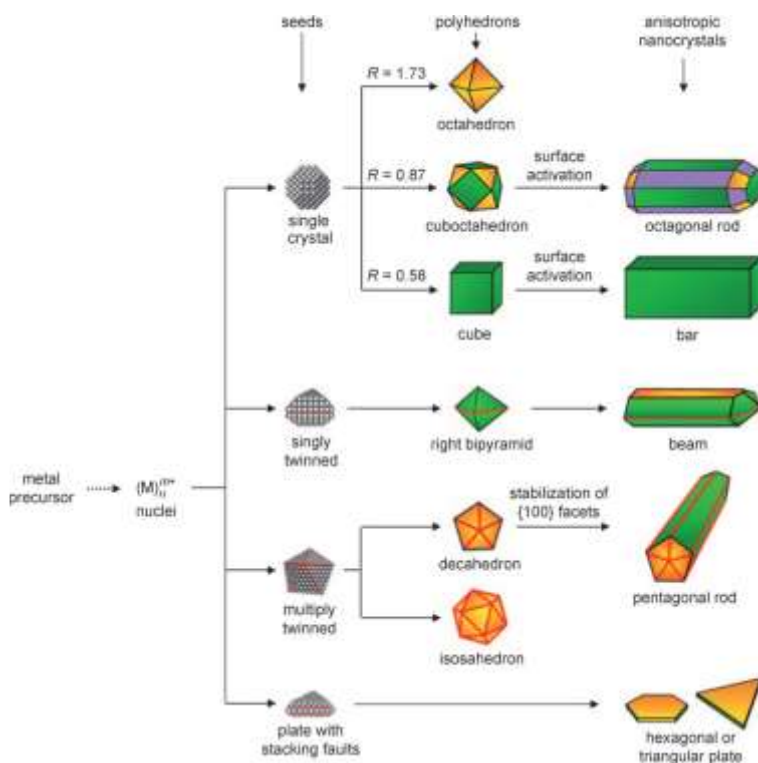


*Figure 5-10 Reaction pathways that lead to fcc metal nanocrystals with different shapes. First, a precursor is reduced or decomposed to form the nuclei (small clusters). After a certain size is reached, seeds are formed and they can have a single-crystal, singly twinned, or multiply twinned structure. The green, orange, and purple colors represent the  $\{100\}$ ,  $\{111\}$ , and  $\{110\}$  facets, respectively.<sup>190</sup>*

Iron oxide NPs with a plate-like morphology is very rare. Li *et al.* synthesized hexagonal nanoplates of  $\text{Fe}_3\text{O}_4$  using supercritical  $\text{CO}_2$  under high pressure and temperatures between 650-750 °C.<sup>199</sup> Jian *et al.* induced the formation of iron oxide triangular plate-like NPs starting from Pt seeds as nucleation spots to orient the shape of the forming iron oxide crystal.<sup>200</sup> Xu *et al.* instead used a seed mediate growth to produce ultra-thin triangular magnetite nanoplates of around 14 nm while Wang *et al.* produced 90 nm hexagonal plates with excellent heating performances by decomposing  $\text{Fe}(\text{acac})_3$  in a mixture of oleic acid and stearic acid in benzyl ether.<sup>201</sup> In this study, it has been shown that HDA-Cl had a fundamental effect on the formation of plate-like NPs, as a source of chloride. If no chloride source was used, just spherical NPs were observed. When chloride was added, plate-like NPs appeared and increasing the amount led to more defined and bigger plates-like NPs (Fig 5.6). This

suggests that chloride acted as an agent that limits the availability of Fe atoms by either slowing down the decomposition of  $\text{Fe}(\text{acac})_3$  or interacting with iron oxide nuclei in solution. Although the exact role of chloride was hard to determine, the behaviour was similar to the one found when it was used for the synthesis of Fe NPs, where the presence of halides in solution slows down the growth kinetics of NPs leading to crystalline Fe iron phase.<sup>31</sup>

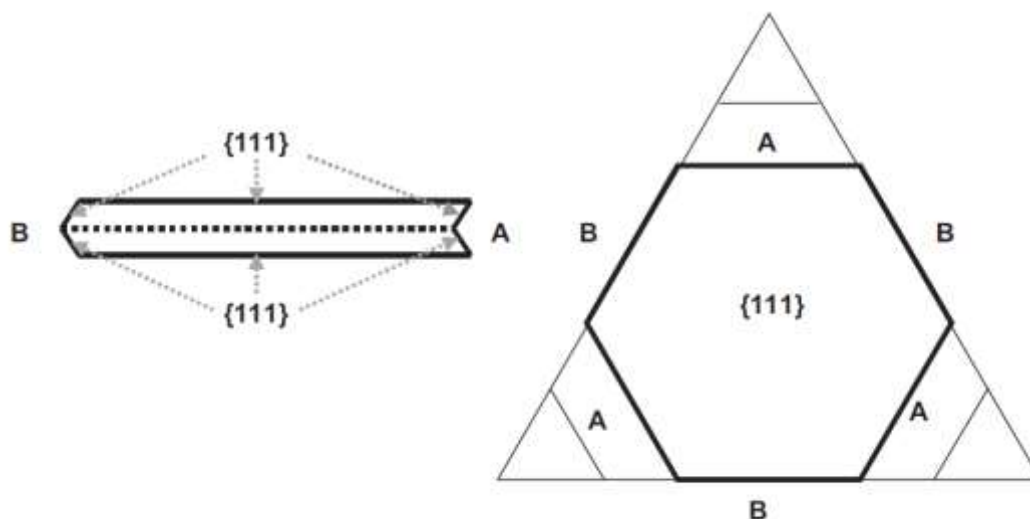


*Figure 5-11 Representation of a silver halide model for a single twin plane. Alternating sides contain A-type and B-type faces. The structure promotes faster growth of the A-type faces, leading to a triangular prism.<sup>202</sup>*

The final shape of the plates here reported can vary, and this has to do with the shape evolution during the growth of the particle's crystal. Lofton and Sigmund reported that for the case of AgCl NPs, the stacking faults in combination with the atoms nucleating through random hexagonal close packing, the sixfold symmetry promotes the formation of hexagonal plates in the early-stage of nanoplates growth.<sup>202</sup> These planes have six side surfaces with an alternating concave and convex orientations as shown in Figure 5.11 (defined, as "A" side and "B" side, respectively). The authors proposed that the addition of more atoms is energetically more favourable on the concave side, as atoms being added to the tip of side B are not stabilised by the presence of surrounding atoms and, thus, they tend to re-dissolve in solution. The

faster addition of material to the “A” sides leads to the disappearance of those faces, generating a triangular plate. Importantly, this suggests that the size of the NPs is defined by the size of the particle at the time of twinning because once the A-type faces grow itself out, the triangular prism is left with only slow-growing B-type faces.

### 5.3.5 Effect of the ligands on size and shape of nanoplates

Different ligands were tested to evaluate the effect on the size and shape of the final plates obtained. As previously shown, OAm is a weakly binding capping agent and does not control the size and shape of the NPs, whereas the chloride was found to be the most important parameter affecting mainly shape but also size. The nanoplates' size is determined at the time of twinning of the seed, and it is hypothesised that more strongly binding ligand could interact with the forming crystal and provide more control over the final morphology. Three of the most commonly used ligands in the synthesis of Fe<sub>3</sub>O<sub>4</sub> NPs were tested, being trioctylphosphine oxide (TOPO),<sup>203</sup> oleic acid (OA),<sup>116</sup> and sodium oleate (SO).<sup>187</sup> The molecular structure in the ligands, being phosphorus-oxygen moiety, carboxylic acid and carboxylate group respectively, show strong affinity with Fe atoms and the forming iron oxide crystal structure, and they have been reported to control size and shapes of Fe<sub>3</sub>O<sub>4</sub> NPs.<sup>203</sup> To evaluate the effect of the ligands onto the Fe<sub>3</sub>O<sub>4</sub> nanoplates, three reactions were carried out adding 0.4 equivalents of one of the capping ligand aforementioned.

Figure 5.12 shows the TEM images and XRD of the three samples obtained adding either TOPO (Experiment VIII), OA (Experiment IX) or SO (Experiment X), with the conditions shown in Table 5.1. When OA was used, the sample appeared highly disperse in size (Fig 5.12 a) with an average height of  $14.4 \pm 4.3$  nm. Hexagonal and triangular shaped NPs are clearly observed, confirming that the addition of OA does not affect the twinning process that leads to the plate morphology.

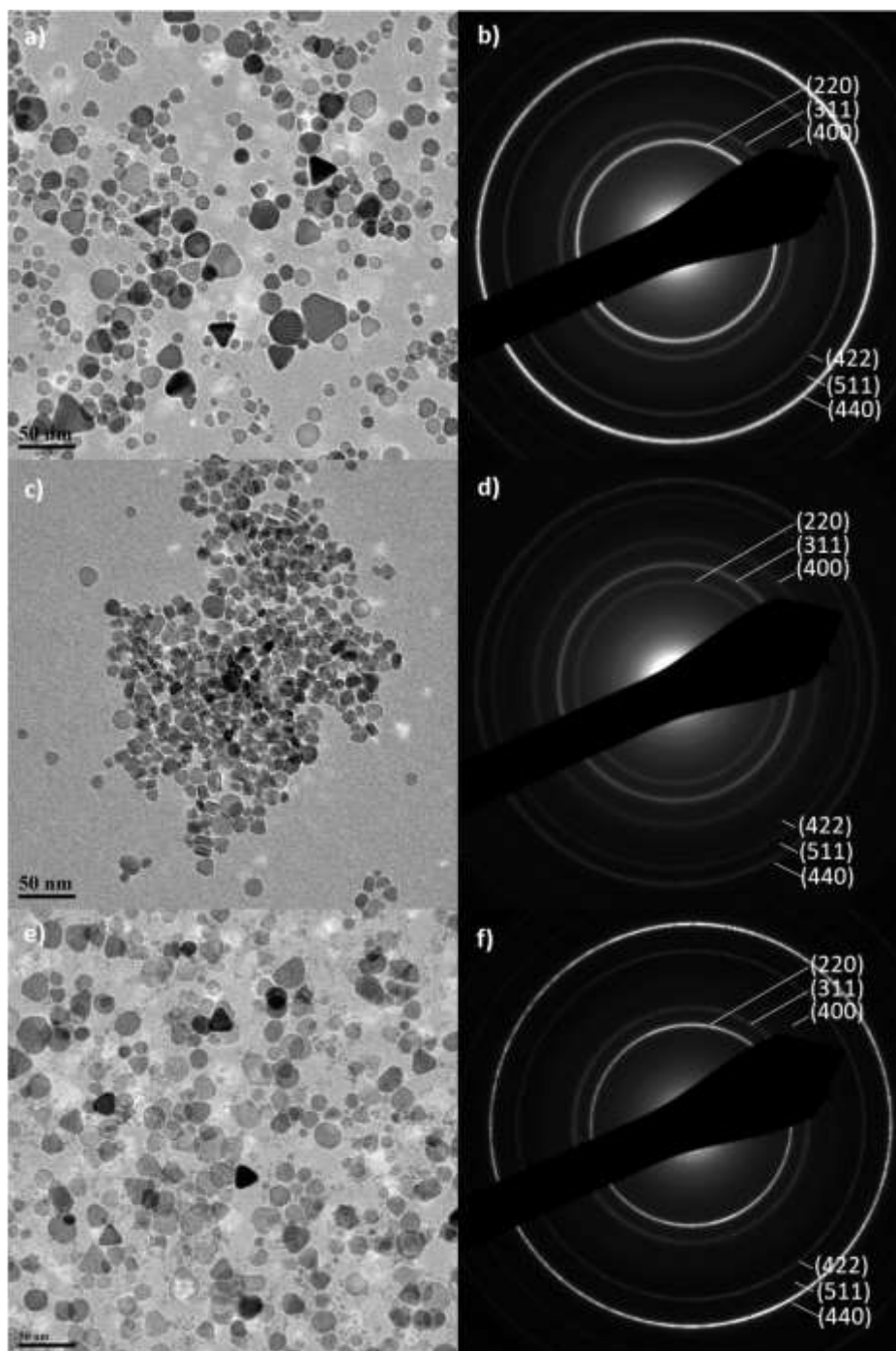


*Figure 5-12 TEM images and ED pattern of the sample obtained when 0.4 mmol of extra ligand was added. a) & b) corresponds to the sample obtained using OA. c) & d) corresponds to the sample formed with SO and e) & f) was formed using TOPO.*

The phase detected using ED (Fig 5.12 b) matched the magnetite pattern. When SO is used, the average calculated height is  $13.1 \pm 3.0$  nm with the morphology of the

sample being very heterogeneous; hexagonal, triangular, squared and rounded NPs are all observed suggesting again the formation of plates NPs, although other morphologies cannot be excluded. The ED pattern (Fig 5.12 d) showed that the crystal phase of the particles corresponds to  $\text{Fe}_3\text{O}_4$ .

Finally, when TOPO was used the size of the particles obtained was  $17.2 \pm 5.0$  nm with the sample being made of bigger triangular shaped NPs and much smaller undefined particles. The ED pattern (Fig 5.12 f) showed that the NPs are made of  $\text{Fe}_3\text{O}_4$ .

It was concluded that the addition of strongly binding ligands such as OA, SO and TOPO does not prevent the twinning process and plate-like NPs are still formed. While the use of OA and TOPO forms very disperse NP both in size and shape, SO provides more control over the size of the NPs, with the sample being the one with the narrowest size distribution. Therefore, SO ligand was selected for further investigation.

#### 5.3.5.1 The effect of sodium oleate on the size and shape of nanoplates

Different quantities of sodium oleate were used to evaluate the effect on the size and shape of the final NPs obtained. In particular, it was used 0.2 mmol(Experiment XI), 0.8 mmol(Experiment XII) and 1.0 mmol(Experiment XIII) of sodium oleate in relation to the amount of Fe precursor, keeping the rest of the parameters unchanged with 20 ml of OAm and 1 mmol of HDA-Cl. Table 5.1 shows a summary of the synthetic conditions used.

Figure 5.11 shows the TEM images and ED pattern taken for the samples obtained with different quantities of SO used. When the amount of SO used was 0.2 mmol the size of the NPs was  $17.2 \pm 6$  nm. When the SO was increased to 0.8 mmol the NPs have a size of  $15.6 \pm 4.0$  nm, with hexagonal and triangular shaped NPs clearly

observed. When SO is further increased to 1.0 mmol, the size increases to  $11.6 \pm 5.5$  with NPs having a square-shaped than the previous sample making not trivial to discern the exact morphology.

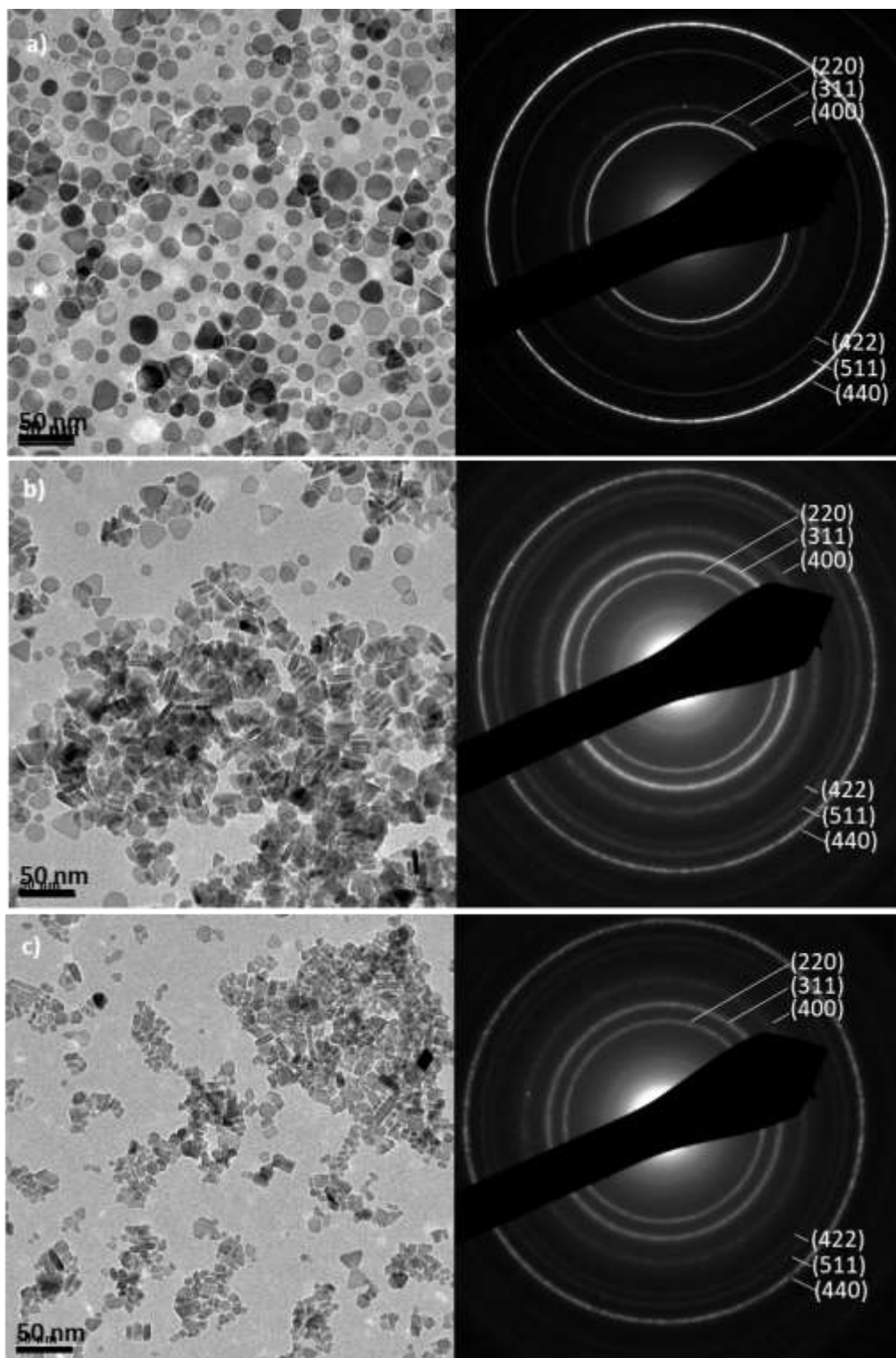


*Figure 5-13 TEM images and ED pattern of the sample obtained when a) 0.2 mmol of SO, b) 0.8 mmol of SO & c) 1.0 mmol of SO were added.*

At 0.8 mmol of SO used, the platelet morphology appears to be predominant compared to the other sample, with triangular and hexagonal shaped particles clearly observed. The measured proportion of triangular and hexagonal shape was 22% for 0.2 mmol used, 58% for 0.8 mmol used and 30 % for 1.0 mmol used.

The sample formed with 0.8 mmol of SO showed the highest proportion of triangles present and it was, therefore, further investigated through the tilting of the sample holder to confirm the plates morphology. Figure 5.13 shows the series of TEM images of the sample obtained with 0.8 mmol of SO, taken at different tilting angles of the sample grid. The red and green circles highlight NPs starting with different orientation. At 0° tilting angle, the red circle shows particle on their top/bottom, while the green one highlights an area where platelet-shaped NPs are lying on the grid with both their side surface (being also piled up next to each other) and bottom/top surface. As the sample is tilted, in the red circled area, the top/bottom surface of the plates starts disappearing until eventually only their side surface can be observed at 60°. Similarly, the green circled area highlights nanoplates that show their side surface at 0°, while their top/bottom surface is shown at 60°. This confirms the fact that the NPs have a plate-like morphology.

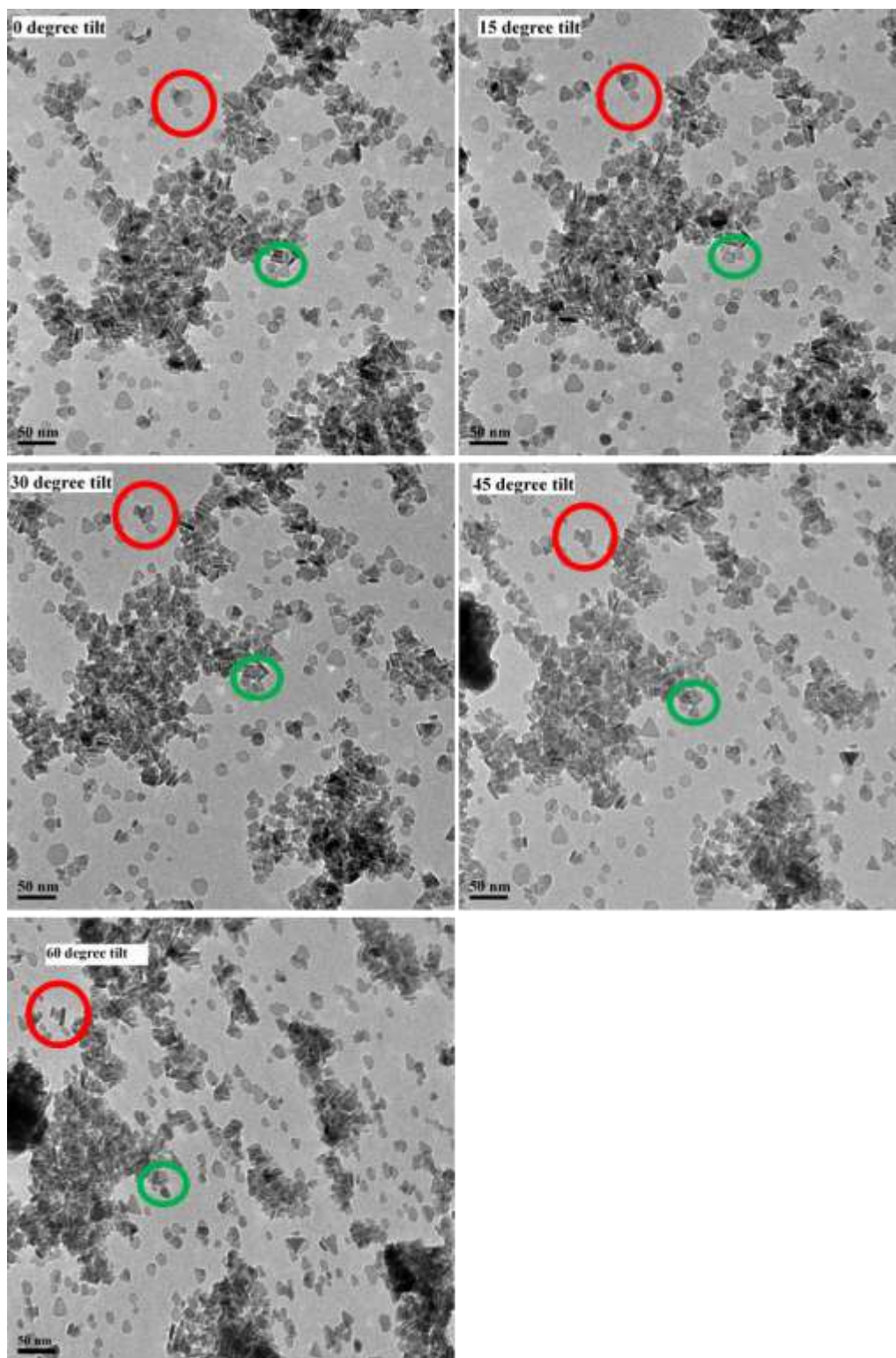


*Figure 5-14 TEM images of NPs obtained with 0.8 mmol of SO, taken by tilting the sample holder at different angles from 0 to 60 degrees.*

The sample obtained with 0.8 mmol of SO (Experiment XII) was chosen for further use and characterisation along with sample obtained in Experiment IV, obtained in the same reaction conditions (1.2 mmol of Fe(acac)<sub>3</sub> and 1.0 mmol of HAD-Cl in 20 ml of OAm) but without SO. They were chosen because the two samples showed similar shape features, but different size as summarised in Table 5.2. This would allow evaluating the effect of size and shape on the final hyperthermia outcome.

*Table 5-2 Summary of sample' feature for Experiment IV (without SO) and XII (with 0.8 mmol SO).*

<b>Experiment</b>	<b>Average Height (nm)</b>	<b>Triangles (%)</b>
<b>IV</b>	24.4±5.8	58%
<b>XII</b>	15.6±4.0	80%

### 5.3.6 Magnetic properties

The magnetic properties of the two samples Experiment IV and Experiment XII, (respectively without additional ligand and with 0.8 mmol of SO, respectively) synthesised in OAm, with 1.2 mmol of Fe(acac)<sub>3</sub> and 1 mmol of HDA-Cl, were analysed via SQUID-VSM. Figure 5.14 shows the hysteresis loops at 300 K for both samples. The  $M_s$  value for the NPs obtained without SO (Experiment IV) is 84 emu/g while for the other one (Experiment XII) is 46 emu/g. The  $M_s$  of the Experiment IV is very close to the bulk value for magnetite, (92 emu/g)<sup>71</sup> showing that the particles have a high degree of crystallinity. The value of 46 emu/g for the sample obtained using additional SO as ligand (Experiment XII) may be due to the increased fraction of spin disordered atoms exposed on the surface, which reduces the  $M_s$  value to almost half the  $M_s$  value of bulk magnetite. However, the value obtained here for the smaller NPs (Experiment XII) is almost double the  $M_s$  value of triangles iron oxide NPs of

similar size obtained through seed-mediated NPs (23 emu/g for  $14 \pm 2$  nm NPs.),<sup>204</sup> and similar to the triangular NPs of 20 nm obtained by Liu *et al.* via decomposition of  $\text{Fe}(\text{acac})_3$  precursor.<sup>205</sup> This means that, to the best of our knowledge, the sample with an average particle size of 24.4 nm (Experiment IV, no SO used as additional ligand) possess the highest  $M_s$  value reported for triangular iron oxide plates. The coercivity of 24.4 nm nanoplates is equal to 15 Oe at 300 K, indicating that the NPs are in superparamagnetic state. In the case of the sample with NPs of average size equal to 15.6 nm (Experiment XII, with SO used as additional ligand) the coercivity is 26 Oe; the sample looked more aggregated from TEM analysis and this may favour magnetic interactions that increase the coercivity of the sample, even though it is still very close to the superparamagnetic state.

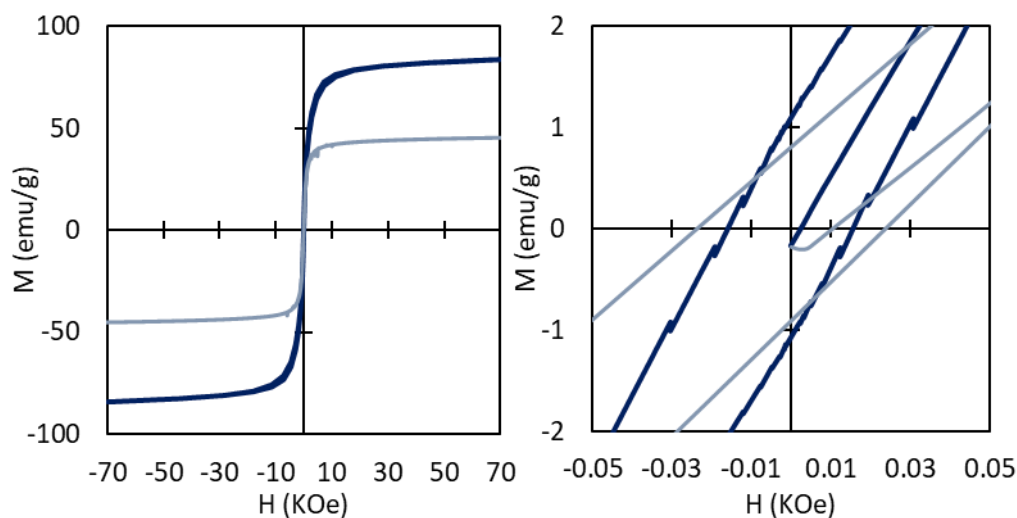


*Figure 5-15 Magnetic hysteresis loop taken at 300 K for 24.4 nanoplates dark blue and 15.6 nm nanoplates light blue (left). Zoom-in of the magnetic hysteresis for both samples at low fields (right)*

### 5.3.7 Ligand Exchange

The transfer in water of the two samples (Experiment IV and Experiment XII) was attempted to test the materials for magnetic hyperthermia. The as-synthesised NPs are coated with OAm in the case of Experiment IV, and a mixture of OAm and oleate

anions in the case of Experiment XII. This makes the samples insoluble in polar solution. To make the nanoplates soluble in water, the native ligand on the surface is exchanged with the dopamine-functionalised PIMA. This has been successfully used in this study to replace long-chain amines present on the surface of Fe (Chapter 3) and Fe<sub>2</sub>C NPs (Chapter 4), making the particles water-dispersible and provide the colloidal stability necessary for the use of NPs in biomedical applications. The followed procedure was the same used in the case of Fe and Fe<sub>2</sub>C NPs (ligand exchange with Mod PIMA-Dopa in Chapter 3). The colloidal stability of the two samples was measured after the ligand exchange. Figure 5.16 shows that Experiment IV' NPs ( $24.4 \pm 5.8$  nm) had an average  $D_H$  of 87.8 nm, while the NPs obtained with SO (Experiment XII,  $15.6 \pm 4.0$ ) showed an average  $D_H$  of 143.8 nm

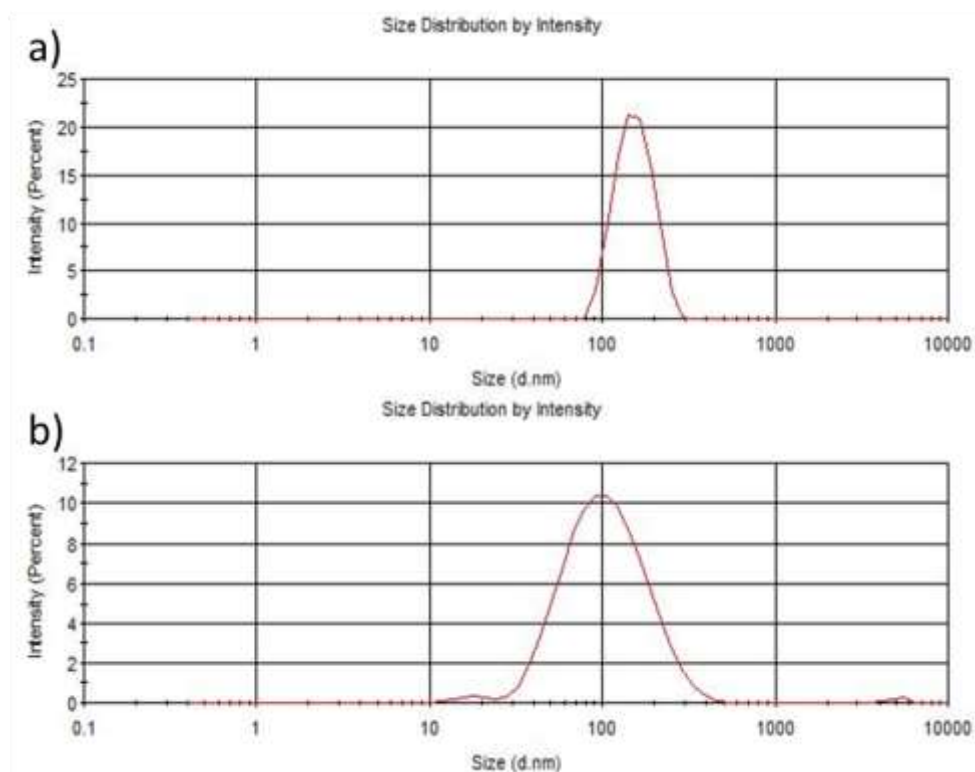


*Figure 5-16 DLS measurements in water after ligand exchange of NPs from a) Experiment XII and NPs from b) Experiment IV*

Although the NPs from Experiment XII are smaller in size, their  $D_H$  was larger. A possible explanation could be due to the fact the as shown on the TEM images, the

NPs from Experiment XII are highly interacting, forming a chain-like structure which may favour the ligand exchange of bigger aggregates altogether rather than single particles. Another possible explanation may be related to the presence of SO, which is a strongly binding ligand and harder to replace. This could hinder the ligand exchange process and favour aggregation in water, hence the higher  $D_H$ .

To further assess the colloidal stability of NPs from Experiment XII in water, the colloidal stability of the system was investigated at different pH values (3.2 to 10), as shown in Figure 5.17. At all pH, the values of  $D_H$  remain almost constant at around 150 nm, indicating colloidal stability within the whole range studied. For the Z-potential values, at low pH (3.2) the value is -21 mV and progressively becomes more negative when the pH is increased, reaching a maximum of -55 mV at pH 8.5. This agrees with the fact that the surface of the nanocomposites is surrounded by carboxylic acid moieties. At low pH (<4.5), they are mostly protonated, thus the Z-potential has a less negative value. As the pH increases more carboxylic group get deprotonated, and the NPs surface becomes more negative. Pictures of the solutions taken after 4 d show that the NPs crash out of solution in the case of  $\text{pH} \leq 4.5$  suggesting that electrostatic repulsion is the main factor contributing to the NPs colloidal stability.

Furthermore, stability tests were carried out at different NaCl concentrations (Figure 1.18). Initially, the  $D_H$  increases slightly when the concentration of NaCl is increased, with a  $D_H$  value of 173 nm in 300 mM NaCl solution. This suggests that the NaCl does not significantly affect the colloidal stability of NPs. The Z-potential value passed from -62 mV in ddH<sub>2</sub>O to -25 mV in 75 mM NaCl and remained almost constant also when the concentration of NaCl was increased to 300 mM. The less negative value observed in NaCl solution can be explained by the presence of Na<sup>+</sup> ions interacting with the

negative carboxylate moieties on the surface of the NPs. Pictures of the solutions

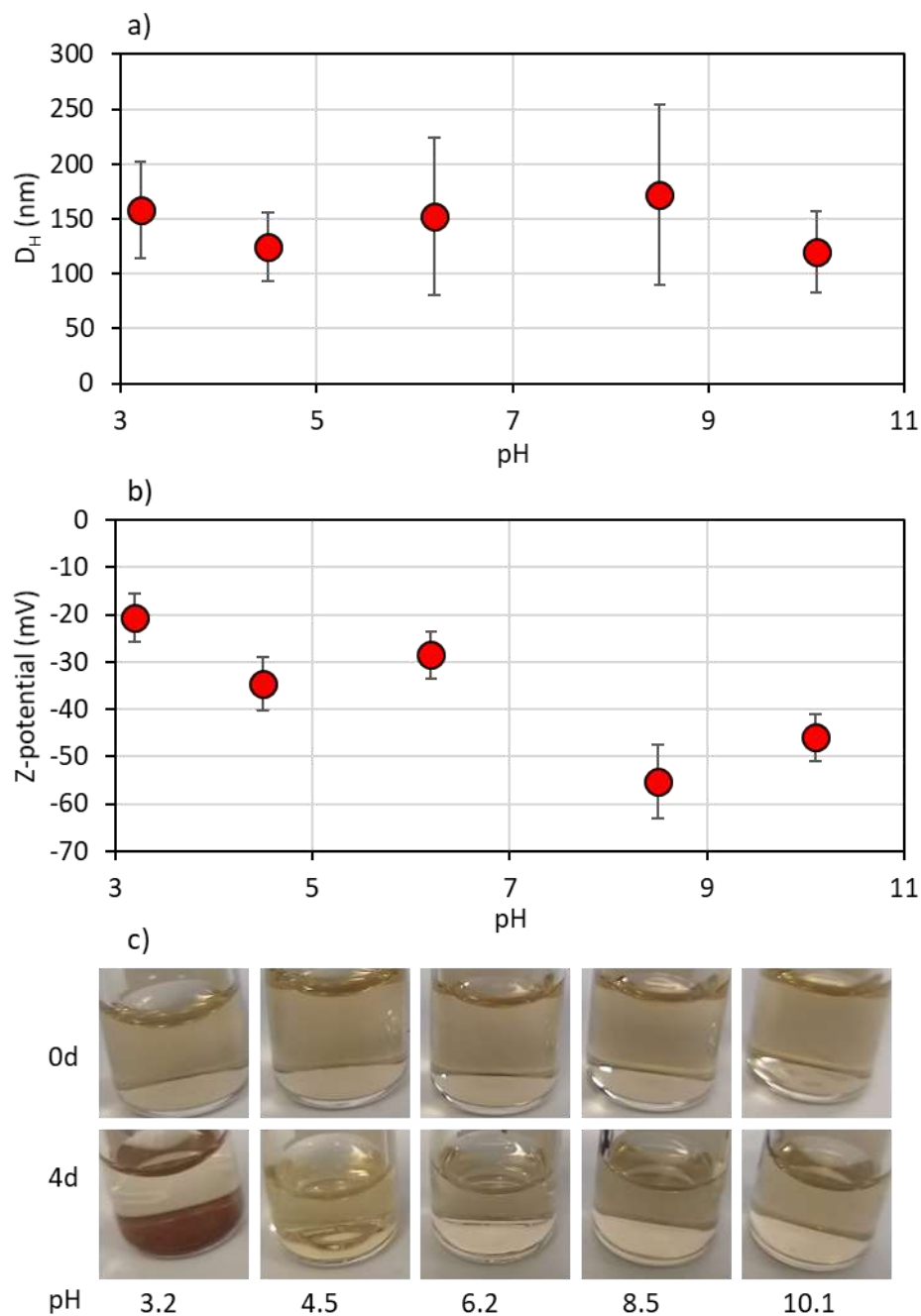


*Figure 5-17 Colloidal stability study of the Experiment XII (15.6 nm NPs) in different pH solutions: a) hydrodynamic diameter in different pH, b) zeta-potential value at different pH, c) picture of the dispersion at 0 and 4 d.*

taken after 4 d show that the NPs remain well dispersed in solution with no sign of aggregation observed.

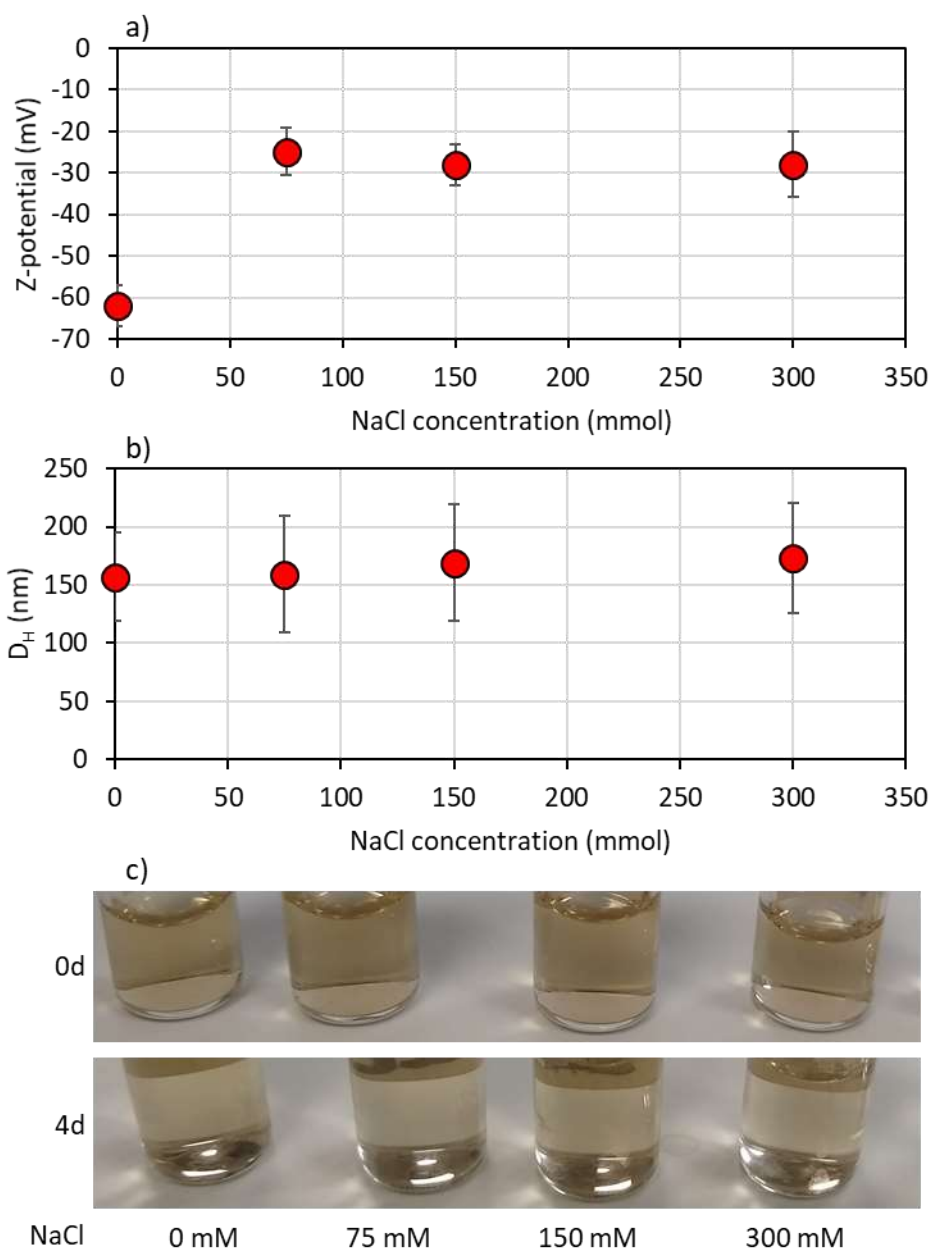


*Figure 5-18 Colloidal stability study of the Experiment XII (15.6 nm NPs) in NaCl solutions at various concentrations: a) zeta-potential value in different NaCl concentrations, b) hydrodynamic diameter in different NaCl concentrations, c) picture of the dispersion at 0 and 4 d.*

Overall, the system was found to be stable over a broad range of pH (pH 4.5 to pH 10) and up to 300 mM of NaCl solution which makes the system suitable for use in biomedical applications.

### 5.3.8 Magnetic hyperthermia

Finally, the heating efficiency of the two samples (Experiment IV, synthesised with no additional ligand in solution and Experiment XII, synthesised with additional 0.8 mmol of SO) was evaluated by magnetic hyperthermia measurement. For the Experiment IV (average NPs size of 24.4 nm) it was observed a SAR value of 372 W/g<sub>Fe</sub>, at 303 KHz used and 872 W/g<sub>Fe</sub> at 633 KHz used. For Experiment XII (average NPs size of 15.6 nm) it was obtained a SAR value of 164 W/g<sub>Fe</sub>, at 303 KHz used and 309 W/g<sub>Fe</sub> at 488 KHz used. For all the measurements reported, the field amplitude used was 24 KA m<sup>-2</sup>. The ILP value was then calculated to compare the outcomes of the sample taken at different conditions. For the 24.4 nm sample, the ILP was found to be 2.0 at lower frequency (303 KHz) and 2.2 at a higher frequency (633 KHz), showing little variation, as expected. For the 15.6 nm sample instead, the ILP was found to be 0.9 at a lower frequency (303 KHz) and 1.1 at a higher frequency (488 KHz). The value for bigger NPs is double the one for small NPs.

*Table 5-3 Magnetic Hyperthermia measurements for Experiment IV and XII and relative conditions used.*

<b>Measurement</b>	<b>Frequency (KHz)</b>	<b>Field (KA m<sup>-2</sup>)</b>	<b>SAR (W g<sup>-1</sup>)</b>	<b>ILP (nHm<sup>2</sup> kg<sup>-1</sup>)</b>
Experiment IV (d= 24.4 nm)	303	24.5	372	2.0
Experiment IV (d= 24.4 nm)	633	24.5	872	2.2
Experiment XII (d = 15.6 nm)	303	24.1	164	0.9
Experiment XII (d = 15.6 nm)	488	24.1	309	1.1

This is in line with the magnetic properties of the two samples where the 24.4 nm nanoplates possess an  $M_s$  double the one of 15.6 nm nanoplates, being therefore more performant in magnetic hyperthermia applications. In addition, the enhanced

heating power may be also linked to an increase in the Brownian contribution to the overall heating capability of the larger plates since it increases when the particle size increases.

The only report in the literature for similarly shaped NPs is for hexagonal nanoprism of 45 nm edge length.<sup>201</sup> The author reported that the material is highly heating and show a SAR of 765 W/g at 366 KHz and 5 KA m<sup>-2</sup>, the ILP value calculated from these parameters was 85 nHm<sup>2</sup> kg<sup>-1</sup>, which seems unrealistic suggesting a possible error in the reported conditions used. This does not allow to compare the results with the existing literature, however, the ILP of 2 is high enough to make Fe<sub>3</sub>O<sub>4</sub> nanoplates suitable for biomedical applications.<sup>91</sup>

#### 5.4 Conclusion

In this chapter anisotropic NPs have been synthesised. It was observed that chloride plays a fundamental role in the formation of plates NPs. It was investigated the possibility of controlling the size of the nanoplates, with SO resulting in the best ligand for it. Two samples with 24.4 nm (Experiment IV) and 15.6 nm (Experiment XII) nanoplates, with most of them having a triangular shape, were transferred in water via a ligand-exchange method with Mod-PIMA-Dopa. The magnetic hyperthermia outcomes of both samples were tested and the 24.4 nm nanoplates showed a higher efficiency as heating probes with an ILP of 2, compared to the smaller particles (ILP = 1). The study shows that the source of chloride can be used as an agent to induce anisotropic growth in nanocrystals. This is a novel and unexplored way for the synthesis of anisotropic Fe<sub>3</sub>O<sub>4</sub> NPs and has the potential to be further exploited for other shapes and materials, with the possibility to be easily scaled up, given the limited number of reagents and parameters to be controlled. Secondly, platelets NPs are also promising heating probes for magnetic hyperthermia with an ILP value of about 2 for NPs of 24.4 nm.

# Chapter 6 Conclusions and future works

## 6.1 Conclusions

In this thesis different kind of iron-based NPs were investigated as a possible tool in magnetic hyperthermia therapy. In particular, the NPs were made of metallic Fe, Fe<sub>2</sub>C alloy and Fe<sub>3</sub>O<sub>4</sub> with plates morphology.

Chapter 3 focused on how to control the size of Fe NPs and produce Fe NPs with an average diameter larger than 15 nm which had not been produced before. A novel synthetic strategy was developed adding the Fe(CO)<sub>5</sub> precursor in a continuous fashion. The method was able to form Fe NPs of different size and it allowed to push the growth of the nanocrystals in solution to an average size of ≈20 nm. Such improvement compared to the literature, allowed to study the resilience of Fe NPs in aqueous media. Indeed, metallic Fe is sensitive towards oxidation, but this process is size-dependent. After transferring the particles in water, it was confirmed that ≈18 nm Fe NPs were resilient towards oxidation, retaining an α-Fe core, while smaller NPs underwent deep oxidative process driven by the Kirkendall effect which eroded the α-Fe phase of the NPs. Such evidence was confirmed in MH testing.

Chapter 4, instead, focused on how to form uniform and fully-characterised Fe<sub>2</sub>C NPs of controlled composition in a single reaction step. In this chapter, the parameters affecting the formation of Fe<sub>2</sub>C were investigated, with the kind of amine used having the bigger effect on the uniformity of the final sample. Indeed, ODA resulted able to act as ligand and carbon source for the forming Fe<sub>2</sub>C NPs. After transferring the particles in water, it was confirmed that Fe<sub>2</sub>C NPs are resilient towards oxidation, with no difference between NPs before and after the ligand exchange. Indeed, Fe<sub>2</sub>C phase was resistant towards oxidation and did not require any specific size-tuning to be stable in biological conditions. As Fe<sub>2</sub>C NPs have been recently considered for biomedical applications, this study shed a light on the synthesis and characterisation of such material. The use of Octadecylamine and temperature of the carbidization process were shown to be the most important parameter affecting the uniformity of

Fe<sub>2</sub>C phase in NPs, with chloride amount and time of carbidization having a lesser impact.

Chapter 5 studied the possibility of obtaining plates-like Fe<sub>3</sub>O<sub>4</sub> NPs using Hexadecylammonium Chloride. It was shown that chloride ions from Hexadecylammonium Chloride played a fundamental role in the formation of twinned plane in the initial phase of NPs formation and this eventually led to the formation of plate-like NPs with the most common shape being the triangular one, among others. Specifically, to Fe<sub>3</sub>O<sub>4</sub> NPs, plates-like morphology has been rarely reported or not easily achieved. The synthetic method was simple and straightforward, and showing new avenues in the formation of anisotropic NPs can have wider implications on the literature as a whole.

To transfer to water all the NPs studied here, it was developed a polymeric ligand based on PIMA and functionalised with dopamine. As all the NPs were iron-based, dopamine was chosen for its high affinity towards Fe atoms. Indeed, the polymer can efficiently replace the native ligand and once the maleic anhydride moieties in the polymer are hydrolysed, the nanocomposite became water-soluble with also good colloidal stability thanks to its steric hinderance and ionic repulsion. The method proved to be working for any size of Fe NPs, Fe<sub>2</sub>C and for Fe<sub>3</sub>O<sub>4</sub> NPs of different size and plate-like morphology. Such findings are useful for the development of water-dispersible nanocomposites made of ferromagnetic and/or highly interacting magnetic NPs.

The magnetic hyperthermia potential was also evaluated for each kind of particle. Table 6.1 summarises the ILP values obtained for the materials synthesised in this work. Among the results achieved here, Fe NPs resulted as the most performant system in magnetic hyperthermia with an ILP of 3.6. Iron oxide based nanoplates can also be considered as efficient heating probes, especially considering the biggest sample (24 nm). Fe<sub>2</sub>C is the least performing materials among the one tested in this

work with an ILP value reaching 0.6. If we consider that the core active material for Fe<sub>2</sub>C is effectively of about 9 nm, the ILP obtained was very close to the one of the small nanoplates which are around 15 nm. This suggested that the it may be worth studying iron carbide NPs of large size to improve Fe<sub>2</sub>C NPs output in magnetic hyperthermia.

*Table 6-1 Summary of heating efficiency of different magnetic NPs*

<b>Sample</b>	<b>Coating</b>	<b>Material</b>	<b>Size (nm)</b>	<b>ILP (nHm<sup>2</sup> kg<sup>-1</sup>)</b>
Fe NPs 18 nm	Mod-PIMA-Dopa	Fe@Fe <sub>3</sub> O <sub>4</sub> core@shell	18	3.6
Fe NPs 18 nm (after 2 months)	Mod-PIMA-Dopa	Fe@Fe <sub>3</sub> O <sub>4</sub> core@shell	18	3.8
Fe <sub>2</sub> C	Mod-PIMA-Dopa	Fe <sub>2</sub> C@Fe <sub>3</sub> O <sub>4</sub> core@shell	14	0.6
Nanoplates	Mod-PIMA-Dopa	Fe <sub>3</sub> O <sub>4</sub>	15	1.1
Nanoplates	Mod-PIMA-Dopa	Fe <sub>3</sub> O <sub>4</sub>	24	2.2

## 6.2 Future works

The different magnetic NPs synthesised in this work constitute a step forward towards the development of nano-systems that could be designed and envisioned for clinical applications.

For the Fe NPs, which were the most performing NPs in this study, the next assessment would involve the study of their toxicity *in vitro* towards healthy cell. Furthermore, magnetic hyperthermia would be applied on different cell lines to test

the efficiency of each NPs system to kill cancer cell *in vitro*. Such kind of studies constitutes the next step to confirm the suitability of NPs for biomedical applications.

In the case of Fe<sub>2</sub>C NPs, further synthetic improvement are necessary to optimise the NPs for magnetic hyperthermia application. One of the parameters to control would be the size, which could be increased by following a similar strategy to Chapter 3 with Fe NPs, where a continuous injection of the precursor was used to produce 18 nm Fe NPs. Starting from larger Fe NPs would produce larger Fe<sub>2</sub>C NPs which could possess enhanced heating efficiency.

The synthetic protocol of anisotropic Fe<sub>3</sub>O<sub>4</sub> NPs, instead, needs to be further optimised. Although the magnetic hyperthermia outputs showed promising results with an ILP of 2.2 nHm<sup>2</sup> kg<sup>-1</sup>, a greater control on the final shape would allow to deepen the understanding of anisotropic NPs in relation to magnetic hyperthermia outputs. For example, it would be interesting to evaluate the effect of different chloride sources, heating rate and solvent on the final NPs shape and the following effect on magnetic hyperthermia outputs.

## Appendix: Publications and conferences attended

### Publications

- **Chemistry of Materials. 2018, 30, 24, 8897-8904**

**Simone Famiani**, Alec P. LaGrow, Maximilian O. Besenhard, Shinya Maenosono\*,  
Nguyen Thi Kim Thanh\*

*Synthesis of Fine-Tuning Highly Magnetic Fe@FexOy Nanoparticles through  
Continuous Injection and a Study of Magnetic Hyperthermia*

- **Reaction Chemistry & Engineering (under revision)**

Maximilian O. Besenhard, **Simone Famiani**, Alec P. LaGrow, Martina Pucciarelli, Paola  
Lettieri, Nguyen T.K. Thanh\* and Asterios Gavriilidis\*

*Continuous Production of Magnetic Iron Oxide Nanoparticles via Fast and Economical  
High Temperature Synthesis*

### Conferences

- **April 2016, EU COST Meeting, Synthesis and functionalisation of magnetic  
nanoparticles for magnetic hyperthermia and radiotherapy, London, (UK).** Oral  
presentation:

Simone Famiani, Shinya Maenosono, Nguyen T. K. Thanh. *Synthesis and  
characterization of Iron@Silica nanoparticles for magnetic hyperthermia*

- **May 2016, 2016 EU-Japan collaborative research on Next Generation Nanomagnetic Medicine, London (UK).** Oral presentation:

Simone Famiani, Shinya Maenosono, Nguyen T. K. Thanh. *Synthesis and characterization of Iron@Silica nanoparticles for magnetic hyperthermia*

- **May 2016, The 11th International Conference on the Scientific and Clinical Applications of Magnetic Carriers, Vancouver (Canada).** Poster presentation:

Simone Famiani, Shinya Maenosono, Nguyen T. K. Thanh. *Synthesis and characterization of Iron@Silica nanoparticles for magnetic hyperthermia*

- **March 2017, The 97th annual meeting 2015 of Chemical Society of Japan, Tokyo (Japan).** Talk presentation:

Simone Famiani, Shinya Maenosono, Nguyen T. K. Thanh. *Synthesis and Functionalization of Chemically-Stable Water-Dispersible Iron Nanoparticles*

- **August 2017, ICAM-MRS The 15<sup>th</sup> international conference on Advanced Materials, Kyoto (Japan).** Talk presentation:

Simone Famiani, Shinya Maenosono, Nguyen T. K. Thanh. *Synthesis and Functionalization of Chemically-Stable Water-Dispersible Iron Nanoparticles*

Poster presentation:

Simone Famiani, Shinya Maenosono, Nguyen T. K. Thanh. *Controlling the Size of Iron@Iron Oxide Nanoparticles through Continuous Injection of Precursor*

- March 2018, EU COST Meeting. Synthesis and functionalisation of magnetic nanoparticles for magnetic hyperthermia and radiotherapy, Timisoara (RO).

Attendance only

# Bibliography

- 1 A. Quarta, A. Curcio, H. Kakwere and T. Pellegrino, *Nanoscale*, 2012, **4**, 3319.
- 2 M. Takahashi, P. Mohan, A. Nakade, K. Higashimine, D. Mott, T. Hamada, K. Matsumura, T. Taguchi and S. Maenosono, *Langmuir*, 2015, **31**, 2228–2236.
- 3 A. Hervault and N. T. K. Thanh, *Nanoscale*, 2014, **6**, 11553–11573.
- 4 Cancer Statistics - National Cancer Institute, <https://www.cancer.gov/about-cancer/understanding/statistics>, (accessed 5 March 2019).
- 5 B. Pelaz, C. Alexiou, R. A. Alvarez-Puebla, F. Alves, A. M. Andrews, S. Ashraf, L. P. Balogh, L. Ballerini, A. Bestetti, C. Brendel, S. Bosi, M. Carril, W. C. W. Chan, C. Chen, X. Chen, X. Chen, Z. Cheng, D. Cui, J. Du, C. Dullin, A. Escudero, N. Feliu, M. Gao, M. George, Y. Gogotsi, A. Grünweller, Z. Gu, N. J. Halas, N. Hampp, R. K. Hartmann, M. C. Hersam, P. Hunziker, J. Jian, X. Jiang, P. Jungebluth, P. Kadhiresan, K. Kataoka, A. Khademhosseini, J. Kopeček, N. A. Kotov, H. F. Krug, D. S. Lee, C.-M. Lehr, K. W. Leong, X.-J. Liang, M. Ling Lim, L. M. Liz-Marzán, X. Ma, P. Macchiarini, H. Meng, H. Möhwald, P. Mulvaney, A. E. Nel, S. Nie, P. Nordlander, T. Okano, J. Oliveira, T. H. Park, R. M. Penner, M. Prato, V. Puntès, V. M. Rotello, A. Samarakoon, R. E. Schaak, Y. Shen, S. Sjöqvist, A. G. Skirtach, M. G. Soliman, M. M. Stevens, H.-W. Sung, B. Z. Tang, R. Tietze, B. N. Udugama, J. S. VanEpps, T. Weil, P. S. Weiss, I. Willner, Y. Wu, L. Yang, Z. Yue, Q. Zhang, Q. Zhang, X.-E. Zhang, Y. Zhao, X. Zhou and W. J. Parak, *ACS Nano*, 2017, **11**, 2313–2381.
- 6 X. Peng, J. Wickham and A. P. Alivisatos, *J. Am. Chem. Soc.*, 1998, **120**, 5343–5344.

- 7 Y. Yin and A. P. Alivisatos, *Nature*, 2005, **437**, 664–670.
- 8 J. Park, J. Joo, G. K. Soon, Y. Jang and T. Hyeon, *Angew. Chemie - Int. Ed.*, 2007, **46**, 4630–4660.
- 9 C. de Mello Donegá, P. Liljeroth and D. Vanmaekelbergh, *Small*, 2005, **1**, 1152–1162.
- 10 C. B. Murray, D. J. Norris and M. G. Bawendi, *J. Am. Chem. Soc.*, 1993, **115**, 8706–8715.
- 11 T. Hyeon, Su Seong Lee, J. Park, Y. Chung and Hyon Bin Na, *J. Am. Chem. Soc.*, 2001, **123**, 12798–12801.
- 12 J. Park, K. An, Y. Hwang, J.-G. Park, H.-J. Noh, J.-Y. Kim, J.-H. Park, N.-M. Hwang and T. Hyeon, , DOI:10.1038/nmat1251.
- 13 S. G. Kwon and T. Hyeon, *Small*, 2011, **7**, 2685–2702.
- 14 H. Reiss, *J. Chem. Phys.*, 1951, **19**, 482–487.
- 15 P. W. Voorhees, *J. Stat. Phys.*, 1985, **38**, 231–252.
- 16 E. C. Vreeland, J. Watt, G. B. Schober, B. G. Hance, M. J. Austin, A. D. Price, B. D. Fellows, T. C. Monson, N. S. Hudak, L. Maldonado-Camargo, A. C. Bohorquez, C. Rinaldi and D. L. Huber, *Chem. Mater.*, 2015, **27**, 6059–6066.
- 17 G. C. Bleier, J. Watt, C. K. Simocko, J. M. Lavin and D. L. Huber, *Angew. Chemie Int. Ed.*, 2018, **57**, 7678–7681.
- 18 J. Ren and R. D. Tilley, *J. Am. Chem. Soc.*, 2007, **129**, 3287–3291.
- 19 L. T. Lu, N. T. Dung, L. D. Tung, C. T. Thanh, O. K. Quy, N. V. Chuc, S. Maenosono and N. T. K. Thanh, *Nanoscale*, 2015, **7**, 19596–19610.
- 20 R. Hachani, M. Lowdell, M. Birchall, A. Hervault, D. Mertz, S. Begin-Colin and N. T. K. Thanh, *Nanoscale*, 2016, **8**, 3278–3287.
- 21 S. Carencio, C. Boissière, L. Nicole, C. Sanchez, P. Le Floch and N. Mézailles, *Chem. Mater.*, 2010, **22**, 1340–1349.
- 22 J. Park, E. Kang, S. U. Son, H. M. Park, M. K. Lee, J. Kim, K. W. Kim, H. J. Noh, J. H. Park, C. J. Bae, J. G. Park and T. Hyeon, *Adv. Mater.*, 2005, **17**, 429–434.
- 23 L. A. W. Green, T. T. Thuy, D. M. Mott, S. Maenosono and N. T. Kim Thanh, *RSC Adv.*, 2014, **4**, 1039.
- 24 A. Sathya, P. Guardia, R. Brescia, N. Silvestri, G. Pugliese, S. Nitti, L. Manna and T. Pellegrino, *Chem. Mater.*, 2016, 1–17.
- 25 A. Sathya, P. Guardia, R. Brescia, N. Silvestri, G. Pugliese, S. Nitti, L. Manna and T. Pellegrino, *Chem. Mater.*, 2016, **28**, 1769–1780.
- 26 Y. Zhang, M. E. Grass, J. N. Kuhn, F. Tao, S. E. Habas, W. Huang, P. Yang and G. A. Somorjai, *J. Am. Chem. Soc.*, 2008, **130**, 5868–5869.
- 27 † Yujie Xiong, † Honggang Cai, ‡ Benjamin J. Wiley, § Jinguo Wang, § and Moon J. Kim and † Younan Xia\*, , DOI:10.1021/JA0688023.
- 28 A. Demortière, P. Launois, N. Goubet, P.-A. Albouy and C. Petit, *J. Phys. Chem. B*, 2008, **112**, 14583–14592.
- 29 L.-M. Lacroix, N. Frey Huls, D. Ho, X. Sun, K. Cheng and S. Sun, *Nano Lett.*, 2011, **11**, 1641–1645.
- 30 C. Yang, H. Zhao, Y. Hou and D. Ma, *J. Am. Chem. Soc.*, 2012, **134**, 15814–15821.
- 31 S. Zhang, G. Jiang, G. T. Filsinger, L. Wu, H. Zhu, J. Lee, Z. Wu and S. Sun,

- Nanoscale*, 2014, **6**, 4852–4856.
- 32 C. J. Orendorff and C. J. Murphy, *J. Phys. Chem. B*, 2006, **110**, 3990–3994.
- 33 M. Liu and P. Guyot-Sionnest, *J. Phys. Chem. B*, 2005, **109**, 22192–22200.
- 34 R. M. Pallares, X. Su, S. H. Lim and N. T. K. Thanh, *J. Mater. Chem. C*, 2015, **4**, 53–61.
- 35 E. K., *Neoplasma*, 1994, **41**, 269–276.
- 36 H. R. Moyer and K. A. Delman, *Int. J. Hyperth.*, 2008, **24**, 251–261.
- 37 R. Cavaliere, E. C. Ciocatto, B. C. Giovanella, C. Heidelberger, R. O. Johnson, M. Margottini, B. Mondovi, G. Moricca and A. Rossi-Fanelli, *Cancer*, 1967, **20**, 1351–1381.
- 38 J. F. R. Kerr, C. M. Winterford and B. V Harmon, *Cancer*, 1994, **73**, 2013–2026.
- 39 C. J. Diederich, in *International Journal of Hyperthermia*, 2005, vol. 21, pp. 745–753.
- 40 P. Golstein and G. Kroemer, *Trends Biochem. Sci.*, 2007, **32**, 37–43.
- 41 R. K. Jain, *Nat. Med.*, 2001, **7**, 987–989.
- 42 C. W. Song, J. G. Rhee and S. H. Levitt, *JNCI J. Natl. Cancer Inst.*, 1980, **64**, 119–124.
- 43 E. E. Cumming and A. W. Diamond, *Can. Field-Naturalist*, 2002, **116**, 69–75.
- 44 A. Chicheł, J. Skowronek, M. Kubaszewska and M. Kanikowski, *Reports Pract. Oncol. Radiother.*, 2007, **12**, 267–275.
- 45 F. K. Storm, D. L. Morton, L. R. Kaiser, W. H. Harrison, R. S. Elliott, T. H. Weisenburger, R. G. Parker and C. M. Haskell, *Natl. Cancer Inst. Monogr.*, 1982, **61**, 343–50.
- 46 T. Motomura, K. Ueda, S. Ohtani, E. Hansen, L. Ji, K. Ito, K. Saito, Y. Sugita and Y. Nosé, *Oncol. Rep.*, 2010, **24**, 591–8.
- 47 H. Kakwere, M. E. Materia, A. Curcio, M. Prato, A. Sathya, S. Nitti and T. Pellegrino, *Nanoscale*, , DOI:10.1039/c7nr06726g.
- 48 D. Fourmy, J. Carrey and V. Gigoux, *Nanomedicine*, 2015, **10**, 893–896.
- 49 N. A. Spaldin, *Magnetic Materials*, Cambridge University Press, Cambridge, 2010, vol. 9780521886.
- 50 S. P. (Sergeï P. Gubin, *Magnetic nanoparticles*, Wiley-VCH, 2009.
- 51 L. Néel, *Adv. Phys.*, 1955, **4**, 191–243.
- 52 S. Mornet, S. Vasseur, F. Grasset and E. Duguet, *J. Mater. Chem.*, 2004, **14**, 2161.
- 53 J. M. D. Coey, *Magnetism and magnetic materials*, Cambridge University Press, Cambridge, 2010, vol. 9780521816.
- 54 R. Hergt, S. Dutz, R. Müller and M. Zeisberger, *J. Phys. Condens. Matter*, 2006, **18**, S2919–S2934.
- 55 Q. A. Pankhurst, J. Connolly, S. K. Jones and J. Dobson, *J. Phys. D. Appl. Phys.*, 2003, **36**, R167–R181.
- 56 C. Blanco-Andujar, A. Walter, G. Cotin, C. Bordeianu, D. Mertz, D. Felder-Flesch and S. Bégin-Colin, *Nanomedicine*, 2016, **11**, 1889–1910.
- 57 A. Demortière, P. Panissod, B. P. Pichon, G. Pourroy, D. Guillon, B. Donnio and S. Bégin-Colin, *Nanoscale*, 2011, **3**, 225–232.

- 58 R. Di Corato, A. Espinosa, L. Lartigue, M. Tharaud, S. Chat, T. Pellegrino, C. Ménager, F. Gazeau and C. Wilhelm, *Biomaterials*, 2014, **35**, 6400–6411.
- 59 R. E. Rosensweig, *J. Magn. Magn. Mater.*, 2002, **252**, 370–374.
- 60 M. Kallumadil, M. Tada, T. Nakagawa, M. Abe, P. Southern and Q. A. Pankhurst, *J. Magn. Magn. Mater.*, 2009, **321**, 1509–1513.
- 61 A. Muela, D. Muñoz, R. Martín-Rodríguez, I. Orue, E. Garaio, A. Abad Díaz de Cerio, J. Alonso, J. Á. García and M. L. Fdez-Gubieda, *J. Phys. Chem. C*, 2016, **120**, 24437–24448.
- 62 R. Hergt and S. Dutz, *J. Magn. Magn. Mater.*, 2007, **311**, 187–192.
- 63 B. Mehdaoui, A. Meffre, L. M. Lacroix, J. Carrey, S. Lachaize, M. Gougeon, M. Respaud and B. Chaudret, *J. Magn. Magn. Mater.*, 2010, **322**, L49–L52.
- 64 R. Hergt, R. Hiergeist, M. Zeisberger, G. Glöckl, W. Weitschies, L. . Ramirez, I. Hilger and W. . Kaiser, *J. Magn. Magn. Mater.*, 2004, **280**, 358–368.
- 65 B. Mehdaoui, A. Meffre, J. Carrey, S. Lachaize, L. M. Lacroix, M. Gougeon, B. Chaudret and M. Respaud, *Adv. Funct. Mater.*, 2011, **21**, 4573–4581.
- 66 S. A. Majetich, T. Wen and O. T. Mefford, *MRS Bull.*, 2013, **38**, 899–903.
- 67 A. H. Habib, C. L. Ondeck, P. Chaudhary, M. R. Bockstaller and M. E. McHenry, *J. Appl. Phys.*, 2008, **103**, 305–308.
- 68 I. Sharifi, H. Shokrollahi and S. Amiri, *J. Magn. Magn. Mater.*, 2012, **324**, 903–915.
- 69 A. G. Kolhatkar, A. C. Jamison, D. Litvinov, R. C. Willson and T. R. Lee, *Tuning the magnetic properties of nanoparticles*, 2013, vol. 14.
- 70 V. Marneli, A. Musinu, A. Ardu, G. Ennas, D. Peddis, D. Niznansky, C. Sangregorio, C. Innocenti, N. T. K. Thanh and C. Cannas, *Nanoscale*, 2016, **8**, 10124–10137.
- 71 A. López-Ortega, M. Estrader, G. Salazar-Alvarez, A. G. Roca and J. Nogués, *Phys. Rep.*, 2015, **553**, 1–32.
- 72 J. H. Lee, J. T. Jang, J. S. Choi, S. H. Moon, S. H. Noh, J. W. Kim, J. G. Kim, I. S. Kim, K. I. Park and J. Cheon, *Nat. Nanotechnol.*, 2011, **6**, 418–422.
- 73 J. T. Jang, H. Nah, J. H. Lee, S. H. Moon, M. G. Kim and J. Cheon, *Angew. Chemie - Int. Ed.*, 2009, **48**, 1234–1238.
- 74 Z. Yang, T. Zhao, X. Huang, X. Chu, T. Tang, Y. Ju, Q. Wang, Y. Hou and S. Gao, *Chem. Sci.*, 2017, **8**, 473–481.
- 75 D. L. Huber, *Small*, 2005, **1**, 482–501.
- 76 D. Farrell, S. A. Majetich and J. P. Wilcoxon, , DOI:10.1021/jp0351831.
- 77 A. Shavel, B. Rodríguez-González, M. Spasova, M. Farle and L. M. Liz-Marzán, *Adv. Funct. Mater.*, 2007, **17**, 3870–3876.
- 78 W. Pei, S. Kakibe, I. Ohta and M. Takahashi, in *IEEE Transactions on Magnetics*, 2005, vol. 41, pp. 3391–3393.
- 79 L. M. Lacroix, S. Lachaize, A. Falqui, M. Respaud and B. Chaudret, *J. Am. Chem. Soc.*, 2009, **131**, 549–557.
- 80 H. Yang, F. Ito, D. Hasegawa, T. Ogawa and M. Takahashi, *J. Appl. Phys.*, 2007, **101**, 09J112.
- 81 S. Peng, C. Wang, J. Xie and S. Sun, *J. Am. Chem. Soc.*, 2006, **128**, 10676–10677.

- 82 A. Meffre, B. Mehdaoui, V. Kelsen, P. F. Fazzini, J. Carrey, S. Lachaize, M. Respaud and B. Chaudret, *Nano Lett.*, 2012, **12**, 4722–4728.
- 83 C. G. Hadjipanayis, M. J. Bonder, S. Balakrishnan, X. Wang, H. Mao and G. C. Hadjipanayis, *Small*, 2008, **4**, 1925–1929.
- 84 D. A. J. Herman, P. Ferguson, S. Cheong, I. F. Hermans, B. J. Ruck, K. M. Allan, S. Prabakar, J. L. Spencer, C. D. Lendrum and R. D. Tilley, *Chem. Commun. Chem. Commun*, 2011, **47**, 9221–9223.
- 85 S. Cheong, P. Ferguson, K. W. Feindel, I. F. Hermans, P. T. Callaghan, C. Meyer, A. Slocombe, C. H. Su, F. Y. Cheng, C. S. Yeh, B. Ingham, M. F. Toney and R. D. Tilley, *Angew. Chemie - Int. Ed.*, 2011, **50**, 4206–4209.
- 86 D. A. J. Herman, S. Cheong-Tilley, A. J. McGrath, B. F. P. McVey, M. Lein and R. D. Tilley, *Nanoscale*, 2015, **7**, 5951–4.
- 87 F. Dumestre, B. Chaudret, C. Amiens, P. Renaud and P. Fejes, *Science (80-. )*, 2004, **303**, 821–823.
- 88 C. Martinez-Boubeta, K. Simeonidis, A. Makridis, M. Angelakeris, O. Iglesias, P. Guardia, A. Cabot, L. Yedra, S. Estradé, F. Peiró, Z. Saghi, P. A. Midgley, I. Conde-Leborán, D. Serantes and D. Baldomir, *Sci. Rep.*, 2013, **3**, 1652.
- 89 K. Kohara, S. Yamamoto, L. Seinberg, T. Murakami, M. Tsujimoto, T. Ogawa, H. Kurata, H. Kageyama and M. Takano, *Chem. Commun.*, 2013, **49**, 2563.
- 90 M. Li, X. Chen, J. Guan, X. Wang, J. Wang, C. T. Williams and C. Liang, *J. Mater. Chem.*, 2012, **22**, 609–616.
- 91 C. Blanco-Andujar, A. Walter, G. Cotin, C. Bordeianu, D. Mertz, D. Felder-Flesch and S. Begin-Colin, *Nanomedicine*, 2016, **11**, 1889–1910.
- 92 H. L. Ding, Y. X. Zhang, S. Wang, J. M. Xu, S. C. Xu and G. H. Li, *Chem. Mater.*, 2012, **24**, 4572–4580.
- 93 A. Glaria, S. Soulé, N. Hallali, W.-S. Ojo, M. Mirjolet, G. Fuks, A. Cornejo, J. Allouche, J. C. Dupin, H. Martinez, J. Carrey, B. Chaudret, F. Delpech, S. Lachaize and C. Nayral, *RSC Adv.*, 2018, **8**, 32146–32156.
- 94 V. Davydov, A. Rakhmanina, I. Kireev, I. Alieva, O. Zhironkina, O. Strelkova, V. Dianova, T. D. Samani, K. Mireles, L. 'Hocine Yahia, R. Uzbekov, V. Agafonov and V. Khabashesku, *J. Mater. Chem. B*, 2014, **2**, 4250–4261.
- 95 V. Amendola, P. Riello and M. Meneghetti, *J. Phys. Chem. C*, 2011, **115**, 5140–5146.
- 96 Z. Schnepf, S. C. Wimbush, M. Antonietti and C. Giordano, *Chem. Mater.*, 2010, **22**, 5340–5344.
- 97 G. Huang, J. Hu, H. Zhang, Z. Zhou, X. Chi and J. Gao, *Nanoscale*, 2014, **6**, 726–730.
- 98 J. Yu, C. Yang, J. Li, Y. Ding, L. Zhang, M. Z. Yousaf, J. Lin, R. Pang, L. Wei, L. Xu, F. Sheng, C. Li, G. Li, L. Zhao and Y. Hou, *Adv. Mater.*, 2014, **26**, 4114–4120.
- 99 J. Yu, Y. Ju, L. Zhao, X. Chu, W. Yang, Y. Tian, F. Sheng, J. Lin, F. Liu, Y. Dong and Y. Hou, *ACS Nano*, 2016, **10**, 159–169.
- 100 J. Yu, F. Chen, W. Gao, Y. Ju, X. Chu, S. Che, F. Sheng and Y. Hou, *Nanoscale Horiz.*, 2017, **2**, 81–88.
- 101 A. Bordet, L.-M. Lacroix, P.-F. Fazzini, J. Carrey, K. Soulantica and B. Chaudret,

- Angew. Chemie Int. Ed.*, 2016, **55**, 15894–15898.
- 102 T. Hyeon, *Chem. Commun.*, 2003, **0**, 927–934.
- 103 T.K.N. Thanh (Ed.), *CRC Press*, 2012, 584.
- 104 C. Grüttner, K. Müller, J. Teller and F. Westphal, *Int. J. Hyperth.*, 2013, **29**, 777–789.
- 105 S. Vikram, M. Dhakshnamoorthy, R. Vasanthakumari, A. R. Rajamani, M. Rangarajan and T. Tsuzuki, *J. Nanosci. Nanotechnol.*, 2015, **15**, 3870–8.
- 106 H. Rui, R. Xing, Z. Xu, Y. Hou, S. Goo and S. Sun, *Adv. Mater.*, 2010, **22**, 2729–2742.
- 107 S. Mourdikoudis and L. M. Liz-Marzán, *Chem. Mater.*, 2013, **25**, 1465–1476.
- 108 A. B. Salunkhe, V. M. Khot and S. H. Pawar, *Curr. Top. Med. Chem.*, 2014, **14**, 572–594.
- 109 D. Ortega and Q. A. Pankhurst, 2013, **1**, 60–88.
- 110 E. C. Vreeland, J. Watt, G. B. Schober, B. G. Hance, M. J. Austin, A. D. Price, B. D. Fellows, T. C. Monson, N. S. Hudak, L. Maldonado-camargo, A. C. Bohorquez, C. Rinaldi and D. L. Huber, *Chem. Mater.*, 2015, **27**, 6059–6066.
- 111 Z. Nematy, J. Alonso, I. Rodrigo, R. Das, E. Garaio, J. Á. García, I. Orue, M. H. Phan and H. Srikanth, *J. Phys. Chem. C*, 2018, **122**, 2367–2381.
- 112 P. Guardia, R. Di Corato, L. Lartigue, C. Wilhelm, A. Espinosa, M. Garcia-Hernandez, F. Gazeau, L. Manna and T. Pellegrino, *ACS Nano*, 2012, **6**, 3080–3091.
- 113 M. Darbandi, F. Stromberg, J. Landers, N. Reckers, B. Sanyal, W. Keune and H. Wende, *J. Phys. D. Appl. Phys.*, , DOI:10.1088/0022-3727/45/19/195001.
- 114 S. Mørup, E. Brok and C. Frandsen, *J. Nanomater.*, 2013, **2013**, 1–8.
- 115 D. Serantes, K. Simeonidis, M. Angelakeris, O. Chubykalo-Fesenko, M. Marciello, M. del P. Morales, D. Baldomir and C. Martinez-Boubeta, *J. Phys. Chem. C*, 2014, **118**, 5927–5934.
- 116 Y. Lv, Y. Yang, J. Fang, H. Zhang, E. Peng, X. Liu, W. Xiao and J. Ding, , DOI:10.1039/c5ra12558h.
- 117 P. Hugounenq, M. Levy, D. Alloyeau, L. Lartigue, E. Dubois, V. Cabuil, C. Ricolleau, S. Roux, C. Wilhelm, F. Gazeau and R. Bazzi, *J. Phys. Chem. C*, 2012, **116**, 15702–15712.
- 118 G. Lee, *J. Anal. Sci. Technol.*, 2010, **1**, 130–133.
- 119 V. Salgueiriño-Maceira, L. M. Liz-Marzán and M. Farle, *Langmuir*, 2004, **20**, 6946–6950.
- 120 A. Dong, X. Ye, J. Chen, Y. Kang, T. Gordon, J. M. Kikkawa and C. B. Murray, *J. Am. Chem. Soc.*, 2011, **133**, 998–1006.
- 121 C. Xu, K. Xu, H. Gu, R. Zheng, H. Liu, X. Zhang, Z. Guo and B. Xu, *J. Am. Chem. Soc.*, 2004, **126**, 9938–9939.
- 122 W. Wang, X. Ji, H. Bin Na, M. Safi, A. Smith, G. Palui, J. M. Perez and H. Mattoussi, *Langmuir*, 2014, **30**, 6197–6208.
- 123 P. Guardia, A. Riedinger, S. Nitti, G. Pugliese, S. Marras, A. Genovese, M. E. Materia, C. Lefevre, L. Manna and T. Pellegrino, *J. Mater. Chem. B*, 2014, **2**, 4426.

- 124 A. Lassenberger, O. Bixner, T. Gruenewald, H. Lichtenegger, R. Zirbs and E. Reimhult, *Langmuir*, 2016, **32**, 4259–4269.
- 125 R. Di Corato, A. Quarta, P. Piacenza, A. Ragusa, A. Figuerola, R. Buonsanti, R. Cingolani, L. Manna and T. Pellegrino, *J. Mater. Chem.*, 2008, **18**, 1991.
- 126 J. Liu, J. P. Larson, H. Liu, F. Peale, M. P. Bruchez, X. Wu, K. N. Haley, N. Ge and J. A. Treadway, *Nat. Biotechnol.*, 2003, **21**, 41–46.
- 127 H. M. Yang, H. J. Lee, K. S. Jang, C. W. Park, H. W. Yang, W. Do Heo and J. D. Kim, *J. Mater. Chem.*, 2009, **19**, 4566–4574.
- 128 R. J. Hickey, A. S. Haynes, J. M. Kikkawa and S. J. Park, *J. Am. Chem. Soc.*, 2011, **133**, 1517–1525.
- 129 W. J. Parak, P.-Y. Li, M. Zanella, R. A. Sperling, T.-Y. Yang, C.-A. J. Lin, W. H. Chang and J. K. Li, *Small*, 2008, **4**, 334–341.
- 130 D. Jańczewski, N. Tomczak, M. Y. Han and G. J. Vancso, *Nat. Protoc.*, 2011, **6**, 1546–1553.
- 131 T. Pellegrino, L. Manna, S. Kudera, T. Liedl, D. Koktysh, A. L. Rogach, S. Keller, J. Rädler, G. Natile and W. J. Parak, *Nano Lett.*, 2004, **4**, 703–707.
- 132 M. Moros, B. Pelaz, P. López-Larrubia, M. L. García-Martin, V. Grazú and J. M. de la Fuente, *Nanoscale*, 2010, **2**, 1746.
- 133 S. R. Deka, A. Quarta, R. Di Corato, A. Riedinger, R. Cingolani and T. Pellegrino, *Nanoscale*, 2011, **3**, 619–629.
- 134 W. W. Yu, E. Chang, J. C. Falkner, J. Zhang, a M. Al-Somali, C. M. Sayes, J. Johns, R. Drezek and V. L. Colvin, *J. Am. Chem. Soc.*, 2007, **129**, 2871–2879.
- 135 L. M. Bronstein, E. V. Shtykova, A. Malyutin, J. C. Dyke, E. Gunn, X. Gao, B. Stein, P. V. Konarev, B. Dragnea and D. I. Svergun, *J. Phys. Chem. C*, 2010, **114**, 21900–21907.
- 136 E. E. Lees, T. L. Nguyen, A. H. A. Clayton and P. Mulvaney, *ACS Nano*, 2009, **3**, 1121–1128.
- 137 F. Zhang, E. Lees, F. Amin, P. Rivera-Gil, F. Yang, P. Mulvaney and W. J. Parak, *Small*, 2011, **7**, 3113–3127.
- 138 L. Latterini and L. Tarpani, *J. Phys. Chem. C*, 2011, **115**, 21098–21104.
- 139 P. Qiu, C. Jensen, N. Charity, R. Towner and C. Mao, *J. Am. Chem. Soc.*, 2010, **132**, 17724–17732.
- 140 H. Tan, J. M. Xue, B. Shuter, X. Li and J. Wang, *Adv. Funct. Mater.*, 2010, **20**, 722–731.
- 141 J. Kim, J. E. Lee, J. Lee, J. H. Yu, B. C. Kim, K. An, Y. Hwang, C. H. Shin, J. G. Park, J. Kim and T. Hyeon, *J. Am. Chem. Soc.*, 2006, **128**, 688–689.
- 142 P. G. Rudakovskaya, V. M. Gerasimov, O. N. Metelkina, E. K. Beloglazkina, N. V. Zyk, A. G. Savchenko, I. V. Shchetinin, S. V. Salikhov, M. A. Abakumov, N. L. Klyachko, Y. I. Golovin and A. G. Mazhuga, *Nanotechnologies Russ.*, 2015, **10**, 896–903.
- 143 J. C. Park, D. A. Gilbert, K. Liu and A. Y. Louie, *J. Mater. Chem.*, 2012, **22**, 8449–8454.
- 144 M. Giersig and G. B. Khomutov, *NATO Sci. Peace Secur. Ser. B Phys. Biophys.*, 2008, 187.

- 145 E. Mansfield, D. L. Kaiser, D. Fujita and M. Van de Voorde, *Metrology and Standardization of Nanotechnology*, John Wiley & Sons, Incorporated, 2017.
- 146 D5 CoilSets | nB nanoScale Biomagnetics, <http://www.nbnanoscale.com/d5-coilsets/>, (accessed 12 March 2019).
- 147 J. W. Fleming and J. Chamberlain, *Infrared Phys.*, 1974, **14**, 277–292.
- 148 H. Khurshid, S. Chandra, W. Li, M. H. Phan, G. C. Hadjipanayis, P. Mukherjee and H. Srikanth, *J. Appl. Phys.*, 2013, **113**, 17B508.
- 149 D. L. Huber, E. L. Venturini, J. E. Martin, P. P. Provencio and R. J. Patel, *J. Magn. Mater.*, 2004, **278**, 311–316.
- 150 Z. Zhou, Y. Sun, J. Shen, J. Wei, C. Yu, B. Kong, W. Liu, H. Yang, S. Yang and W. Wang, *Biomaterials*, 2014, **35**, 7470–7478.
- 151 K. Matsumura, M. Takakura, H. Arai and T. Taguchi, *ACS Omega*, 2017, **2**, 4929–4937.
- 152 S. Cheong, P. Ferguson, I. F. Hermans, G. N. L. Jameson, S. Prabakar, D. A. J. Herman and R. D. Tilley, *Chempluschem*, 2012, **77**, 135–140.
- 153 Z. Nemati, J. Alonso, H. Khurshid, M. H. Phan and H. Srikanth, *RSC Adv.*, 2016, **6**, 38697–38702.
- 154 W. Wang, X. Ji, H. Bin Na, M. Safi, A. Smith, G. Palui, J. M. Perez and H. Mattoussi, *Langmuir*, 2014, **30**, 6197–6208.
- 155 M. Takahashi, K. Higashimine, P. Mohan, D. M. Mott and S. Maenosono, *CrystEngComm*, 2015, **17**, 6923–6929.
- 156 V. K. Lamer and R. H. Dinegar, *J. Am. Chem. Soc.*, 1950, **72**, 4847–4854.
- 157 A. P. Lagrow, B. Ingham, M. F. Toney and R. D. Tilley, *J. Phys. Chem. C*, 2013, **117**, 16709–16718.
- 158 J. Santoyo Salazar, L. Perez, O. De Abril, L. T. Phuoc, D. Ihiawakrim, M. Vazquez, J.-M. Greneche, S. Begin-Colin and G. Pourroy, *Chem. Mater.*, 2011, **23**, 1379–1386.
- 159 S. A. Majetich\*, T. Wen and O. T. Mefford\*, *MRS Bull.*, 2013, **38**, 899–903.
- 160 M. P. Morales, S. Veintemillas-Verdaguer, M. I. Montero, C. J. Serna, A. Roig, L. Casas, B. Martínez and F. Sandiumenge, *Chem. Mater.*, 1999, **11**, 3058–3064.
- 161 A. J. McGrath, S. Cheong, A. M. Henning, J. J. Gooding and R. D. Tilley, *Chem. Commun.*, 2017, **53**, 11548–11551.
- 162 S. Foglia, M. Ledda, D. Fioretti, G. Iucci, M. Papi, G. Capellini, M. G. Lolli, S. Grimaldi, M. Rinaldi and A. Lisi, *Nat. Publ. Gr.*, , DOI:10.1038/srep46513.
- 163 N. S. Karan, A. M. Keller, S. Sampat, O. Roslyak, A. Arefin, C. J. Hanson, J. L. Casson, A. Desiredy, Y. Ghosh, A. Piryatinski, R. Iyer, H. Htoon, A. V. Malko and J. A. Hollingsworth, *Chem. Sci.*, 2015, **6**, 2224–2236.
- 164 E. Valeur and M. Bradley, *Chem. Soc. Rev.*, 2009, **38**, 606–631.
- 165 C. A. G. N. Montalbetti and V. Falque, *Tetrahedron*, 2005, **61**, 10827–10852.
- 166 S. Y. Hong, D. H. Chun, J.-I. Yang, H. Jung, H.-T. Lee, S. Hong, S. Jang, J. T. Lim, C. S. Kim and J. C. Park, *Nanoscale*, 2015, **7**, 16616–16620.
- 167 K. Xu, B. Sun, J. Lin, W. Wen, Y. Pei, S. Yan, M. Qiao, X. Zhang and B. Zong, *Nat. Commun.*, 2014, **5**, 5783.
- 168 X. W. Liu, Z. Cao, S. Zhao, R. Gao, Y. Meng, J. X. Zhu, C. Rogers, C. F. Huo, Y.

- Yang, Y. W. Li and X. D. Wen, *J. Phys. Chem. C*, 2017, **121**, 21390–21396.
- 169 W. Tang, Z. Zhen, C. Yang, L. Wang, T. Cowger, H. Chen, T. Todd, K. Hekmatyar, Q. Zhao, Y. Hou and J. Xie, *Small*, 2014, **10**, 1245–1249.
- 170 S. Famiani, A. P. Lagrow, M. O. Besenhard, S. Maenosono and N. T. K. Thanh, *Chem. Mater.*, 2018, **30**, 8897–8904.
- 171 S. Yao, C. Yang, H. Zhao, S. Li, L. Lin, W. Wen, J. Liu, G. Hu, W. Li, Y. Hou and D. Ma, *J. Phys. Chem. C*, 2017, **121**, 5154–5160.
- 172 D. Hatchell, O. Namjoshi, K. Fischer and G. T. Rochelle, in *Energy Procedia*, 2014, vol. 63, pp. 1558–1568.
- 173 C. M. Wang, D. R. Baer, J. E. Amonette, M. H. Engelhard, J. J. Antony and Y. Qiang, *Ultramicroscopy*, 2007, **108**, 43–51.
- 174 P. Mohan, M. Takahashi, K. Higashimine, D. Mott and S. Maenosono, *Langmuir*, 2017, **33**, 1687–1694.
- 175 J.-J. Kim, K. Kobayashi, E. Ikenaga, M. Kobata, S. Ueda, T. Matsunaga, K. Kifune, R. Kojima and N. Yamada, *Phys. Rev. B*, 2007, **76**, 115124.
- 176 J. Hodkiewicz, *Characterizing Carbon Materials with Raman Spectroscopy*, .
- 177 A. Bordet, R. F. Landis, Y. Lee, G. Y. Tonga, J. M. Asensio, C.-H. Li, P.-F. Fazzini, K. Soulantica, V. M. Rotello and B. Chaudret, , DOI:10.1021/acsnano.8b05671.
- 178 J. M. Asensio, J. Marbaix, N. Mille, L. M. Lacroix, K. Soulantica, P. F. Fazzini, J. Carrey and B. Chaudret, *Nanoscale*, 2019, **11**, 5402–5411.
- 179 E. Myrovali, N. Maniotis, A. Makridis, A. Terzopoulou, V. Ntomprougkidis, K. Simeonidis, D. Sakellari, O. Kalogirou, T. Samaras, R. Salikhov, M. Spasova, M. Farle, U. Wiedwald and M. Angelakeris, *Sci. Rep.*, 2016, **6**, 1–11.
- 180 S. C. Kim, Y. Hwang, J.-G. Park, T. Hyeon, J. Park, H.-J. Noh, E. Lee, J.-Y. Kim, J.-H. Park, N.-M. Hwang and M. Kang, *Angew. Chemie Int. Ed.*, 2005, **44**, 2872–2877.
- 181 D. Kim, N. Lee, M. Park, B. H. Kim, K. An and T. Hyeon, *J. Am. Chem. Soc.*, 2009, **131**, 454–455.
- 182 S. Palchoudhury, Y. Xu, J. Goodwin and Y. Bao, in *Journal of Applied Physics*, American Institute of Physics, 2011, vol. 109, p. 07E314.
- 183 L. M. Bronstein, J. E. Atkinson, A. G. Malyutin, F. Kidwai, B. D. Stein, D. G. Morgan, J. M. Perry and J. A. Karty, *Langmuir*, 2011, **27**, 3044–3050.
- 184 A. Orza, H. Wu, Y. Xu, Q. Lu and H. Mao, *ACS Appl. Mater. Interfaces*, 2017, **9**, 20719–20727.
- 185 J. Wu, H. Liao, L. Zhang, S. Gao and Y. Hou, *Chem. Commun.*, 2009, **0**, 4378.
- 186 J. Cheon, N.-J. Kang, S.-M. Lee, J.-H. Lee, J.-H. Yoon and S. J. Oh, *J. Am. Chem. Soc.*, 2004, **126**, 1950–1951.
- 187 A. Lak, D. Niculaes, G. C. Anyfantis, G. Bertoni, M. J. Barthel, S. Marras, M. Cassani, S. Nitti, A. Athanassiou, C. Giannini and T. Pellegrino, *Sci. Rep.*, 2016, **6**, 33295.
- 188 Z. Zhao, Z. Zhou, J. Bao, Z. Wang, J. Hu, X. Chi, K. Ni, R. Wang, X. Chen, Z. Chen and J. Gao, *Nat. Commun.*, 2013, **4**, 1–7.
- 189 Y. Yu, W. Yang, X. Sun, W. Zhu, X. Z. Li, D. J. Sellmyer and S. Sun, *Nano Lett.*, 2014, **14**, 2778–2782.

- 190 Y. Xia, Y. Xiong, B. Lim and S. E. Skrabalak, *Angew. Chemie - Int. Ed.*, 2009, **48**, 60–103.
- 191 B. Ingham, T. H. Lim, C. J. Dotzler, A. Henning, M. F. Toney and R. D. Tilley, *Chem. Mater.*, 2011, **23**, 3312–3317.
- 192 M. Imran, V. Caligiuri, M. Wang, L. Goldoni, M. Prato, R. Krahne, L. De Trizio and L. Manna, *J. Am. Chem. Soc.*, 2018, **140**, 2656–2664.
- 193 D. Ingerter, J. Li, V. Germain, M. P. Pileni and Z. L. Wang, *J. Phys. Chem. B*, 2003, **107**, 8717–8720.
- 194 V. Radmilovic, C. J. D. Hetherington, U. Dahmen, S. Q. Xiao, E. Johnson and C. P. Luo, *Microsc. Microanal.*, 2002, **8**, 247–256.
- 195 Y. Xiong, A. R. Siekkinen, J. Wang, Y. Yin, M. J. Kim and Y. Xia, *J. Mater. Chem.*, 2007, **17**, 2600–2602.
- 196 P.-F. Ho and K.-M. Chi, *Nanotechnology*, 2004, **15**, 1059–1064.
- 197 B. Lim, P. H. C. Camargo and Y. Xia, *Langmuir*, 2008, **24**, 10437–10442.
- 198 Y. Xiong, Y. Yin, Y. Xia, Z.-Y. Li, J. Chen and J. M. McLellan, *J. Am. Chem. Soc.*, 2005, **127**, 17118–17127.
- 199 Z. Li, J. F. Godsell, J. P. O’byrne, N. Petkov, M. A. Morris, S. Roy and J. D. Holmes, , DOI:10.1021/ja105079y.
- 200 X. Peng, Z. Jiang, S. Wei, W. Liu, M. Jiang, X. Yang and T. Yao, *ACS Nano*, 2015, **9**, 10950–10960.
- 201 H. Wang, T. B. Shrestha, M. T. Basel, M. Pyle, Y. Toledo, A. Konecny, P. Thapa, M. Ikenberry, K. L. Hohn, V. Chikan, D. L. Troyer and S. H. Bossmann, *J. Mater. Chem. B*, 2015, **3**, 4647–4653.
- 202 C. Lofton and W. Sigmund, , DOI:10.1002/adfm.200400091.
- 203 G. Palui, F. Aldeek, W. Wang and H. Mattoussi, *Chem. Soc. Rev.*, 2015, **44**, 193–227.
- 204 Z. Xu, Z. Wei, P. He, X. Duan, Z. Yang, Y. Zhou and D. Jia, *Chem. Commun.*, 2017, **53**, 11052–11055.
- 205 Y. Ma, X. Liu, D.-L. Peng, D. Zeng, L.-S. Wang, Q. Zhang, K. Cao, Y. Chen and X. Liu, *Mater. Chem. Phys.*, 2017, **192**, 339–348.
- 206 C. Blanco-Andujar, D. Ortega, P. Southern, Q. A. Pankhurst and N. T. K. Thanh, *Nanoscale*, 2015, **7**, 1768–1775.